

UNIVERSITY OF CALIFORNIA

SANTA CRUZ

EXCLUSIVE PHOTOPRODUCTION OF OMEGA MESONS

AT FERMILAB ENERGIES

A Dissertation submitted in partial satisfaction of the  
requirements for the degree of

DOCTOR OF PHILOSOPHY

in


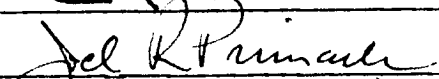
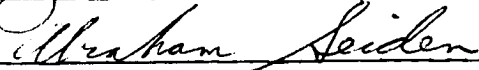
PHYSICS

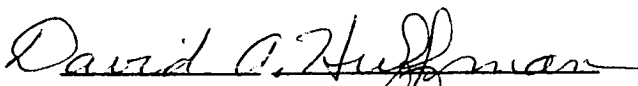
by

Vittorio Palladino

June 1980

The dissertation of Vittorio Palladino  
is approved

  
\_\_\_\_\_  
  
\_\_\_\_\_  
  
\_\_\_\_\_

  
\_\_\_\_\_  
Dean of the Graduate Division

a mio padre

## ACKNOWLEDGMENTS

I would like to express my gratitude to the many people who have helped me during my years in graduate school at UCSC. First of all, in particular, Prof. Nauenberg, Prof. Primack, Prof. Brower, Prof. Perl and Prof. Seiden for providing me with an excellent exposure to current ideas in elementary particle physics.

The success of my thesis experiment is due to the joint effort of hundreds of people. I could not possibly mention all of them. The most outstanding contributions have come, in my opinion, from Abe Seiden and Alex Grillo. The first has provided leadership and example of competence, serenity and equilibrium. The second has been for many years, as senior graduate student, the very soul of the experiment.

I wish to thank Alan Breakstone for his seven years of hard and intelligent work; and for sharing with me the loneliness of the Fermilab dorms and the joy of a splendid cross-country trip back to California.

Dennis Smith has been following all of us students for many years with his experienced outlook on all the problems of the experiment. We got great relief on the experimental floor from the help of Terry Schalk David Dorfan, and Francesco Grancagnolo. To David I am indebted for the crucial ideas of my data analysis work.

Many people have worked in our workshop to build our experimental equipment: Walter Nilsson, Leonard Bazzani and Bill Rowe above everybody else. Three outstanding undergraduates (Chris Tacklind, Mike Recce and Dan Nguyen) have greatly helped us at different stages. In Georgia Hamel we had the best of secretaries.

It will be impossible to forget the friendliness of all the people in the Physics Department. For all of them I will thank, in his own language, Fred Faria, para todos os cigarros que me tem dado e ainda mais para sua companhia durante tantas tardes solitarias.

Nora Rogers typed my illegible manuscript and Ann Wells and Larry Wendell drafted all my figures: the most welcome help in the moment of greatest pressure.

Last, but not least, I wish to thank my advisor Clemens Heusch for making the experiment possible; and for providing me with constant financial support during all these years.

grazie a tutti

## TABLE OF CONTENTS

Chapter	Page No.
1. The Experiment. Background and Motivations	1
A) Introduction	1
B) The Experiment	7
C) Omega Photoproduction	14
2. The Experiment Method	26
A) The Initial State: The Photon Beam	26
B) The Initial State: The Hydrogen Target	27
C) Final State Photons Detection	27
D) Final State Proton Detection	30
3. The Apparatus	33
A) The Beam Line	33
B) The Tagging System	37
C) The Shower Counters	40
D) The X-Y Hodoscope. Photon Localization and Separation	47
E) The Recoil Chambers	51
F) The Time-Of-Flight Recoil Counters	58
G) Forward Charged Particle Detectors	59
H) Monitors	60
4. Data-Taking Procedure	65
A) Trigger Logic	65
B) CAMAC System	70
C) Computer Configuration	72
D) Foreground Program. Data Acquisition	72

Chapter	Page No.
5. The Data Sample	75
A) Data Runs	75
B) Forward Detector Calibration Runs	76
C) Tagging System Calibration Runs	78
D) Cosmic Rays Runs	80
E) Electron Runs	83
6. Data Reduction	84
7. Data Analysis	96
A) Introduction	96
B) Second Pass Filter	104
C) Omega Analysis	
D) Detection Efficiency. Monte Carlo Simulation	
E) Results	
Appendix A. The Recoil Drift Chambers	A1

## CHAPTER ONE

## THE EXPERIMENT. BACKGROUND AND MOTIVATIONS

## A) Introduction

In investigating atomic, molecular, and to a lesser extent, nuclear structure, the emission and absorption of electromagnetic radiation has been a key tool, and the same appears more and more to be true for hadron structure. Traditionally, electromagnetic spectroscopy has played two roles. The first is the establishment of the states, their spin, parity and energy. The second is to give information about the wave function of the states from the electromagnetic matrix elements (or at least transition rates).

With the advent of high energy electron accelerators, intense beams of real photons ( $m^2 = 0$ ) were produced by electron bremsstrahlung and have been used to study the interactions of high energy photons with protons and neutrons in nuclei.

Generally, in hadron physics, electromagnetic radiation has not played the first role mentioned above. Energy level information has been usually given by the strong formation (or production) of hadron resonances; a notable exception to this rule was the observation, first in photopion production off nucleons, of the prominent isospin  $\frac{1}{2}$  nucleon resonance around 1500 Mev.<sup>1)</sup> One should also mention the observation<sup>2)</sup> of narrow-width states at about 3.5 Gev and, most likely, at 2.9 Gev,<sup>3)</sup> from the radiative decay of the  $\psi'$ . More states could well emerge from radiative decays of heavy mesons produced at electron-positron storage rings and conventional accelerators.

Photon beams of relatively high energy, on the other hand, have fulfilled the second role in providing information about the hadron's wave function. Nearly all our knowledge<sup>4)</sup> on electromagnetic transitions of nucleon resonances comes from pion photoproduction; a considerable basis for comparison with any theory of hadron structure, the prime candidate being the constituent quark model.

The hope, however, that very high energy real photon-nucleon interactions would probe deeper into the nucleon and provide direct information about the nucleon constituents has not yet proved valid. The main conclusion of some fifteen years of high energy photon physics can be summarized by stating that high energy photons behave like hadrons.  $\gamma N$  interactions share basically all the properties of  $\pi N$  interactions.

Total cross sections in both cases exhibit the clear excitation of the same nucleon ( $N^*$ ) resonances and above 2 Gev level out to become approximately independent of energy (fig. 1.1). The only (important) difference is in the magnitude of the cross section, about 200 times smaller for photons, approximately the value of the fine structure constant.

Elastic (Compton) scattering of photons on nucleons also reproduces the features of elastic pion-nucleon scattering; namely, a sharp exponential forward peak (fig. 1.2) with very little energy dependence of the forward cross section and the slope of the scattering distribution. The scattering amplitude is mainly imaginary.

The total cross section of photons on protons and neutrons (from deuterium data) are essentially the same.<sup>5)</sup> Charge independence seems to imply that photon nucleon interactions are not electromagnetic in



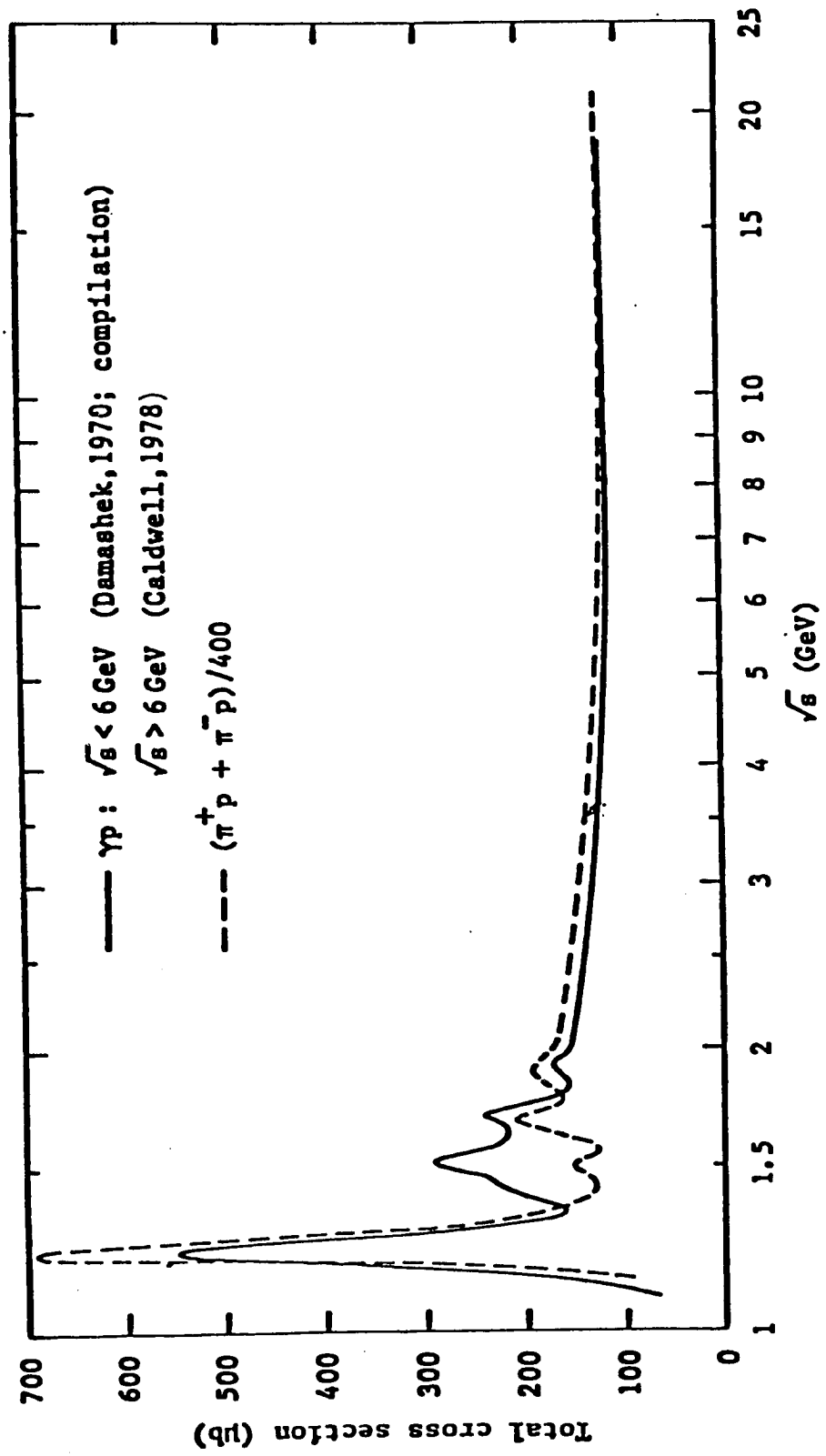


Figure 1.1. Total Photon-proton cross section

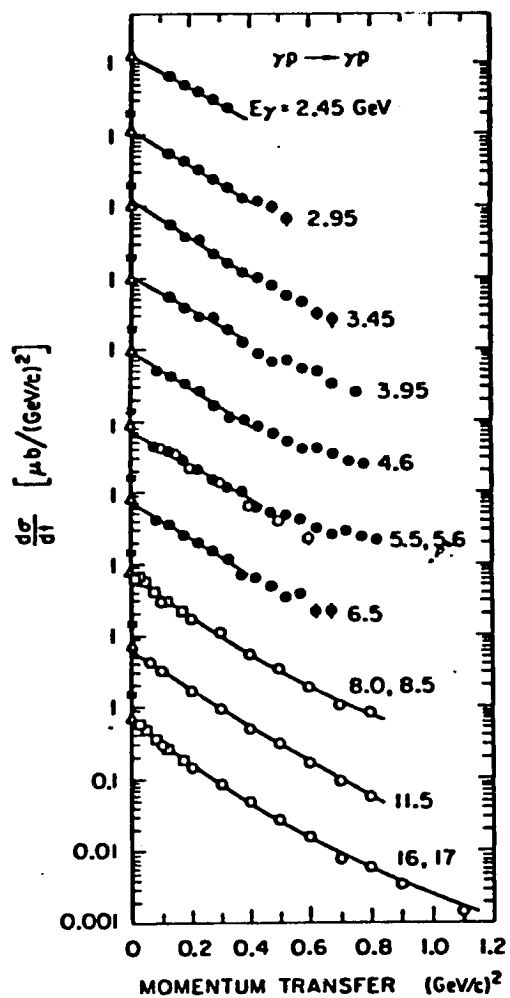


Figure 1.2. The Differential Cross Section for Compton Scattering for Energies in the Range of 2 - 18 Gev.

nature. Similarly, multiplicity and inclusive yields of hadrons in  $\gamma N$  and  $\pi N$  interactions display the same gross features for both types of beam particles. The conclusion that photon-hadron interactions are essentially hadron-like was strongly confirmed by the copious production<sup>5)</sup> of neutral vector mesons ( $\rho, \omega, \phi$ ) with same spin and parity as the photon ( $J^P = 1^-$ ). About 15 to 20% of the total  $\gamma N$  cross section is to be attributed to the exclusive production of vector mesons and inclusive yields<sup>6)</sup> are even larger. Here the vector mesons tend to preserve a large fraction of the photon momentum (leading particle effect).

Another compelling reason to believe in the hadron-like character of the photon comes from the study of photon interactions with complex nuclei at high energy. The total  $\gamma N$  cross section being of the order of 115  $\mu\text{barn}$  ( $1 \mu\text{barn} = 10^{-30} \text{cm}^2$ ), one would expect a mean free path of photons in nuclear matter much larger than nuclear dimensions (a few fermi, 1 fermi =  $10^{-13} \text{cm}$ ) and therefore an increase of the photon-nucleus cross section proportional to  $A$ , the number of nucleons in the nucleus. But, exactly as in hadron physics, this cross section<sup>7)</sup> grows less rapidly than that (shadowing). The photon is absorbed by the first nucleons on its path as though the interaction cross section on individual nucleons were of hadronic magnitude (20 to 40 mbarns, i.e., a mean free path of a fraction of a fermi).

More recently, the materialization of (virtual time-like  $m^2 > 0$ ) photons into hadrons has been observed<sup>8)</sup> in electron-positron annihilation. The probability of such a materialization is particularly large when  $m^2$  equals the square of the rest mass of a vector meson.

All these observations have resulted in the formulation of the vector dominance model (VDM) for photon-hadron interactions. The photon is viewed as a (well defined) superposition of hadron states with its own quantum numbers. A high energy real photon can virtually exist as a non-massless hadron state for a time

$$\Delta t = \hbar/\Delta E = 2\hbar E_{\gamma}/m_H^2 c^4,$$

where  $m_H$  is the mass of the hadron state,  $E_{\gamma}$  the photon energy and

$$\Delta E = E_H - E_{\gamma} \simeq m_H^2 c^4 / 2E_{\gamma} \quad \text{for } E \gg m_H c^2.$$

The distance  $\Delta = c\Delta t$  covered by the virtual hadron state in the time  $\Delta t$  increases with energy and becomes larger than nuclear dimensions for a few Gev. Photon-nucleon scattering would be the result of the interaction of this hadronic state with the nucleon. The interaction would share all the properties of hadron-hadron scattering. The hadron state, being mostly a vector meson, would provide a large yield of them in the final state. In complex nuclei photons would behave like hadrons do.

This picture, however, is not complete. It fails to explain inelastic electron nucleon scattering, a process thought to occur via the exchange of a virtual space-like ( $m^2 < 0$ ) photon. Inelastic scattering cross sections were found to be large.<sup>9)</sup> The most striking feature of the data for highly virtual, highly energetic photons was "scaling;" that is, the dependence of the cross section on photon energy and mass is predictable on the basis of dimensional analysis, without reference to any other mass or cross section. The results were understood by picturing the nucleon as made of point-like constituents called partons.

A space-like photon, unlike a real one, would be able to probe deeper into the nucleon and to have point-like coupling with its constituents (fig. 1.3a). The total (virtual) photon-nucleon cross section would actually just be the incoherent sum of these individual point-like interactions.

Bjorken and Paschos<sup>10)</sup> pointed out, in 1969, that the parton picture would imply the existence of the elementary graphs in fig. 1.3b, that is Compton scattering of real photons on partons. The incoherent sum of these point-like interactions would result in final states containing a photon plus anything else. Its contribution could be isolated by detecting a large transverse momentum photon in photon-nucleon interactions at large c.m. energies. The transverse momentum dependence of the direct process would be  $p_T^{-4}$ , gentler than that predicted by all graphs involving communication between the parton lines before re-emission of the photon ( $p_T^{-n}$ ,  $6 < n < 12$ ). The ratio of inelastic eN scattering to inelastic  $\gamma$ N scattering, under the same kinematical conditions, would be

$$R = \frac{\langle \sum_i Q_i^2 \rangle}{\langle \sum_i Q_i^4 \rangle}$$

(where the sum is over the partons) and would yield a measure of the mean charges of the partons involved in the interaction.

In other words, although for a very small part of the cross section, real photons could be good probes of nucleon structure.

## B) The Experiment

The most recent generation of real photon beams, at Fermilab and at the Cern SPS, must start from a proton beam and build from it the

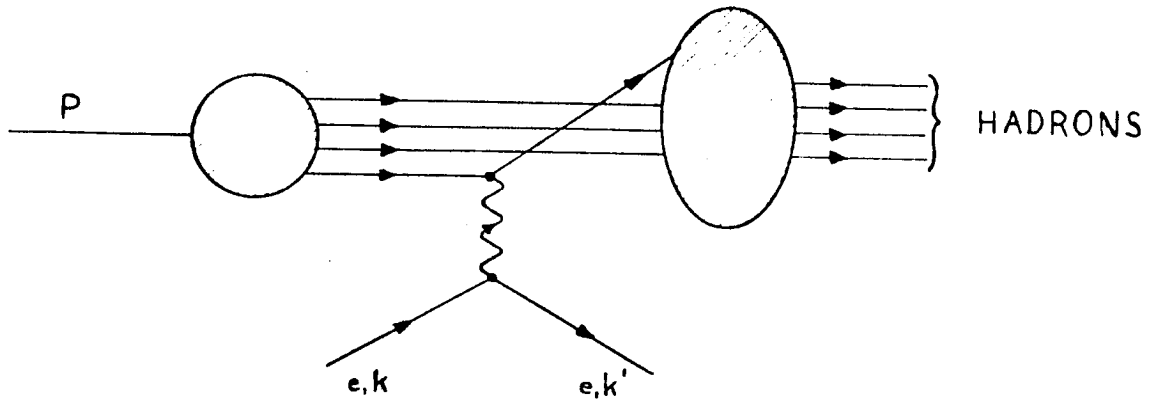


Figure 1.3a. Inelastic Electron-Proton Scattering in the Parton Model.

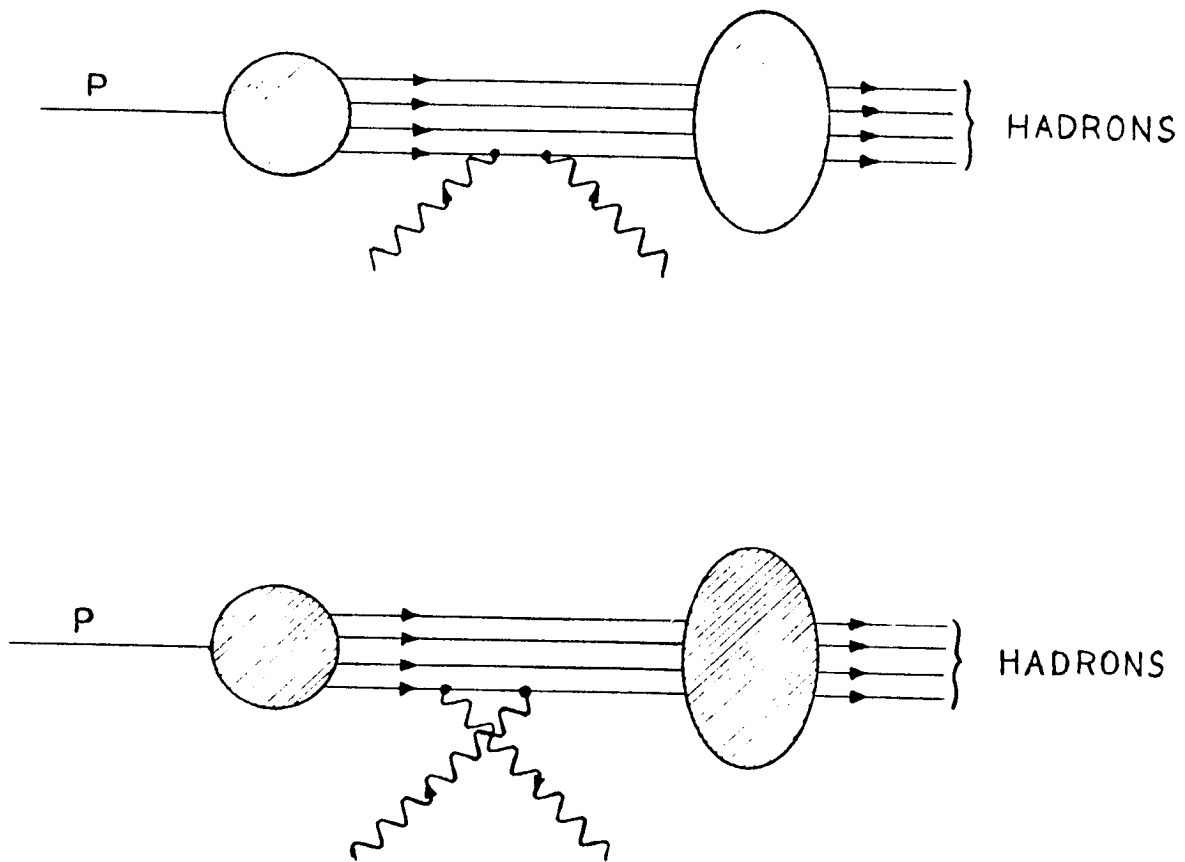


Figure 1.3b. Inelastic Photon-Proton Scattering for the Parton Model.  
(Two Diagrams Contribute)

beam that will generate bremsstrahlung photons. Higher energy photons are so obtained, at the expense of photon flux.

The Fermilab photon program started in 1976 in the newly built tagged photon laboratory with an experiment (E25) measuring<sup>7)</sup> the total cross section of real photons on protons and heavier nuclei. The experiment also provided a measurement<sup>11)</sup> of the cross section for exclusive production of  $\rho, \omega, \phi$ . Our experiment (E152) was the second to be performed. Our experimental program has been centered on the detection of (multiple) final state photons to study, in the first place, elastic Compton scattering on protons

$$\gamma p \rightarrow \gamma p, \quad (1.1)$$

in the new energy range, and inelastic Compton scattering

$$\gamma p \rightarrow \gamma X \quad (1.2)$$

at (relatively) large transverse momenta, to test the Bjorken and Paschos ideas mentioned earlier. The capability of our photon detector to detect multiphoton final states makes our experiment sensitive also to the exclusive photoproduction of the mesons having sizeable radiative decay modes, namely

$$\begin{aligned} \gamma p &\rightarrow \pi^0 p \quad \text{with} \quad \pi^0 \rightarrow \gamma\gamma \\ \gamma p &\rightarrow \eta^0 p \quad \text{with} \quad \eta^0 \rightarrow \gamma\gamma \\ \gamma p &\rightarrow \omega^0 p \quad \text{with} \quad \omega^0 \rightarrow \pi^0 \gamma \quad \text{and} \quad \pi^0 \rightarrow \gamma\gamma \\ \gamma p &\rightarrow \phi^0 p \quad \text{with} \quad \phi^0 \rightarrow \eta^0 \gamma \quad \text{and} \quad \eta^0 \rightarrow \gamma\gamma \\ \gamma p &\rightarrow \psi^0 p \quad \text{with} \quad \psi^0 \rightarrow e^+e^- \end{aligned} \quad (1.3)$$

and to inclusive photoproduction of the same mesons. A measurement of the inclusive yield of neutral pions versus transverse momentum, in particular, is crucial for background subtraction to the inelastic Compton process. This thesis discusses a procedure for the isolation of the exclusive final states of type (1.1) and (1.3). Their common kinematic features make possible a global treatment of the raw data towards this goal.

Production rates for these various exclusive processes are, however, very different. If we indicate the amplitude of each process as  $T(s,t)$  the differential cross section will be given, at high energy, by

$$\frac{d\sigma}{dt} \approx \frac{1}{16\pi s^2} |T|^2 \sim \frac{|T|^2}{s^2}$$

with  $t = 4$ -momentum transfer and  $s =$  square of c.m. energy.

Two-body scattering is described, phenomenologically, in Regge pole language. In this framework the amplitudes for two-body (and quasi two-body scattering) are, at high energy, of the form

$$T \sim s^{\alpha(t)}$$

where  $\alpha(t)$  is the leading Regge trajectory exchanged in the scattering. The energy dependence of the forward cross sections will therefore be

$$\left. \frac{d\sigma}{dt} \right|_{t=0} \sim s^{2\alpha(0)-2} .$$

Compton scattering and vector meson photoproduction are found to be<sup>5)</sup> of diffractive nature (see next section). The exchange involved has the quantum numbers of the vacuum. In Regge language, they are dominated by the



exchange of the Pomeron trajectory, with  $\alpha(0) = 1$ . Forward cross sections are therefore energy independent and differential cross sections are of the form

$$\frac{d\sigma}{dt} = Ae^{-bt}$$

with slopes  $b$  essentially independent of energy (no shrinkage). Values of the forward cross sections and slopes  $b$  are <sup>5)</sup>

	$A = d\sigma/dt \Big _{t=0}$	$b$
$\gamma p \rightarrow \gamma p$	$\approx 7 \mu\text{b}/\text{Gev}^2$	$\approx 7 \text{ Gev}^{-2}$
$\rightarrow \omega p$	$\approx 9 \mu\text{b}/\text{Gev}^2$	$\approx 8 \text{ Gev}^{-2}$
$\rightarrow \phi p$	$\approx 2.5 \mu\text{b}/\text{Gev}^2$	$\approx 5 \text{ Gev}^{-2}$
$\rightarrow \psi p$	$\approx 0.05 \mu\text{b}/\text{Gev}^2$	$\approx 4 \text{ Gev}^{-2}$

Photoproduction of pseudoscalar ( $\pi^0, \eta^0$ ) mesons<sup>12)</sup> cannot proceed via the exchange of a Pomeron trajectory. A meson trajectory has to be exchanged, with  $\alpha(0) < 1$ . (Forward) cross sections will die out with energy. Differential cross sections, in general, are not simple exponentials. They can exhibit more than one maximum and have forward peaks shrinking with increasing energy. A scaling law

$$s^2 \frac{d\sigma}{dt} \sim \text{constant}$$

(which would imply  $\alpha(0) = 0$ ) holds only approximately. Exclusive  $\pi^0$  photoproduction data favor a value of  $\alpha(0)$  of about 0.2. The differential cross section exhibits a dip at  $t = 0.5$ , followed by a secondary maximum and a turnover near the forward direction, due to the impossibility of pion exchange (C parity violating). This last statement holds

true for  $\eta^0$  photoproduction also, where, however, no dip at  $t = 0.5$  is observed and the data are too sparse to make definite statements about the validity of the scaling law. Production of both pseudoscalar mesons is expected<sup>13)</sup> to rise again after the turnover in the very forward direction, due to a one photon exchange contribution, usually referred to as the Primakoff effect (fig. 1.4b). A hint of a forward spike is indeed present in the  $\pi^0$  data (fig. 1.4a). If one takes the scaling law seriously, for order of magnitude estimate, one gets from the data

$$\begin{aligned} s^2 \left. \frac{d\sigma}{dt} \right|_{t=0} &\approx 100 \mu\text{b Gev}^2 && \text{for } \gamma p \rightarrow \pi^0 p \\ &\approx 20 \mu\text{b Gev}^2 && \text{for } \gamma p \rightarrow \eta^0 p. \end{aligned}$$

For 100 Gev incident photons, this reads ( $s = 2ME_\gamma$ ,  $M =$  mass of the proton)

$$\begin{aligned} \left. \frac{d\sigma}{dt} \right|_{t=0} &\approx 2.5 \text{ nb/GeV}^2 && \text{for } \gamma p \rightarrow \pi^0 p \\ &\approx 0.5 \text{ nb/GeV}^2 && \text{for } \gamma p \rightarrow \eta^0 p. \end{aligned}$$

Decay modes visible in our apparatus have the branching ratios<sup>14)</sup>

$$\begin{aligned} \pi^0 &\rightarrow \gamma\gamma && \approx 100\% \\ \eta^0 &\rightarrow \gamma\gamma && \approx 38\% \\ \omega^0 &\rightarrow \pi^0\gamma && \approx 9\% \\ \phi^0 &\rightarrow \eta^0\gamma && \approx 1.5\% \\ \psi^0 &\rightarrow e^+e^- && \approx 7\% \end{aligned}$$

Therefore, the magnitude of the forward cross sections our experiment

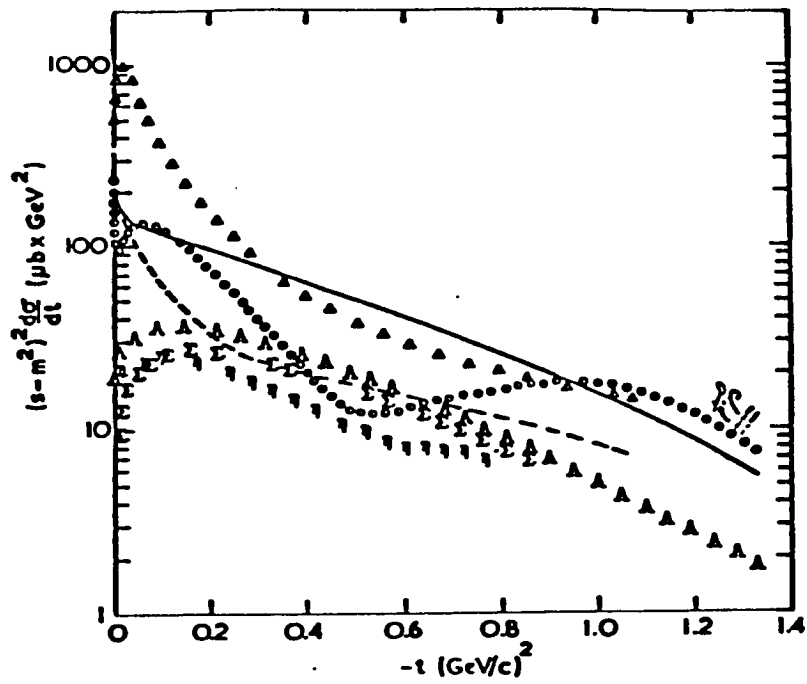


Figure 1.4a. Diebold Plot for Forward Pseudoscalar Photoproduction, In particular (o)  $\gamma p \rightarrow \pi^0 p$ ; ( $\eta$ )  $\gamma p \rightarrow \eta p$ .

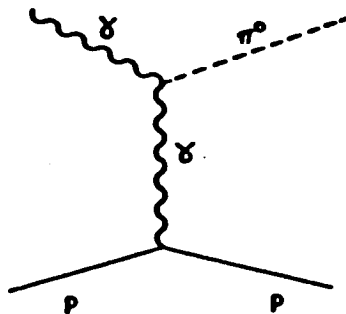


Figure 1.4b. One Photon Exchange Contribution to Exclusive  $\pi^0$  Photoproduction (Primakoff Effect).

is sensitive to are respectively (at 100 Gev)

$$\begin{aligned} \left. \frac{d\sigma}{dt} \right|_{t=0} &\approx 700 \text{ nb/GeV}^2 && \text{for } \gamma p \rightarrow \gamma p \\ &800 \text{ nb/GeV}^2 && \text{for } \gamma p \rightarrow \omega p \\ &20 \text{ nb/GeV}^2 && \text{for } \gamma p \rightarrow \phi p \\ &3.5 \text{ nb/GeV}^2 && \text{for } \gamma p \rightarrow \psi p \\ &2.5 \text{ nb/GeV}^2 && \text{for } \gamma p \rightarrow \pi^0 p \\ &0.2 \text{ nb/GeV}^2 && \text{for } \gamma p \rightarrow \eta^0 p \end{aligned} .$$

Elastic scattering and omega production provide us with the largest yields. Having its largest radiative decay mode ( $\rho^0 \rightarrow \pi^0 \gamma$ ) down to 0.024% the rho meson, in spite of its large production cross section ( $d\sigma/dt|_{t=0} \approx 100 \mu\text{b/GeV}^2$ ), will be seen in our apparatus only as a (3%) background to omega production. Compton scattering is the object of another doctoral dissertation.<sup>15)</sup> This thesis discusses omega photoproduction of which the next section briefly reviews our experimental and theoretical understanding.

### C) Omega Photoproduction

Vector mesons ( $\rho, \omega, \phi$ , and more recently observed higher states  $\rho', \rho'', \psi, \psi'$ ) are photoproduced with large rates. Rho production accounts for most (10%) of their total contribution (15 to 20%) to the photon-nucleon total cross section. Vector meson photoproduction (and Compton scattering) all display the characteristic of diffractive scattering.

Diffractive scattering is usually discussed in terms of two alternative pictures. One is Regge exchange models, where the scattering is thought to proceed via exchange of a singularity called the Pomeron.

The other, reminiscent of wave optics, interprets diffraction as the shadow cast by all the inelastic (absorptive) reactions taking place. A satisfactory theoretical understanding is lacking. Rather, a set of phenomenological rules identifies what we mean by diffraction. These rules are<sup>5)</sup>

1. An energy independent cross section
2. A sharp (exponential) forward peak in the differential cross section
3. Mainly imaginary scattering amplitude
4. Exchange processes characterized by the quantum numbers of the vacuum
5. Change in parity in the scattering following the natural spin-parity series  $P_0 = (-1)^{\Delta J} P_1$ , where  $\Delta J$  is the spin exchange,  $P_0$  and  $P_1$  the intrinsic parities of incoming and outgoing particles.

The cross section for omega photoproduction is plotted versus photon energy in fig. 1.5. It rises from threshold (about 1.1 Gev) to about 7  $\mu\text{b}$  at about 2 Gev and then drops to about 2 $\mu\text{b}$  at 5 Gev. A gentle fall-off continues at least up to 10 Gev. A measurement of omega photoproduction at Fermilab energy has been recently performed.<sup>11)</sup> Quasi-elastic events, however, are not isolated by the detection of a recoil proton. The inelastic background is estimated and subtracted from the signal. Beyond 50 Gev the cross section is consistent with a constant value of about 1  $\mu\text{b}$ . The contribution of the highest non-leading Regge trajectory (the pion trajectory) falling down approximately like  $E_\gamma^{-2}$  has by then vanished.

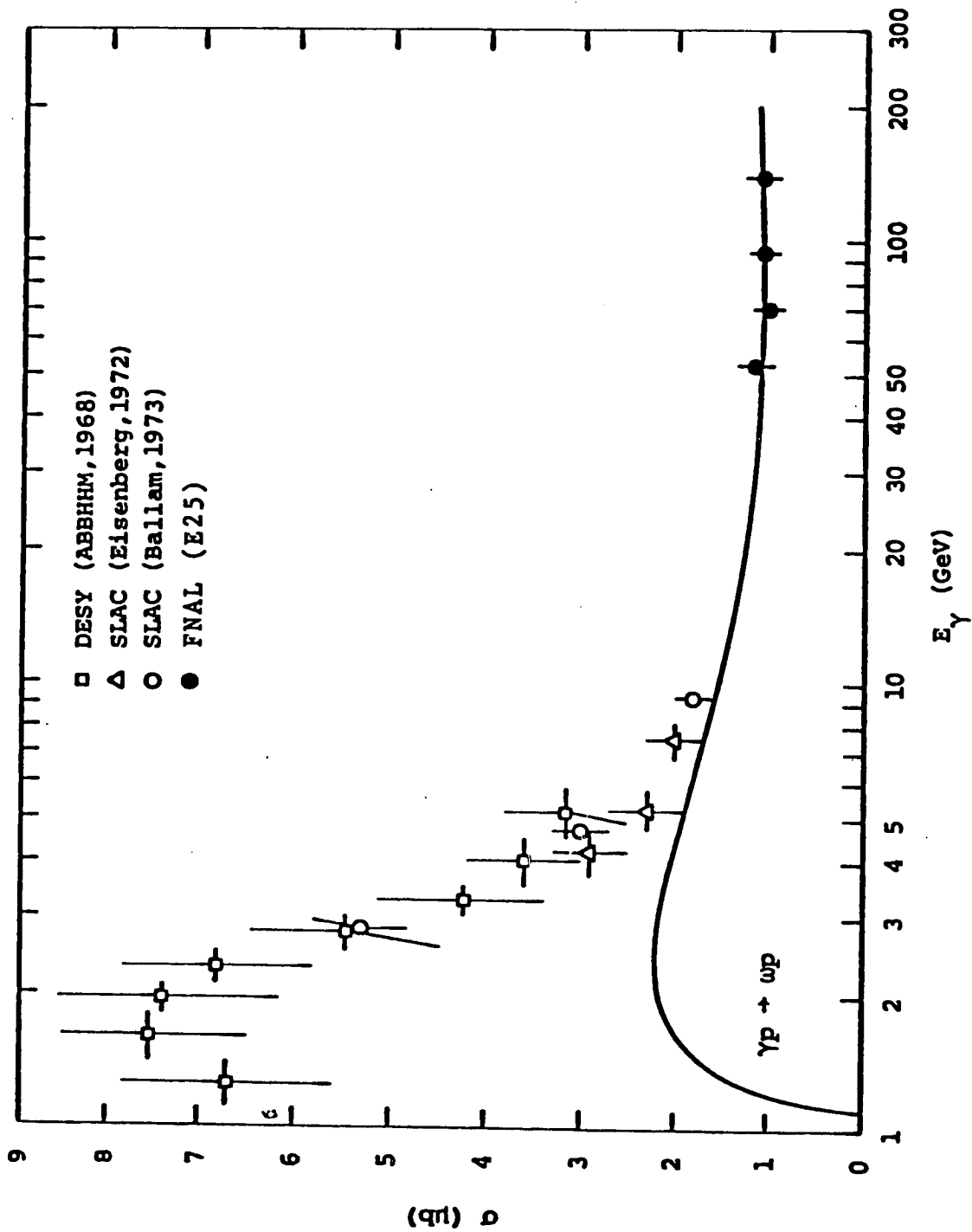


Figure 1.5. Omega Photoproduction Cross Section vs. Energy. Solid Line is Quark-Model Prediction Normalized to the Data in Reference 11).

The slope of the forward exponential peak is shown versus energy in fig. 1.6. It has a rather constant value of about  $7-8 \text{ Gev}^{-2}$ . About the same value is measured<sup>5)</sup> for Compton scattering and rho photoproduction. A measurement of the ratio of the real to the imaginary part of the forward scattering amplitude is not presently available. A (difficult) experiment<sup>16)</sup> has determined it for rho photoproduction. Its value is about  $\frac{1}{4}$  and it is obtained by studying the asymmetry (under exchange of electron and positron) resulting from the interference of the real Bethe-Heitler pair production amplitude and the amplitude for rho photoproduction, with the rho detected by its leptonic decay mode  $\rho \rightarrow e^+e^-$ .

The contribution to the omega photoproduction amplitude from an isovector exchange cannot be excluded at the moment by the data comparing production on protons and neutrons. It is small for Compton scattering and rho production.<sup>5)</sup>

Experiments<sup>17)</sup> with linearly polarized photon beam have shown that already at 9.3 Gev the spin parity of the exchange is consistent with natural parity exchange dominance.

The decay  $\omega \rightarrow \pi^0\gamma$  ( $1^- \rightarrow 1^-0^-$ ) of photoproduced omegas is expected to exhibit a  $1+\cos^2\theta$  dependence on the polar angle,  $\theta$ , of the decay products in the omega c.m. system, if the omega preserves the helicity ( $\pm 1$ ) of the incoming photon. High energy data<sup>11)</sup> confirm this observation (fig. 1.7).

The vector meson dominance model (VDM) and the quark model provide a set of definite predictions to be tested against photoproduction data. The VDM statement that the photon is a superposition of vector meson

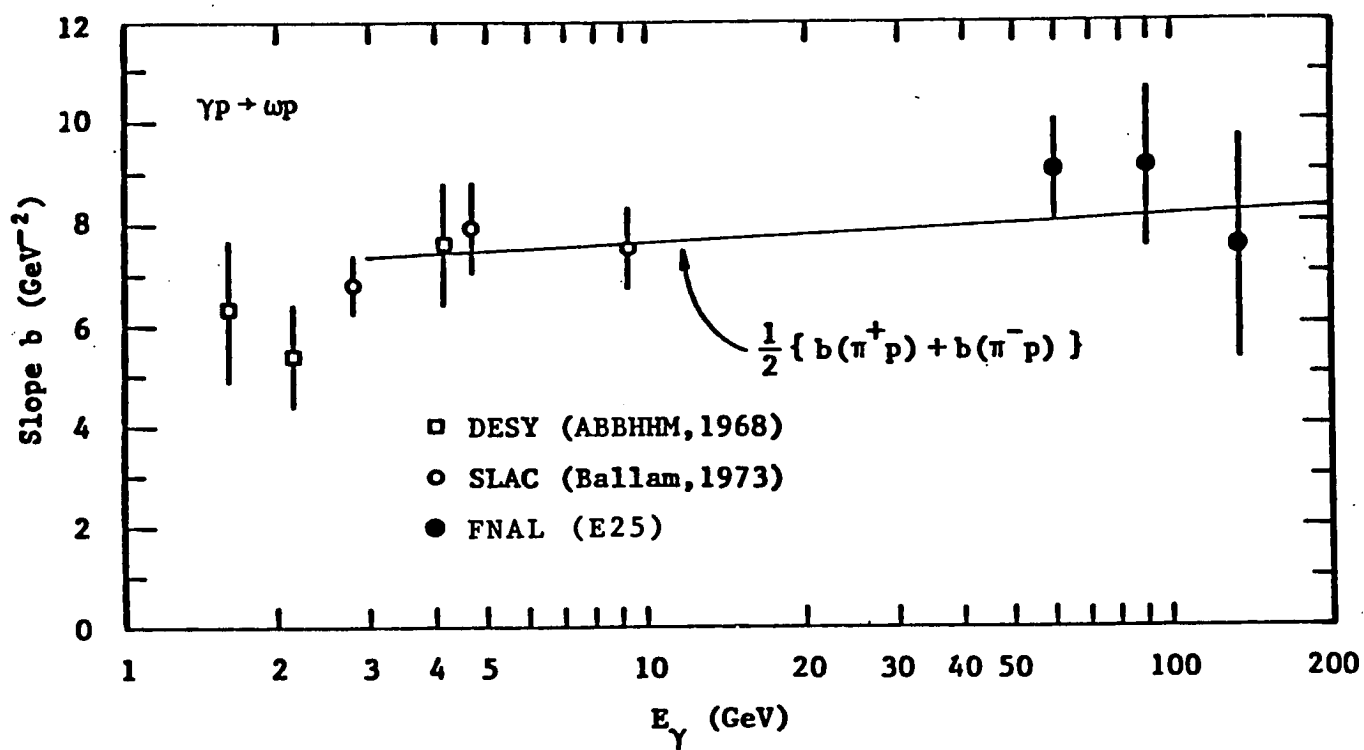


Figure 1.6. Slope of Exponential Forward Peak for Exclusive  $\omega$  Photoproduction. Solid Curve is Quark-Model Prediction.



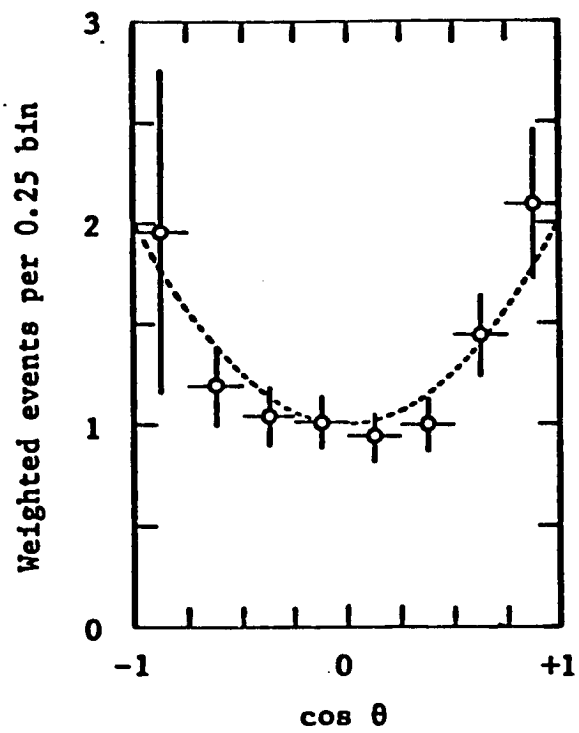


Figure 1.7. Decay Polar Angle Distribution for  $\omega^0 \rightarrow \pi^0\gamma$ . Data from Reference 11).

states is expressed by the current-field identity<sup>18)</sup>

$$J(x) = \sum_{\mathbf{v}} \frac{e}{2} \frac{m_{\mathbf{v}}^2}{\gamma_{\mathbf{v}}} V(x) = \frac{e}{2} \left\{ \frac{m_{\rho}^2}{\gamma_{\rho}} \rho(x) + \frac{m_{\omega}^2}{\gamma_{\omega}} \omega(x) + \frac{m_{\phi}^2}{\gamma_{\phi}} \phi(x) + \dots \right\} . \quad (1.4)$$

The hadronic part of the electromagnetic current  $J(x)$  is linked to the vector meson fields  $V(x)$ . The  $m_{\mathbf{v}}$ 's are the masses of the mesons and the  $\gamma_{\mathbf{v}}$ 's are dimensionless coupling constants of the electromagnetic current to the field  $V(x)$ . They are assumed to be independent of the energy and mass of the photon.

The quark model gives a prediction<sup>19)</sup> for the  $\gamma_{\mathbf{v}}$ 's. Given the quark composition of the vector mesons

$$\begin{aligned} \rho &= (u\bar{u}-d\bar{d})/\sqrt{2} & \omega &= (u\bar{u}+d\bar{d})/\sqrt{2} \\ \phi &= s\bar{s} & \psi &= c\bar{c} \end{aligned}$$

and the quark charges ( $q_u = q_c = 2/3$ ,  $q_d = q_s = -1/3$ ) we obtain by comparison with (1.4)

$$\gamma_{\rho}^{-2} : \gamma_{\omega}^{-2} : \gamma_{\phi}^{-2} : \gamma_{\psi}^{-2} = 9 : 1 : 2 : 8 .$$

Various symmetry breaking schemes<sup>20)</sup> alter these ratios to

$$\begin{aligned} \gamma_{\rho}^{-2} : \gamma_{\omega}^{-2} : \gamma_{\phi}^{-2} &= 9 : 0.65 : 1.33 \\ &9 : 1.2 : 1 . \end{aligned}$$

Electron-positron storage ring data provide a direct measurement of the  $\gamma_{\mathbf{v}}$ 's. When the square of the total energy in the center of the mass (that is the mass  $q^2 > 0$  of the virtual photon) is close to the square of the mass  $m_{\mathbf{v}}^2$  of a meson vector, the cross section for

$$e^+e^- \rightarrow \text{hadrons}$$

is dominated by the production of that meson. The meson has a decay width into lepton pairs related<sup>21)</sup> to the coupling constant by ( $\alpha = e^2/4\pi$ )

$$\Gamma(V \rightarrow e^+e^-) = \frac{\alpha^2}{12} \frac{4\pi}{\gamma_V^2} m_V .$$

The values obtained<sup>5)</sup> for the  $\gamma_V$ 's from decay width measurements are

	$\rho$	$\omega$	$\phi$	$\psi$
$\gamma_V^2/4\pi$	$0.64 \pm 0.1$	$4.60 \pm 0.5$	$2.83 \pm 0.2$	$2.9 \pm 1.0$ ,

that is,

$$\gamma_\rho^{-2} : \gamma_\omega^{-2} : \gamma_\phi^{-2} : \gamma_\psi^{-2} = 9 : 1.25 : 2.04 : 2.22 .$$

The agreement with the quark model prediction is reasonable for the "old" mesons, but the  $\psi$  meson misses by about a factor of 4.

The current-field identity relates the matrix element for reactions initiated by photons and vector mesons

$$T(\gamma A \rightarrow B) = \langle B | J(x) | A \rangle = \sum_V \frac{e m_V^2}{2\gamma_V} \frac{1}{m_V^2 - q^2} T(VA \rightarrow B) .$$

Figure 1.8 illustrates this relation. The photon virtually transforms into the vector meson;  $1/m_V^2 - q^2$  is the vector meson propagator. The vector meson interacts with the hadronic state  $|A\rangle$ .

For real photons ( $q^2 = 0$ )

$$T(\gamma A \rightarrow B) = \sum_V \frac{e}{2\gamma_V} T(VA \rightarrow B) .$$

For vector meson photoproduction, assuming that  $V'N \rightarrow VN$  transitions (fig. 1.8c) do not occur (diagonality), one obtains (fig. 1.8b)

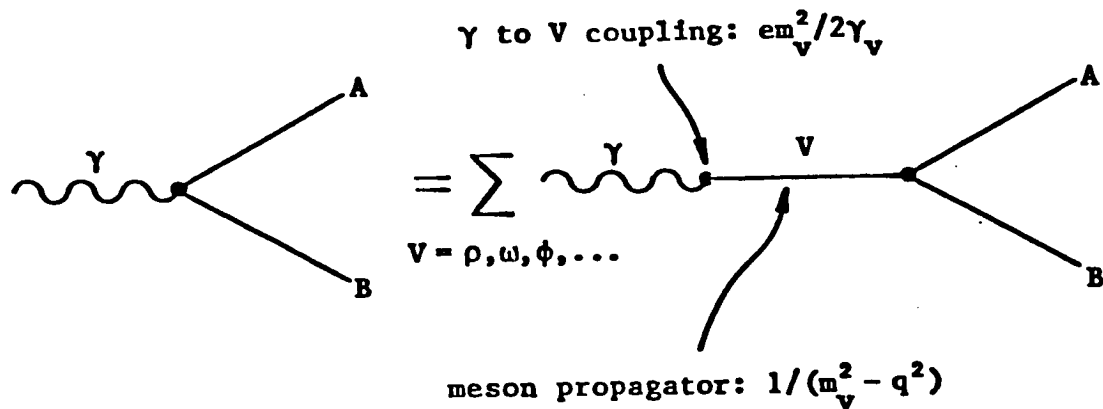


Figure 1.8a. The Vector Meson Dominance Model for Photon-Hadron Interactions.

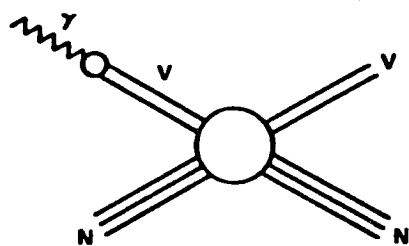


Figure 1.8b. Vector Meson Photoproduction in the Vector Meson Dominance Model.

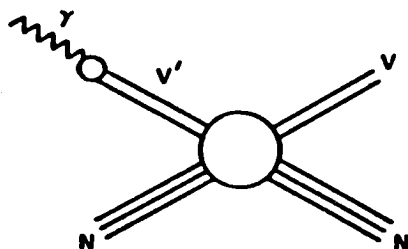


Figure 1.8c. Non-diagonal Contribution to Vector Meson Photoproduction in the Vector Meson Dominance Model.

$$T(\gamma N \rightarrow VN) = \frac{e}{2\gamma_V} T(VN \rightarrow VN) .$$

That is,

$$\frac{d\sigma}{dt} (\gamma N \rightarrow VN) = \frac{e^2}{4\gamma_V^2} \frac{d\sigma}{dt} (VN \rightarrow VN) \quad (1.5)$$

$$\sigma (\gamma N \rightarrow VN) = \frac{e^2}{4\gamma_V^2} \sigma (VN \rightarrow VN) .$$

Using the optical theorem one obtains

$$\left. \frac{d\sigma}{dt} \right|_{t=0} (\gamma N \rightarrow VN) = \frac{e^2}{4\gamma_V^2} \frac{1+\eta^2}{16\pi^2} \sigma_T^2 (VN) \quad (1.6)$$

where  $\eta$  is the ratio of real to the imaginary part of the elastic vector meson-nucleon forward scattering amplitude.

A measurement of forward photoproduction of vector mesons, therefore, with some knowledge of  $\sigma_T(VN)$  (and of the phase  $\eta$ ) provides an independent measurement of the constants  $\gamma_V$ 's.

The quark model,<sup>19)</sup> if we assume that the amplitude for hadron-hadron scattering is the sum of the amplitude for scattering of their quark constituents and that the forward amplitude is purely imaginary ( $\eta = 0$ ) predicts

$$\sigma_T(\rho p) = \sigma_T(\omega p) = \frac{1}{2} [\sigma_T(\pi^+ p) + \sigma_T(\pi^- p)] = 27 \text{ mb}$$

$$\sigma_T(\phi p) = \sigma_T(K^+ p) + \sigma_T(K^- p) - \sigma_T(\pi^- p) = 13 \text{ mb} ,$$

and (via optical theorem)

$$\frac{d\sigma}{dt}(\rho p) = \frac{d\sigma}{dt}(\omega p) = \frac{1}{4} \left[ \sqrt{\frac{d\sigma}{dt}(\pi^+ p)} + \sqrt{\frac{d\sigma}{dt}(\pi^- p)} \right]^2 \quad (1.7)$$

$$\frac{d\sigma}{dt}(\phi p) = \left[ \sqrt{\frac{d\sigma}{dt}(K^+ p)} - \sqrt{\frac{d\sigma}{dt}(K^- p)} - \sqrt{\frac{d\sigma}{dt}(\pi^- p)} \right]^2 .$$

This implies, if the cross sections are of the form  $d\sigma/dt = Ae^{-bt}$

$$b_{\rho p} = b_{\omega p} = \frac{b_{\pi^+ p} + b_{\pi^- p}}{2} . \quad (1.8)$$

From (1.6), using forward vector meson photoproduction data<sup>5)</sup>

	$\rho$	$\omega$	$\phi$
$\gamma_V^2/4\pi$	$0.67 \pm .06$	$5.3 \pm 0.9$	$5.8 \pm 0.7$

The value of  $\gamma_\phi^2$  is significantly larger than the  $e^+e^-$  result. For omega photoproduction, substituting (1.7) and (1.8) into (1.5), one obtains the solid curves of fig. 1.5 and fig. 1.6. The slope prediction is consistent with the data over the entire energy range. The total cross section equals the  $\pi^+$  and  $\pi^-$  average at high energy, after the disappearance of the one pion exchange contribution dominant at low energy.

The total cross section  $\sigma_T(Vp)$  can be (indirectly) measured in coherent photoproduction on complex nuclei of different A number. Since the photoproduced vector meson, above a few Gev, lives long enough to traverse the nucleus,  $\sigma_T(Vp)$  can be determined by measuring the relative yields of vector mesons transmitted through varying path lengths of

nuclear matter. The extraction of  $\sigma_T(Vp)$  involves nuclear optics theory<sup>22)</sup> and an estimate of  $\eta$ . Results<sup>5)</sup> are roughly consistent with quark model predictions

	$\rho$	$\omega$	$\phi$	$\psi$
$\sigma_T(Vp)$	$28 \pm 1.5$ mb	$25.4 \pm 2.7$ mb	10-12 mb (at 7 Gev)	3.5 mb (at 17 Gev)

yielding for the  $\gamma_V$ 's the values

	$\rho$	$\omega$	$\phi$	
$\gamma_V^2/4\pi$	$.61 \pm .03$	$7.5 \pm 1.3$	$5.5 \pm 2.4$	.

The agreement between the various determinations is only approximate. An analogous conclusion is to be made for the so-called Compton sum rule, relating elastic photon-proton scattering to the sum of the vector meson photoproduction cross sections.  $\rho, \omega, \phi$  account only for about 80% of the total.<sup>5)</sup>

## CHAPTER TWO

## THE EXPERIMENTAL METHOD

## A) The Initial State: The Photon Beam

The tagged photon beam at Fermilab is the result of a multistage process. 400 Gev protons hit a 36 cm long beryllium target to produce secondary particles. Non interacting protons and charged secondaries are bent away from the forward direction. Neutral secondaries (neutral pions, neutral kaons, neutrons) at 0 degrees proceed on. The high  $A/Z^2$  ratio of beryllium (atomic number  $Z = 4$  and nuclear number  $A = 9$ ) maximizes the yield of photons (from neutral pion decay) with respect to photon losses due to electron pair production. A converter downstream (high  $Z^2/A$  materials like lead ( $A = 207$ ,  $Z = 82$ ) or copper ( $A = 64$ ,  $Z = 29$ ) maximize electron pair yield with respect to hadronic interactions of kaons and neutrons) creates electrons and positrons. Positive particles are magnetically bent away, while a 290 meters long beam transport system selects and focuses an electron beam of the desired energy. Negatively charged hadrons produced in the converter have larger transverse momentum than the electrons from photoproduced pairs (typically 300 Mev/c instead of 1 Mev/c) and are substantially rejected by tight collimation. In a copper radiator a fraction of the electrons will produce bremsstrahlung photons proceeding towards our experimental liquid hydrogen target. A system of 3 dipole "C" magnets will deflect by a small angle the energetic non radiating electrons into a beam dump and the less energetic non radiating ones by larger angles into a system of scintillation counters and shower counters (the tagging system) which



will measure position and energy of the electron. If the dipole (tagging) magnets are turned off and the copper converter removed, the monochromatic electron beam will hit our experimental target. The copper radiator thickness is kept small (5% of a radiation length) to minimize the number of "bad" tags and "false" tags (Chapter 3A) while still providing a sizeable yield of clean tags for our experimentation. A schematic view of the photon beam line is given in fig. 2.1.

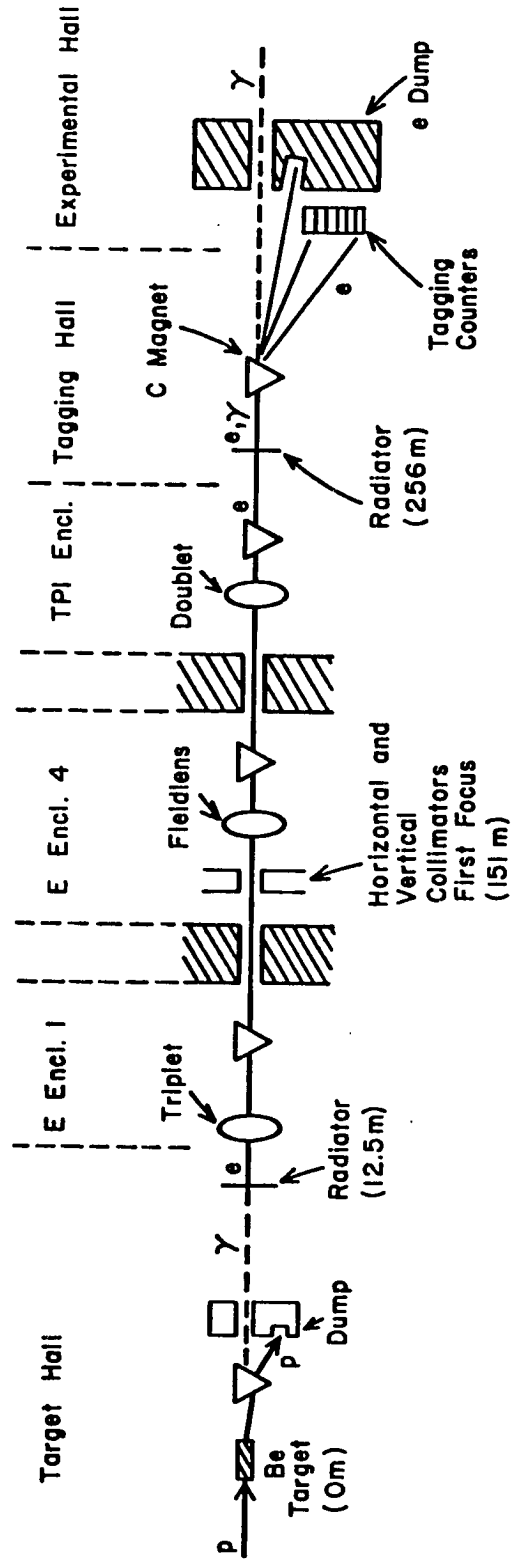
#### B) The Initial State: The Hydrogen Target

Our target consists of a 75 cm long vessel containing liquid hydrogen (about .1 r.l.). Its radius is 1.5 cm to roughly match the beam cross section. It is kept small, together with all the target support material thicknesses, to reduce the energy loss and multiple scattering undergone by recoiling protons before reaching our recoil detector. For elastic and quasi-elastic scattering this amount of material introduces a 4-momentum transfer cutoff,  $t_{\min}$ , above which protons from the center of the target will be able to emerge. 75 cm of liquid hydrogen (density  $\rho = .0743 \text{ gr/cm}^3$ ) gives a yield of about 3 events/photon/barn.

#### C) Final State Photon Detection

A large solid angle electromagnetic shower detector in the forward direction measures the 4-momentum of scattered photons (for elastic and inelastic Compton events) as well as of photons (and electrons) produced in other final states (radiative decay of various mesons). It moves by rails toward and from the target, and internally perpendicularly to the beam axis. Its acceptance varies with its distance from the target and the incident photon energy. We ran with the detector 10 meters and

Figure 2.1. Electron Beam Line Schematic



30 meters away from the target and at electron energies of 80,135,160 Gev. It is able to detect showering particles from a few Gev to about 200 Gev. It provided us with the crucial task of insuring integrity and stability of the pulse height responses of its various components. Its two functions are performed separately. The energy of the showers is measured by total absorption in two banks of lead-acrylic plastic sandwiches (called the U and the V counters) with pulse height response proportional to the energy of the shower. Each bank is segmented in 16 separate units to facilitate multiphoton identification. The measurement of the direction of the showering particle (as well as the separation of neighbouring showers) is accomplished by two orthogonal sets (called the X and the Y counters) of 52 low grade scintillator strips a few centimeters wide. In each coordinate, the central position of the shower is calculated as

$$x = \frac{\sum_i p_i x_i}{\sum_i p_i}$$

where  $p_i$  and  $x_i$  are the pulse height and the coordinate of the center of the  $i$ -th scintillator strip. Both shower counters and scintillator strips are assembled with a central beam hole. Behind the beam hole of V counters a beam plug (BP) counter (two successive total absorption counters made of lead-radiator sandwiches) absorbs non interacting photons and can catch secondary photons produced in interactions and heading towards the U/V beam hole.

A bank of scintillation counters (called the J counters) in front of the U counters covers the entire active area of the shower detector

and distinguishes between showers initiated by charged and neutral particles.

#### D) Final State Proton Detection

The vector velocity  $\vec{\beta}$  of the recoil proton in elastic and quasi-elastic two body final states is measured by 8 planes of drift chambers and a time-of-flight (TOF) system. The chambers measure the direction of  $\vec{\beta}$ , the TOF system its magnitude. The 8 drift planes are grouped in two stacks of 4 each, each plane measuring a different coordinate (x,y,u,v). Eight measurements per track facilitate the resolution of the right-left ambiguity intrinsic in drift chambers and multiparticle ambiguities. The amount of material traversed by the proton is due only to chamber windows, gas and, mostly, to the wires themselves. The polar ( $\theta$ ) acceptance depends on the interaction point in the target, the azimuthal ( $\phi$ ) acceptance is limited to 78% due to the support frames of the chambers. The time-of-flight is measured in between a (start) counter located in front of the tagging system and any of 16 recoil counters surrounding the target. The recoil counters also provide pulse height information to help proton identification.

A schematic view of the experimental layout is given in fig. 2.2 and fig. 2.3.

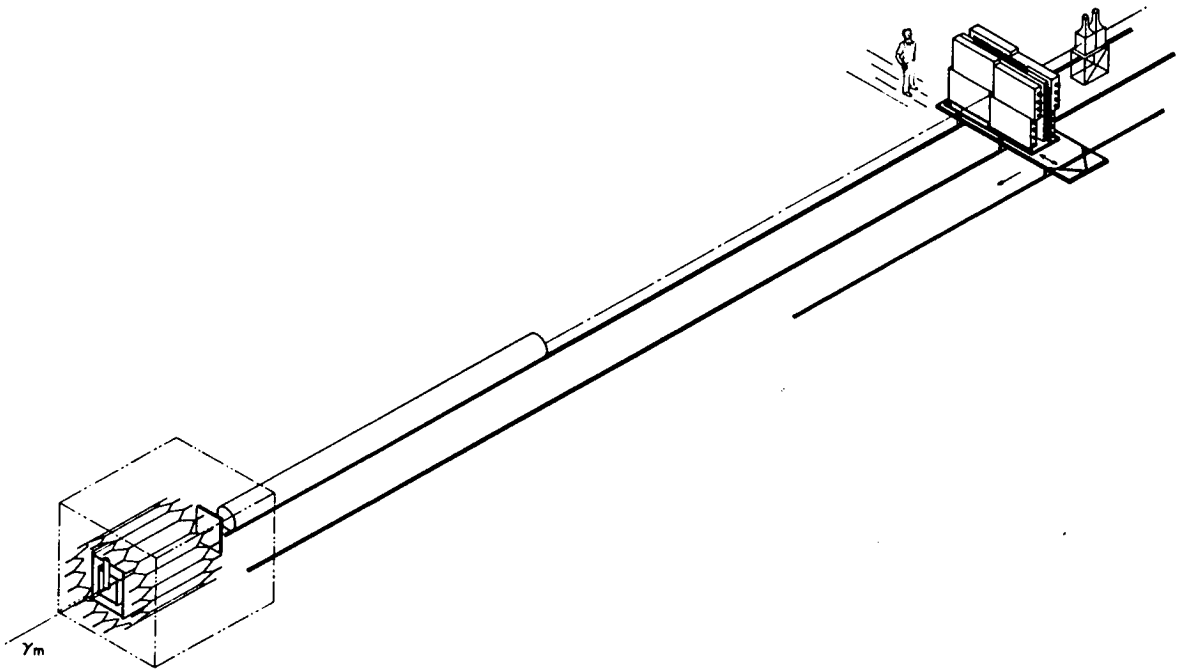
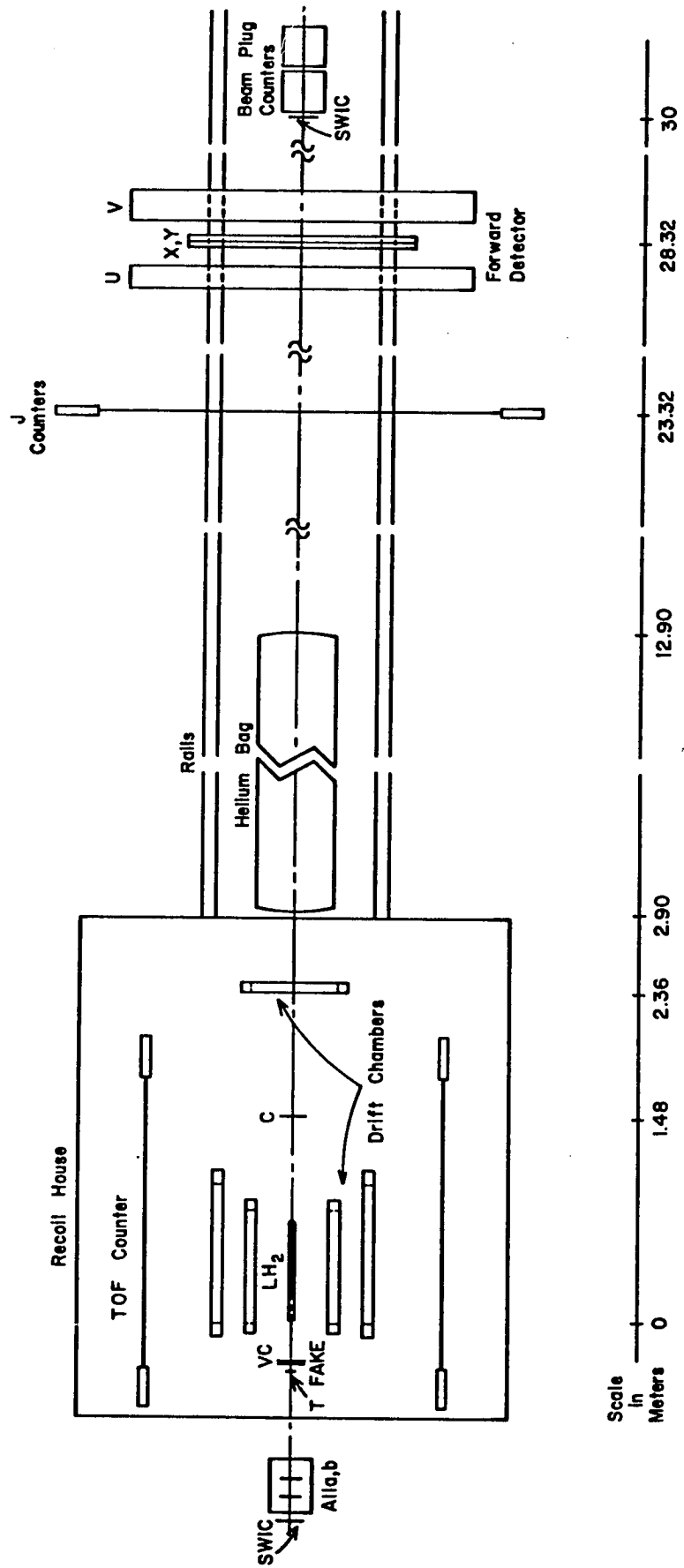


Figure 2.2. Detector Assembly in the Tagged Photon Laboratory

Figure 2.3. Experimental Equipment Plan View



## CHAPTER THREE

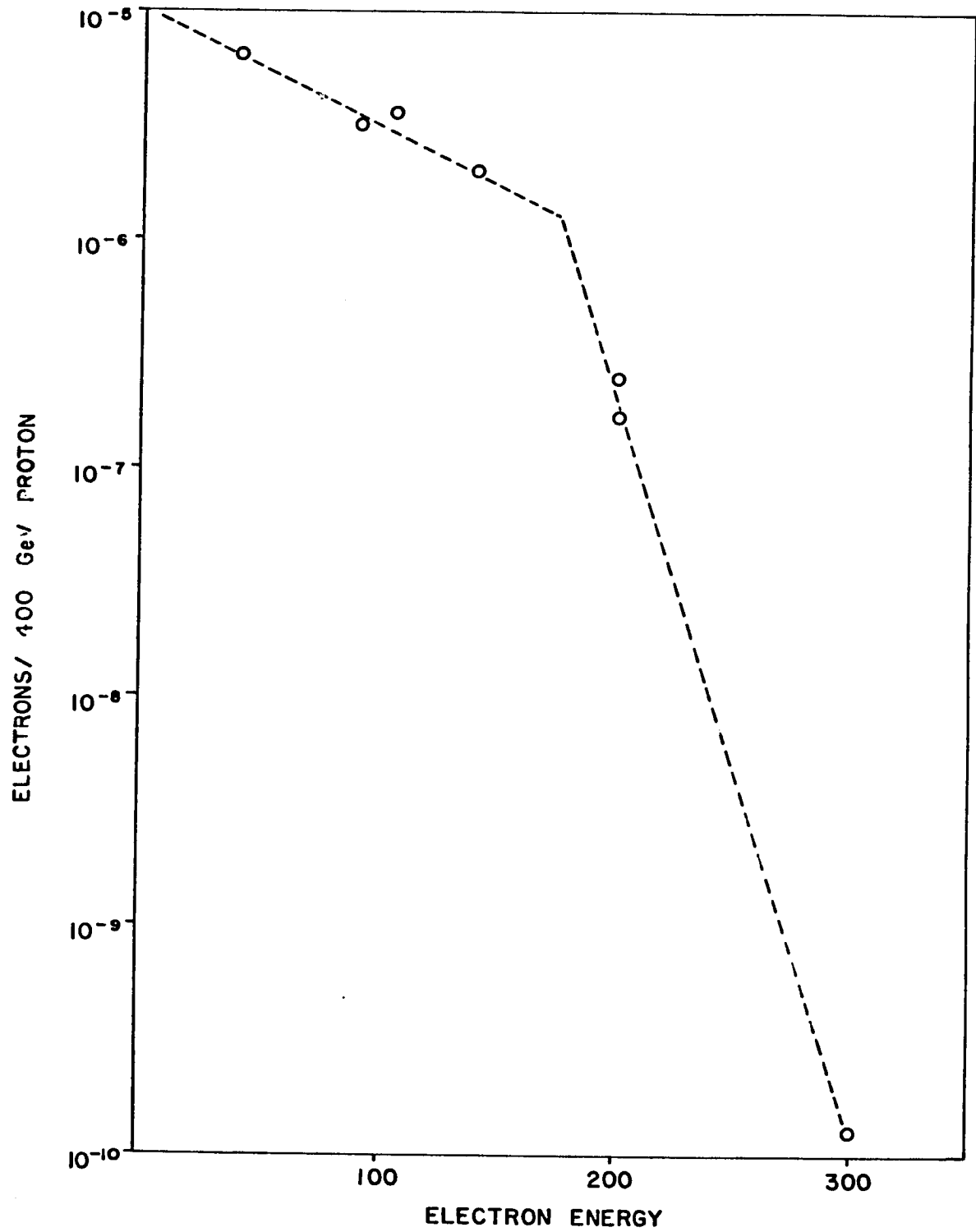
## THE APPARATUS

## A) The Beam Line

The separation in between spills extracted from the Fermilab synchrotron is, at 400 Gev, about 10 sec. The spill has a flat-top about 1 sec long. The flat-top contains some 100 million buckets 2 nsec long, separated by a 19 nsec interval. The proton intensity per spill is measured by the reading of a secondary emission monitor (SEM). The accelerator control also provides a spill start and a spill stop signal to strobe our trigger logic.

The electron beam intensity as a function of the electron energy (for 400 Gev protons) is given in fig. 3.1. The absolute momentum resolution is  $\pm 10\%$ , due primarily to uncertainties in power supply regulations of the beam line magnets. The momentum width is about 2%, the pion contamination less than 1%, the muon halo  $10^5/\text{pulse}/\text{meter}^2$  for a typical proton intensity of  $3 \cdot 10^{12}$  protons per pulse (ppp) onto our production target. The electrons produce in the copper radiator the bremsstrahlung photons ( $e^-N \rightarrow e^-\gamma N$ ) for our experimentaion. Contamination from double bremsstrahlung ( $e^-N \rightarrow e^-\gamma\gamma N$ ), electromagnetic tridents ( $eN \rightarrow e^-e^+e^-N$ ), electron-electron scattering ( $e^-e^- \rightarrow e^-e^-$ ) increases with radiator thickness. Negative pion can interact hadronically in the radiator. Double bremsstrahlung induces bad tags, that is tags where the photon energy information is incorrect. The other processes cause false tags, i.e., a tag occurrence with no photon having been

Figure 3.1. ELECTRON YIELDS





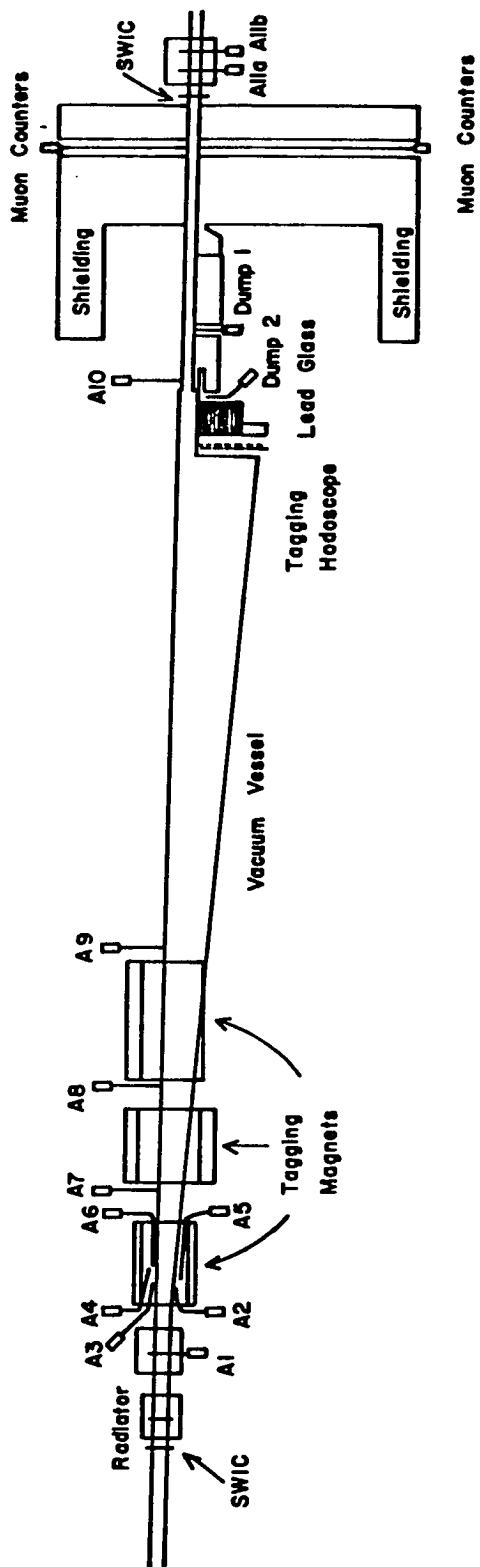
produced. The magnetic separation of charged particles begins 1 meter downstream of the radiator. Non-interacting electrons hit the beam dump counter  $D_1$  located inside the beam dump hole (fig. 3.2). The dump counter  $D_2$  covers the region between the dump and the tagging system. Both counters provide a logic signal. Energetic radiating electrons (and energetic negative pions) are bent into the tagging system. Lower energy positive particles are detected by the veto counters ("anti" counters)  $A_3, A_4, A_6, A_7, A_8, A_9, A_{10}$ . Lower energy negative particles hit the anti counters  $A_2$  and  $A_5$ .  $A_1$  is not used in our experiment. All just upstream of the hydrogen target vetoes wide angle bremsstrahlung photons converted in a 4.4 cm thick lead block.

A large bank ( $3 \times 3 \text{ m}^2$ ) of 6 " $\mu$ " scintillation counters with a central hole for the beam pipe detects muons and other halo particles. The logic sum  $A = \mu + D_1 + D_2 + \sum_i A_i$  ( $\mu = \sum_1^6 \mu_i$ ) will inhibit the issue of a valid tag from the tagging system.

$D_1$  and  $D_2$  are used to veto tags accompanied by a second electron in the same bucket. The stability of the current level in the  $D_1$  phototube monitors continuously on a visual display the quality of the spill. Shape and position of the beam is monitored several times along the beam line by sets of two orthogonal planes of segmented wire ionization chambers (SWIC's). In particular SWIC 440 monitors the electron beam just upstream of the radiator. Insertion of a lead sheet in front of SWIC 441 allows periodic monitoring of the photon beam just upstream of the liquid hydrogen target.

An additional veto counter (VC) with a circular beam hole of smaller radius (1.5 cm) than  $A_{11}$  (3 cm) is necessary in our own trigger

Figure 3.2. TAGGING SYSTEM SCHEMATIC



logic due to the small radius of our target (1.5 cm) to veto photon interactions upstream of the target. The shape of the photon beam at the target is roughly elliptical around the beam axis with about 90% of the beam within  $\pm 2.2$  cm horizontally and  $\pm 2.0$  cm vertically.

A helium filled bag 10 meters long follows the target (when running with the forward detector in the far position (30 meters)) in order to reduce photon interactions in air and early development of showers from photons scattered in the target. Beyond the hole in the forward detector the beam is monitored again by SWIC 442 (with a permanent lead mask in front) before being absorbed in the beam plug counters. (Their total depth of 28 r.l. insure full containment of the showers.) The first counter is a lead-plastic sandwich, the second a lead-scintillator sandwich. The task of this counter (providing a logic signal, a latch and a pulse height response) is to catch secondary photons hitting the beam hole and to identify bad tags. It was also to provide a running calibration of the tagging system and an estimate of the number of false tags. At high rates (more than a million photons/sec if we include the large yield of non-tagged photons) the counters performance (counting efficiency and pulse height response) deteriorate badly. This poses severe problems to our experiment.

#### B) The Tagging System

Nineteen meters downstream of the radiator, the electrons that have radiated away less than 45% of their energy are recorded by the dump counters  $D_1$  or  $D_2$ . The energy and the momentum of the electrons retaining from 5% to 55% of the electron beam energy ( $E_b$ ) are measured in the

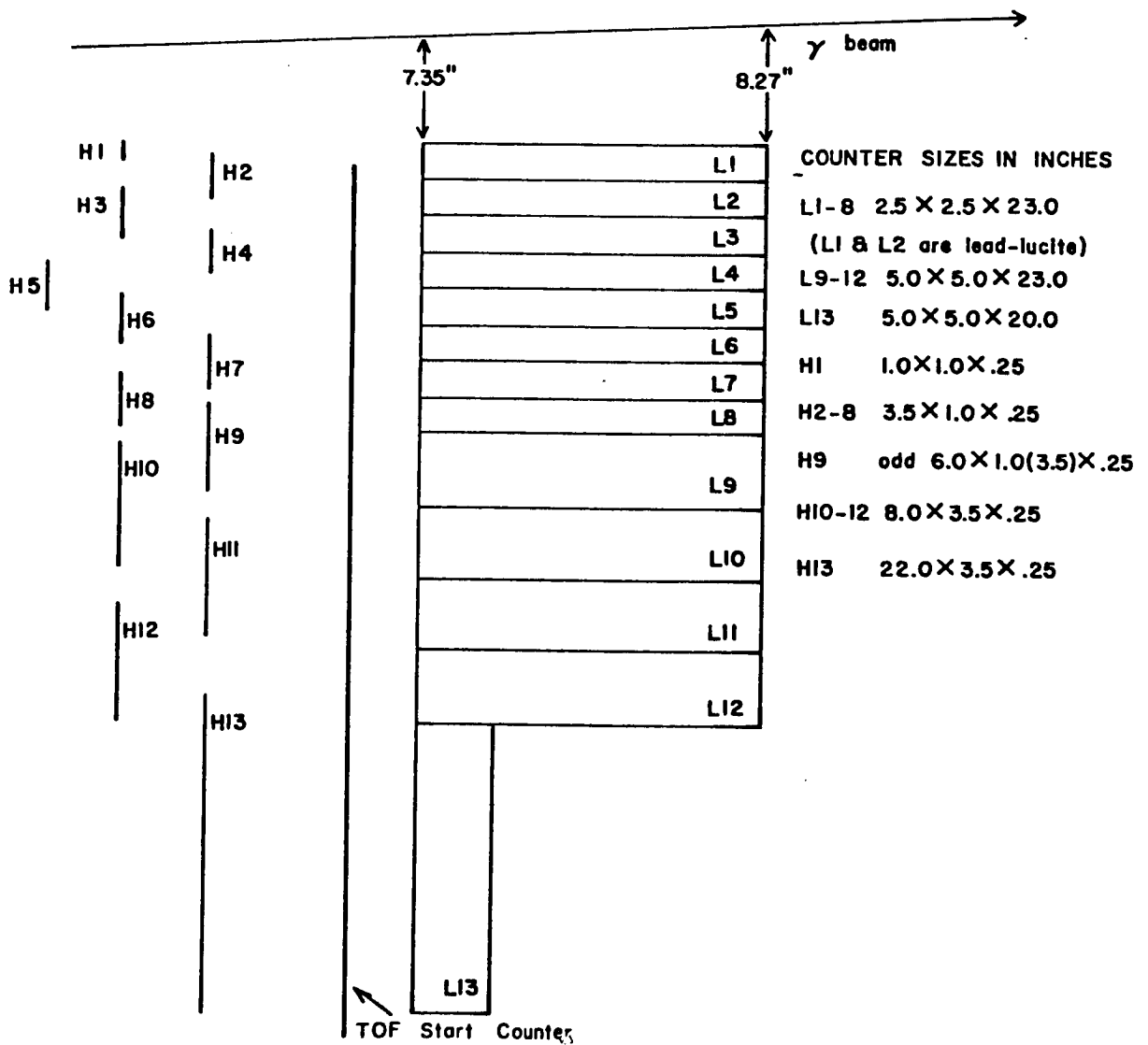
tagging system to provide the energy of the radiated photons in the range  $.45 E_b$  to  $.95 E_b$  where  $E_b$  is the electron beam energy. The tagging system consists of 13 scintillation counters  $H_i$  ( $i = 1,13$ ) in front of a bank of 13 total absorption shower counters  $L_i$  ( $i = 1,13$ ). The independent measurement of the electron momentum from the H counter latches and of the electron energy from the L counter pulse height allows hadrons and muons to be rejected. The shower counters  $L_3$  through  $L_{13}$  are lead glass blocks viewed from the back by low gain phototubes.  $L_1$  and  $L_2$  absorb the high intensity, high energy part of the electron spectrum. To avoid problems induced by changes in optical properties from radiation damage in the lead glass, they are made of 20 layers of lead and lucite viewed from the side.

Each L counter provides a logic signal  $L_i$ , is latched and pulse-height analyzed. The 13 hodoscope counters are positioned to partially overlap in pairs to form  $2 \times 13 - 1 = 25$  tagging channels. The overlap of  $H_i$  and  $H_{i+1}$  shadows the center region of shower counter  $L_i$  (fig. 3.3). The H counter's vertical size defines the vertical acceptance of the tagging system so that showers initiated near the upper and lower edges of the L counters (with consequent loss of shower energy) are not tagged. Each of the counters provides a logic signal and is latched. A valid tag requires the coincidence between a shower counter and the matching elements of the hodoscope. If  $T'$  is the logical OR of all these possible coincidences

$$T' = \sum_i L_i \cdot (H_i + H_{i+1})$$

Figure 3.3

TAGGING HODOSCOPES AND LEAD GLASS



then the tag is generated as

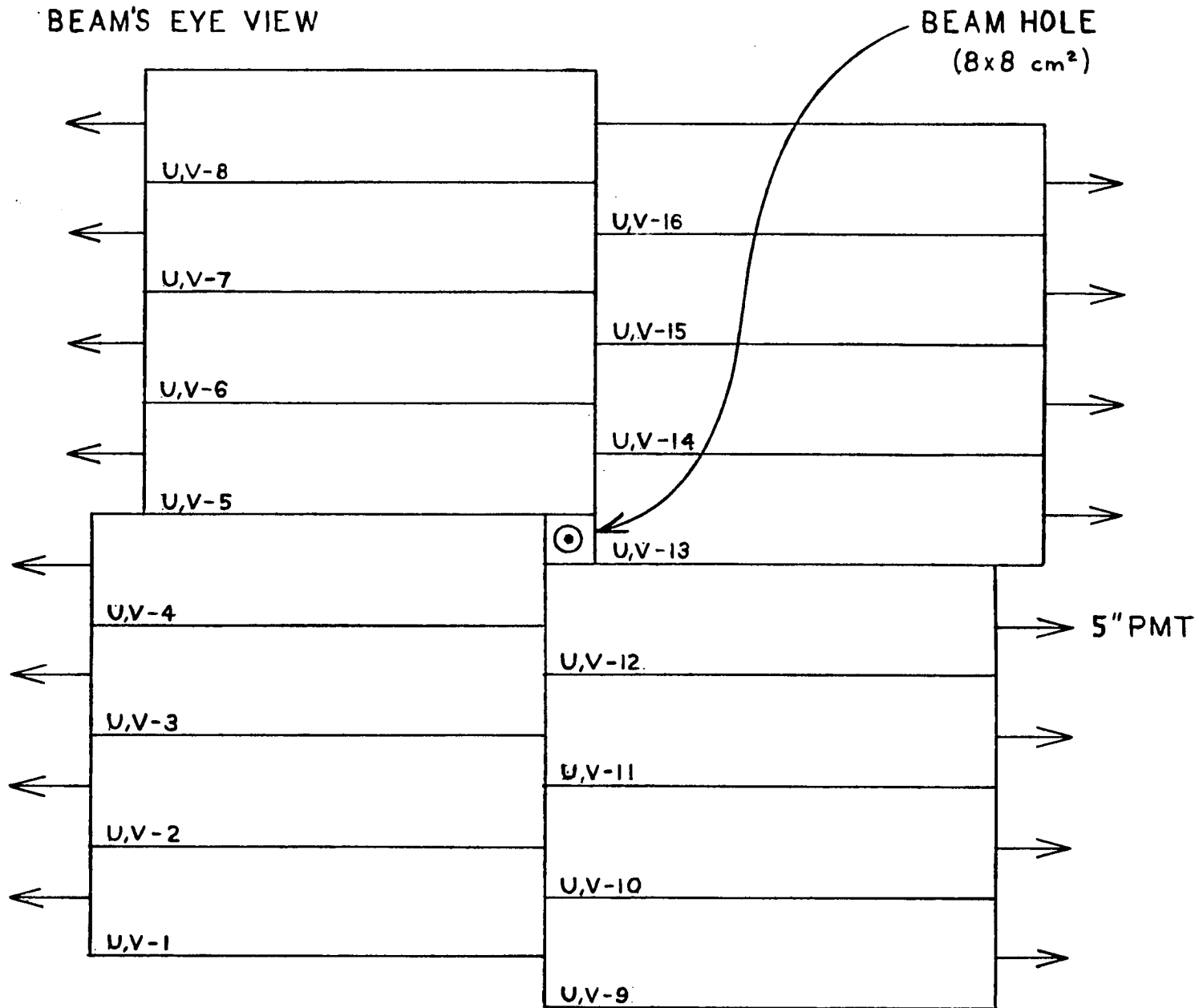
$$T = T' \cdot A \cdot L_1 \cdot L_D$$

where A was defined in section A),  $L_1$  is used as veto (its high rate due to low energy photons would otherwise dominate the experiment) and  $L_D$  is a delayed logical OR of all L counters used to veto tags following a tag in the previous bucket. The very short separation in between buckets (20 nsec) requires this precaution. The bremsstrahlung spectrum of tagged photons is shown in fig. 5.1b for an electron beam of 135 Gev/c, where the bulk of our data was taken. The yield is about  $2 \cdot 10^5$  tags/spill for  $3 \cdot 10^{12}$  ppp on the beryllium target. The resolution in the energy measurement from the tagging system is of the order of 2% for the highest energy electrons.

#### C) The Shower Counters

The total absorption shower counters perform the measurement of the shower energy. The requirements of large solid angle, high resolution and large dynamic range dictated the design. Two sets of 16 shower counters, the U counters and V counters, are assembled around the beam hole in the geometry of fig. 3.4. The U counters are in front of the V counters. Each counter has an area of  $72 \times 18 \text{ cm}^2$ . The central hole for both U's and V's is  $8 \times 8 \text{ cm}^2$  to contain the beam and prevent the large electromagnetic yield from the photon conversions in the target (Bethe-Heitler pairs have a cross section of about 20 millibarns, some 180 times bigger than the total hadronic cross section of 115 micro-barns) from triggering the apparatus. Each of 32 (16 U and 16 V)

Figure 3.4. SHOWER SPECTROMETER LAYOUT



shower counters is a sandwich of lead converter sheets ( $\frac{1}{4}$ " thick, about 1.1 r.l.) and UVT acrylic plastic radiator (plexiglas) fingers, viewed sideways by a common 5", 10 stage phototube (RCA 4525). The number of lead sheets and plexiglas fingers are respectively 8 (9 r.l.) and 7 for the U counters and 9 (10 r.l.) and 10 for the V counters (fig. 3.5). The light produced in the plexiglas is of the Cerenkov type, peaked in the ultraviolet with a  $1/\lambda$  spectrum, but the plastic itself has a sharp transmission cutoff at  $\lambda = 300$  nmeters. Good energy resolution demands forced the use of tubes with bialkali photocathodes (with highest quantum efficiency around 300 nmeters and light pipes (designed by Montecarlo studies) avoiding severe reflection angles. The average collection efficiency is 10% for the best (central) fingers, somewhat worse for the outer strips because of steeper light pipe bends onto the phototube face.

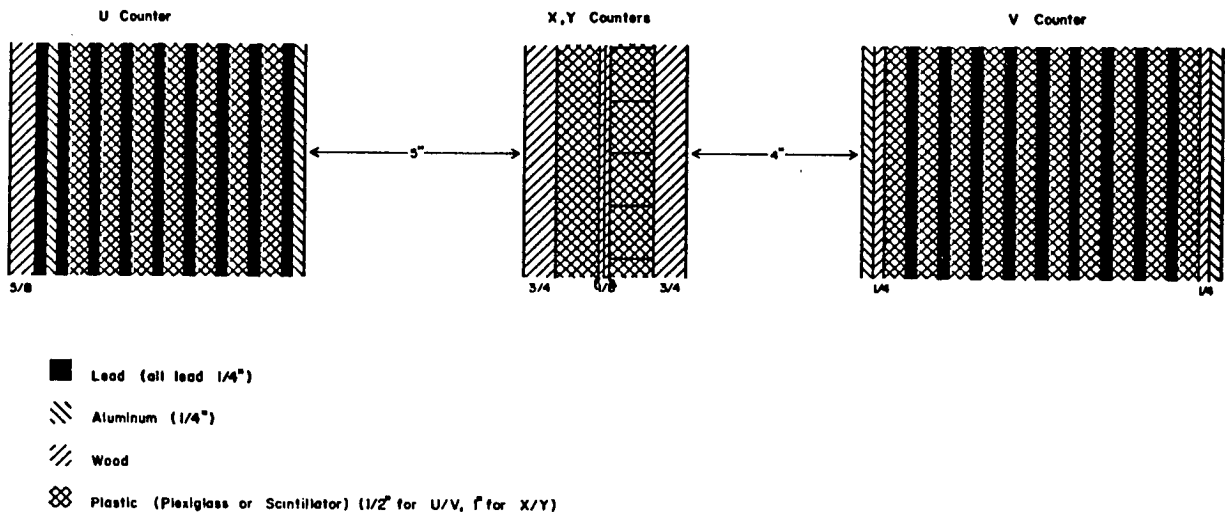
Montecarlo studies of the relative merits of parallel and perpendicular orientation of the V counters with respect to the U counters showed that multishower ambiguity resolution is not greatly helped by the perpendicular orientation. The parallel configuration was chosen to simplify the task of the shower reconstruction. The dimensions of the detector (overall size about  $150 \times 150$  cm<sup>2</sup>) are such that the maximum 4-momentum transfer for the detection of photons elastically scattered is well above  $1$  (Gev/c)<sup>2</sup> for the lowest photon energies with the detector at the farthest distance. The design intended to provide a sizeable acceptance for (deeply) inelastically scattered photons up to a few Gev in transverse momentum.

The entire forward detector assembly (including the X and Y hodoscopes is movable sideways on top of the cart that moves parallel to



Figure 3.5

## Cross Section Of Forward Detector



the beam. Higher acceptance for large transverse momentum photons is therefore possible. In this configuration the beam hits counters  $U_{13}$  and  $V_{13}$ ; this turned out very useful for periodic calibration of the shower counters and the tagging system.

Pulses from the 32 U and V counters (typically 30 picocoulombs for a 50 Gev shower) are linearly fanned together to generate three analog signals  $U = \sum_i U_i$ ,  $V = \sum_i V_i$  and  $F = U + V$ . The 32 counters are individually pulse height analyzed by 10 bit linear ADC's with a sensitivity of  $\frac{1}{4}$  picocoulomb/count.

The pulse height response of the U + V banks is linear (fig. 3.6d) in the shower energy range from 15 to 185 Gev with a slope of 6.01 ADC counts/GeV. Because of the large fluctuations in the initial photon conversion point and in the longitudinal development of the shower, the resolution of the U and V banks individually is rather poor (figs. 3.6a, 3.6b). The U + V resolution is dramatically better ( $18\%/\sqrt{E}$ ), i.e., about 2% at 100 Gev (fig. 3.6c). Attenuation corrections are rather flat along most of the length of the counters, to become steep only very close to the phototubes for a maximal correction of 30%. This is a purely geometrical effect and concerns only the less populated end of the counter. The longitudinal shower development is deeper into the counters only with weak (logarithmic) dependence on the showers energies. Only 3% of a 200 Gev shower leaks in the back of the V counters. Electron initiated showers typically begin 1 r.l. earlier than photons and exhibit larger U/V ratios. Hadronic showers, on the other end, often start developing well inside the counters and have large V/U ratios.

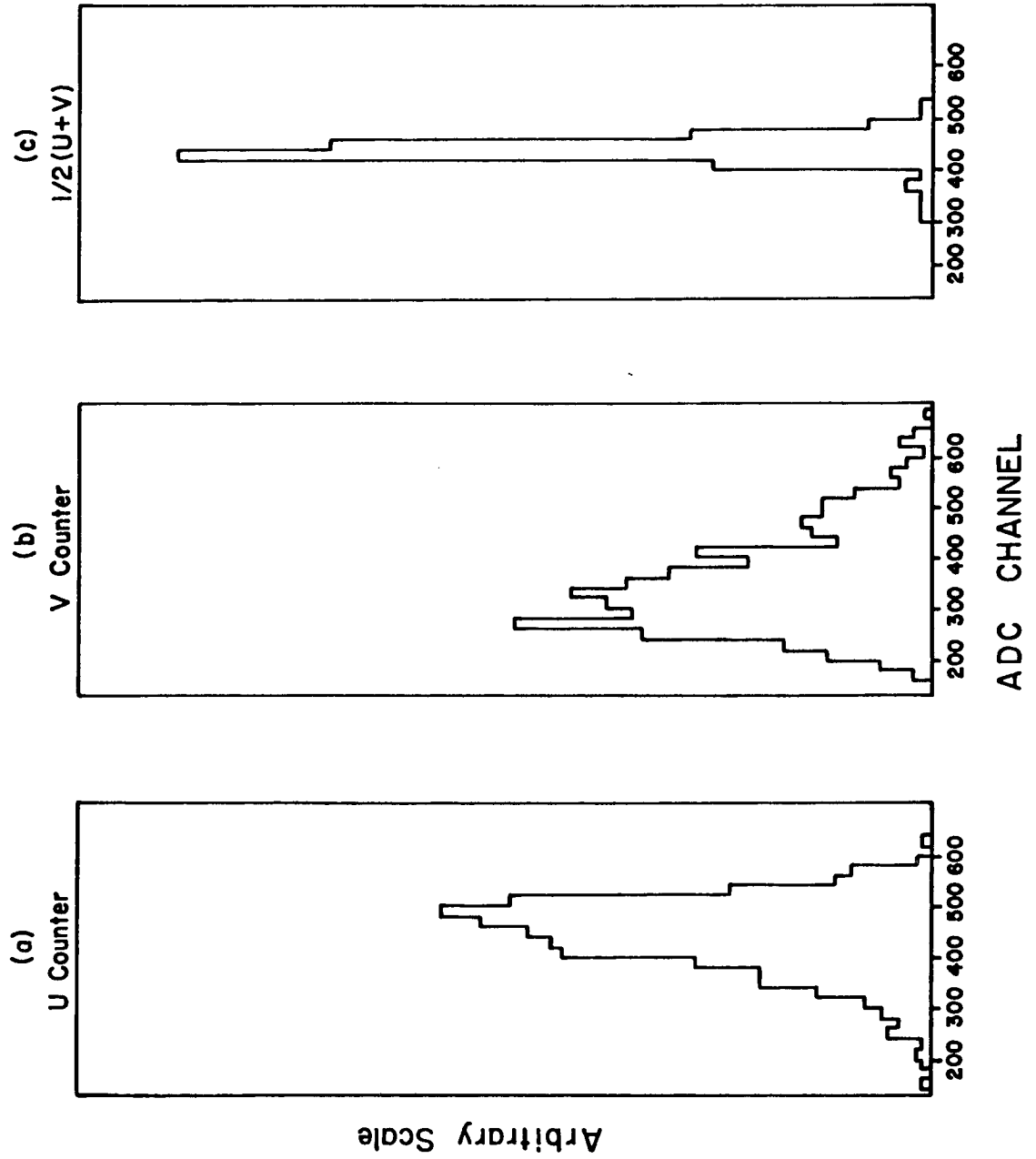
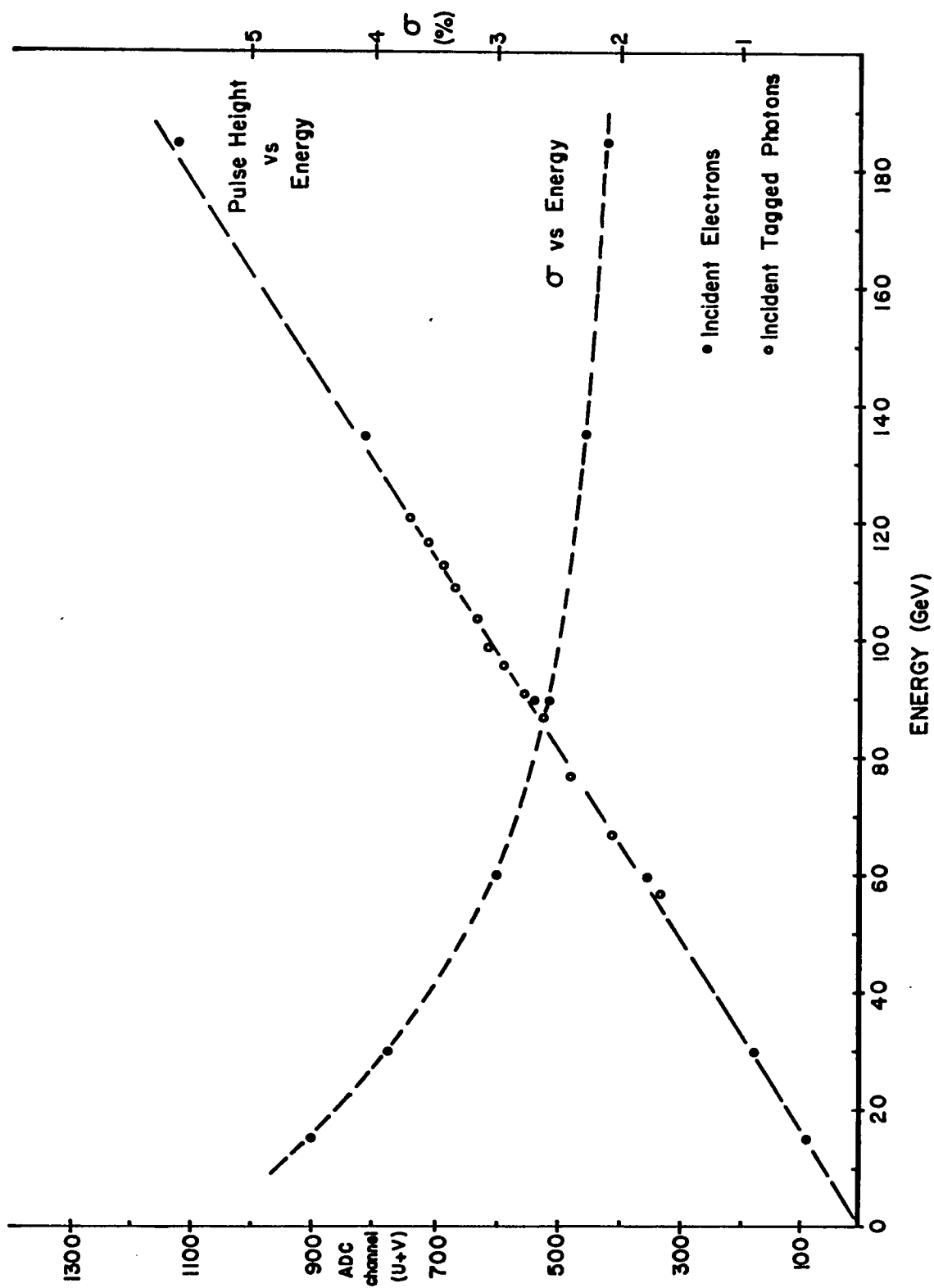
Figure 3.6. 135 GeV  $e^-$ 

Figure 3.6d. Pulse-Height Response and Resolution vs. Energy of Forward Shower Counters (U + V).



## D) The X-Y Hodoscope. Photon Localization and Separation

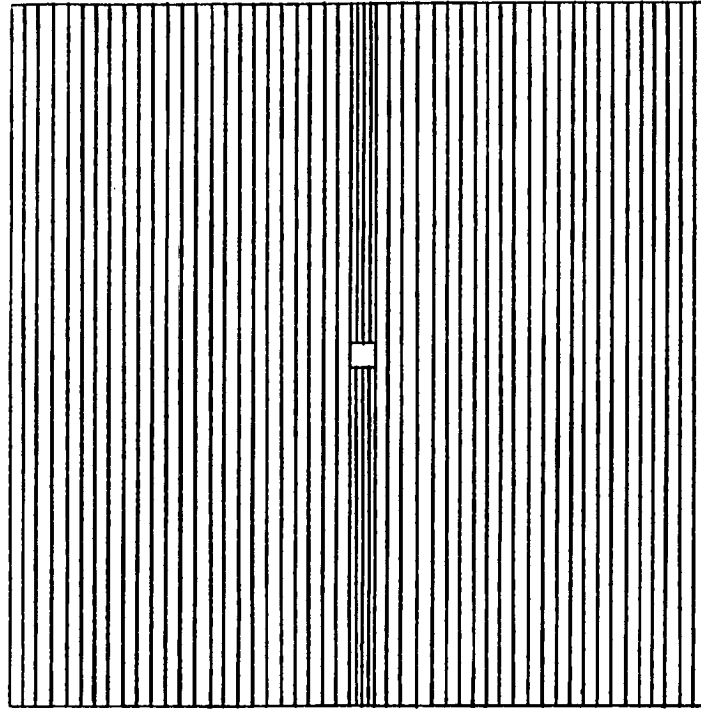
The X and Y hodoscopes (fig. 3.7) perform two important functions. They measure the x and y coordinates of each shower and provide neighbouring shower separation. This is often impossible in the coarsely segmented U and V counters, even for well-separated showers. Coalescing showers have to be resolved, too, in particular to separate single photons from close photon pairs from decay of (energetic) neutral pions. The minimum, and most probable, photons' opening angle is

$$\theta \simeq 2m_{\pi^0}/E_{\pi^0} .$$

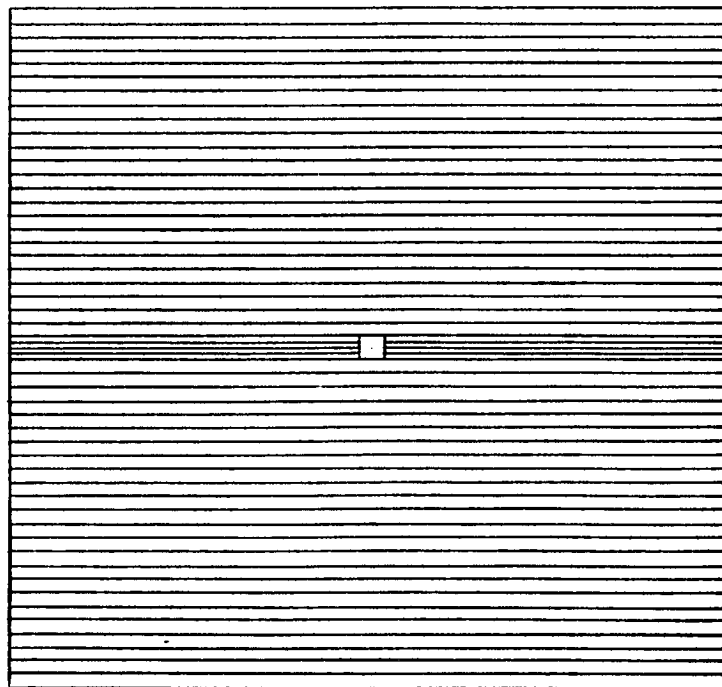
In the 30 meters position, this gives a separation of about 7.5 cm for 100 Gev neutral pions. The spatial resolution in the two planes and consequently the mass resolution for neutral pion identification improve for smaller strip widths. The large lateral shower fluctuations, however, make unprofitable strip widths much smaller than a few cm. The poor sampling thickness (1") of the strips and the longitudinal shower fluctuations make their energy resolution poor, but often adequate for resolution of ambiguities.

Lower energy tests performed at SLAC determined experimentally that the longitudinal positions of the X and Y arrays in the forward detector that optimized position resolution is slightly beyond shower maximum. The hodoscope sits in between the U and V counters. Its location is optimal for showers of energies of about 15-20 Gev. The air gaps (needed for mechanical assembly) turned out to be responsible for significant lateral spread of the showers. It was for us impractical to reduce them. The X and Y strips make respectively 0 and 90 degree

Figure 3.7 X and Y Hodoscope



Y HODOSCOPE



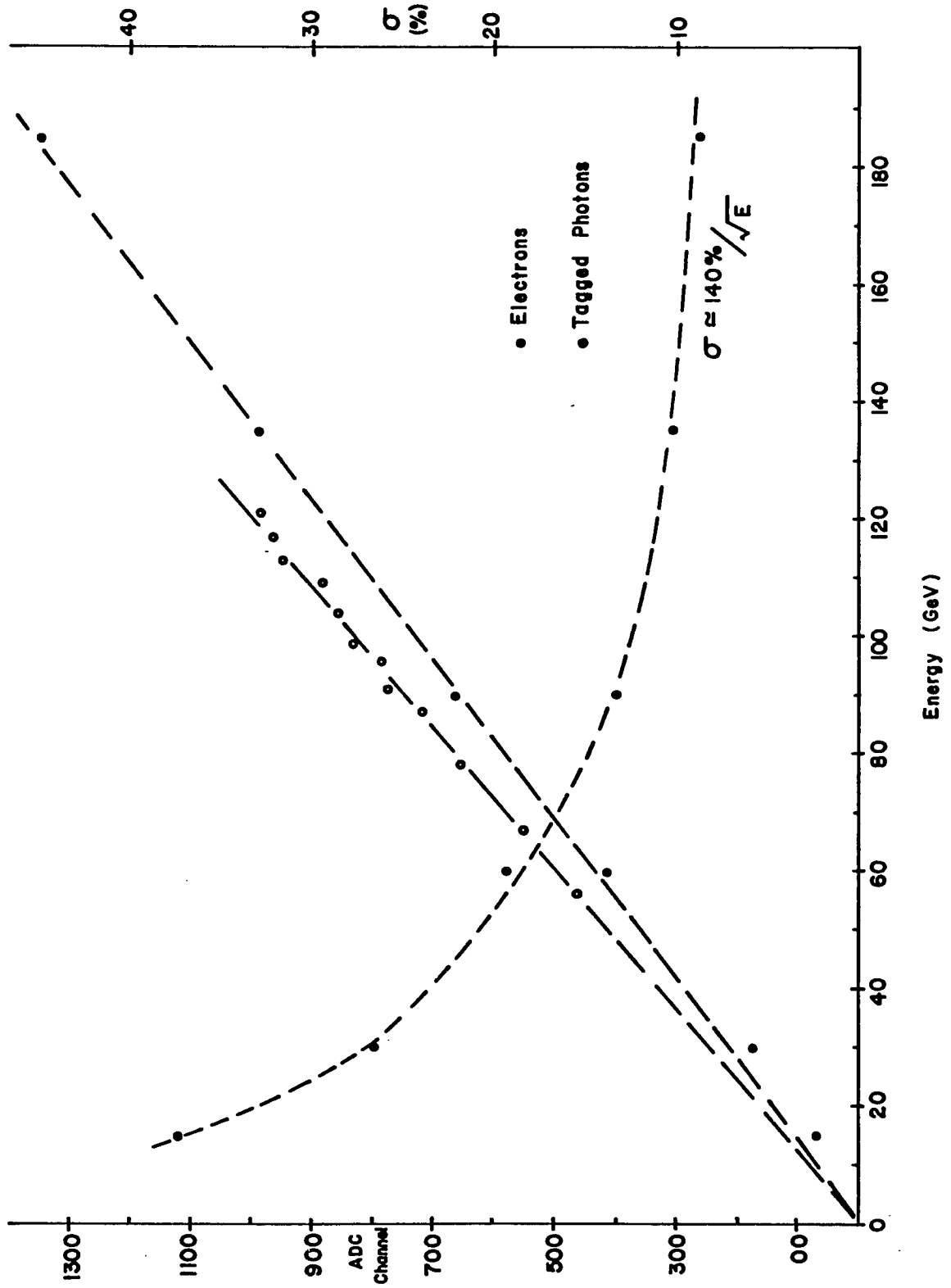
X HODOSCOPE

angles with the U and V counters. Montecarlo studies showed that even a 45 degree rotation would induce only 4% improvement in ambiguity resolution. The X hodoscope on each side of the  $8 \times 8 \text{ cm}^2$  beam hole consists of 24 3 cm wide, 158 cm long, low grade scintillator strips (Rohaglass 1921). The central 8 cm containing the beam hole have 2 sets of 4 2 cm wide, 92 cm long strips above and below the beam hole (fig. 3.7). The same design, in the orthogonal dimension, was used for the Y strips. Each hodoscope has therefore  $2 \times (24+4) = 56$  strips. 1.5" phototubes (RCA 4157) with bialkali photocathodes are attached to alternate edges of the scintillator strips, coupled to them by plexiglas blocks. Scintillators are used (instead of Cerenkov radiators) in order to obtain enough light from a thin sampling device.

The 112 analog signals  $X_i$  and  $Y_i$  are pulse height analyzed by 8 bit bilinear ADC's (LRS 2248) with 2 slopes of  $\frac{1}{4}$  and 1 picocoulomb/count respectively. The bilinearity increases the dynamic range at the expense of precision. A few of the X and Y counters produce logic signals for the construction of special (monitor) triggers. The energy resolution of each hodoscope plane is  $140\%/\sqrt{E}$  (fig. 3.8). The resolution of multi-showering ambiguities in pairing clusters from the two sets of strips uses this moderately precise energy information. The pulse height response is approximatively linear with energy. Attenuation corrections vary up to a factor of two along the strip length.

Experimentally, showers in the hodoscopes deposit most of their energy in a few central strips with tails extending over quite a few strips, with significant contribution from the spread in the air gaps. A typical shower extends over a total of 9 strips, with a fwhm of about

Figure 3.8. Pulse-Height Response (for Electrons and Photons) and Resolution vs. Energy of X and Y Hodoscopes.





10 cm. Energy dependence of transverse shower dimension is small. Position resolution is 2.6 mm in each coordinate for 135 Gev showers.

#### E) The Recoil Chambers

Four quadrants of drift chambers, each containing two modules of 4 drift planes, surround the target (fig. 3.9) to measure the track parameters of recoil protons from two body final states. Drift chambers, with a long drift cell (4 cm), are used to reduce cost per unit area in the low rate, low multiplicity environment of the recoil system. The 4 planes in each module have wires strung at different angles with respect to the beam line (90,0,72,108 degrees). A straight track in space is identified by four parameters. Eight planes of chambers in each quadrant provide useful redundancy against ambiguities (fig. 3.10). The active area of the drift planes is  $48 \times 80 \text{ cm}^2$  for the ones in the smaller module closer to the beam and  $90 \times 96 \text{ cm}^2$  for the ones in the larger module. Interplane separation within a module is about 2 cm. The modules in a quadrant are separated by about 25 cm. Chamber support frames reduce the azimuthal ( $\phi$ ) acceptance to 78%. The  $\theta$  (polar angle) acceptance for interaction at the upstream edge of the target is about  $45^\circ \leq \theta \leq 90^\circ$  (fig. 3.11). A typical drift cell is shown in fig. 3.12. Amplification ("sense") wires, made of gold-plated tungsten, have a 20 micron radius and are 8 cm apart. Halfway in between them a thicker (125 micron radius) copper-beryllium "field" wire separates neighbouring cells. Cathode planes are also made of these copper beryllium wires. They are 2 mm apart. These "field-shaping" wires are at uniformly decreasing negative electrical potentials from the edge (-4.9 kV) of the

Figure 3.9. Recoil Detector Assembly - Front View

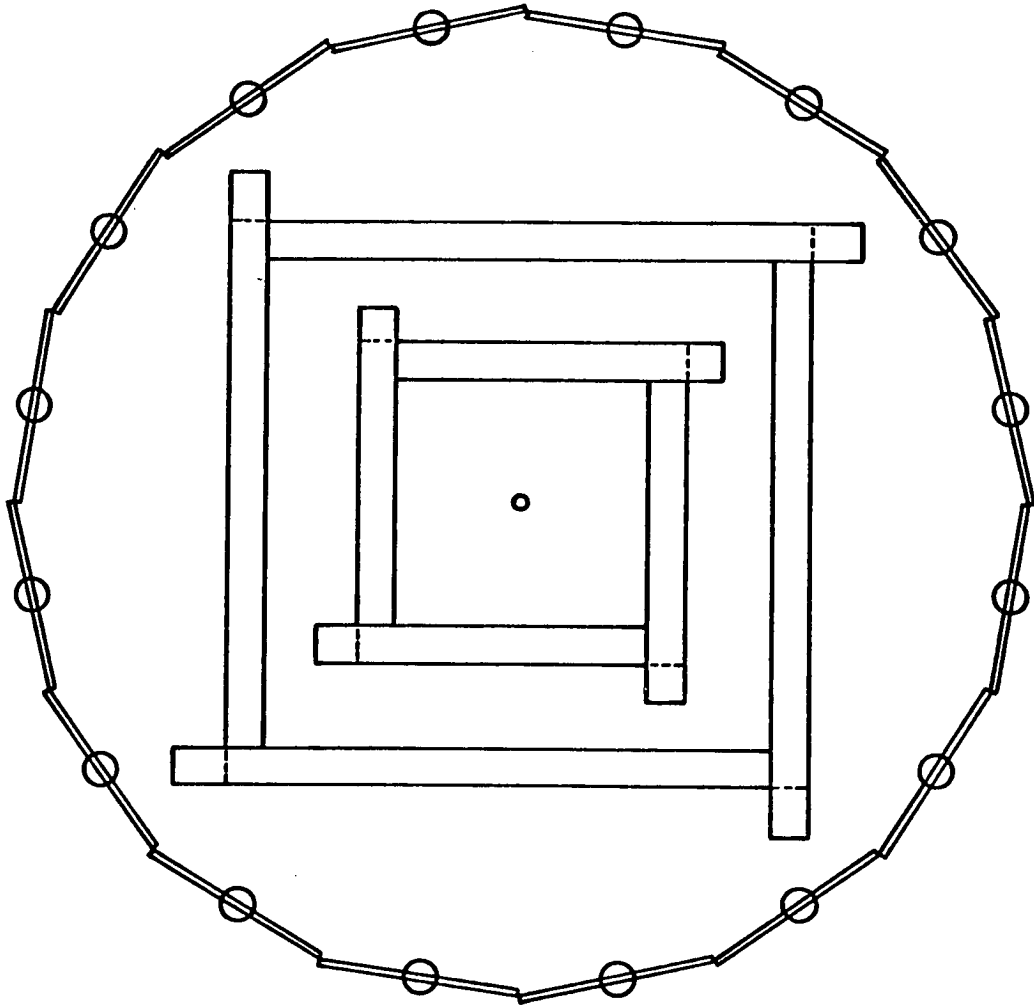


Figure 3.10. Left-Right Ambiguity on the Eight Drift Chambers Planes in a Quadrant. Track Identification Involves a Choice Among  $2^8 = 256$  Combinations.

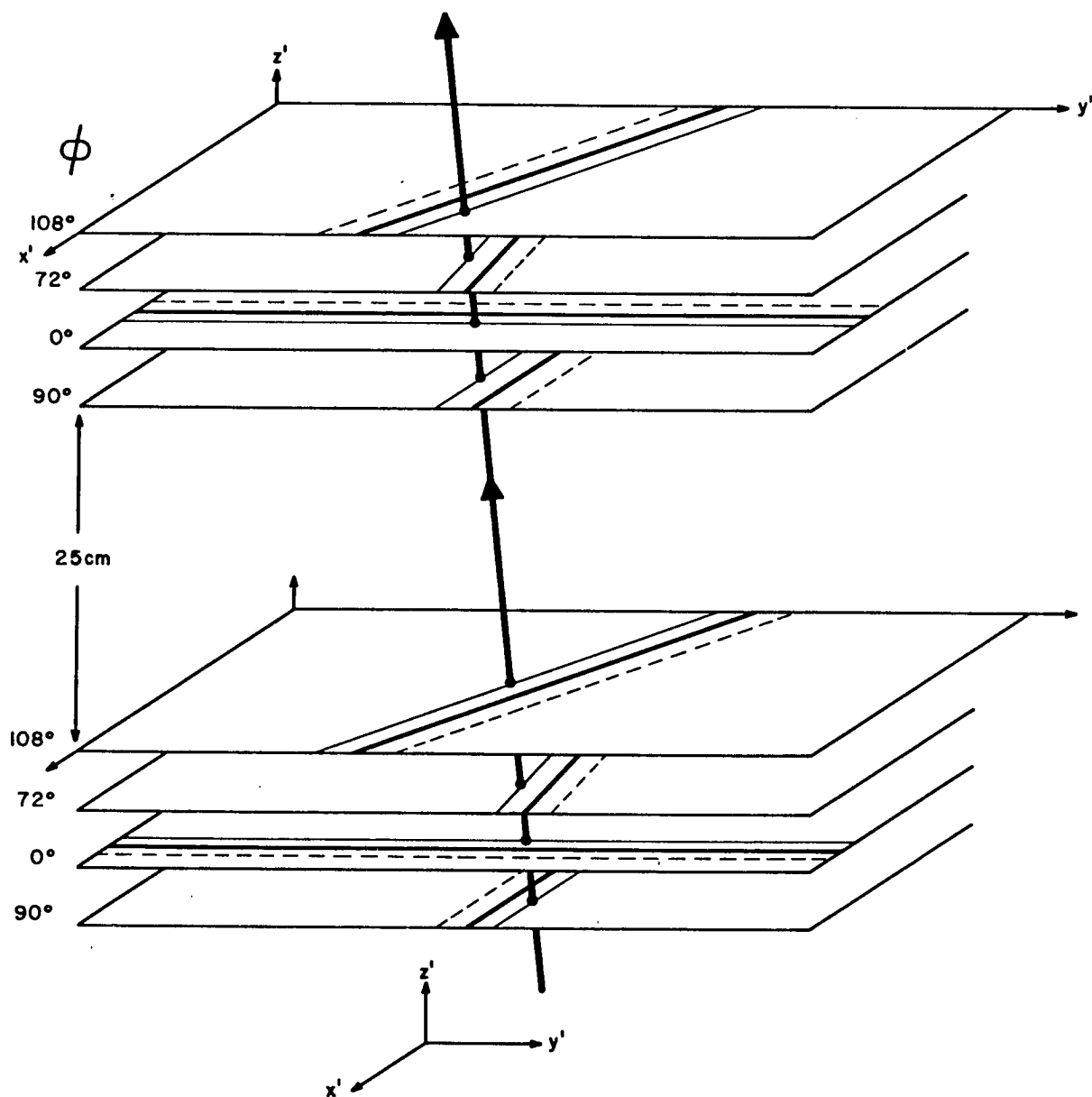


Figure 3.11. Recoil Detector Assembly, Side View

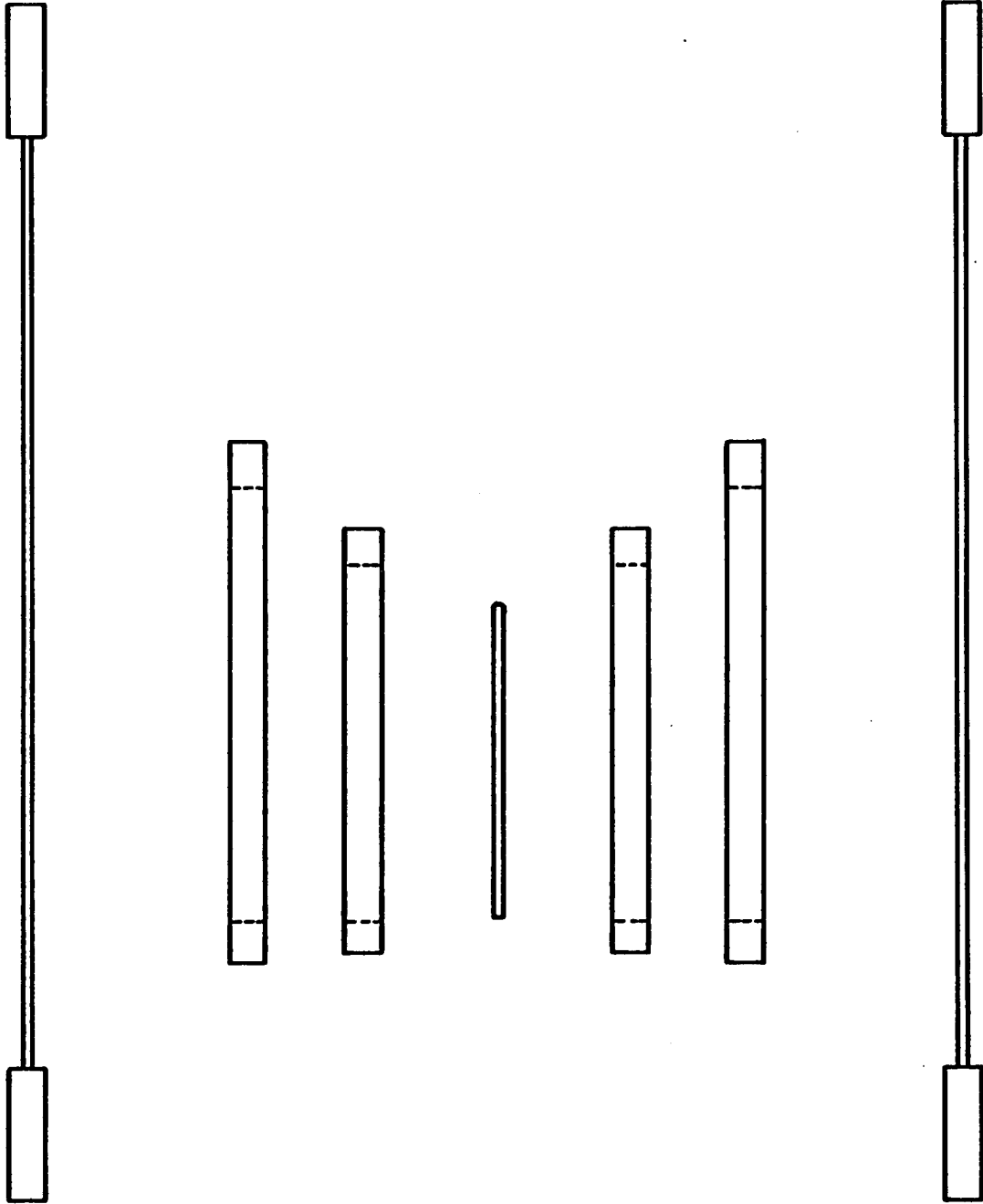
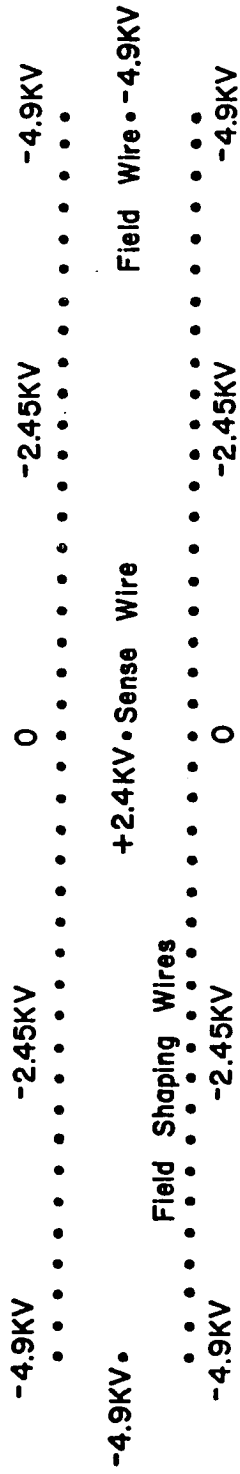


Figure 3.12. Typical Drift Cell



cell to its center (0 kV). "Field" wires are held at the largest negative potential (-4.9 kV). The electric field in the cell is therefore uniform to a good approximation until the drifting electrons approach the "sense" wire, held at positive potential (2.4 kV). The constant value of the electric field is  $E = 1.25$  kV/cm. The gas filling the chamber is pure ethylene, with nearly constant ("saturated") drift velocity of 50 microns/nsec around that value of  $E$ . Constancy of  $E$  and saturation will insure a linear relation in between particle hit distance from the wire and measured drift time.

Pulses from the sense wires travel on coaxial cables to a receiver-amplifier-shaper circuit a few meters away from the chambers. The time in between a drift pulse (start) and the (delayed) event trigger (common stop) is digitized by a TDC designed at Fermilab. Only one drift pulse (the one with the longest drift time) is recorded in case of multiple hits on a wire. Only non-zero CAMAC words are read out from the TDC.

The entire recoil cart (supporting the chambers and the recoil scintillating counters) is enclosed by a metallic environmental housing also acting as electrical shield. The chambers operated for a year with very few broken wires replaced during beam-off time.

The intrinsic resolution of the chambers and the associated electronics was measured to be about 200 microns. The mechanical tolerances in the construction of the chambers are worse than that and dominate the error per plane on reconstructed tracks (700 microns). The corresponding error on the 4-momentum transfer,  $t$ , of recoil protons is plotted vs.  $t$  in fig. 3.13. Its order of magnitude is still below the one resulting

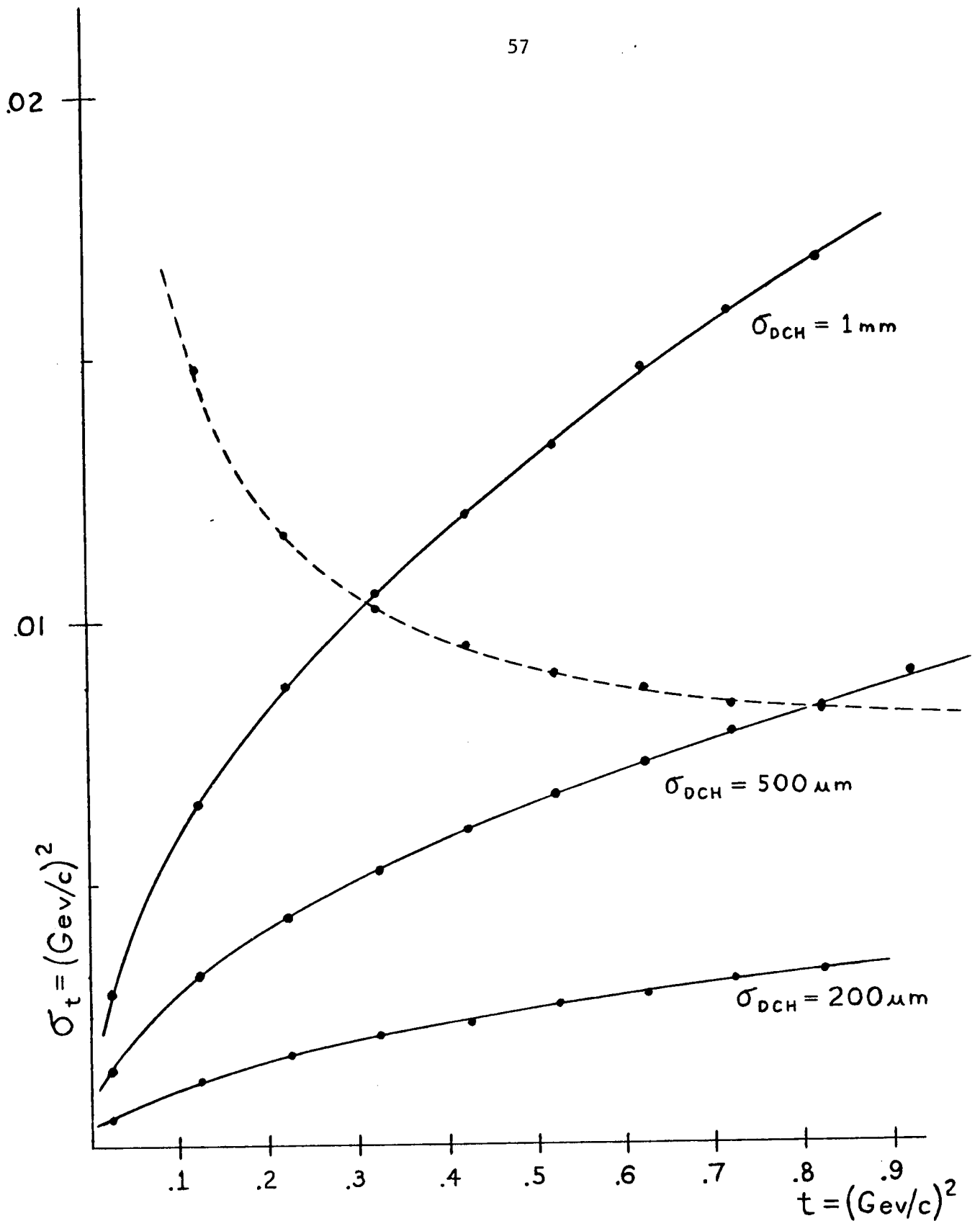


Figure 3.13. Error in  $t$  vs.  $t$  for Three Different Values of the Error per Plane in the Drift Chamber Measurement. Dash-Dotted Curve is Multiple-Scattering Contribution to the Error.

from the multiple scattering of the slowly recoiling protons, at least for the (most populated) low  $t$  region.

#### F) The Time-Of-Flight Recoil Counters

The time-of-flight recoil counter system measures the magnitude of the velocity vector of the recoil protons and provides also a  $dE/dx$  measurement. Sixteen scintillation counters (NE110),  $\frac{1}{2}$ " thick, with active area  $150 \times 40 \text{ cm}^2$  each, surround the target and the recoil chambers (figs. 3.9 and 3.11) in a cylindrical array about 1 meter away from the target. They are viewed by one phototube on each side. Light pipes are trapezoidal (fish tail) to optimize time resolution (at partial expense of light collection efficiency). The time-of-flight system is completed by a long counter, also viewed by two phototubes. This counter, the start counter, is positioned in front of the tagging system hodoscope bank (H counters, fig. 3.3).

A trigger from our apparatus for a two-body photoproduction event will be accompanied by a pulse from the radiating electron in the start counter and by a pulse from the recoil counter hit by the proton. Time digitizers measure the time interval in between each of these two pulses and the trigger. The difference of these two times, if the origin and the direction of the proton are known from the drift chambers, will measure its velocity. Note that the time jitter of our trigger (its timing is set by the tag signal, with an intrinsic jitter of about 2 nsec) is present in both measurements and cancels out in the difference.

Each counter produces two logic levels ( $R_i^A$  and  $R_i^B$  for  $i = 1, 16$  and  $S^A$  and  $S^B$  for the start counter) from each phototube (dynodes). A



recoil logic level  $R = \sum_i R_i = \sum_i (R_i^A \cdot R_i^B)$  and a start logic level are generated. All pulses are latched and scaled. Two anode pulses from each tube go respectively to an ADC for  $dE/dx$  measurement and (after a discriminator) to a TDC (LRS 2228) for the time measurement. The TDC's have 10 bits, with resolution of about 100 psec/count.

In order to significantly reduce the time slewing induced by the rather large range of pulse heights (energy deposition) from recoiling protons in the R counters, we used constant fraction discriminators to discriminate the anode pulses that go to the TDC's.

The resolution of the time-of-flight system was about 500 psec. Drift chambers and time-of-flight system together provide excellent rejection of the (mostly diffractive)  $N^*$  production. This is the most copious background to the elastic and quasi-elastic channels.

#### G) Forward Charged Particle Detectors

The detection of forward charged particles is crude. A counter, immediately downstream of the target ( $20 \times 20 \text{ cm}^2$ )  $\frac{1}{4}$ " thick, with a 3 cm radius circular hole safely shadowing the forward detector active area in the 30 meters configuration) latches events with charged particles at relatively large angles that do not hit the forward detector. It will be referred to as the C counter. Next along the beam line a single module of 4 drift chambers follows, identical to the small modules of chambers in the recoil detector. Because of its long memory time (about 1 microsec) and the very large rate at very small angles of Bethe-Heitler pairs produced in the target, the wires sensitive to the beam on each drift plane are constantly on and are not useful.

The separation in the forward detector of showers induced by neutral ( $\gamma$ ) and charged ( $e^+, e^-$ ) particles is entrusted to a bank of scintillation counters located upstream of the shower bank (J counters). Eight counters, in the arrangement of fig. 3.14, with a central square beam hole, entirely shadow the forward detector and latch charged particles hitting them. We ran initially with the counter bank right in front of the U counters and found the rates to be prohibitive. A large contribution was probably due to backplash from the shower counters. Rates were substantially reduced by moving the J bank 10 meters upstream.

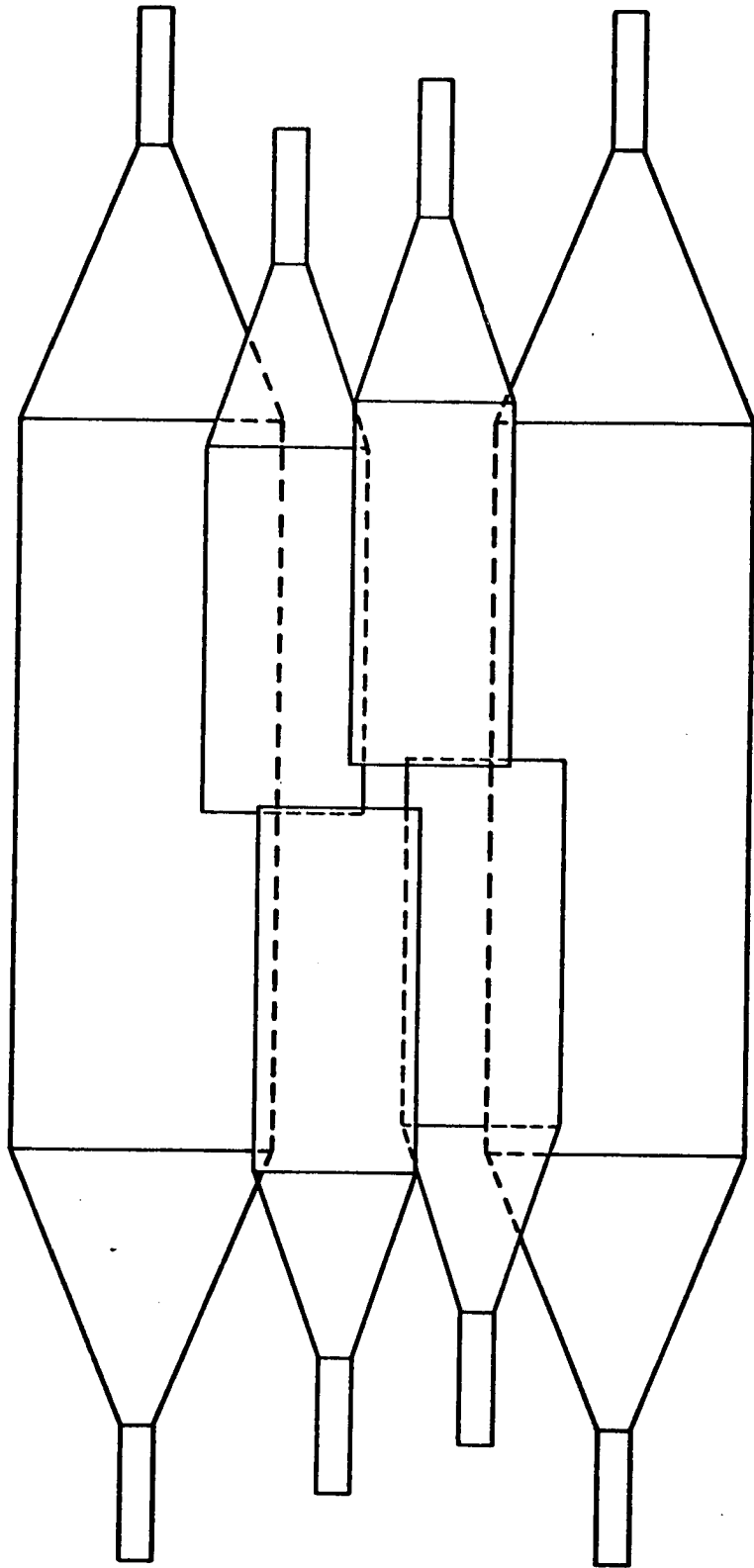
Early conversion of photons in air, upstream of the detector, however, reduce its usefulness.

#### H) Monitors

The energy-pulse height responses (gains) of the counters in the forward detector and the tagging system were periodically measured during special calibration runs. In addition, data from several monitoring systems were routinely taken in the course of the experiment to check (and leave a record of) the integrity and stability of these gains. Special monitor runs were also frequently performed.

The high voltages on counters and drift chambers were continuously scanned, read into the computer, checked against nominal values and written to tape thanks to a CAMAC digital voltmeter system. If there were discrepancies, the system would issue warnings. Two voltage levels proportional to the currents in the magnets defining the electron beam energy and the tagged photon energy window, as well as two proportional to the temperature and pressure in the  $LH_2$  target were also collected. Very rarely adjustments were needed.

Figure 3.14. Charged Particle Counters (J Counters)



The gains of the U and V shower counters have to be known within 2%. Three types of monitor "events" generating reference "spectral lines" in the dynamic range of the counter can trigger the data acquisition system. Redundancy is necessary, none of the monitors being perfectly stable.

The counters' response to minimum ionizing particles is monitored by accumulating spectra from the beam halo muons. The light emitted by Na-I crystals (5.64 Mev  $\alpha$  particles from Americium sources imbedded in the crystals range out inside them) mounted on the face of the phototubes monitor the response in the region of 40 Gev showers. Phototubes respond also to the light emitted (in controllable amount) by bright light-emitting-diodes (LED's) and transported by optical fiber bundles to the face of the counters light-pipes. The LED system tests the short term drifts in the gains of the phototubes and the transparency of the optical couplings. LED data are taken both in and out of beam spill. Fast tests of integrity, linearity, saturation and rate studies on selectable counters are possible. LED lines have 2% fwhm in the ADC's.

Spectra from Americium disintegrations are accumulated for 100 milli-sec at the end of the beam spill. Part of the pulse (about 20 mV) in the firing counter is split and amplified to generate a trigger. The ADC line is about 2% fwhm.

Spectra from halo muons are taken at low rate during spill and at higher rate in special muon runs. They provide absolute energy calibration (500 Mev equivalent showers, before amplification) and test the counter integrity. The muon "line" (40% fwhm) is poor because of the low photoelectron statistics and the amplifier fluctuations. Sixteen special coincidences in between 2 Y hodoscope strips and 8 X hodoscope strips

select muons in very localized areas ( $3 \times 3 \text{ cm}^2$ ) of the U and V counters active surface (fig. 3.15). U and V pulses from muon triggers are amplified and read in from an independent set of ADC's.

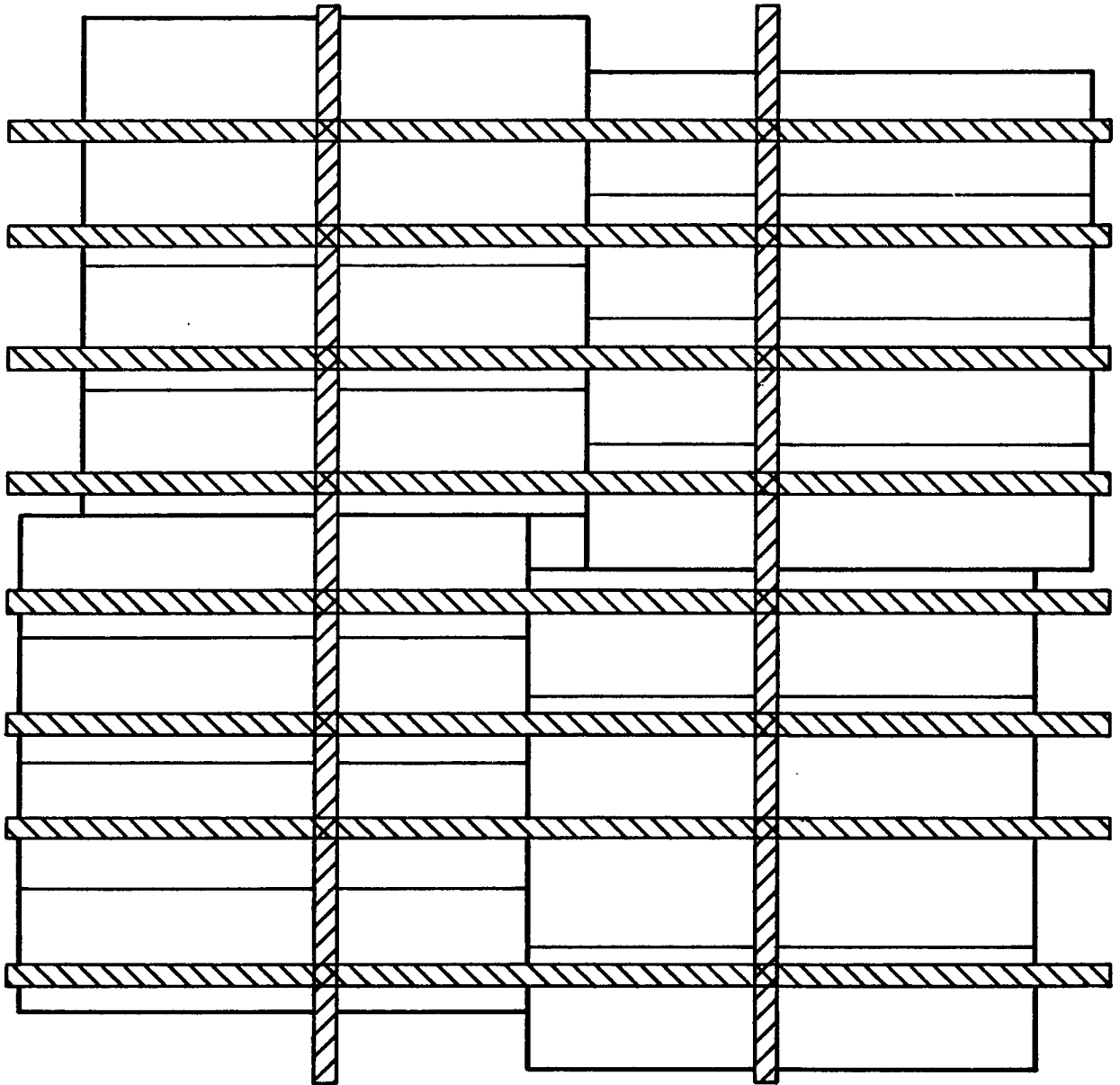
The gains of the X and Y scintillator strips have to be known at the 15% level. They are monitored by a less redundant system consisting of LED's and fiber optic bundles on every counter and of americium sources on every eighth counter. Narrow LED "lines" are accumulated in and out of spill. Americium triggers are taken at the end of the spill. The Americium sources are imbedded in scintillators.

Line width in the X and Y ADC's is 40% fwhm.

The time-of-flight and the start counter are also equipped with LED's shining light into the scintillator half way in between the two phototubes. A short light pulse of fast risetime on the LED provides a 500 psec fwhm line in the TDC spectra. LED pulse height spectra are also taken. They give a broad line at about the pulse height of a minimum ionizing particle in the counters.

From the readings of all the ADC channels in our system, a pedestal has to be subtracted. Pedestals, due to a small background current in the circuitry integrated over the duration of the gate, are typically about 20 ADC counts. Pedestals' values are learned (and monitored) from special pedestal "events," when an asynchronous pulser triggers data acquisition and gates on the ADC's.

Figure 3.15. Choice of X and Y Hodoscope Strips Relevant for the Muon Monitor Trigger.



## CHAPTER FOUR

## DATATAKING PROCEDURE

## A) Trigger Logic

Two logic signals, originating at the accelerator control station, signal the beginning (spill start) and the end (spill stop) of the beam spill and time our trigger logic and data acquisition. They start and stop, respectively, a gate generator, providing a beam gate logic level (BG).

The occurrence of a valid tag in the tagging system is signaled by a tag signal (T). This pulse is made very short (6 nsec) and sets the timing of our real event trigger. The halo muon counter bank provides a  $\mu$  trigger. Part of the beam plug counters pulses are fanned together and discriminated to make a beam plug trigger (BP). Similarly, part of the pulses from the U and V counters are fanned together to provide the two linear sums  $U = \sum_i U_i$  and  $V = \sum_i V_i$ . U and V are again summed linearly to give the signal  $F = U + V$ . F is discriminated to provide the forward trigger  $F_H$  (F high). U and V are also amplified to provide  $U_A$  and  $V_A$ , in turn linearly fanned together to provide  $F_A$ .  $U_A$  is discriminated to provide a  $U_H$  (U high) trigger.  $F_A$  goes through a window discriminator consistent with the pulse height range due to an americium disintegration in any of the 32 Na-I crystals on the counters' phototubes. An U-V americium trigger ( $UV_{AM}$ ) is generated. A normal discriminator on  $F_A$  provides a  $F_{AH}$  trigger.

Pulses from the X and Y strips equipped with americium sources are fanned together, amplified and window discriminated to provide the

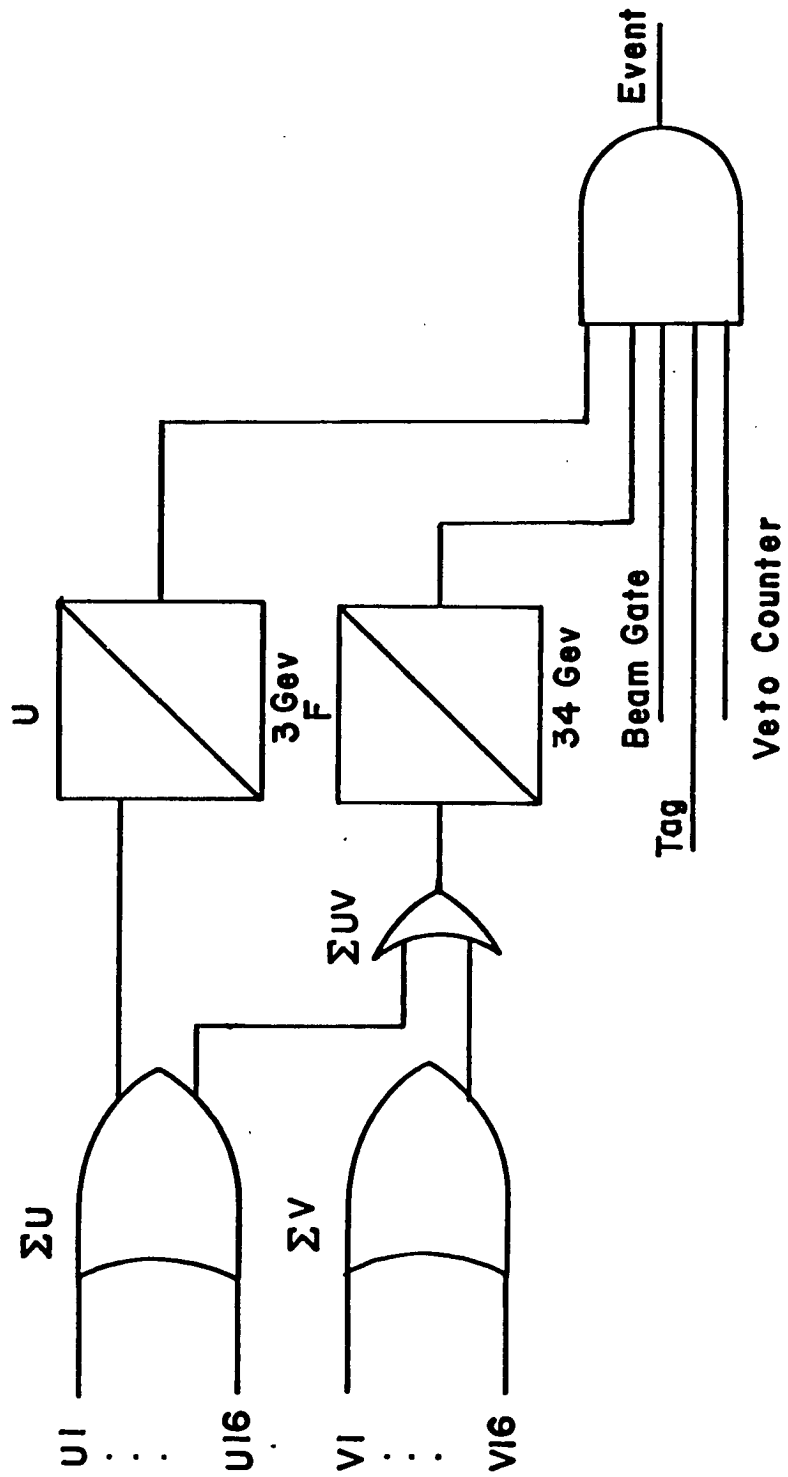
hodoscope americium trigger ( $XY_{AM}$ ). Pulses from X and Y strips relevant for the accumulation of halo muon spectra are separately fanned together to provide two muon triggers ( $X_{\mu}, Y_{\mu}$ ).

The logical or of the 16 coincidences of the logic levels  $R_i^A, R_i^B$  from each recoil counter provide a recoil trigger  $R = \sum_i R_i = \sum_i (R_i^A \cdot R_i^B)$ . These logic levels and combinations of them provide the following 8 triggers for data acquisition.

1. Spill start trigger
2. Spill stop trigger
3. Real event trigger  $BG \cdot T \cdot F_H \cdot U_H \cdot \overline{VC}$  (fig. 4.1) requiring beam gate, a tag, a sizeable amount of energy in the forward detector, a sizeable amount of energy in the U counters and the veto counter VC not to be on. The  $F_H$  threshold is about 20% of the electron beam energy. The  $U_H$  threshold is equivalent to 3 Gev showers and helps to discriminate against hadron-induced showers, which typically develop rather late in the forward detector.
4. U/V americium trigger  $UV_{AM} \cdot (\text{spillstop})$  normally enabled 100 millisecc after the end of spill.
5. U/V muon trigger  $X_{\mu} \cdot Y_{\mu} \cdot BG \cdot \overline{F_{AH}}$ . This trigger had a variable dead time built in to limit the numbers of muon triggers to a few per spill during routine running.
6. X/Y americium trigger  $XY_{AM} \cdot (\text{spill stop}) \cdot \overline{F_{AH}}$  also normally active only during .1 sec after end of spill. The  $\overline{F_{AH}}$  requirement in the last two triggers insures the absence of showers (= large pulse height) in the U/V counters.



Figure 4.1.1. Simplified Event Trigger Logic

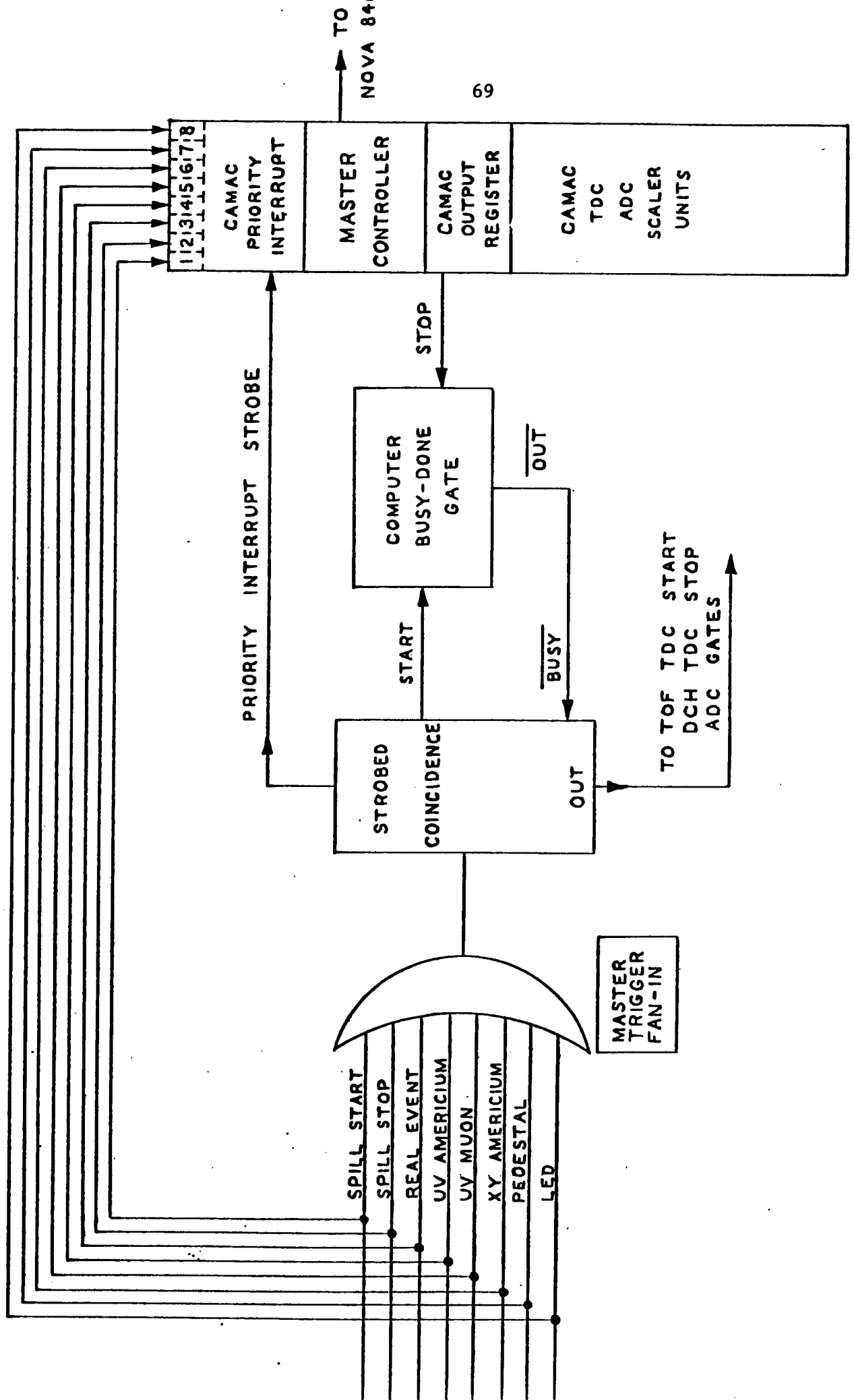


7. Pedestal trigger, generated by an asynchronous pulser triggering data acquisition at random times in and out of beam spill.
8. LED trigger, consisting of the OR of 3 (U/V, X/Y, recoil) LED triggers, generated by the pulser driving the LED system. LED data are routinely taken in spill and out of spill. The rate of data acquisition and the pattern of shining LED's is controlled by the on-line monitoring program, when not manually overridden.

These eight triggers are fanned together to generate the master trigger of the experiment (fig. 4.2).

Our event trigger is sensitive to a large fraction of the total photon-proton cross sectional (115 microbarn). Relevant exceptions are some important diffractive final states, like  $\gamma p \rightarrow \gamma p$ . A recoil trigger  $BG \cdot T \cdot R \cdot \overline{VC}$ , sensitive to these events, was originally meant to compete with trigger 3. for computer attention. It had to be abandoned because of prohibitively high rates in the R counters, due to very high delta ray production by electron pairs produced in the target. The bad performance of the beam plug counters prevented their reliable use as veto in this trigger. More manageable rates would be achieved by this requirement of a non purely electromagnetic interaction. A  $T \cdot BP$  trigger had to be modified for the same reason. It was to trigger data acquisition for the running time on-line monitoring of the gains of lead glass blocks in the tagging system. Periodic calibration runs with the forward detector moved sideways (with the beam hitting it) were taken instead. One  $T \cdot BP$  event per spill was still taken from the first tag of each spill, so

Figure 4.2. Master Trigger Fan-In and Computer Busy-Done Logic



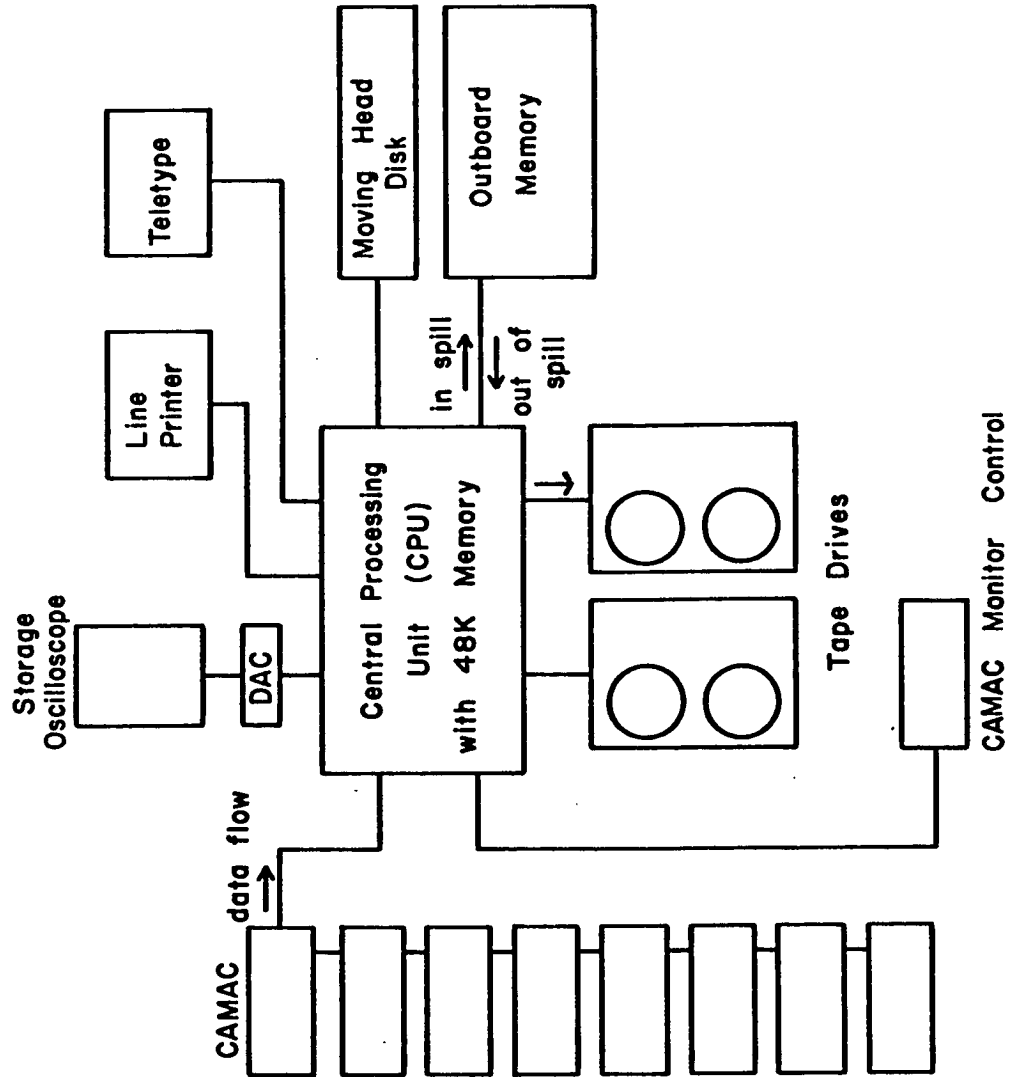
that the BP rate problems would not affect it. These events monitor the shape of the incident photon spectrum.

#### B) CAMAC System

The data acquisition program associates to each trigger a command list of CAMAC units to be read out for that trigger. The CAMAC system consists of three different interfaces:

1. A system crate organized CAMAC system containing seven crates, each equipped with its own crate controller. These are daisy-chained together with a branch highway going into a master controller that talks to the computer. The crates contain ADC units, TDC units, latches and scalers. The scalers count rates on various components of our detection system and the various partial and main triggers. This interface contains also a (strobed) priority interrupt CAMAC unit continuously interrogated by the data acquisition program and an output register CAMAC unit providing the computer "done" level to our master trigger logic (fig. 4.2).
2. A ninth CAMAC crate independent from the previous ones, with its own controller, talking to the computer. It contains the CAMAC input and output registers used by the monitor program to activate different special runs (pedestals runs, LED tests, etc.) with software selectable patterns.
3. A DVM unit CAMAC interface allowing the readings of the DVM's to be read in by the data acquisition system.

Figure 4.3 NOVA 840 Configuration



### C) Computer Configuration

The heart of the data acquisition system is a DGC Nova 840 mini-computer (fig. 4.3) system with 48K 16 bit words of main frame memory. 256K words of fast outboard memory, a moving head disk, two tape drives, a teletype, a line printer and a storage scope for graphic display are attached to the computer, together with the three CAMAC interfaces.

The Nova operation system (RDOS) is continuously running. A hardware partitioning of memory allows two programs to run simultaneously and independently of each other. Both the foreground (data acquisition) and background (monitoring and pre-analysis) programs in the two areas of memory consist of several tasks (independent sequences of instructions) running asynchronously and competing for CPU time. RDOS supervises all input-output, foreground-background environment and task scheduling. One (PI) of the two (ALADIN and PI) tasks composing the background program is simply a continuous loop interrogating the teletype for operator's commands. Commands can be given to PI to turn on and off the datataking program (JINNI) in the foreground area of memory. PI can also activate and deactivate individual monitoring-control functions and/or preanalysis subsets in the other background task (ALADIN).

### D) Foreground Program. Data Acquisition

All the eight main triggers of the experiment, fanned together into the master trigger fan-in (fig. 4.2) are also sent to individual bits of the CAMAC priority interrupt unit. The output of the fan-in is gated by the computer "done" level and used to strobe the priority interrupt unit, set busy the computer "done-busy" gate generator and provide gates

(ADC's and latches), start pulses (TOF TDC's) and stop pulses (drift chamber TDC's). When JINNI completes the processing of a trigger, the CAMAC output register resets the computer "done-busy" gate generator and gates on the master trigger fan-in.

JINNI main task consists of a 3-phase repetitive loop. The start of phase one is signaled by a spill start trigger interrupt. During this in-spill phase, JINNI will acknowledge interrupts, read CAMAC according to the command list of the interrupt, fill memory buffers with event records, store full buffers into the fast outboard memory. A spill stop trigger will signal the start of the second (end-of-spill) phase. Data are retrieved from the outboard memory and written to tape by the slow tape drives. Once data are on tape, the third (out-of-spill) phase will suspend JINNI's operation. Particular care is taken so that, if the computer is busy upon arrival of a spill start or spill stop trigger, the trigger state will be held until the computer is free and the interrupt can be processed.

Spill start and stop triggers have special CAMAC read-out lists. The scaler information will be read and stored. The difference in between spill stop and spill start time readings of the scalers gives rates per spill for the various scaled quantities. There are free running scalers, scalers gated on by the beam gate and scalers gated on by both computer "done" and beam gates. Some scalers are reset every spill, others are accumulated over a tape. The number of tags counted by a computer gated scaler, in particular, is used for normalization. We estimate our computer dead time to be in the average of the order of 20%, mostly due to the time for data transfer from CAMAC to memory.

## E) Background Program

The monitor-control-preanalysis background task (ALADIN), when executing, is in a continuous loop reading one event record from JINNI's disk storage area and calling a series of routines performing pre-analysis and control functions, and supervising equipment diagnostic runs (started by means of issuing commands to the apparatus via the second CAMAC interface). The subset of the pool of routines operational at any given time is selected by issuing appropriate teletype commands to PI. Different operations can be performed on event records from different triggers. Hit frequency histograms are routinely accumulated for various elements of our apparatus (individual counters, drift wires, etc.) together with pulse height or time spectra. Averages of spectra are checked periodically against nominal values (with specified tolerances). Warnings are issued when inconsistencies are found. Disagreement of DVM readings with nominal values will also issue a warning. Raw on-line event reconstruction can be performed for a subsample of the triggers. This preliminary reconstruction is displayed on the storage scope. Special pre-analysis routines are written and brought into execution at different times during the experiment.



CHAPTER FIVE  
THE DATA SAMPLE

A) Data Runs

The set-up of the experiment in the tagged photon laboratory began in the late summer of 1977. Most of the effort at the time went into understanding the apparatus performance. In particular, we performed a first careful calibration of the pulse height responses of all the counters in the forward shower detector. A small preliminary sample of data was collected at the end of this (low-intensity) beam period.

Late in May, 1978, we started the first of two datataking periods. We repeated the calibration of the forward detector and then collected the following data samples with the forward detector in the 30 meter position.

- 1) About 750 thousand  $T \cdot F_H \cdot U_H \cdot \overline{VC}$  triggers with a primary electron beam momentum of 160 Gev/C. Photons from about 70 to about 150 Gev were tagged.
- 2) About one and a half million  $T \cdot F_H \cdot U_H \cdot \overline{VC}$  triggers with a primary electron beam momentum of 135 Gev/C. Photons from about 60 to about 130 Gev were tagged.

Just before the end of the period we moved the forward detector upstream to the 10 meter position. A third sample of data was collected, consisting of

- 3) About 50 thousand  $T \cdot F_H \cdot U_H \cdot \overline{VC}$  triggers with a primary electron beam momentum of 135 Gev/C.

A failure in the primary target box (the beryllium target) in our beam

line obliged us to a prolonged shut-down. The target box was rebuilt and late in October we started the last datataking period. The forward detector still being in the 10 meter position, we performed a briefer set of calibration runs for the forward detector and proceeded to collect

- 4) About 500 thousand  $T \cdot F_H \cdot U_H \cdot \overline{VC}$  triggers with a primary electron beam momentum of 135 Gev/C.
- 5) About 350 thousand  $T \cdot F_H \cdot U_H \cdot \overline{VC}$  triggers with a primary electron beam momentum of 80 Gev/C. Photons from about 35 to about 70 Gev were tagged.

We finally moved the forward detector back to the 30 meter position and completed our running by collecting

- 6) About one million  $T \cdot F_H \cdot U_H \cdot \overline{VC}$  triggers with primary electron beam momentum of 135 Gev/C.

About 65 thousand triggers were taken with an empty target over the entire duration of the experiment.

During routine datataking, seven additional triggers were operative. Data accumulation caused from these interrupts was continuously monitoring integrity and performance of the various components of the apparatus.

We will now briefly outline four types of runs with special triggers which we performed at various times in the course of the experiment.

#### B) Forward Detector Calibration Runs

These runs were taken at the beginning of each of the three datataking priods. The full calibration consisted of several steps. We used a 30 Gev/C electron beam during most of it.

A small magnet was installed just downstream of the target. The magnetic field could be adjusted and/or the magnet itself could be rotated to bend the electron beam to hit any pair of U and V counters at any desired position along the length of the counters. We first set all the voltages on the shower counters phototubes to obtain from each of them approximately the same pulse height for a 30 Gev/c electron induced shower. A good uniformity of gains is important to minimize trigger biases when linearly summing the pulse heights in the shower counters to form the forward trigger  $F = U + V$ . Then we mapped the attenuation functions along the length of each of the 32 shower counters.

The absolute gains of the U and of the V counters were determined by moving the detector sideways so that the undeflected beam would hit counters  $U_{13}$  and  $V_{13}$ . The pulse height response was found to be linear for electron showers from 15 to 185 Gev. Using the 30 Gev/c runs we determined the relative gains of all the U counters with respect to  $U_{13}$  and of the V counters with respect to  $V_{13}$ . Gain variations among the various counters in each bank were at most 25%; each one was determined with 2% accuracy.

The relative gains of the V counters with respect to the U counters was determined as the one minimizing the width of the  $F = U + V$  spectrum at each energy setting. They were found to be (almost) independent of energy.

Edge effects were investigated by sweeping in small steps various regions in the active area of the detector where the edges of two (or three) counters would meet. Losses of shower energy deposition into the detector central beam hole were understood by the same method.

With the help of the magnet we performed an analogous routine on the X and Y hodoscope strips. Voltages were set to provide roughly equal gains and attenuation functions mapped. The sum of the pulse height responses of the set of strips containing a shower was determined to be approximately linear over our shower energy range. Relative gain variations were about 40%; each one was determined with about 10% accuracy.

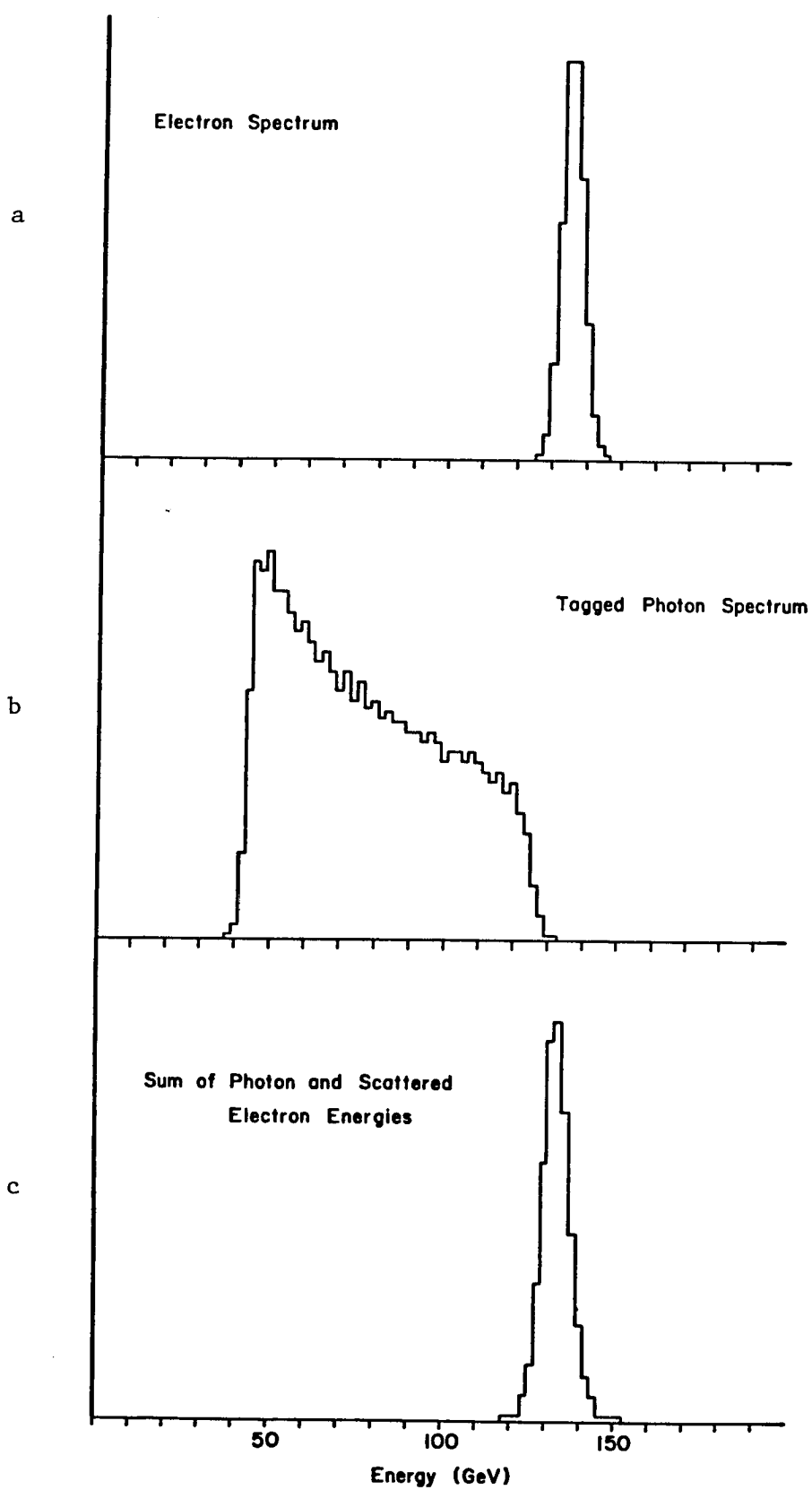
### C) Tagging System Calibration Runs

About ten of these runs were taken during the course of the experiment. The forward detector was moved sideways so that the beam would hit  $U_{13}$  and  $V_{13}$ . First the electron beam was used to generate the spectrum of fig. 5.1a. Then we switched to tagged photons (fig. 5.1b and 5.1c). Events were accumulated with a  $T \cdot F_H$  trigger with a low discrimination threshold for  $F_H$ . The energy in the forward detector  $E_F$  and the electron beam energy  $E_B$  provided the tag energy  $E_T = E_B - E_F$ . The gains of the lead glass blocks were obtained with the following iterative procedure. The gains  $g_i$  ( $i = 1, 13$ ) were initially set to zero. Events were selected (thanks to the H counters latch information) hitting the lead glass blocks in their central region. Most of the energy of the shower was then contained in this central block, the rest leaking no further than the two neighbouring ones. For the events in the center of the  $i$ -th block, we had

$$g_{i-1}p_{i-1} + g_i p_i + g_{i+1}p_{i+1} = E_T$$

(where  $p_j$  is the pulse height in the  $j$ -th block) and could calculate

Figure 5.1. Tagging System Calibration



$$g_i = \frac{E_T - g_{i-1}p_{i-1} - g_{i+1}p_{i+1}}{p_i} .$$

The first estimate for  $g_i$  therefore is

$$g_i = E_T/p_i$$

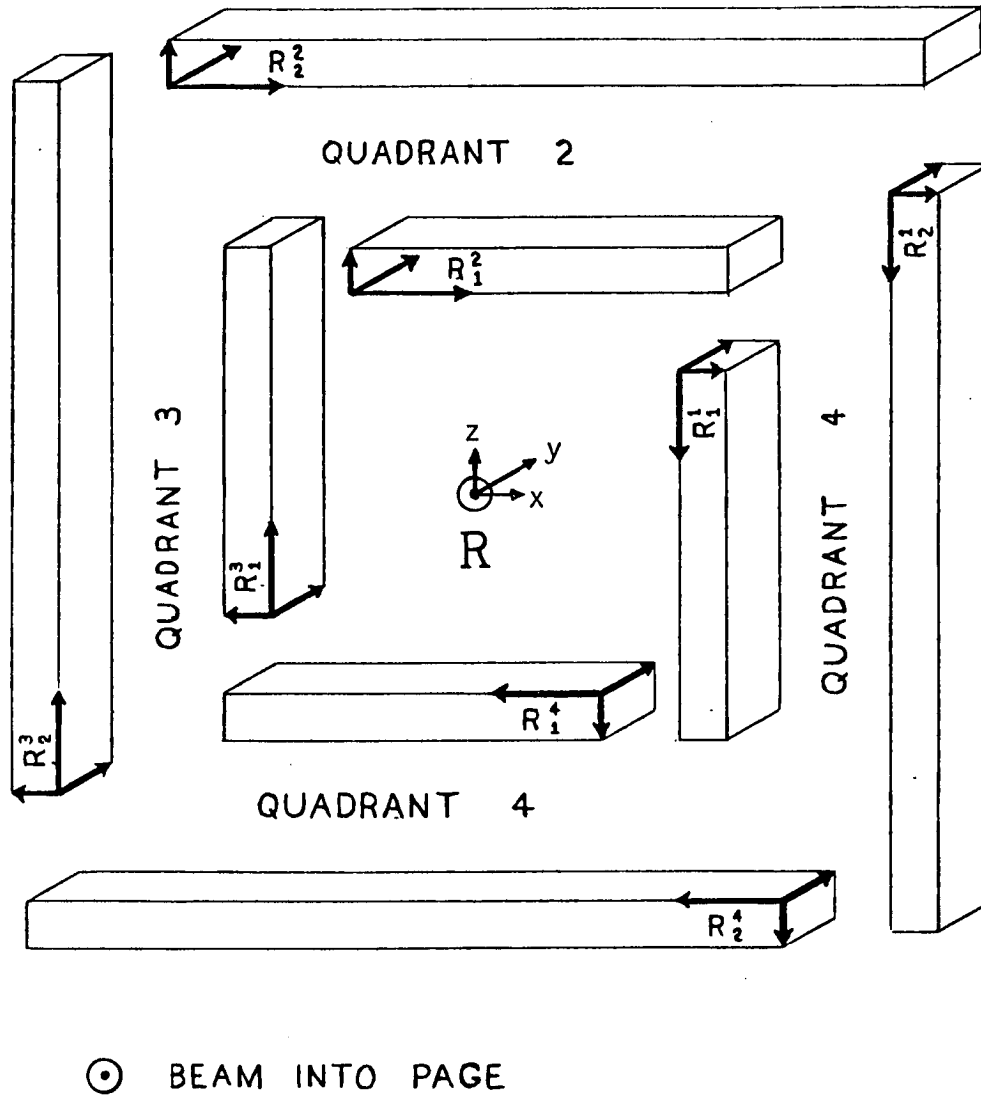
and successive iterations improve these estimates. The procedure converges in a few iterations.

The lead glass blocks gains obtained with this method were found to be equal in various calibration runs within a few percent. Checks performed to insure the constancy of these gains during data runs will be discussed in the next chapter.

#### D) Cosmic Rays Runs

These runs were performed to optimize our knowledge of the relative position (alignment) of the eight modules of drift chambers in the recoil detector. With each of the modules of chambers we associate a reference frame  $R_i^Q$ .  $i=1,2$  is the module index in a quadrant ( $i=1$  for the small module,  $i=2$  for the big module).  $Q = 1,4$  is the quadrant index. These frames and the quadrant numeration convention are sketched in fig. 5.2. A more extensive description will be found in Appendix A. In addition, we define a laboratory reference frame  $R$  with its origin on the beam line and its  $y$  axis coincident with the beam line. A precise knowledge of the coordinates of the origin and of the direction cosines of the axes of  $R_1^Q$  in  $R_2^Q$  for each quadrant  $Q$  is necessary to extract a good estimate of the parameters of tracks recorded by that quadrant. A precise knowledge of the coordinates of the origin and of the direction cosines of the axes

Figure 5.2. The Laboratory Reference Frame and the 8 Reference Frames Associated to the 8 Modules of Drift Chamber.



⊙ BEAM INTO PAGE

of coincidences between recoil counters) to select cosmic rays traversing all the possible pairs of quadrants. A hit on any of the 14 remaining recoil counters vetoed the cosmic ray trigger. These data were accumulated during beam off time.

#### E) Electron Runs

By removing the tagging radiator and switching off the tagging magnets, we could have the electron beam proceed onto our experimental target. We made use of this convenient feature to perform special electron runs. Elastic scattering of electrons on protons has a cross section (within the acceptance of our apparatus) some 25 times larger than photon-proton elastic scattering. The response of our apparatus to both processes being essentially identical (apart from the tagging system information) the larger yield of elastically scattered electrons was very useful in checking the overall good performance of our apparatus, particularly in the early stages of the experiment. The occurrence of a tag signal T was simulated by the occurrence of a  $T_F$  (T fake) signal from a small counter inserted in the beam just upstream of the target to record the passage of an electron. We continued to collect periodically electron data also because they would provide us with a generous yield of protons for the calibration of our time-of-flight system.

The trigger adopted for these electron runs was  $T_F \cdot U_H \cdot F_H \cdot \overline{VC} \cdot R$ . We inserted the recoil trigger R in the event trigger for these runs. We were only interested in the elastic events which do require the presence of a hit on one of the recoil counters.



of  $R_1^Q$  in  $R$  is necessary in order to associate to each proton track detected in quadrant  $Q$  a good estimate of the scattering angle and, therefore, of the 4-momentum transfer.

Fiducial pins on the outside case of each module of drift chambers were surveyed by a Fermilab surveying team with respect to a reference frame with its origin on the nominal beam line in the tagged photon laboratory and its  $y$  axis coincident with the nominal beam line. From these measurements we could obtain a first estimate of the coordinates of the origin and of the direction cosines of the axes of any of the mentioned nine frames in any of the others. These estimates had to be improved by using the information provided by a large sample of reconstructed tracks. We adopted the following strategy.

- 1) Relative alignment of the two module frames  $R_1^Q$  and  $R_2^Q$  in quadrant  $Q$  was obtained from a sample of tracks in that quadrant.
- 2) Relative alignment of  $R_1^1$ ,  $R_1^3$  and  $R_1^4$  with respect to  $R_1^2$  was obtained from three samples of tracks traversing respectively quadrants 2 and 1, 2 and 3, and 2 and 4.
- 3) The parameters of the straight line de facto coinciding with the beam axis in  $R_1^2$  were obtained by fitting the coordinates in  $R_1^2$  of the interaction vertex for inelastic photon induced events producing two tracks in two different quadrants.

The alignment procedure is discussed in more detail in Appendix A. Tracks for steps 1) and 2) were provided by cosmic ray runs. Cosmic ray tracks have the advantage of minimal multiple scattering. We implemented a number of special triggers  $R_i \cdot R_j$  (given by various combinations

CHAPTER SIX  
DATA REDUCTION

The data accumulated in the course of the experiment were stored on some 400 magnetic tapes. About 300 of them were written when our target was exposed to the photon beam. We will describe in this chapter two preliminary analysis passes performed on these tapes.

The first pass was a monitor pass. For each tape in our data sample, we accumulated the following histograms:

- 1) The hit frequencies on all the counters in the tagging system, forward detector and time-of-flight system,
- 2) The hit frequency on all the drift chamber sense wires,
- 3) The spectra of pulse heights in all the lead-glass counters in the tagging system,
- 4) The spectra of pulse heights in all the pairs of U and V counters and the beam plug counter,
- 5) The spectra of arrival time on all the sense wires in the drift chambers,
- 6) The spectra of pulse heights on all the pulse height analyzed counters for pedestal triggers.

This information was used, first of all, as a record of the behavior of the various components of the apparatus at the time each tape was written. Tapes were removed from the data sample, when necessary. The constancy of the gains on all the pulse height analyzed counters in the time interval in between the relevant calibration runs could also be

monitored and corrected when necessary. The stability of the ADC pedestals was also checked.

The information provided by some strategic scalers was also accumulated over all the spills on the tape and saved on special summary tapes. Of particular interest in the following discussion on normalization was the accumulation, over a tape, of the counts in the scalers counting

- 1) The number  $T$  of tags,
- 2) The number  $T_{CG}$  of computer gated tags,
- 3) The number  $V$  of  $T \cdot VC$  triggers.

The set of final states in photon-proton interactions our experiment is sensitive to was outlined in chapter 1. The first natural step in our data analysis was to be the study of the two-body channels, namely elastic scattering

$$\gamma p \rightarrow \gamma p \quad (6.1)$$

and exclusive production of pseudoscalar and vector mesons,

$$\gamma p \rightarrow p(\pi^0, \eta^0, \omega^0, \phi^0, \psi^0, \dots) \quad (6.2)$$

All these mesons have somewhat sizeable branching ratios for decay modes yielding exclusively (two or three) showering particles "visible" in our detector. Notable exception is the rho meson. The final state discussed in this thesis, in particular, belongs to this category. Common features of all these final states are:

- 1) The deposition of a large amount of electromagnetic energy in the forward shower counters. All these processes are expected to have differential cross sections  $d\sigma/dt$  rather

sharply peaked at small values of  $t$ , ( $t = 4$ -momentum transfer squared). They are therefore expected to transfer to the recoil proton only a very small amount of the photon energy (and momentum). Therefore, the energy of elastically scattered photons and the sum of the energies of the decay products of quasi-elastically produced mesons has to be only slightly smaller than the energy of the incoming photon.

- 2) The emergence from the interaction of a (slowly) recoiling proton at angles very close to 90 degrees with the direction of the incoming photon.

We will now outline the filtering procedure performed on all our data tapes in order to proceed towards the isolation of two-body quasi-elastic events. The sum of the raw pulse heights  $p_i$  ( $i = 1, 32$ ) in the U and V counters, multiplied by the gain of the counter, is an estimate of the total energy deposited in the forward detector. It is, in fact, an overestimate. A position dependent attenuation correction has to be made on the pulse height in order to correctly estimate the energy deposition. Such a correction is not possible before reconstruction of the coordinates of the centroid of the showers, with the help of the hodoscope strips. Attenuation functions, however, are mapped along the length of a shower counter so that an arbitrary value of 1 is assigned to the gain in the region of flat dependence of the pulse height response on the position. The (multiplicative) attenuation correction would take values smaller than 1 for showers closer to the phototube (up to a maximal value typically of 0.77 in the very proximity of the tube). Therefore, summing pulse heights without applying any attenuation

correction results in an estimate of the energy  $E_F$  deposited in the forward detector

$$E_F = \sum_i g_i p_i$$

always larger than the real value of the energy deposition. Most showers, however, are far from the region where the correction is large.

The filtering procedure amounted to the following pass/fail requirements

- 1) A good quality tag,
- 2) A value of  $E_F$  at least equal to 70% of the initial photon, energy measured in the tagging system
- 3) The presence of a hit on at least one recoil counter.

Requirement 1) amounted to a series of consistency checks on the responses of various components of the tagging system. The central position of the candidate electron shower along the horizontal length of the tagging system was calculated as

$$x = \sum_i g_i p_i x_i / \sum_i g_i p_i$$

where  $x_i$  is the central coordinate of the  $i$ -th lead glass block,  $g_i$  and  $p_i$  its gain and pulse height ( $i = 1, 13$ ). A shower width  $\sigma$  was calculated around that central position as

$$\sigma^2 = \sum_i g_i p_i (x_i - x)^2 / \sum_i g_i p_i .$$

The electron shower energy was calculated as

$$E_T = \sum_i g_i p_i .$$

The estimate of the position  $x$ , together with the known bending power of the tagging magnets, gave an independent estimate of the energy of the candidate shower.

A tag is named a bad quality tag and rejected in any of the following cases

- 1) The H counter corresponding to the position estimate  $x$  has no signal.
- 2) The shower width is greater than an experimentally determined tolerance width. This requirement, in particular, is effective in rejecting events with more than one cluster in the lead glass array.
- 3) The two independent estimates of the candidate shower energy differ by more than an experimentally determined tolerance.

The number of bad quality tags is typically 20% of the triggers over the entire photon spectrum. A typical tag energy distribution for real event trigger in a 135 GeV/c run is shown in fig. 6.1a. It is strongly biased towards high energy tags because of the fixed threshold (20% of the electron beam energy) on  $F_H$  in our event trigger. The same distribution for triggers with a good quality tag is shown in fig. 6.1b. The tag energy bin is 5 GeV. Thirty-four bins cover the energy range from 0 to 170 GeV. If  $N_i$  is the number of triggers in the  $i$ -th bin and  $N'_i$  the number of triggers in the  $i$ -th bin that have a good quality tag, we define the loss function

$$f_i = 1 - r_i \quad \text{with } r_i = N'_i/N_i \quad i = 1, 34.$$

Figure 6.1

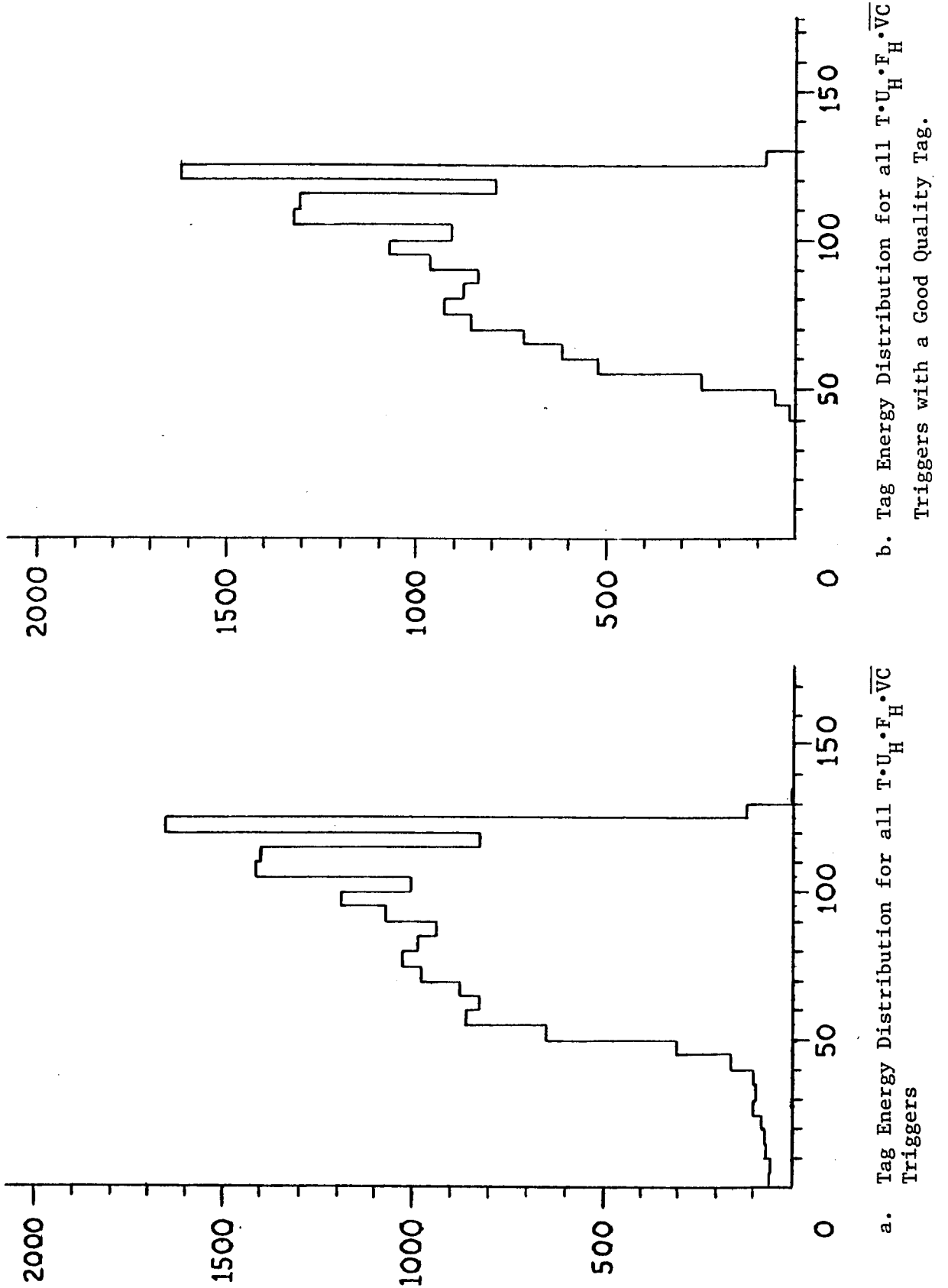


Fig. 6.2 shows the shape of the function  $r$  for a 135 Gev run. The losses are 100% for very low energy tags, below the lower edge of the acceptance window (about 45% of the primary electron energy) of the tagging system. These are obviously bad quality tags and requirement 1) correctly identifies them as such. The loss function is large for low energy photons also within the acceptance of the tagging system, but rapidly falls to zero for higher energy tags. High energy electrons hit the first few lead glass blocks with significantly higher rates than lower energy ones hitting the remaining blocks. On the average, this induces a much higher percentage of bad quality tags in the region of the tagging system closer to the electron beam.

About 68% of the triggers are rejected by requirement 2). A typical distribution of the variable

$$\eta = (E_F - E_T)/E_T$$

is shown in fig. 6.3 Events with  $\eta < -.30$  are rejected.

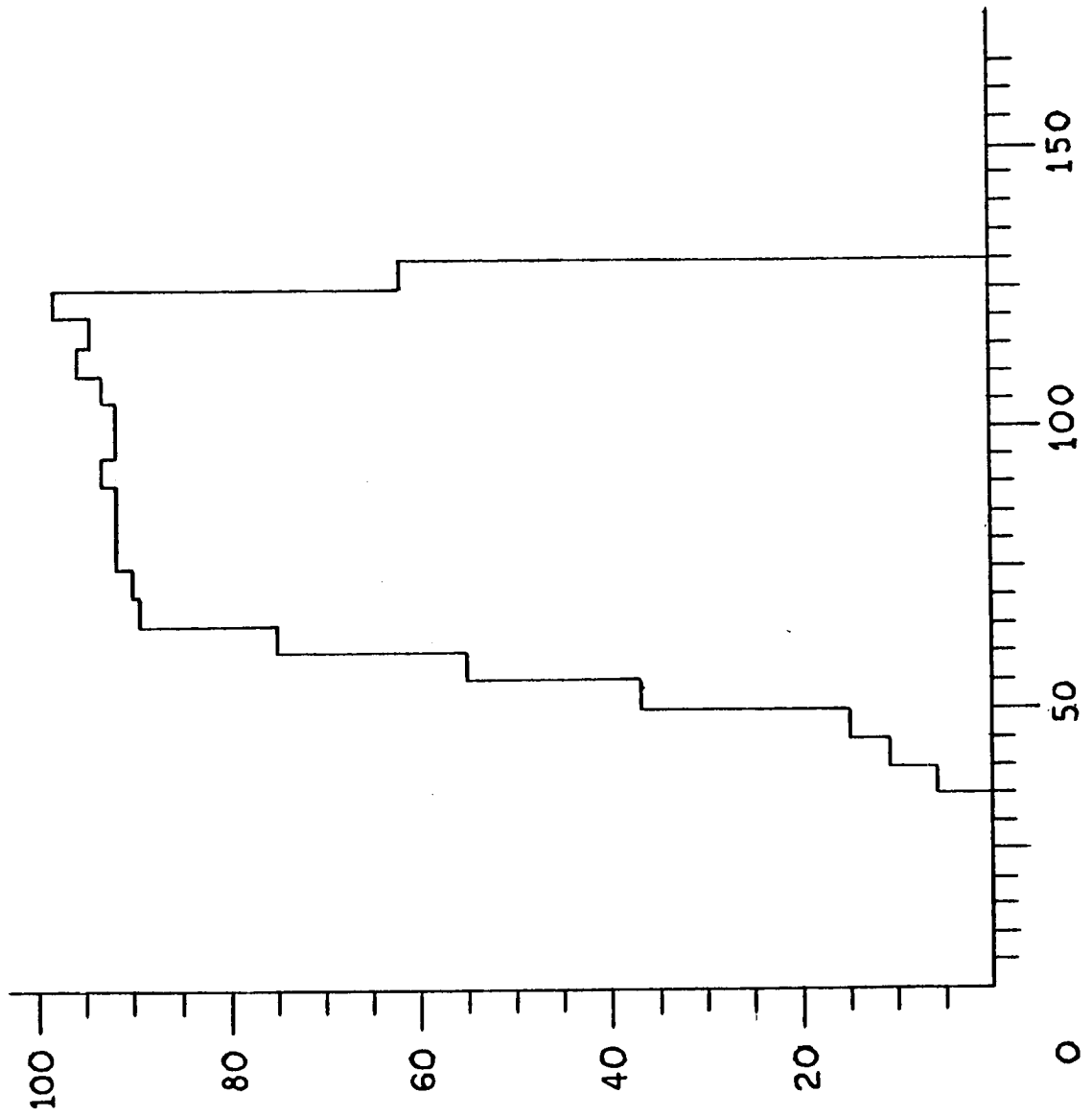
About 60% of the triggers do not have any recoil counter hit and are rejected by requirement 3).

Only about 5 to 6% of the triggers survive requirements 1), 2), 3) and are written to tape for further analysis. Fig. 6.4 shows a distribution of the number of recoil counters that provided a count for these selected events. 28% of them have more than one counter active, 8% of them have more than two counters active.

The absolute normalization, over the entire photon spectrum, is provided, per tape, by the difference



Figure 6.2. The Ratio  $\frac{\text{good quality tags}}{\text{all}}$  versus Tag Energy for  $T \cdot F_H \cdot U_H \cdot \overline{VC}$  Triggers.



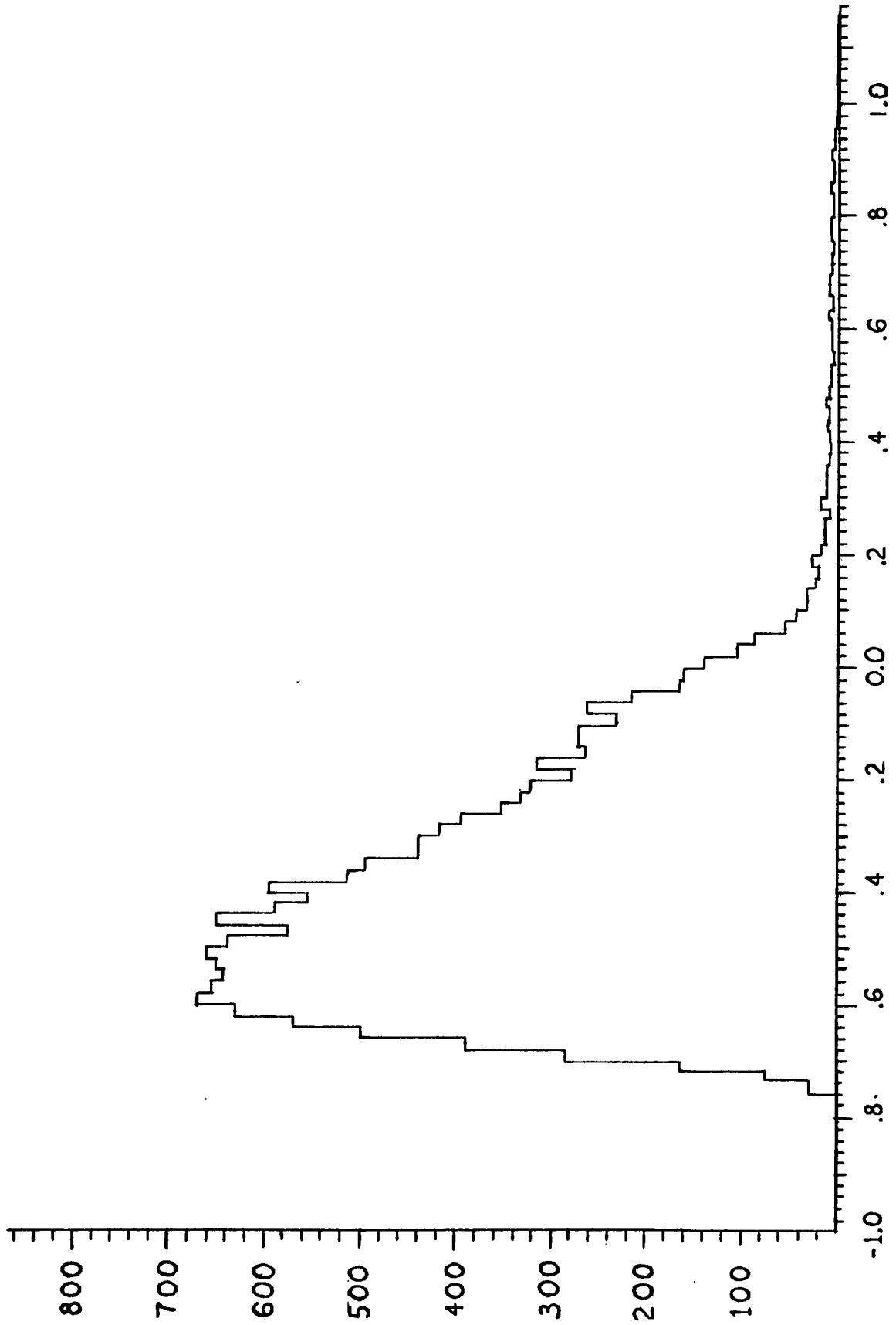


Figure 6.3. Distribution of  $\eta = (E_F - E_T) / E_T$  for  $T \cdot F_H \cdot U_H \cdot VC$  Triggers.  $E_F$  = Forward Detector Energy,  $E_T$  = Tag Energy. Triggers with  $\eta < -.30$  are Rejected.

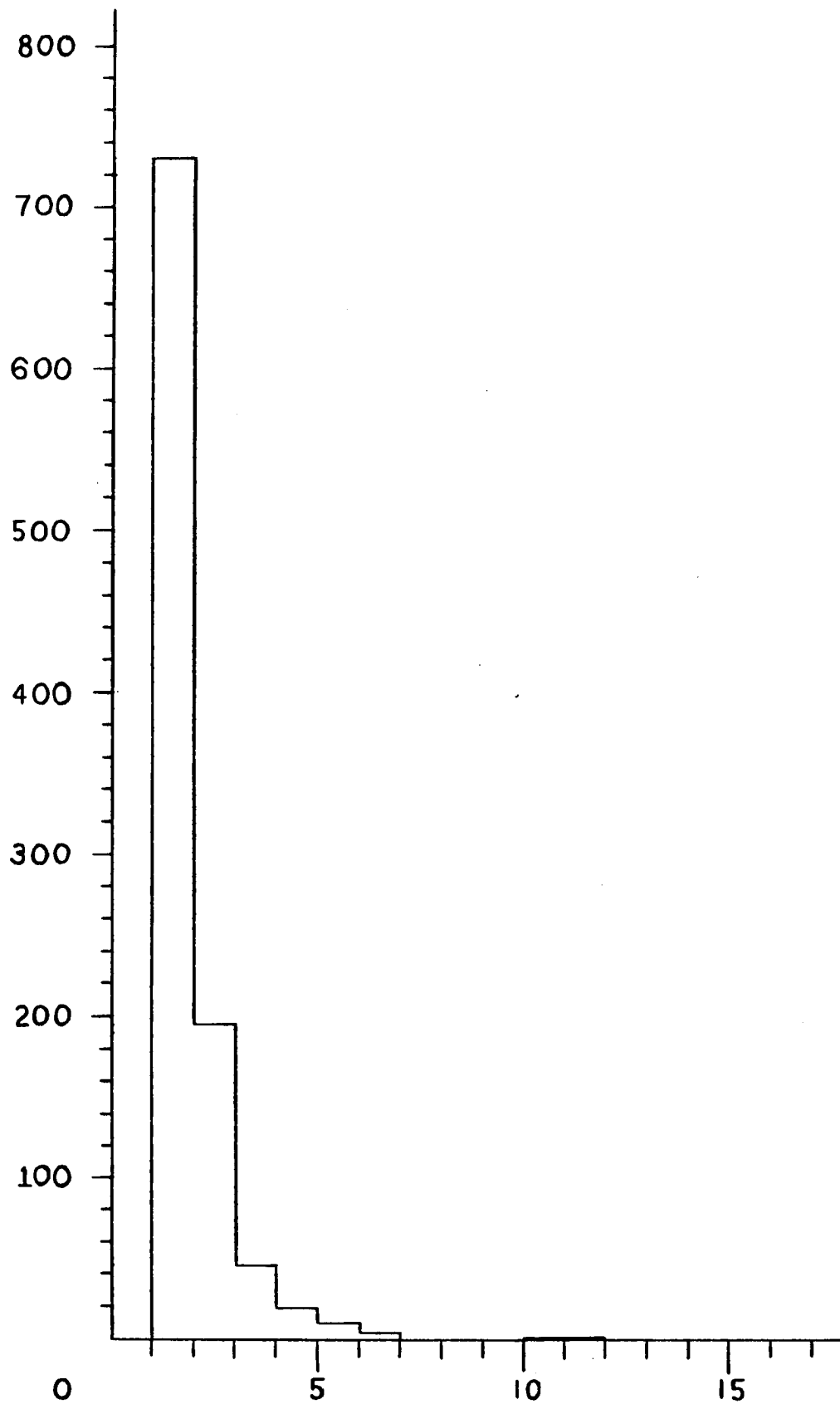


Figure 6.4. Distribution of the Number of Recoil Counters Recording a Pulse for  $T \cdot F_H \cdot U_H \cdot \overline{VC}$  Triggers Serving Requirements 1), 2), 3)

$$T'_{CG} = T_{CG} - V.$$

Our event trigger requires the VC counter not to be on. The number of tags accompanied by a hit on this counter must therefore be subtracted away to obtain the number of tags useful to our experimentation.

A typical (not trigger biased) photon energy spectrum is given (for 135 GeV/C running) in fig. 6.5. It is a bremsstrahlung spectrum. Its entries come from T•BP triggers. The T•BP triggers are also binned in 5 GeV energy bins and the population of the energy bins is used for relative normalization. If  $M_i$  is the number of T•BP entries in the  $i$ -th energy bin, then the number of useful good quality tags of energy  $E_i$

$$(i-1)\Delta < E_i < i\Delta \quad \text{with } \Delta = 5 \text{ GeV}$$

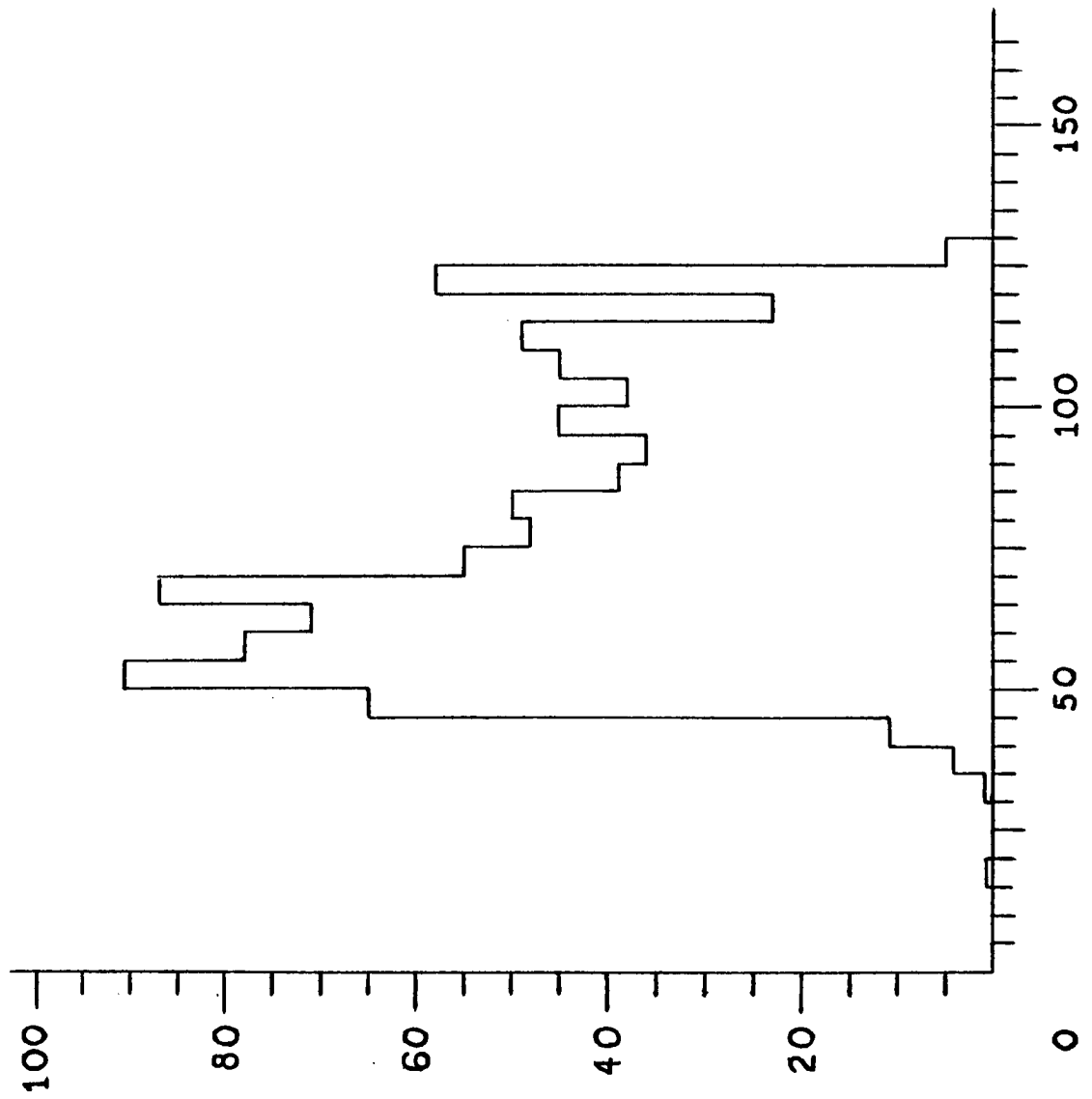
is given, tape by tape, by

$$G_i = T'_{CG} M_i r_i / \sum_i M_i \quad i = 1, 34 \quad (6.3)$$

Our event rates, tape by tape, will be normalized to these numbers. An estimate of our dead time is based on the ratio

$$T_{CG}/T.$$

Figure 6.5. Photon Energy Spectrum (for a 135 GeV/c Electron Beam) from T•BP Triggers.



## CHAPTER SEVEN

## DATA ANALYSIS

## A) Introduction

The subsample of data tapes analyzed in this thesis consists of entries 2) and 6) in section A of chapter 5; i.e., about  $2.3 \times 10^6$   $T \cdot F_H \cdot U_H \cdot \overline{VC}$  triggers collected with the forward detector in the 30 meter position and with an electron beam momentum of 135 Gev/c. Some unreliable data tapes were removed from the original total of about  $2.5 \times 10^6$  triggers.

The filtering procedure outlined in chapter 6, with its rejection power of about 20 to 1, leaves us with about 117 thousand triggers to analyze further. Final states of the type (6.1) and (6.2) are part of this filtered sample. The sample, however, still consists mostly of background events. No kinematic constraint has been applied yet, and the energy match requirement ( $E_F/E_T \geq 70\%$ ) is purposely not very stringent. At this stage, we consider our estimate of the gains of all the shower counters still preliminary. The isolation of clean samples of exclusive events, in fact, is a powerful (and necessary) step towards a final estimate of these gains.

In order to proceed towards the isolation of any of the exclusive final states (6.1) and (6.2) one needs to

- 1) introduce a tighter energy match requirement
- 2) identify a Compton photon (single shower) or a quasi-elastic meson (multi-showers) in the forward detector
- 3) measure the coordinate position  $x_F$  and  $y_F$  of the forward

boson (photon or meson) in the two hodoscope arrays; in cylindrical coordinates (about the beam line)  $x_F$  and  $y_F$  give  $\phi_F = \tan^{-1}(y_F/x_F)$  and  $\theta_F \approx r_F/L$ , where  $r_F = \sqrt{x_F^2 + y_F^2}$  and  $L$  is the distance of the forward detector from the target.

- 4) select events where a coplanarity match is present in between  $\phi_F$  and one of the R counters latched in the event.
- 5) interrogate the quadrant of drift chambers shadowing the R counter selected by requirement 4); if a track is reconstructed, the track parameters will provide a  $\phi_R$  and  $\theta_R$  measurement for the candidate recoiling proton.
- 6) fit the event to an elastic or quasi-elastic kinematic hypothesis.

Steps 1), 2), 3), 4) are grouped in a (second pass) filtering procedure. Separate data summary tapes can be written with events satisfying requirements 2) for each of the exclusive channels. Steps 5) and 6) are grouped together in a final event analysis procedure.

The identification of a single photon or of a photoproduced meson in the forward detector (step 2) involves, in general, the measurement of the invariant mass  $m_F$  of a multiparticle system, with each particle ( $\gamma, e^+, e^-$ ) producing a shower in the detector. The number  $n$  of showering particles will be 1 for elastic scattering, 2 for  $\pi^0, \eta$  and  $\psi$  production, 3 for  $\omega$  and  $\phi$  production. If  $p_i = (E_i, \vec{p}_i)$  is the 4-momentum (in the laboratory frame) of the  $i$ -th showering particle ( $i = 1, n$ ), then the invariant mass of the forward boson is given, for  $n = 2$ , by

$$m_F^2 = (p_1 + p_2)^2 = 2E_1 E_2 (1 - \cos\theta_{12}) \approx E_1 E_2 \theta_{12}^2 \quad (7.1)$$

(where  $m_e^2 \approx m_\gamma^2 = 0$ ) and, for  $n = 3$ , by

$$m_F^2 = (p_1 + p_2 + p_3)^2 \approx \sum_{i,j=1}^3 E_i E_j \theta_{ij}^2 ; i > j \quad (7.2)$$

where  $\theta_{ij}$  is the angle defined by

$$\vec{p}_i \cdot \vec{p}_j = |\vec{p}_i| \cdot |\vec{p}_j| \cdot \cos \theta_{ij} .$$

If  $x_i, y_i$  is the hit point on the forward detector of the  $i$ -th showering particle and  $\Delta_{ij}^2 = (x_i - x_j)^2 + (y_i - y_j)^2$  we have, for any  $n$ ,

$$m_F^2 \approx \sum_{i,j=1}^n E_i E_j \frac{\Delta_{ij}^2}{L^2} ; i > j . \quad (7.3)$$

The positions  $x_F$  and  $y_F$  of the forward boson (step 3) will be given by

$$x_F = \frac{\sum_{i=1}^n E_i x_i}{\sum_{i=1}^n E_i} \quad (7.4)$$

$$y_F = \frac{\sum_{i=1}^n E_i y_i}{\sum_{i=1}^n E_i} .$$

The measurement of  $m_F$ ,  $x_F$ ,  $y_F$ , in general, involves the identification of each shower in the detector and the measurement of its energy  $E_i$  and hit point coordinates  $x_i, y_i$ .

This is a non-trivial pattern reconstruction problem. Independent clusters have to be identified in the  $x$  and  $y$  strips. Pulse height deposition in the  $U$  and  $V$  counters must be assigned to the proper cluster. Coalescing showers (in one or both projections) and multi-cluster ambiguities complicate the problem. A full description of the shower reconstruction program will be found in reference 23).



Once the  $i$ -th cluster is identified, its central coordinates are given by

$$\begin{aligned}x_i &= \sum_j \epsilon_j^x X_j / \sum_j \epsilon_j^x \\y_i &= \sum_j \epsilon_j^y Y_j / \sum_j \epsilon_j^y\end{aligned}\tag{7.5}$$

where the sums are over the strips belonging to the cluster,  $\epsilon_j^x, X_j$  are the energy deposition and the coordinate of the center of  $j$ -th scintillator strip in the  $x$  hodoscope and  $\epsilon_j^y, Y_j$  are similarly defined for the  $y$  hodoscope. Two independent measurements of the energy of the  $i$ -th cluster (shower) are given by

$$\begin{aligned}E_i^x &= \sum_j \epsilon_j^x \\E_i^y &= \sum_j \epsilon_j^y\end{aligned}\tag{7.6}$$

where again the sums are over the strips belonging to the cluster. These measurements are poor. In general, the measurement of the energy of each shower is obtained from the shower counter information. It should be also noticed that the values of  $\epsilon_j^x$  and  $\epsilon_j^y$  in (7.5) and (7.6) are the product of the gain of the strip times its pulse height times a position dependent attenuation correction. This correction is possible after a first estimate of  $x_i$  and  $y_i$  is obtained for (7.5) using the uncorrected values of  $\epsilon_j^x$  and  $\epsilon_j^y$ .

If we substitute (7.5) in (7.4), we obtain

$$\begin{aligned}x_F &= \sum_i \text{clusters} \sum_j \text{strips in cluster} \epsilon_j^x X_j / \sum_i \text{clusters} \sum_j \text{strips} \epsilon_j^x \\y_F &= \sum_i \text{clusters} \sum_j \text{strips in cluster} \epsilon_j^y Y_j / \sum_i \text{clusters} \sum_j \text{strips} \epsilon_j^y\end{aligned}\tag{7.7}$$

i.e.,

$$\begin{aligned} x_F &= \frac{\sum_j \text{all strips } \epsilon_j^x}{\sum_j \text{all strips } \epsilon_j^x} \\ y_F &= \frac{\sum_j \text{all strips } \epsilon_j^y}{\sum_j \text{all strips } \epsilon_j^y} . \end{aligned} \quad (7.8)$$

The content of (7.8) is the following. The positions  $x_F$  and  $y_F$  (apart from attenuation correction) can be measured independently of the number of clusters. The clusters, in fact, do not have to be identified. One simply needs to take the first moments of the energy deposition distributions in each of the two hodoscope arrays. Phototubes are glued to the strips on alternate sides. Attenuation corrections will tend to cancel each other. A good estimate of  $x_F$  and  $y_F$  can be therefore obtained for (7.8) just using the uncorrected energy depositions.

The problem of reconstructing all the showers in the detector can be bypassed (for the specific case of exclusive final states) also with regard to the measurement of  $m_F$ . This involves the evaluation of the second moment of the energy deposition distributions in the hodoscope arrays around the point  $(x_F, y_F)$ . Let us motivate this statement.

Let us consider first the decay of a meson of mass  $m$  to 2 (massless) showering particles. Let us assume that the individual showers have zero width. The line-of-flight of the meson intersects the forward detector at a point  $0 = (x_0, y_0)$ . The two decay particles will hit the detector at two points  $0_1 = (x_1, y_1)$  and  $0_2 = (x_2, y_2)$ . Let  $\theta_1$  and  $\theta_2$  be defined by

$$\cos \theta_i = \frac{\vec{p}_i \cdot \vec{p}}{|\vec{p}_i| \cdot |\vec{p}|} \quad (i = 1, 2) \quad (7.9)$$

and the vector  $\vec{r}_i$  have components

$$\vec{r}_i = (x_i - x_0, y_i - y_0) \quad (7.9')$$

where  $\vec{P}, \vec{p}_1, \vec{p}_2$  are the momenta of the parent meson and of the two decay products. For a two-body decay

$$E_1 \theta_1 \approx E_2 \theta_2 \quad (\text{if } \theta_1, \theta_2 \text{ small}) \quad (7.10)$$

where  $E_1$  and  $E_2$  are the energies of the two decay products.

The second moment of the distribution of points  $0_1, 0_2$  about 0 is

$$M_2^{(0)} = \frac{E_1 |\vec{r}_1|^2 + E_2 |\vec{r}_2|^2}{E} = \sum_i \frac{E_i |\vec{r}_i|^2}{E} \quad (7.11)$$

where  $E = \sum_i E_i$ .

Using  $\theta_1 \approx |r_1|/L$  and  $\theta_2 = |r_2|/L$ , we obtain, if  $E = E_1 + E_2$

$$\frac{E}{L} M_2^{(0)} = E_1 \theta_1^2 + E_2 \theta_2^2 = E_1 \theta_1^2 (1 + E_1/E_2) = E E_1 \theta_1^2 / (E - E_1) \quad (7.12)$$

The opening angle  $\theta_{12}$  is  $\theta_{12} = \theta_1 + \theta_2$ . Using (7.2) we obtain

$$m^2 \approx E_1 E_2 \theta_{12}^2 = E_1 E_2 \theta_1^2 (1 + E_1/E_2) = \frac{\theta_1^2 E_1 E}{E - E_1}$$

that is,

$$m^2 \approx \frac{E^2}{L^2} M_2^{(0)} \quad (7.13)$$

The square of the mass of the parent particle is related to the second moment  $M_2^0$  in a very simple way. For finite width showers we can use the fact that the second moment of each shower about the point 0 is given by the second moment of the shower about its own centroid  $0_i$  ( $i=1,2$ )

plus the energy of the shower times the distance of  $O_i$  from 0. We obtain

$$m^2 \approx \frac{E^2}{L^2} (M_2^{(0)} - M_2^{(1)} - M_2^{(2)}) \quad (7.14)$$

where  $M_1^{(1)}$  and  $M_2^{(2)}$  are the second moments of each shower about  $O_1$  and  $O_2$ . This correction is negligible for large mass mesons (but important, for instance, for the decay  $\pi^0 \rightarrow \gamma\gamma$ ).

For a 3 particle decay, we have

$$m^2 = (E_1 + E_2 + E_3)^2 - (\vec{p}_1 + \vec{p}_2 + \vec{p}_3)^2 = (\sum_i E_i)^2 - (\sum_i p_i)^2$$

Let's define  $\vec{p}_{iL}$  and  $\vec{p}_{iT}$  such that

$$\vec{p}_i = \vec{p}_{iL} + \vec{p}_{iT}$$

where  $\vec{p}_{iL}$  is the component of the momentum  $\vec{p}_i$  along the line of flight of the parent particle,  $\vec{p}_{iT}$  the component transverse to it. We will have

$$\sum_i^3 \vec{p}_{iT} = 0$$

and for massless decay products

$$E_i^2 = |\vec{p}_{iL}|^2 + |\vec{p}_{iT}|^2$$

whence

$$|\vec{p}_{iT}| = \sqrt{E_i^2 - |\vec{p}_{iL}|^2} \approx E_i \left[ 1 - |\vec{p}_{iL}|^2 / 2E_i^2 \right].$$

We obtain, therefore, if  $E = E_1 + E_2 + E_3$  and  $\theta_i, \vec{r}_i$  are defined by (7.9) and (7.9')

$$\begin{aligned}
m^2 &= (\sum_i E_i)^2 - (\sum_i \vec{p}_{iL})^2 = \sum_i E_i^2 + 2 \sum_{i>j} E_i E_j - \sum_i |\vec{p}_{iL}|^2 - 2 \sum_{i>j} |\vec{p}_{iL}| |\vec{p}_{jL}| \\
&= \sum_i |\vec{p}_{iT}|^2 + 2 \sum_{i>j} E_i E_j - 2 \sum_{i>j} E_i E_j \left( 1 - \frac{|\vec{p}_{iT}|^2}{2E_i^2} \right) \left( 1 - \frac{|\vec{p}_{jT}|^2}{2E_j^2} \right) \\
&\approx \sum_i |\vec{p}_{iT}|^2 + \sum_{i>j} E_i E_j \left[ \frac{E_j |\vec{p}_{iT}|^2}{E_i} + \frac{E_i |\vec{p}_{jT}|^2}{E_j} \right] \\
&= \sum_i |\vec{p}_{iT}|^2 + \sum_i \frac{|\vec{p}_{iT}|^2}{E_i} (E - E_i) = E \sum_i \frac{|\vec{p}_{iT}|^2}{E_i} = E \sum_i E_i \theta_i^2
\end{aligned}$$

that is,

$$m^2 = \frac{E^2}{L^2} \sum_i \frac{E_i |r_i|^2}{E} = \frac{E^2}{L^2} M_2^{(0)} \quad (7.15)$$

which is again (7.14), apart from finite width corrections.

We can therefore obtain measurement of the forward boson mass  $m_F$

from

$$m_F^2 = \frac{E^2}{L^2} \left[ \frac{\sum_j \text{strips} \epsilon_j^x (x_j - x_F)^2}{\sum_j \text{strips} \epsilon_j^x} + \frac{\sum_j \text{strips} \epsilon_j^y (y_j - y_F)^2}{\sum_j \text{strips} \epsilon_j^y} \right] \quad (7.16)$$

using once again uncorrected energy depositions in the strips. For the total energy  $E$  one could use (7.6). But for low 4-momentum transfer processes of the type (6.1) and (6.2) we can, with very good approximations, substitute for it the incident photon energy  $E_T$  (tag energy).

Instead of waiting for a full understanding of the problem of pattern recognition in our forward detector, we decided to proceed on

to search for exclusive events using this simple first and second moment algorithm. The masses squared of the  $\pi^0, \eta^0, \omega^0, \phi, \psi$  mesons are respectively  $0.0182 \text{ GeV}^2, .301 \text{ GeV}^2, .613 \text{ GeV}^2, 1.040 \text{ GeV}^2$  and  $9.61 \text{ GeV}^2$ .

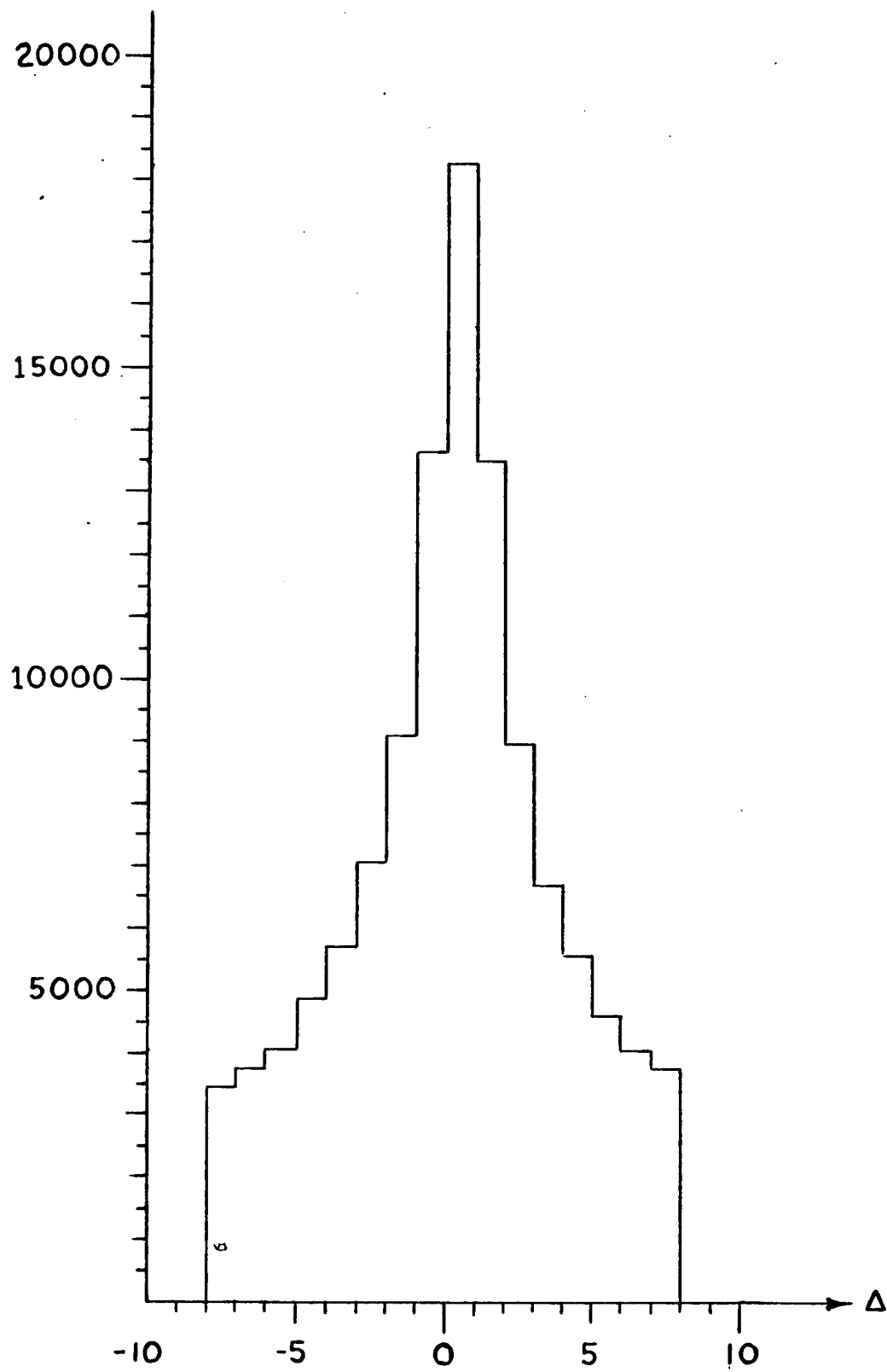
### B) Second Pass Filter

A second pass filtering procedure was applied on the 117 thousand triggers emerging from the first pass filter. The procedure uses the algorithm of section A). Equations (7.16) and (7.8) are used, event by event, to calculate  $m_F^2, x_F, y_F$ . We then calculate  $\phi_F = \tan^{-1}(y_F/x_F)$ . If the event contains an exclusive final state of the type (6.1) or (6.2) we expect a recoil counter to be latched in the  $\phi$  region around the value  $\phi_F' = \phi_F \pm 180^\circ$ . Let's call  $i_{\text{PRED}}$  ( $i_{\text{PRED}} = 1,16$ ) the recoil counter whose boundaries, in terms of azimuthal angle  $\phi$ , contain the value  $\phi_F'$ . At least one recoil counter is latched, as a result of the first pass filter. We define the (integer) variable

$$\Delta = i_{\text{CLOSE}} - i_{\text{PRED}}$$

where, among the recoil counters latched in the event,  $i_{\text{CLOSE}}$  ( $i_{\text{CLOSE}} = 1,16$ ) is the closest to  $i_{\text{PRED}}$ . Fig. 7.1 shows the distribution of the coplanarity variable  $\Delta$  for all the triggers in our sample. A distinct peak at  $\Delta = 0$  hints at the presence of elastic and quasi-elastic events in our filtered sample. We estimate, however, the error  $\sigma_{x_F} = \sigma_{y_F}$  of our  $x_F$  and  $y_F$  measurement to be a few cm. The error  $\sigma_{\phi_F}$  of the variable  $\phi_F$  is given by

$$\sigma_{\phi} = \sigma_{x_F} / r_F \quad (r_F = \sqrt{x_F^2 + y_F^2})$$

Figure 7.1. Distribution of the Coplanarity Variable  $\Delta$  (see Text)

and becomes very large for the (preferentially populated) small  $r_F$  region. A conservative coplanarity cut  $|\Delta| \leq 1$  will be therefore applied to our samples.

Figure 7.2a shows the distribution of the variable  $m_F^2$ . Its dominant feature is a large peak at low value of  $m_F^2$  from single showers from the continuum of inelastic events. Compton scattering and  $\pi^0$  exclusive photo-production events are buried under this peak. No particular structure is evident at higher values of  $m_F^2$ . In fig. 7.2b the same distribution is replotted excluding the low  $m_F^2$  region. A hint of a signal (in the form of a shoulder) appears around the  $\omega$  region ( $m_F^2 \approx .6 \text{ Gev}^2$ ). The shoulder becomes a distinct structure if events with  $E_F/E_T < 85\%$  are excluded from the plot (fig. 7.2c). A similar structure is in fig. 7.2d, where only events with  $|\Delta| \leq 1$  are plotted. The signal to background ratio improves in fig. 7.2e where only  $E_F/E_T > 85\%$  and  $|\Delta| \leq 1$  entries are plotted. Fig. 7.2f contains events with extra requirements that at least 7 planes have a hit in the drift chambers quadrant shadowing  $i_{\text{CLOSE}}$ .

The first and second moment analysis, therefore, appears to be effective in isolating an omega signal. The same is true for the elastic scattering, where the requirement  $m_F^2 \approx 0$  simply amounts to selecting single shower events. Fig. 7.2e and 7.2f possibly also contain an excess of events in the  $\phi^0$  region (around  $1 \text{ Gev}^2$ ). This analysis should also be sensitive to a  $\psi$  signal in the (essentially background free) very large mass region. Two candidate events at a mass of about  $10 \text{ Gev}^2$  are present in plot 7.2f (not visible). This analysis will be soon applied to the 135 Gev (and 80 Gev), 10 meter running where we gain a good factor in



Figure 7.2a. Distribution of the Mass Squared Variable  $m_P^2$  (from second moment estimate)

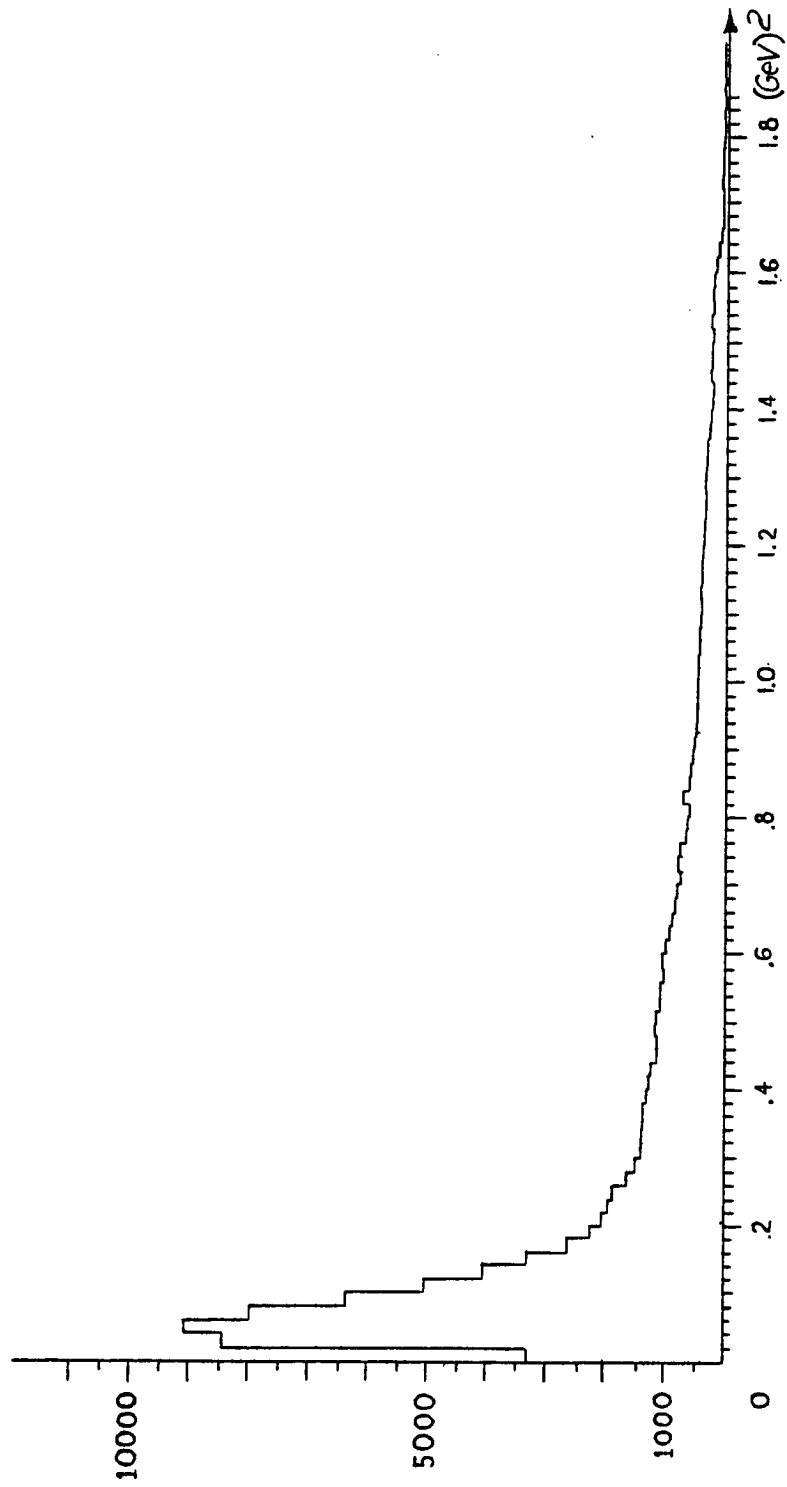


Figure 7.2b. Distribution of Fig. 7.2a ( $m_F^2$ ) Without the Low  $m_F^2$  Region.

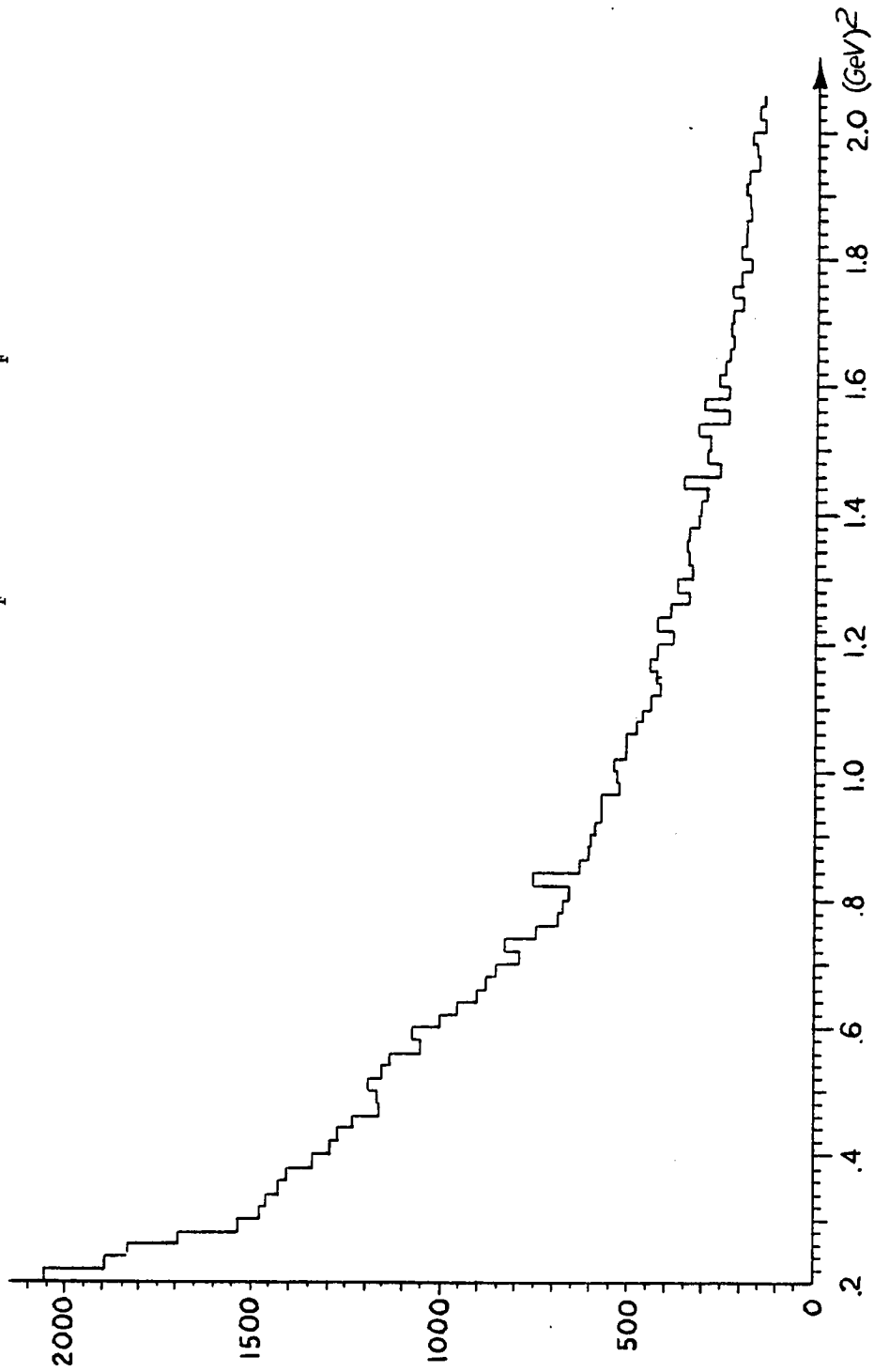


Figure 7.2c.  $m_F^2$  Distribution for Events with  $E_F/E_T > 85\%$ .

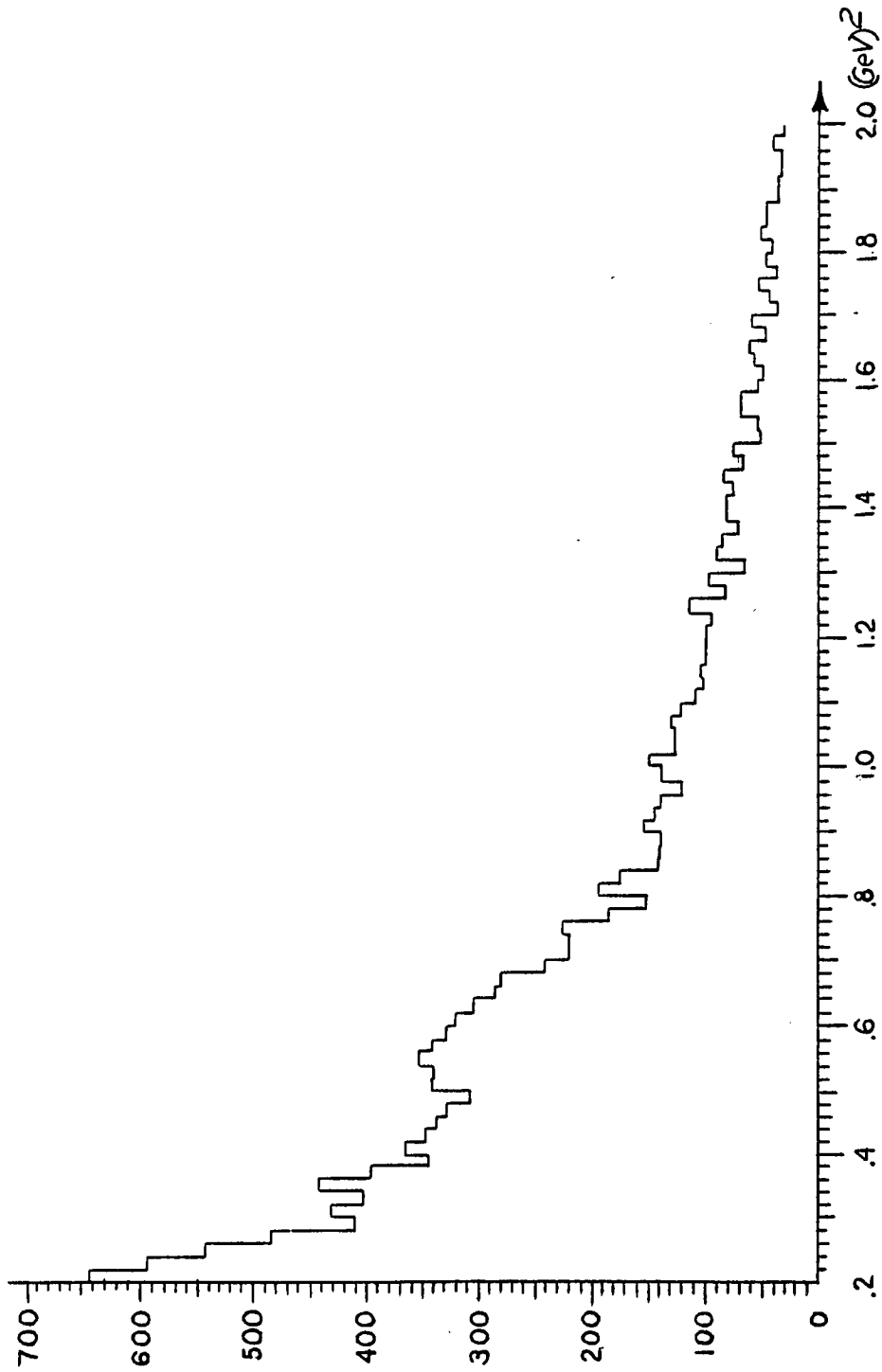


Figure 7.2d.  $m_F^2$  Distribution for Events with  $|\Delta| \leq 1$  ( $\Delta$  = Coplanarity Variable);

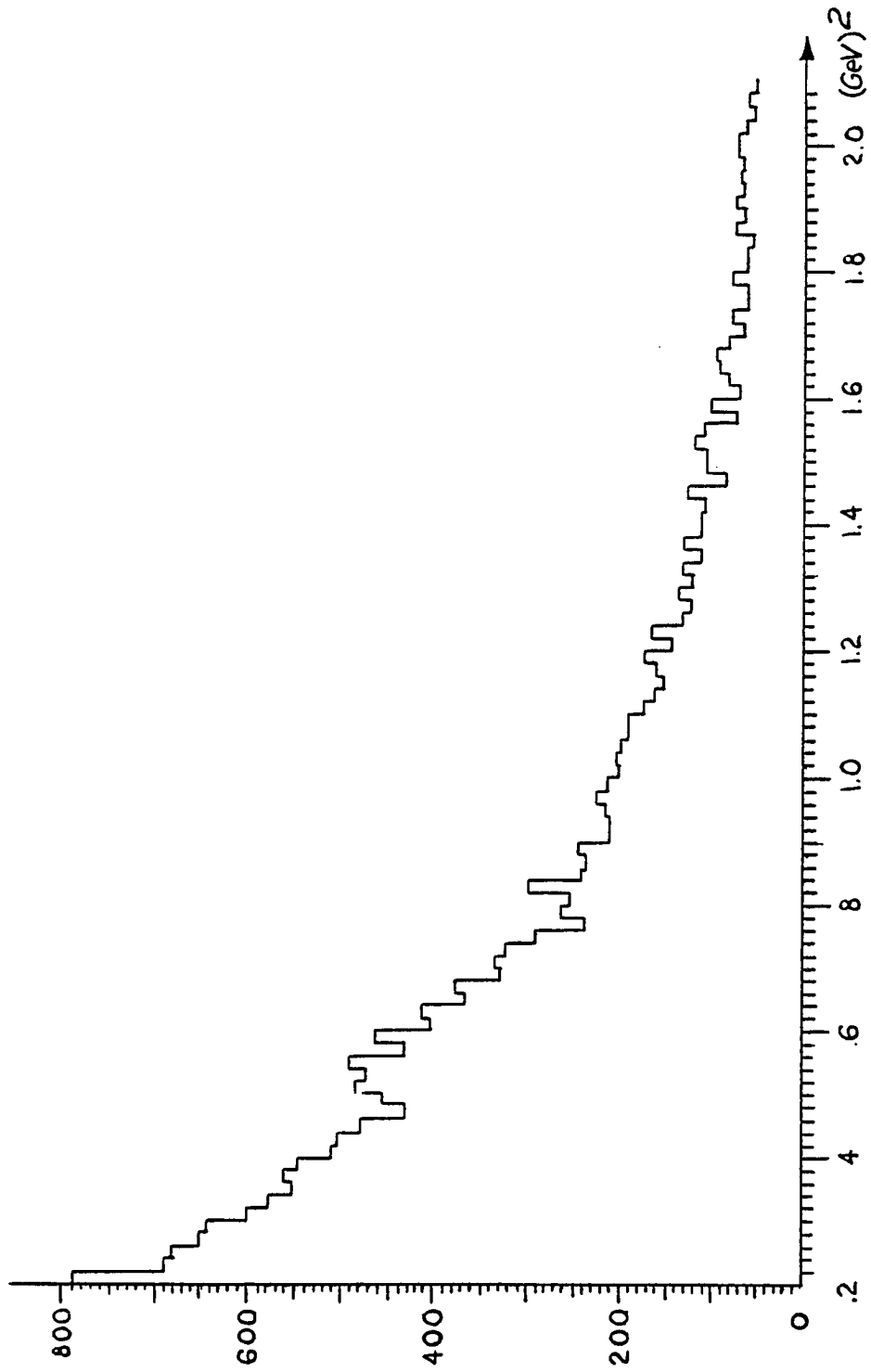


Figure 7.2e.  $m_F^2$  Distribution for Events with  $E_F/E_T > 85\%$  and  $|\Delta| \leq 1$

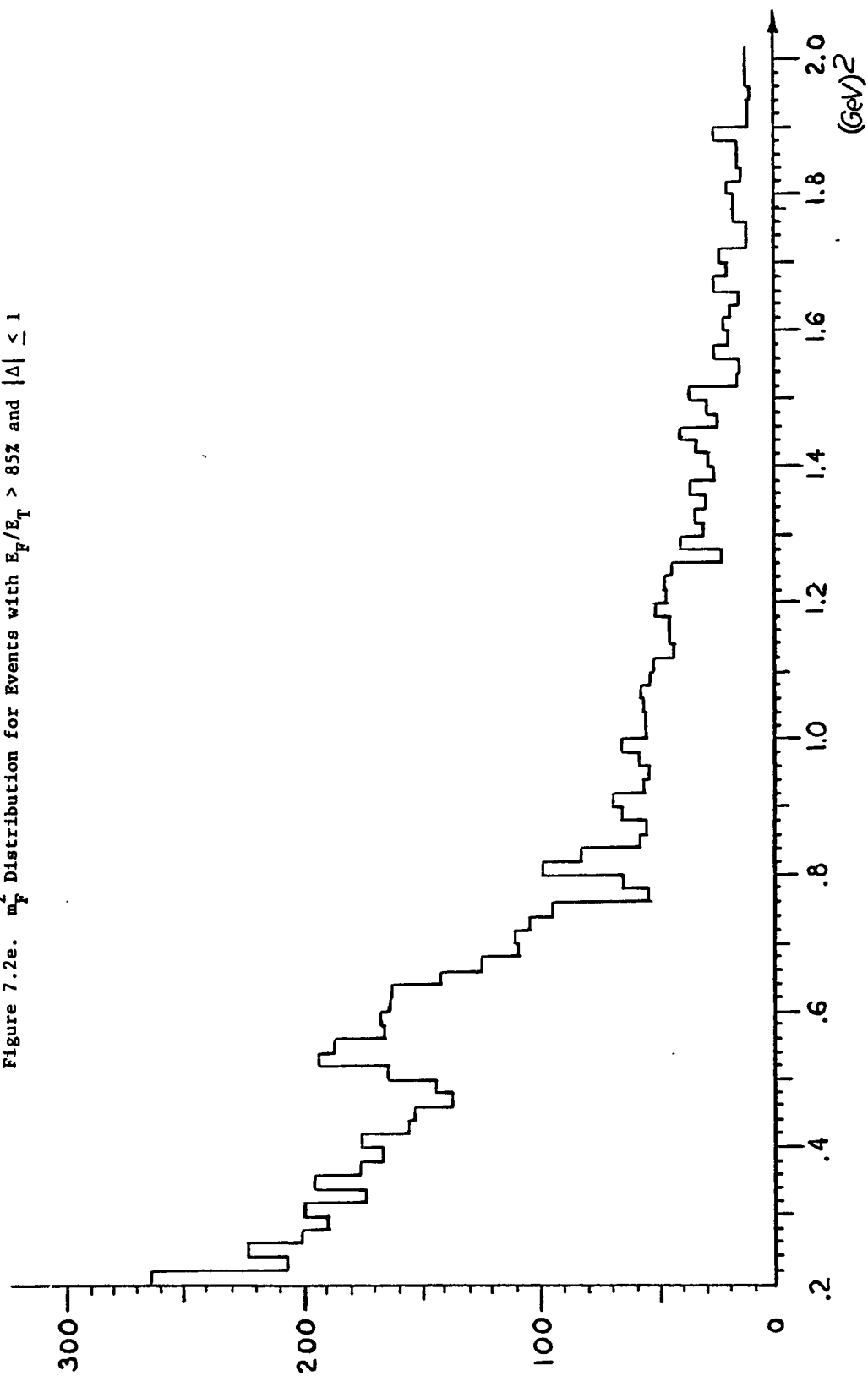
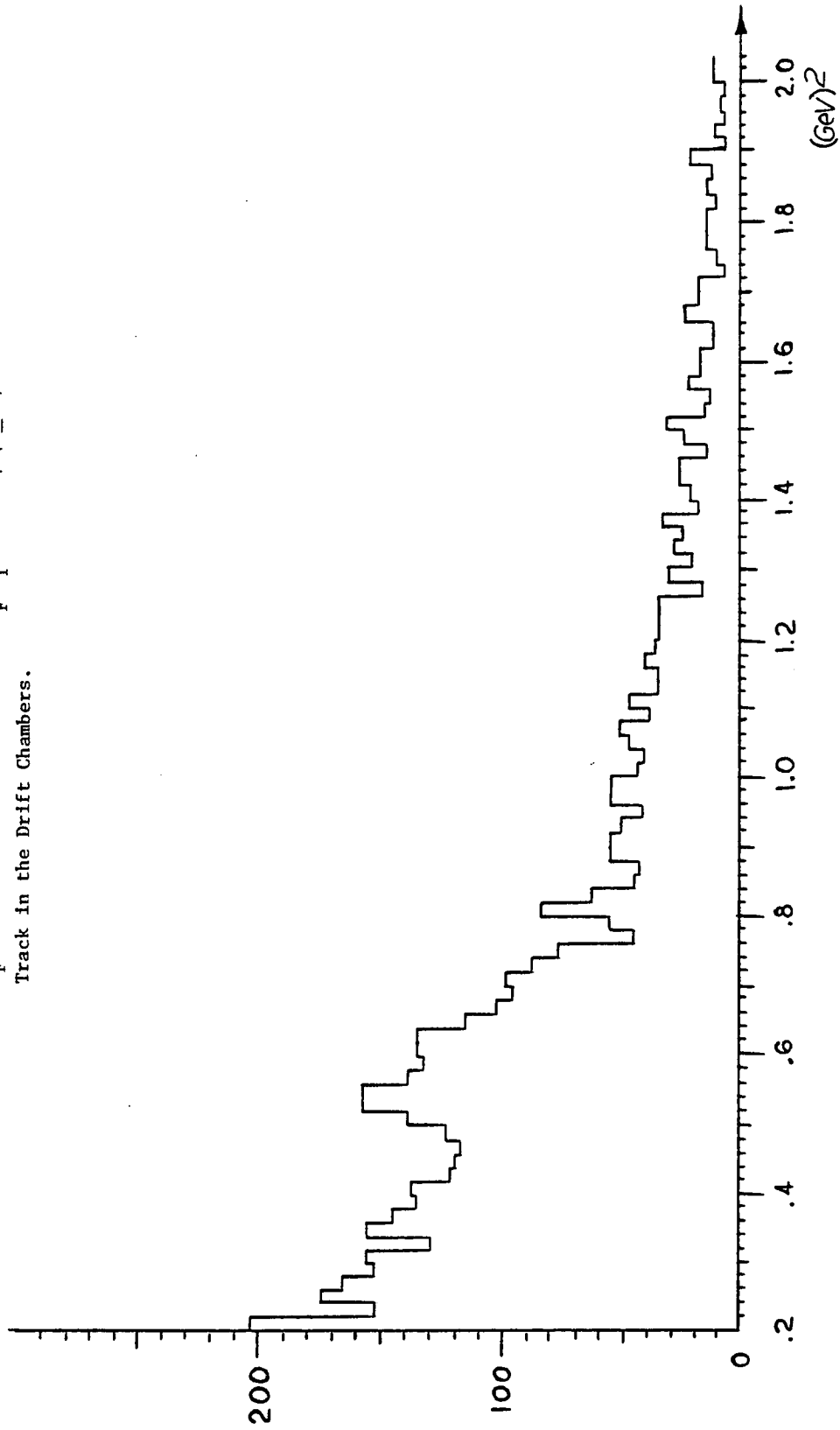


Figure 7.2f.  $m_F^2$  Distribution for Events with  $E_F/E_T > 85\%$ ,  $|\Delta| \leq 1$ , and a Possible Track in the Drift Chambers.



acceptance for the (wide opening angle) decay of  $\psi$  with an electron and a positron.

The remaining discussion will concentrate on the analysis of the omega signal. The events in plot 7.2e (requiring coplanarity and large fractional energy) having a value of  $m_F^2$  such that  $0.3 \leq m_F^2 \leq 1.0 \text{ Gev}^2$  are stored on a data summary tape containing 4372 triggers. We turn now to the analysis of this final sample.

### C) Omega Analysis

Figure 7.3a shows the  $m_F^2$  distribution of the 4372 triggers emerging from the second pass filter. Figure 7.3b shows the distribution of the ratio  $E_F/E_T$ . We proceed now to interrogate the relevant quadrant of drift chambers for a possible track. Fig. 7.3c shows the distribution of number of hits in that quadrant summed over all its planes. It exhibits a distinct peak for a value of 8, characteristic of clean one track events.

Let  $n_i$  ( $i = 1, 2$ ) be the number of hit wires on the  $i$ -th drift plane. The number of possible ways to combine them together to form a track with eight hits is  $N_8 = \prod_i n_i$ . If one (and only one) drift plane has no wires hit, we also search for a track with seven hits in order to be protected against inefficiencies of the chambers. If that plane is the  $j$ -th plane, then  $N_7 = \prod_{i \neq j} n_i$ . In our sample of 4372 triggers we find

- α) 798 triggers with more than 1 drift plane empty. No track is present.
- β) 3220 triggers with at most 1 empty plane and  $\min\{N_8, N_7\} \leq 96$ .
- γ) 354 triggers with at most 1 empty plane and  $\min\{N_8, N_7\} > 96$ .

Figure 7.3a.  $m_F^2$  Distribution of Events in the Omega Mass  
Region ( $|\Delta| \leq 1$ ,  $E_F/E_T > 85\%$ )

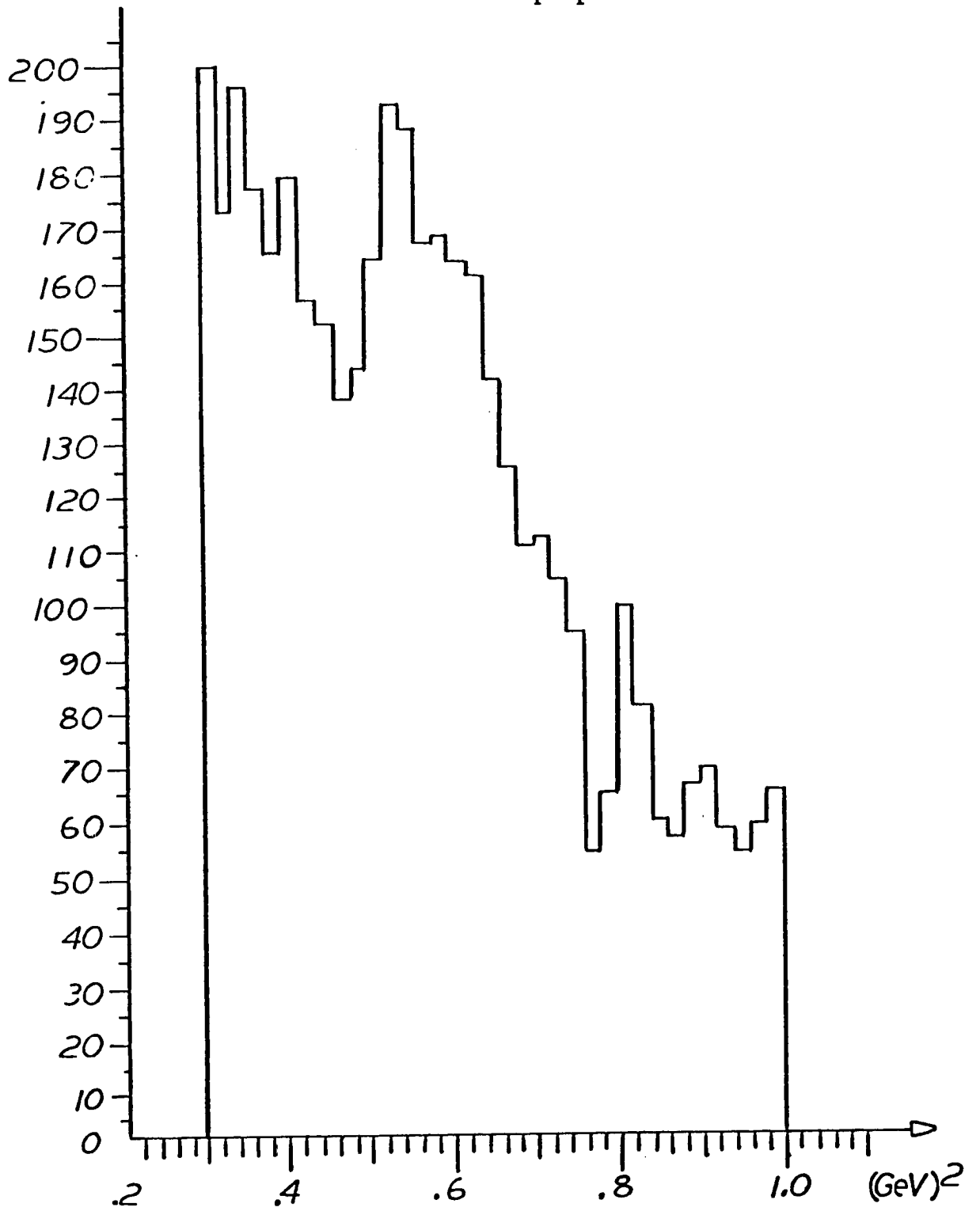




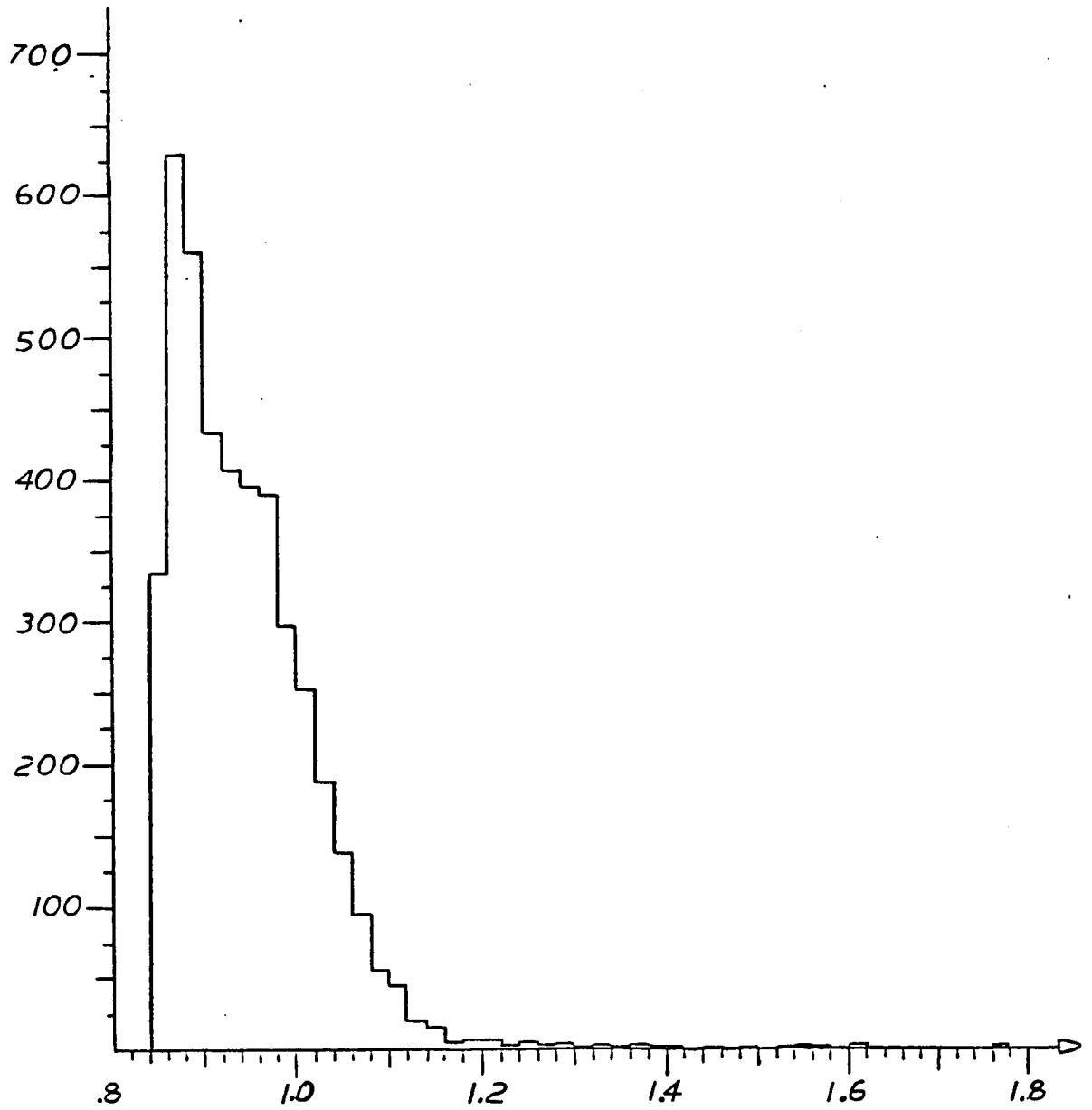
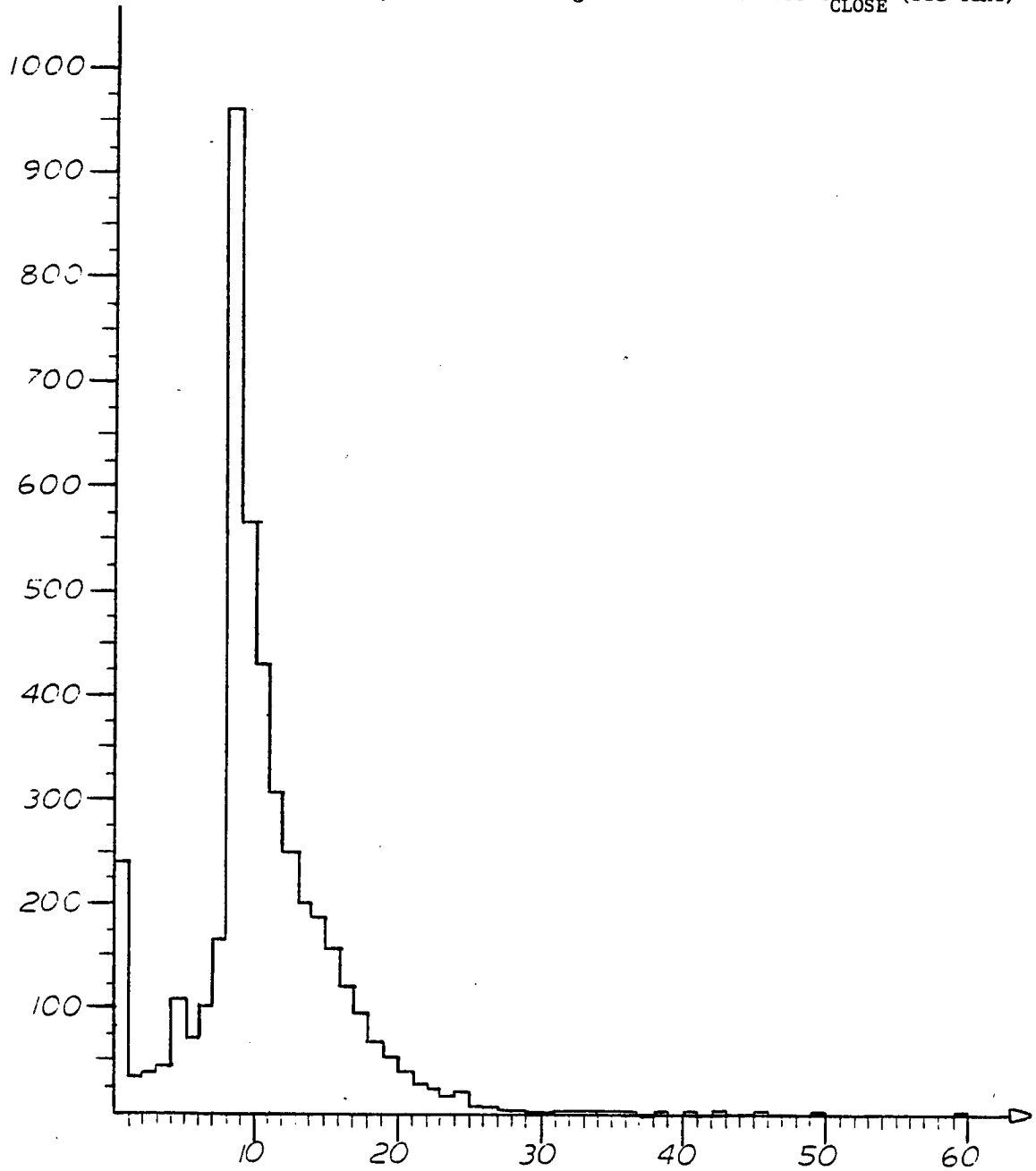
Figure 7.3b.  $E_F/E_T$  Distribution

Figure 7.3c. Distribution of Number of Hits in the Drift Chambers  
Quadrant Shadowing the Recoil Counter  $i_{CLOSE}$  (see text)



Triggers of type  $\beta$ ) and  $\gamma$ ) can possibly contain a track. Events of type  $\gamma$ ), however, have too complicated a topology of hits. We do not try to reconstruct the track for those events. We will instead estimate a correction to our cross section for these dropped events.

The track reconstruction program reconstructs a track for 3080 of the 3220 triggers of type  $\beta$ ). Fig. 7.4a shows the  $m_F^2$  distribution for these events. Fig. 7.4b shows the  $\chi^2$  distribution for the reconstructed track. The  $\chi^2$  is calculated assuming an error of 500 microns per plane. The fit is a 4-parameter fit, with 8 (or 7) measurements. We find correctly a  $\chi^2$  distribution peaked at a value of  $\chi^2 = n_D - 1 = 3$  where  $n_D = 8 - 4$  is the number of degree of freedom of the fit. The long tail of the distribution comes from very slow recoiling protons (small  $t$  region). Multiple scattering is large for these protons and a value of 500 microns is an underestimate of our error per plane.

From the parameters of the reconstructed track we can calculate an azimuthal angle  $\phi_R$  and a polar angle  $\theta_R$  for the recoil proton. If the track is parametrized (in the laboratory reference frame R of chapter 5) as

$$\underline{x} = \underline{x}_0 + \underline{p} \rho$$

where  $\underline{p} = (p_x, p_y, p_z)$  are the direction cosines of the track, then

$$\begin{aligned} \phi_R &= \tan^{-1}(p_z/p_x) \\ \cos \theta_R &= p_y/|p|. \end{aligned}$$

The 4-momentum transfer  $t$  is given by

$$t = t_R \simeq -4 M_p^2 (\cos^2 \theta_R - m_w^2/2M_p E_\gamma) / (\sin^2 \theta_R + 2M_p/E_\gamma)$$

Figure 7.4a.  $m_F^2$  Distribution for Events Where a Track is Reconstructed in the Drift Chambers

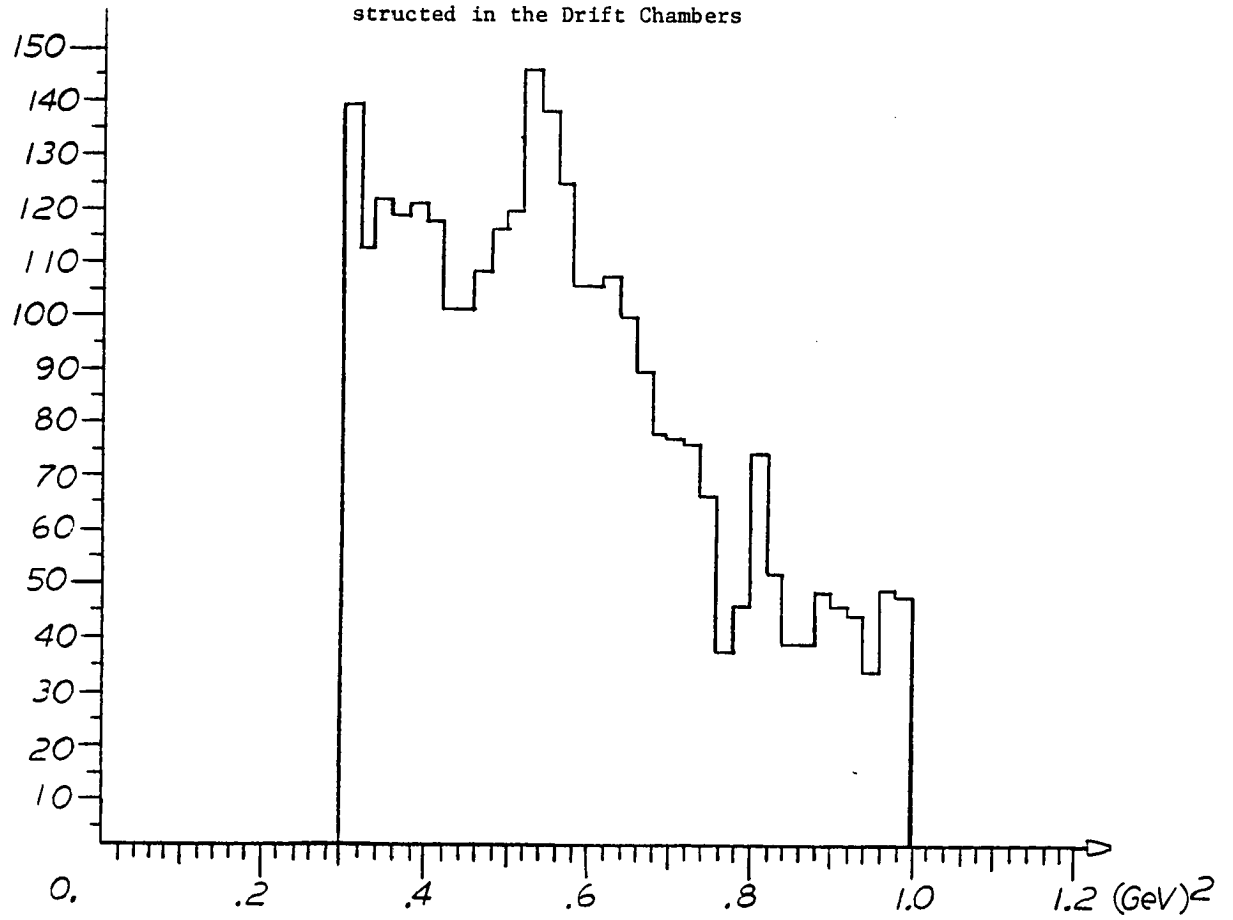
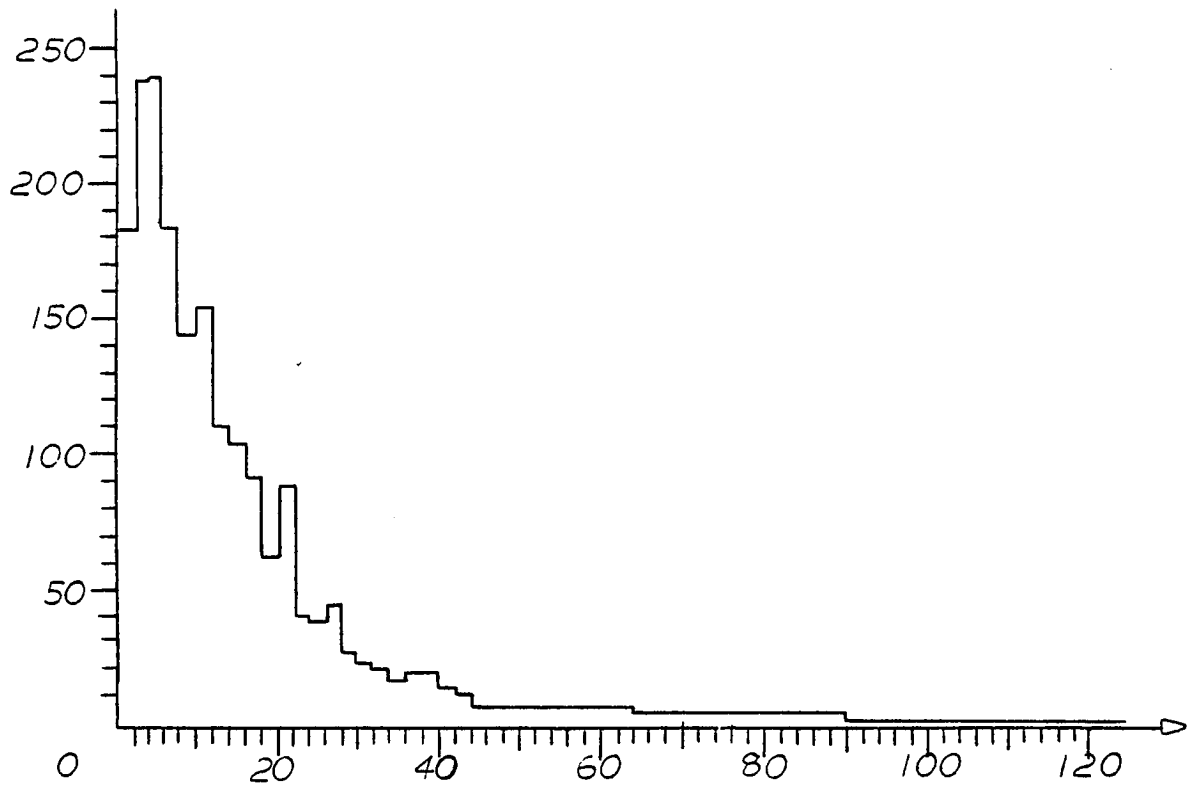


Figure 7.4b.  $\chi^2$  Distribution for Reconstructed Tracks

where  $M_p$  is the mass of the proton,  $m_\omega$  is the omega mass and  $E_\gamma = E_T$  the energy of the incident photon.

The forward detector position  $x_F, y_F$  also provides an estimate of  $t$

$$t = t_F \approx \theta_F^2 \frac{E_\gamma^2}{2}.$$

For each event, we have two independent determinations of  $\phi$  (modulo 180 degrees) and  $t$ . We can fit the 4 measurements to the two parameters  $\phi$  and  $t$ . The fit has (essentially) the following  $\chi^2$

$$\chi_{\text{fit}}^2 = \frac{(t_F - t)^2}{\sigma_{t_F}^2} + \frac{(t_R - t)^2}{\sigma_{t_R}^2} + \frac{(\phi_F + 180^\circ - \phi)^2}{\sigma_{\phi_F}^2} + \frac{(\phi_R - \phi)^2}{\sigma_{\phi_R}^2}.$$

The distribution of  $\chi^2$  from this kinematic fit for the 3080 events where a track has been reconstructed is shown in fig. 7.5a. It peaks at  $n_D - 1 = 1$ .

The following additional requirements (cuts) are demanded from the 3080 events.

- 1)  $\chi_{\text{fit}}^2 < 50$
- 2)  $\cos\theta_R > -0.1$  (the track goes forward; a small negative value of  $\cos\theta_R$  is accepted because of multiple scattering)
- 3) the distance  $d$  of the point  $V = (v_x, v_y, v_z)$  of closest approach of the track to the beam-target axis is less than 3 cm.

Fig. 7.5b shows the distribution of the variable  $d$ . Fig. 7.5c shows the distribution of the longitudinal coordinate  $v_y$ . It has the expected width of 75 cm. (target length).

- 4) The C counter is required not to be on in the event. An event with the C counter latched does contain at least one charged

Figure 7.5a.  $\chi^2$  Distribution for the Kinematic Fit of the Event to the  $\Upsilon_p \rightarrow \omega p$  Hypothesis

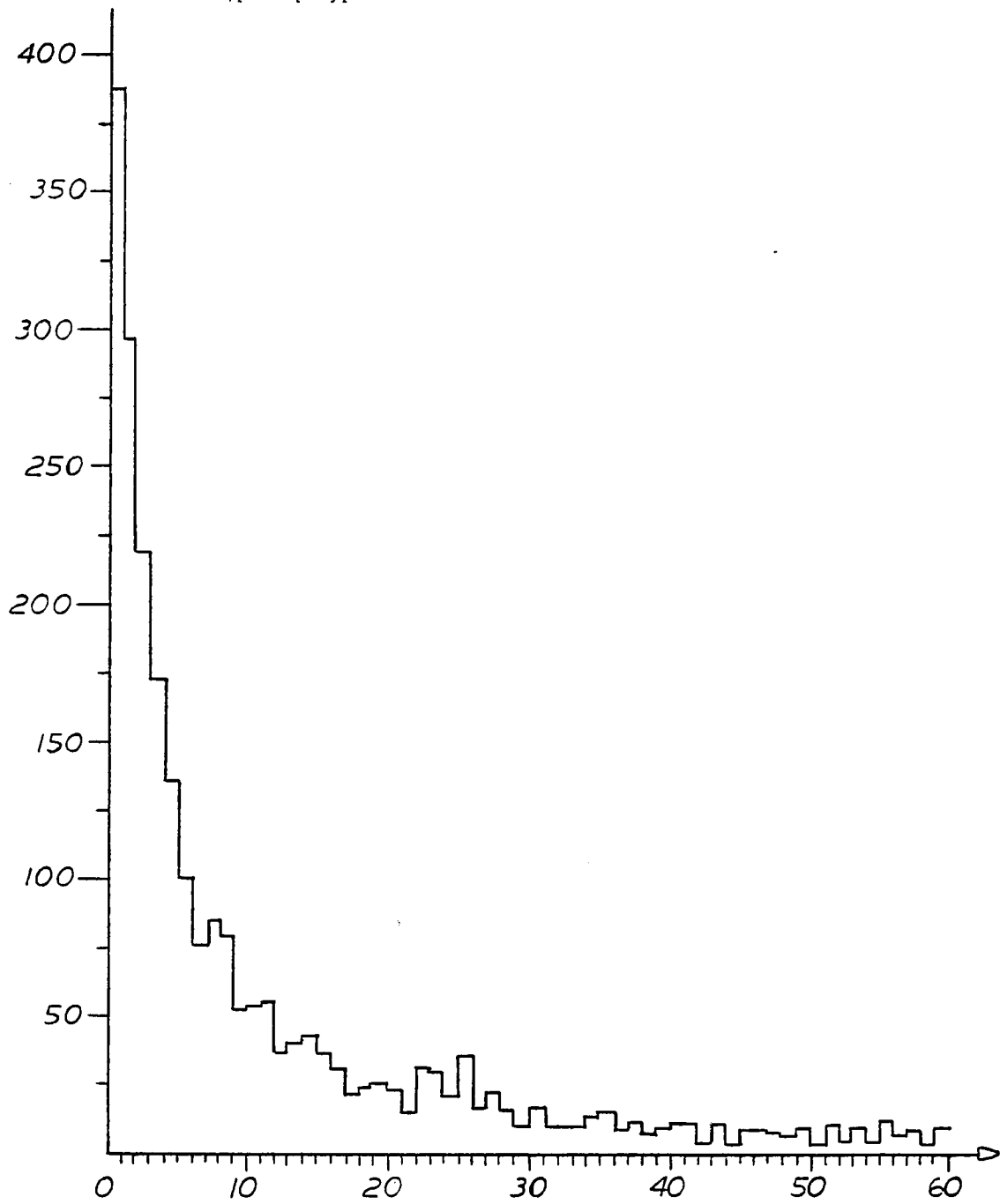


Figure 7.5b. Distance of Closest Approach of the Recoil Track to the Beam-Target Axis

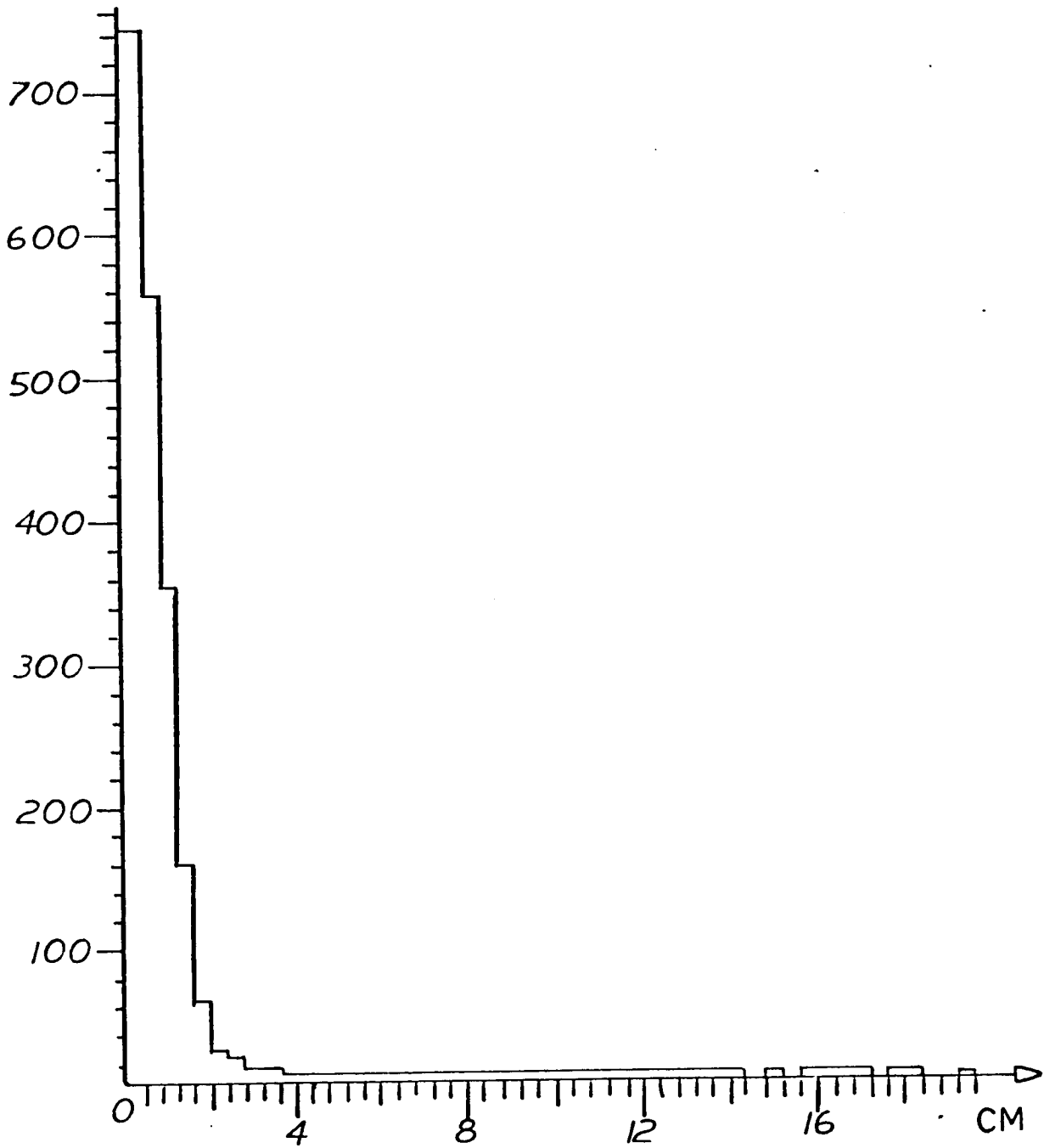
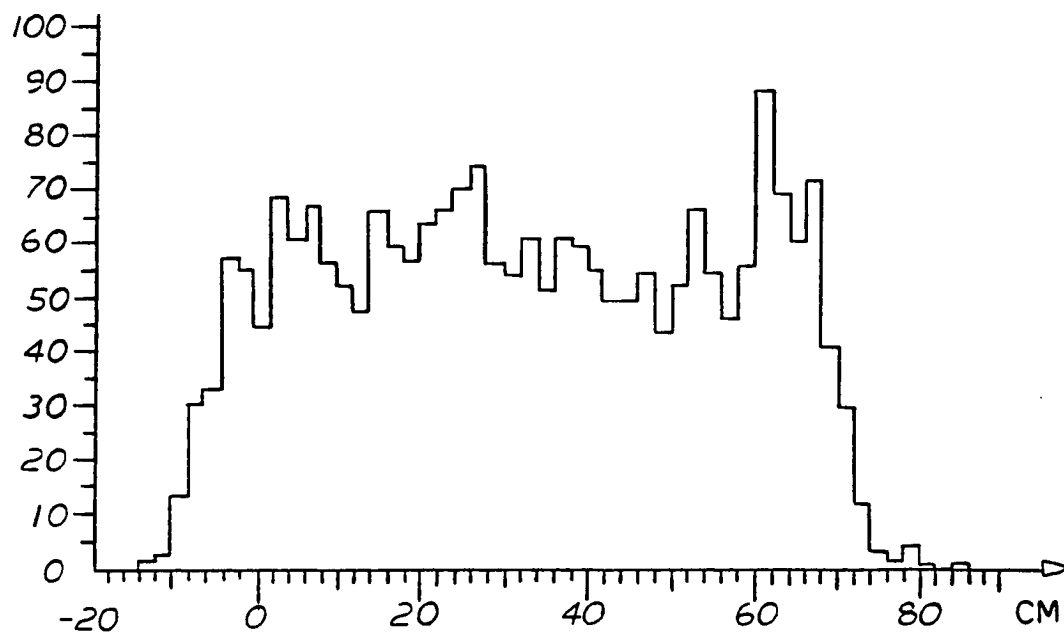




Figure 7.5c. Distribution of the Longitudinal Coordinate of the Point of Closest Approach of the Recoil Track to the Beam Target Axis



particle in the forward direction.

5) a final tighter energy cut  $E_F/E_T > 90\%$  was performed.

Fig. 7.6. shows the  $m_F^2$  distribution of the 1173 events surviving all the cuts. A fit to a gaussian above a quadratic background is performed on these events. It gives a (reduced)  $\chi_R^2$  of 1.38 for

$$m^2 = 0.578 \pm 0.007 .$$

The area of the peak is estimated to correspond to  $324_{-44}^{+56}$  events.

Figures 7.7a through 7.7g show general characteristics of the 1173 events surviving all the cuts. Fig. 7.7a is the  $E_F/E_T$  distribution. Figure 7.7b is the distribution of the number of R counters present in the event. Figure 7.7c is the distribution of pulse height in the beam plug counter. It is consistent with the counter ADC pedestal for all but a few events. Figure 7.7d is the ratio of energy deposition in the U counters over the total energy deposition in the U and V counters. It shows that our sample is not contaminated by  $\gamma p \rightarrow \rho p$  events ( $\rho \rightarrow \pi^+ \pi^-$ ), with the pions producing two hadronic showers in the detector. Figures 7.7e and 7.7f show respectively the azimuthal ( $\phi$ ) and polar match ( $\theta$ , i.e. t) in between the forward and recoil detector. Figure 7.7g shows the azimuthal angle  $\phi$  distribution, clearly displaying the 4 dead regions in the recoil detector due to the drift chambers support frames.

#### D) Detection Efficiency. Monte Carlo Simulation

In order to estimate the detection efficiency of our apparatus for exclusive omega photoproduction events we<sup>\*</sup>) wrote a computer program

---

\* A.M. Breakstone, Dr. D.B. Smith and myself.

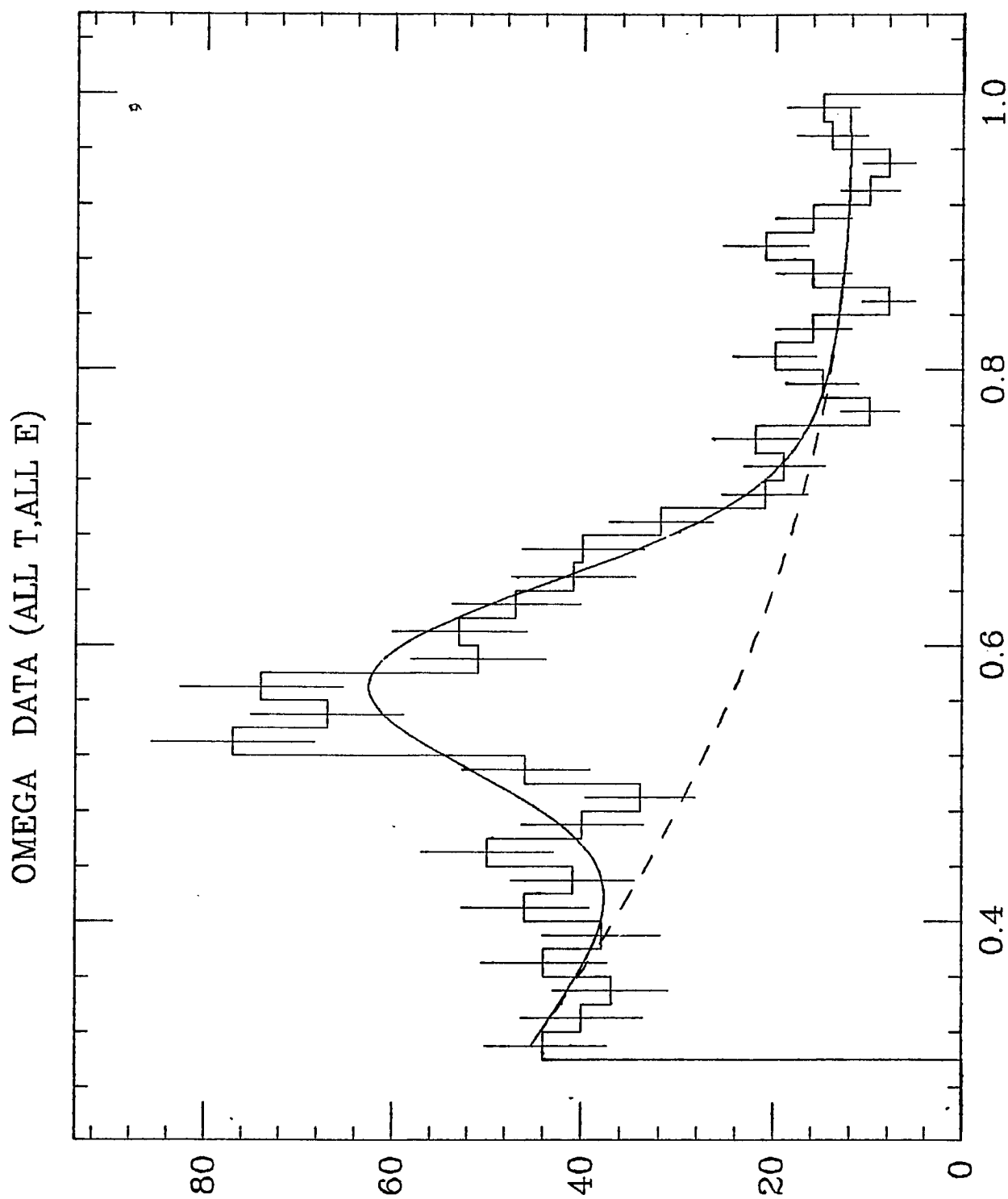


Figure 7.6.  $m_F^2$  Distribution of the Omega Candidates Surviving all the Cuts (1173 Entries).  
Fit is to a Gaussian Above a Quadratic Background.

Figure 7.7a.  $E_F/E_T$  Distribution for Events  
Surviving All the Cuts

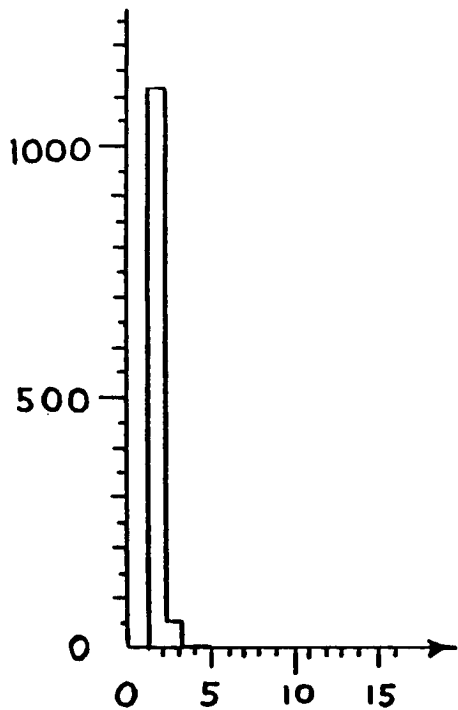
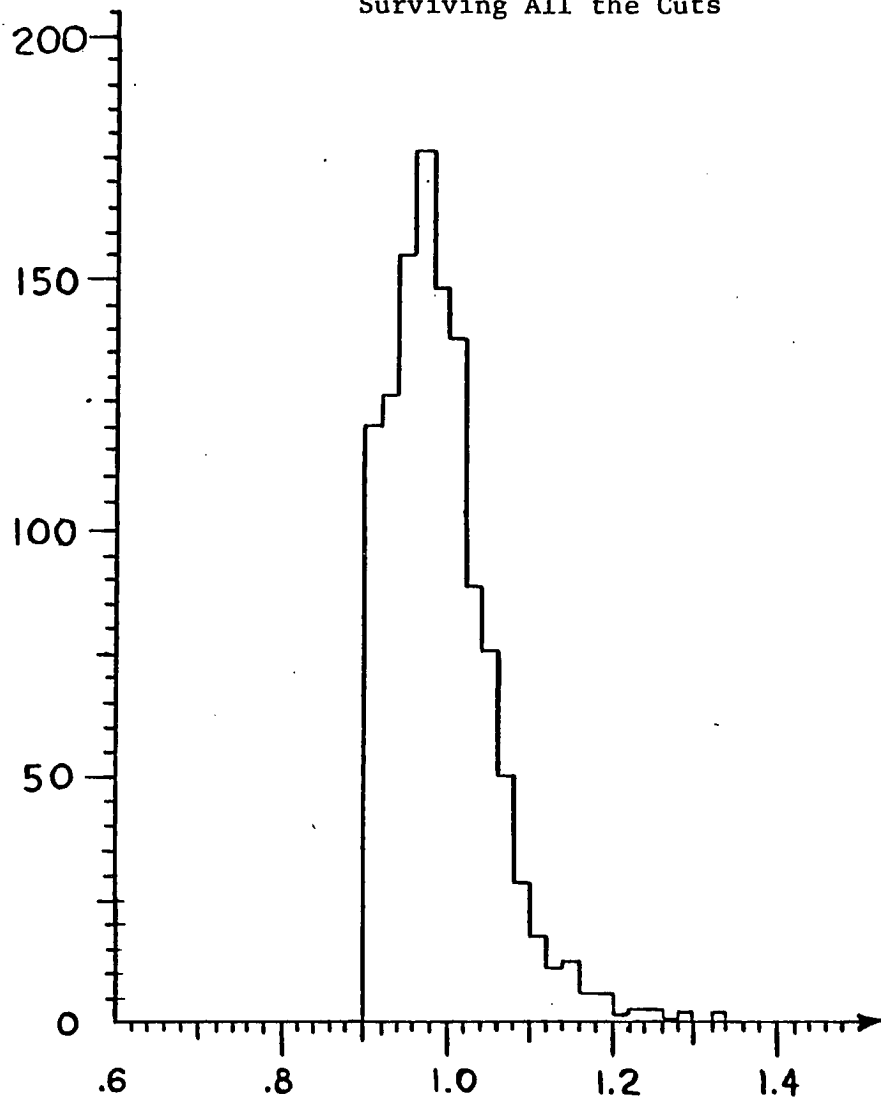


Figure 7.7b. Distribution of  
Number of R Counters Latched

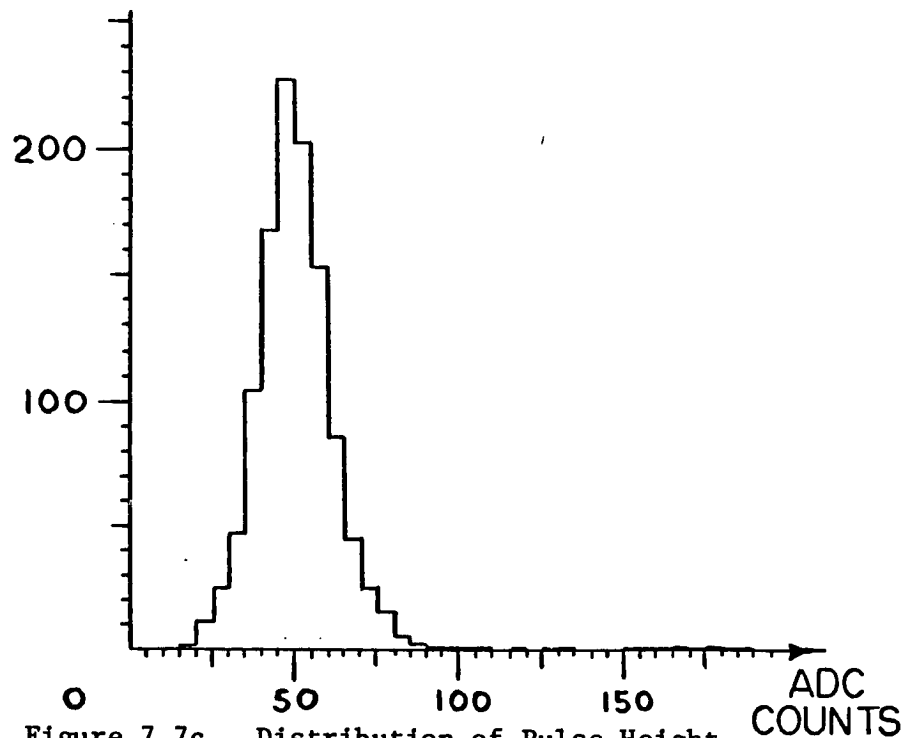


Figure 7.7c. Distribution of Pulse-Height  
in the Beam Plug Counters. ADC Pedestal Value  
is About 50.

ADC  
COUNTS

Figure 7.7d. Ratio of U Energy Deposition Over Total U + V Energy Deposition

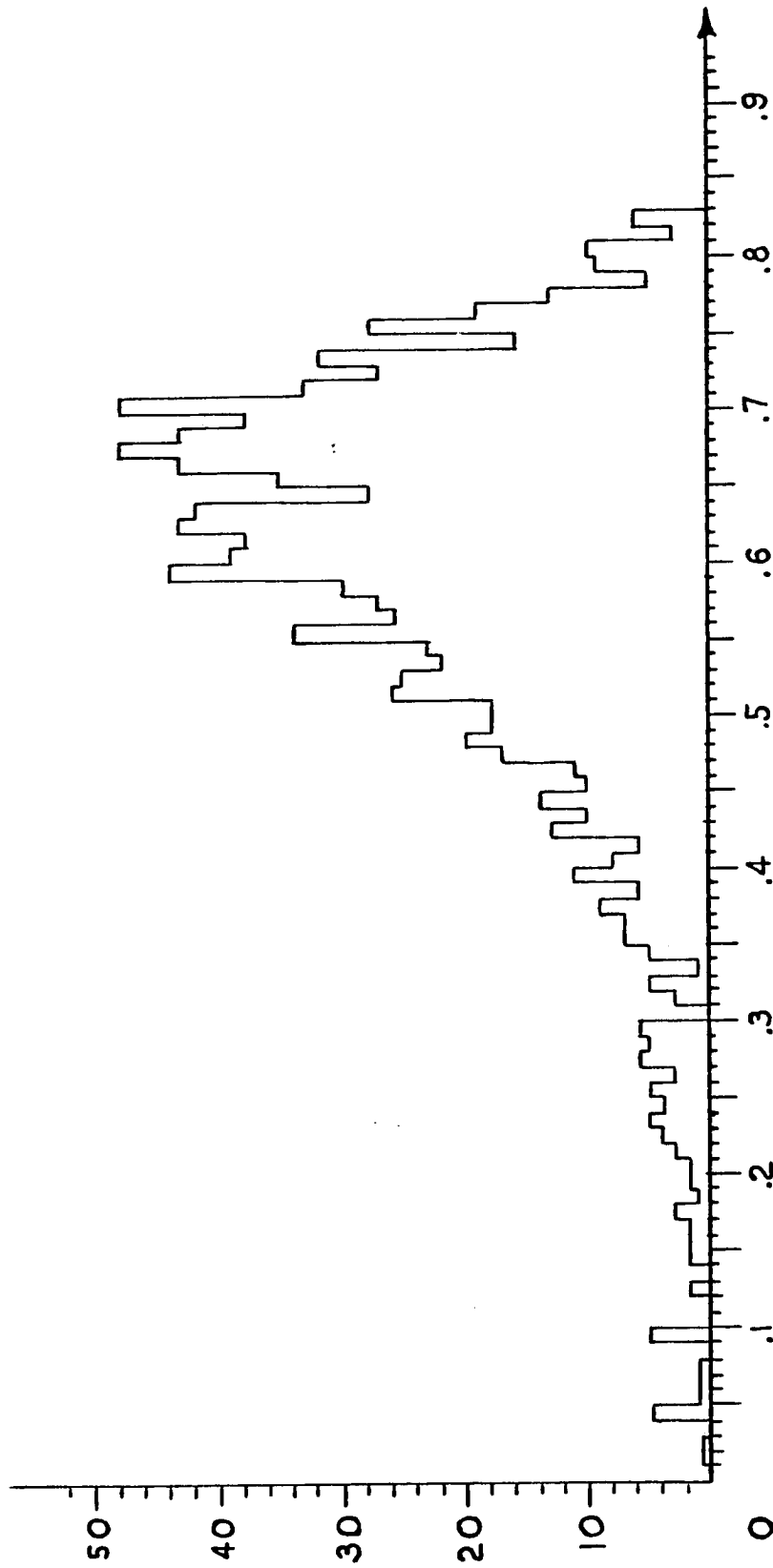


Figure 7.7e. Azimuthal ( $\phi$ ) Match. The Variable Plotted is the Distance in cm. of  $(x_F, y_F)$  from Projection of Track Line on the Forward Detector Plane.

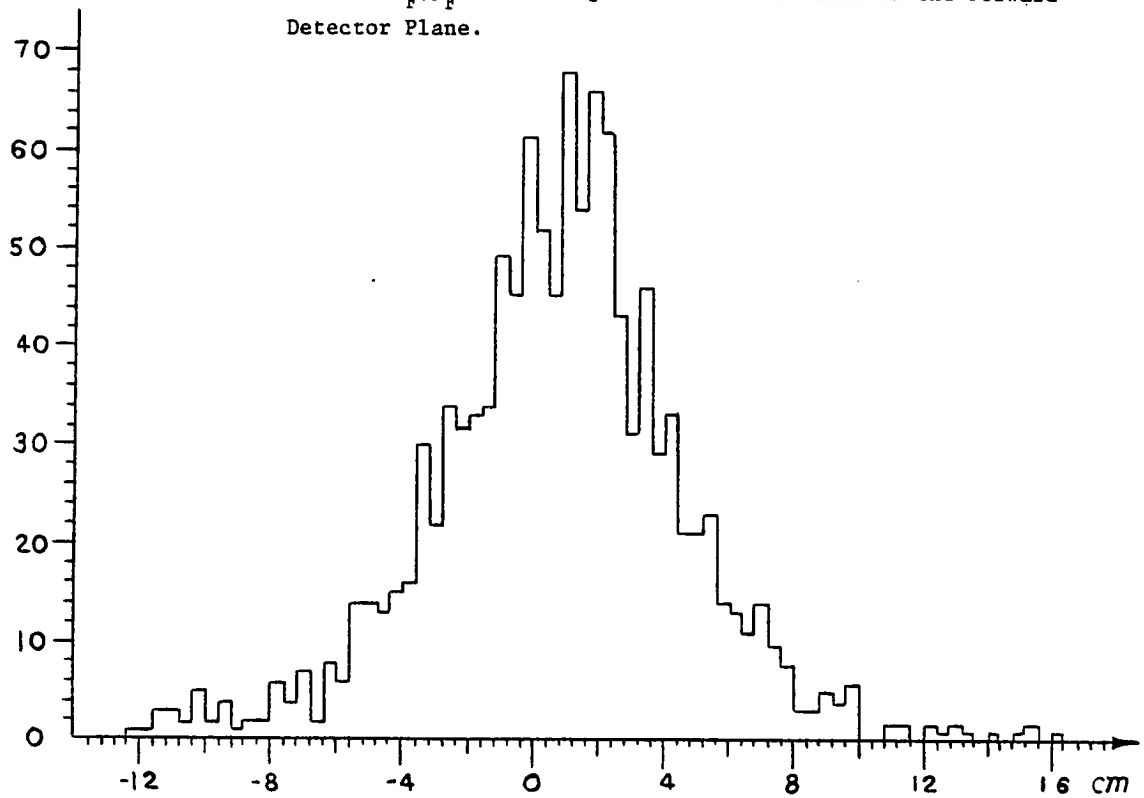


Figure 7.7f. 4-Momentum Transfer Match. The Plotted Variable is  $t_F - t_R$ .

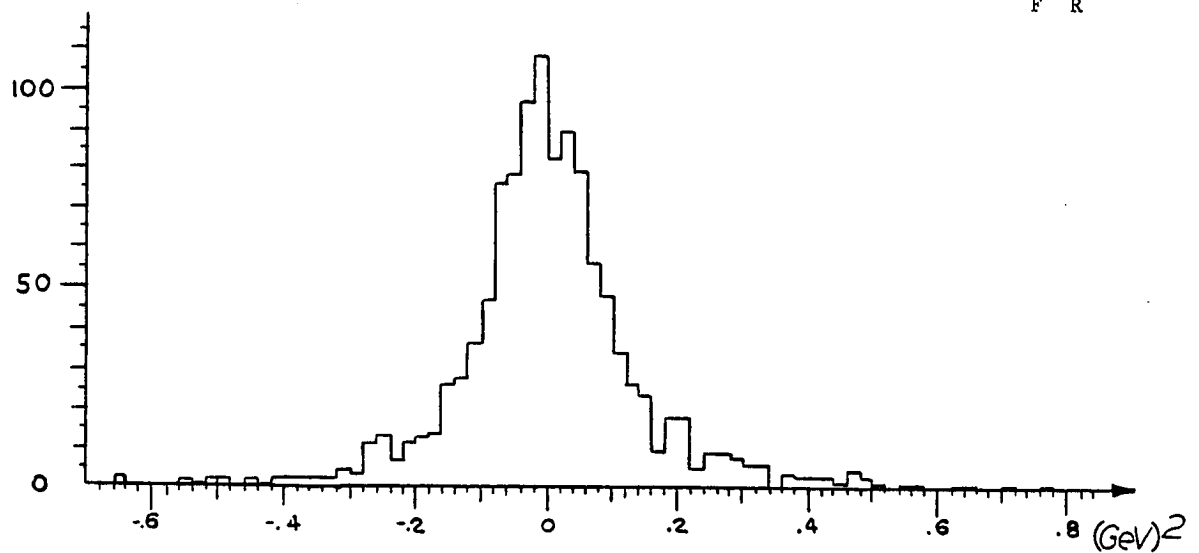
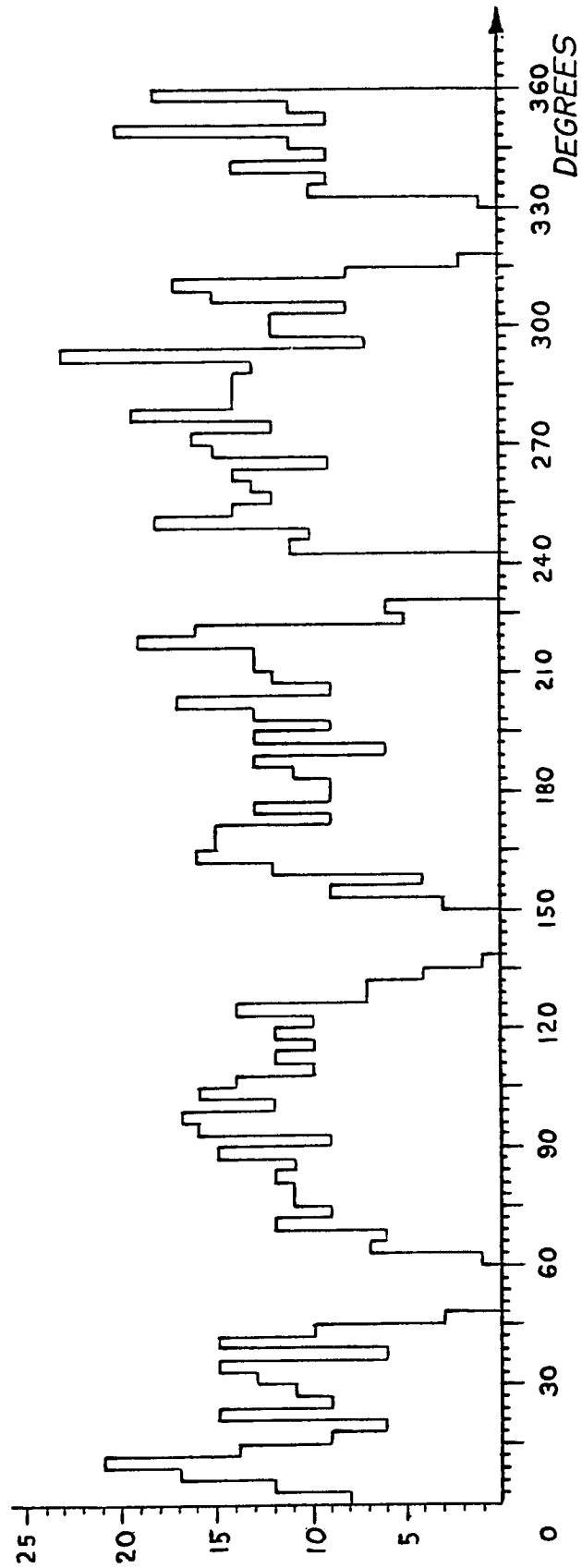


Figure 7.7g.  $\phi_R$  Distribution (in Degrees)

performing a Monte Carlo simulation of the response of our apparatus to this type of event. Photons distributed over the energy interval from 52 to 127 Gev according to a bremsstrahlung ( $1/\text{energy}$ ) spectrum photoproduce (quasi-elastically) omega mesons. The cross section for the process is assumed to be energy independent. The differential cross section  $d\sigma/dt|_{\gamma p \rightarrow \omega p}$  is assumed to be of the form  $Ae^{-b|t|}$  with  $b = 8 \text{ Gev}^{-2}$ . The distribution of interaction vertices is flat along the length of the target and gaussian in both transverse dimensions (with slightly different widths, see chapter 3A). The recoil proton loses at least part of its energy in the target; if energetic enough, it reaches the drift chambers. Hits and drift times are simulated in the chambers. Hits in the recoil time-of-flight counters are also simulated. Proton energy loss in the drift chamber wire material is simulated. Multiple scattering is ignored. The forward photoproduced omega mesons decay into  $\pi^0\gamma$  with a  $1 + \cos^2\theta$  probability distribution (from helicity conservation) for the polar angle  $\theta$  of the decay products in the omega c.m. system. The  $\pi^0$  decay to 2 photons is isotropic in the  $\pi^0$  c.m. system. The three final state photons can hit the forward detector active area. The development of electromagnetic showers is simulated in the forward detector. Energy deposition and pulse height response (including fluctuations) are simulated for each counter, including the x and y hodoscope strips. Details on the shower simulation can be found in ref. 23).

Simulated events are analyzed by the same chain of computer programs used on the data. Event losses are tabulated at various stages. Events are rejected by the first pass filter (chapter 6) when

1. One or more photons, carrying more than 30% of the energy of the



parent omega, miss the forward detector (or hit one of its boundary regions) and deposit no (or only some) fraction of their energy in the shower counters.

2. the recoil proton ranges out in the target or the drift chamber wire material (beryllium-copper) and does not fire a recoil counter.

Events are rejected by the second pass filter (chapter 7B) when

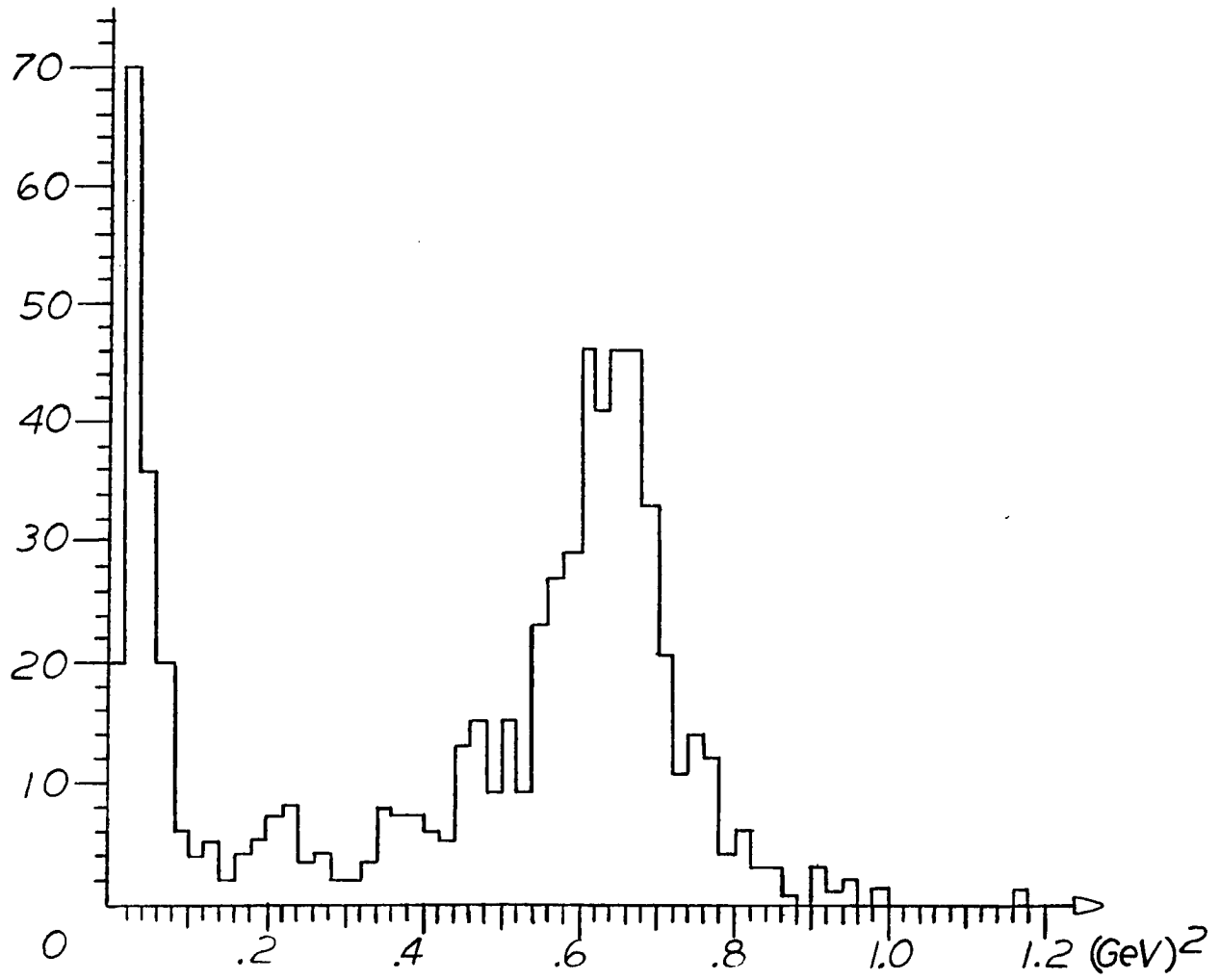
3. less than 85% of the total omega energy is deposited in the shower counters (again a geometrical effect).
4. the value of the coplanarity variable is  $|\Delta| > 1$ , because a large error is made in the determination of  $x_F, y_F$  (photons missing the forward detector; photons being absorbed in the U bank; pulse heights in the hodoscope strips exhibiting large fluctuations).
5. the value of the forward mass squared  $m_F^2$  is outside the range  $0.3 \leq m_F^2 \leq 1.0$  (see 4. above). A typical  $m_F^2$  distribution for simulated events is shown in fig. 7.8.

Events are rejected by the final analysis program (chapter 7C) when

6. the drift chambers do not record the passage of a track (dead area, geometrical effect)
7. the event doesn't survive the cuts (i.e., in practice, the requirement  $E_F/E_T > 90\%$ ).

Monte Carlo runs were performed generating six samples of  $\gamma p \rightarrow \omega p$  events corresponding to six bins in 4-momentum transfer  $t$  (over the entire photon energy spectrum) and three samples corresponding to three bins in the photon energy  $E_T$  (over the entire 4-momentum transfer range).

Figure 7.8. Typical  $m_F^2$  Distribution for Monte Carlo Simulated  $\gamma p \rightarrow \omega p$  Events



The binning is the same adopted for the data (see next section). Fractional losses due to 1. through 7. are tabulated in tables 1 and 2. The detection efficiency, low for small  $t$ , flattens out as a value of about 50% for  $t > 0.07$ . Its dependence on the photon energy is not negligible.

### E) Results

Our liquid hydrogen target of length  $L = 75$  cm and density  $= 0.07043$  gr/cm<sup>3</sup> yields ( $N = \text{Avogadro number}$ ;  $A = \text{nucleon number} = 1$ )

$$\rho L N/A \approx 3.15 \text{ events/barn/photon.}$$

Our useful photon flux is plotted vs. incident photon energy in fig. 7.9. The plotted variable is the variable  $G_i$  ( $i = 1,34$ ) of (6.3). It is therefore already corrected for computer dead time and losses due to bad quality tags. The integrated number of photons over the entire 135 Gev sample analyzed is  $1.78 \cdot 10^{10}$ . Partial totals for the photon energy bins of table 2 are  $.56 \cdot 10^{10}$ ,  $.47 \cdot 10^{10}$  and  $.75 \cdot 10^{10}$ . A total useful flux of  $1.76 \cdot 10^{10}$  photons will yield ( $1 \text{nbarn} = 10^{-33} \text{ cm}^2$ )

$$3.15 \cdot 10^{-24} \text{ cm}^2 \cdot 1.78 \cdot 10^{10} = 56 \text{ events/nbarn.}$$

Our total sample of omegas is estimated to contain

$$324_{-44}^{+56} \quad \gamma p \rightarrow \omega p \text{ events} \quad (\chi^2_R = 1.38)$$

Various corrections have to be applied to this number. Fig. 7.10 shows the  $m_F^2$  distribution of the  $3080 - 1173 = 1907$  events rejected by cuts 1) through 5) in section C). A fit to a gaussian peak above a quadratic background yields a number of

Table 1. Monte Carlo Results

(All Energies)

	$0 < t < 0.07$	$.07 < t < .14$	$.14 < t < .20$	$.20 < t < .30$	$.30 < t < .50$	$.50 < t < .85$
a) $E_F/E_T < 70\%$	9.6%	8.1%	5.8%	3.4%	2.6%	2.6%
b) no R latched	51.1%	0	0	0	0	0
a) + b)	55.3%	8.1%	5.8%	3.4%	2.6%	2.6%
c) $E_F/E_T < 85\%$	3.0%	5.1%	4.2%	5.2%	3.4%	2.6%
d) $ \Delta  > 1$	8.9%	10.4%	7.2%	6.2%	1.6%	1.0%
c) + d)	10.2%	12.9%	9.6%	8.8%	4.0%	3.0%
e) $m_F^2 > 1$ , or $m_F^2 < .3$	7.2%	18.0%	23.2%	25.0%	28.4%	29.2%
c) + d) + e)	17.4%	30.8%	32.8%	33.8%	32.4%	32.2%
f) $E_F/E_T < 90\%$	0.3%	0.9%	0.2%	0.8%	0.6%	0.6%
g) no track found	4.9%	11.6%	11.4%	13.4%	14.6%	16.0%
<b>Total Losses</b>	<b>78.0%</b>	<b>51.3%</b>	<b>50.2%</b>	<b>51.0%</b>	<b>50.2%</b>	<b>52.4%</b>
<b>Total Correction</b>	<b>4.53</b>	<b>2.05</b>	<b>2.01</b>	<b>2.04</b>	<b>2.01</b>	<b>2.06</b>

Table 2. Monte Carlo Results

(All  $t = 4$ -Momentum Transfer)

	$50 \leq E_T < 70$ Gev	$70 \leq E_T < 90$ Gev	$90 \leq E_T < 127$ Gev
a) $E_F/E_T < 70\%$	4.8%	6.9%	9.8%
b) no R latched	22.3%	22.3%	22.3%
a) + b)	25.3%	26.5%	28.3%
c) $E_F/E_T < 85\%$	5.3%	1.9%	2.3%
d) $ \Delta  > 1$	12.5%	6.7%	3.1%
c) + d)	14.5%	8.2%	5.3%
e) $m_F^2 > 1$ , or $m_F^2 < .3$	21.8%	16.6%	10.5%
c) + d) + e)	36.3%	24.8%	15.8%
f) $E_F/E_T < 90\%$	0.5%	0.8%	1.7%
g) no track found	7.1%	9.7%	11.2%
Total Losses	69.1%	61.6%	56.7%
Total Correction	3.23	2.60	2.33

Figure 7.9. Incident Photon Flux vs. Photon Energy

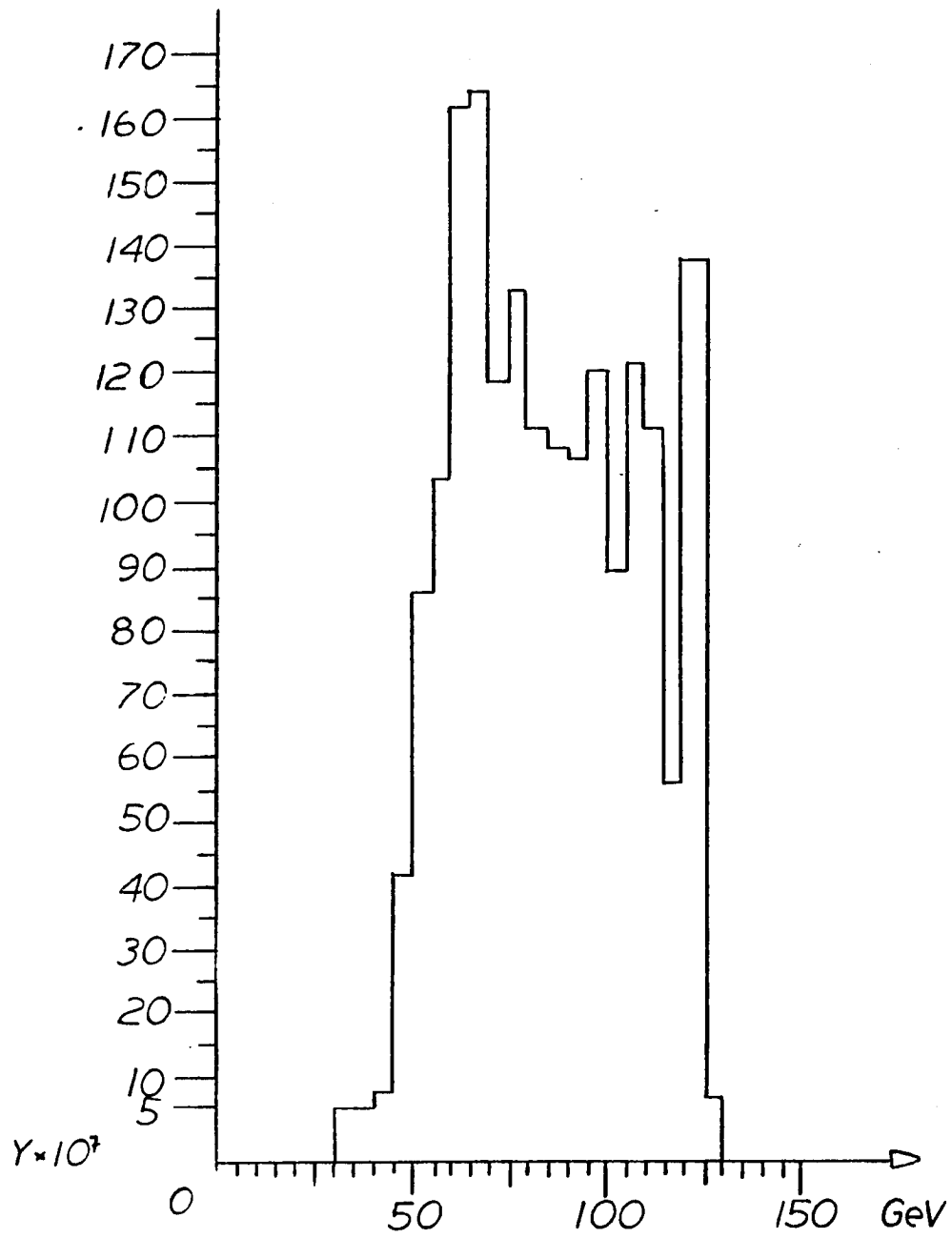
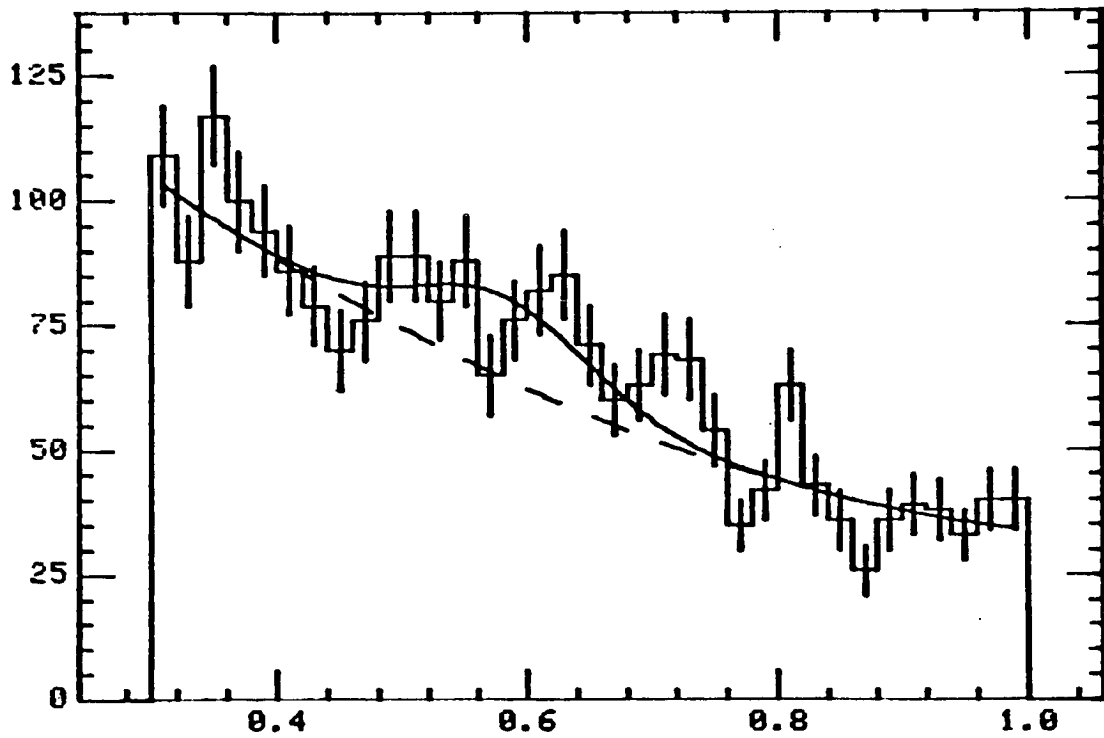


Figure 7.10.  $m_F^2$  Distribution for fitted  $\gamma p \rightarrow \omega p$  Events  
Rejected by any of the Cuts of Section 7C



$$164_{-69}^{+72} \text{ (rejected) } \gamma p \rightarrow \omega p \text{ events} \quad (\chi_R^2 = 1.5)$$

A correction factor  $(324 + 164 = 488)$

$$\frac{488}{324} \pm .3 = 1.51 \pm .3$$

has to be therefore applied to our raw yield. The branching ratio for the  $\omega \rightarrow \pi^0 \gamma$  ( $\pi^0 \rightarrow \gamma \gamma$ ) decay mode is 8.8%. This introduces a correction factor  $(.088)^{-1} = 11.36$ .

Electron-proton pair production in the target attenuates our beam by about 5%. This introduces a correction factor 1.05.

From the flux partial totals and the correction factors of table 2 in the three energy bins mentioned above we obtain an overall detection efficiency correction factor

$$(3.23 \cdot 0.56 + 2.60 \cdot 0.47 + 2.33 \cdot 0.75)/1.78 = 2.69.$$

We measure therefore an exclusive omega photoproduction cross section of  $\sigma = 324 \text{ events} \cdot (1.51 \cdot 11.36 \cdot 1.05 \cdot 2.69)/56 \text{ events/nbarn} \approx .280 \mu\text{barn}$ .

We disagree by about a factor 4 with the measurement of reference 11) yielding a value of about 1  $\mu\text{b}$  for  $(\gamma p \rightarrow \omega p)$ . This casts some doubts on our flux and detection efficiency estimates.

Our sample of 1173 events surviving all the cuts is divided in the 6 t bins of table 1. Fits to a gaussian omega peak above a quadratic background yield the following values (fig. 7.11a through 7.11f)



Figure 7.11a.  $m_F^2$  Distribution for Events Surviving all the Cuts  
( $0.00 \leq t \leq 0.007 \text{ GeV}^2$ )

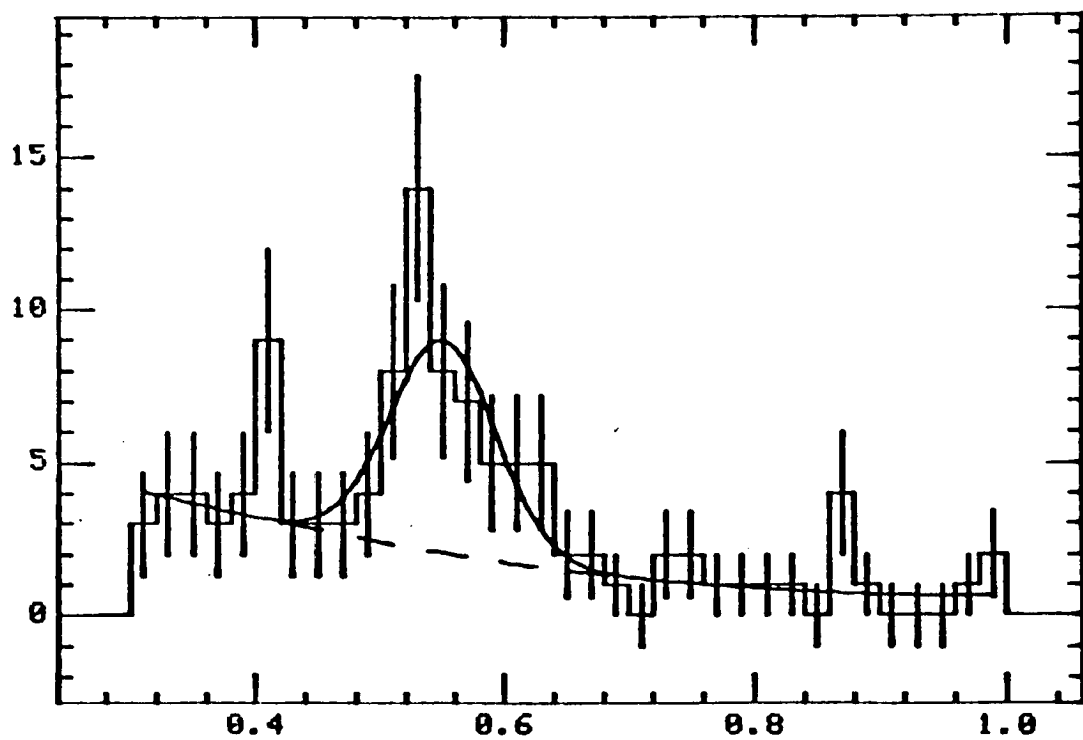


Figure 7.11b.  $m_F^2$  Distribution for Events Surviving all the Cuts  
( $0.07 \leq t \leq 0.14 \text{ GeV}^2$ )

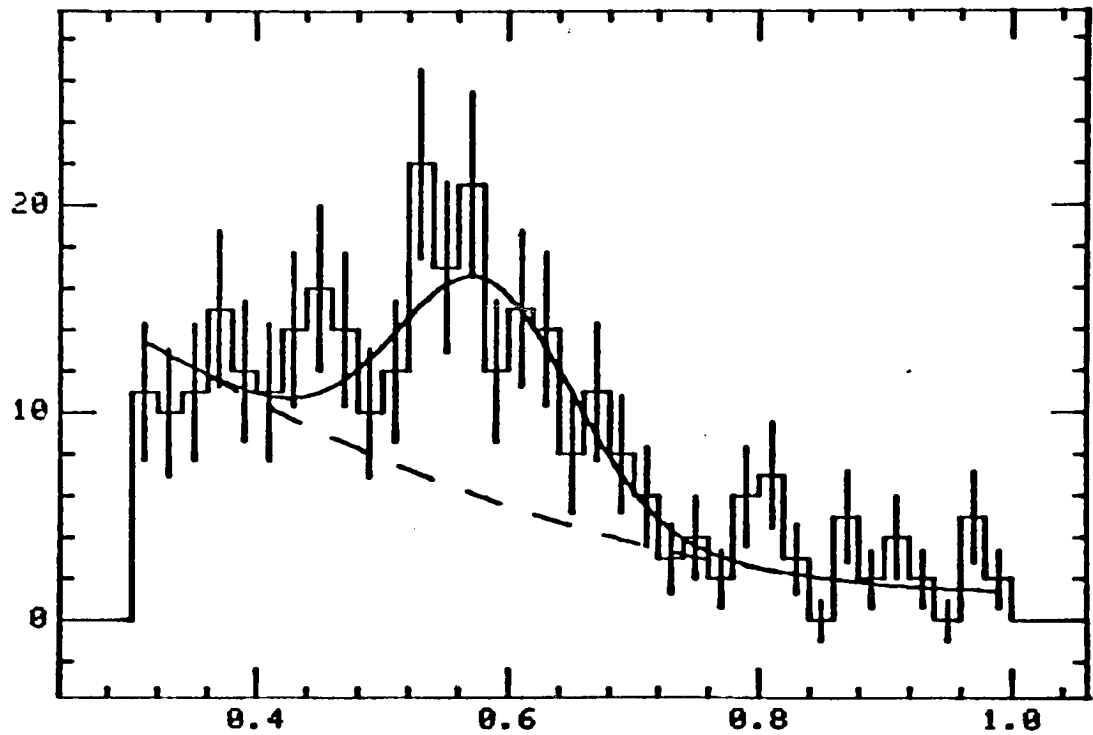


Figure 7.11c.  $m_F^2$  Distribution for Events Surviving all the Cuts  
( $0.14 \leq t \leq 0.20 \text{ GeV}^2$ )

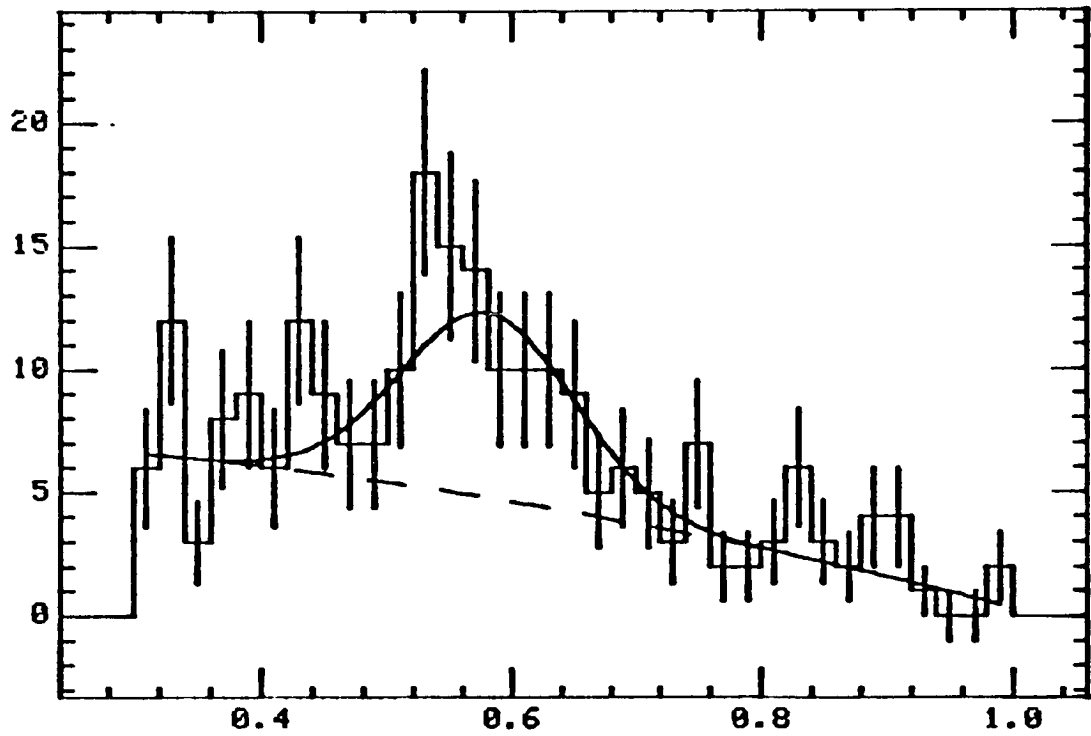


Figure 7.11d.  $m_F^2$  Distribution for Events Surviving all the Cuts  
( $0.20 \leq t \leq 0.30 \text{ GeV}^2$ )

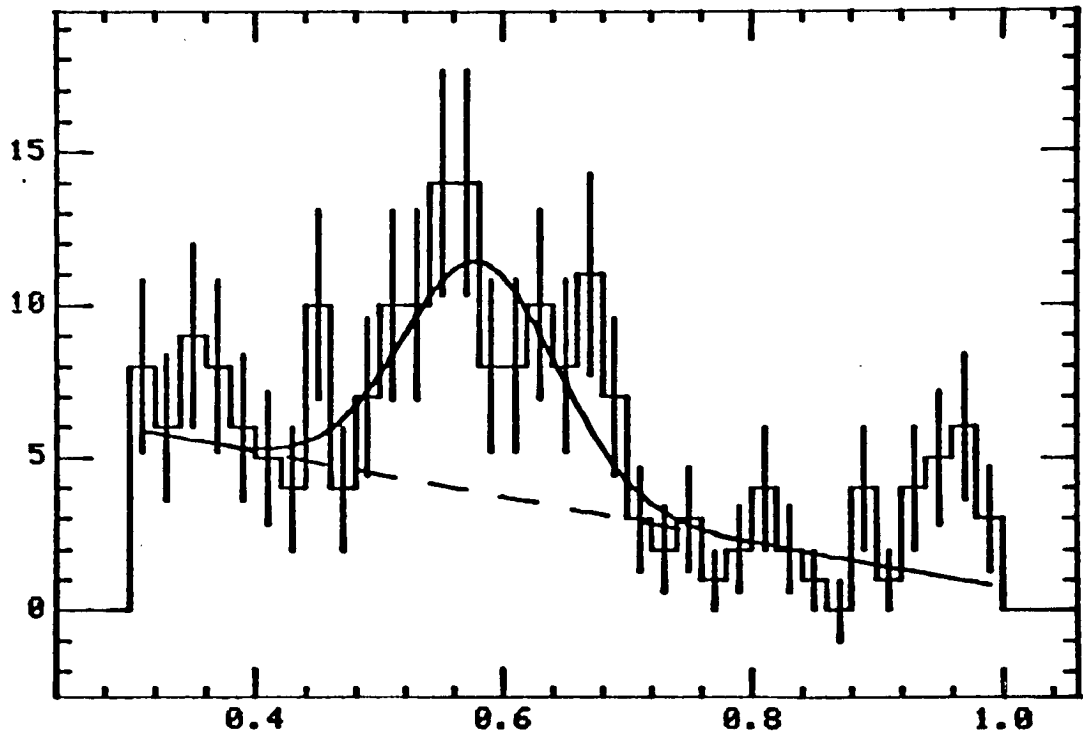


Figure 7.11e.  $m_F^2$  Distribution for Events Surviving all the Cuts  
( $0.30 \leq t \leq 0.50 \text{ GeV}^2$ )

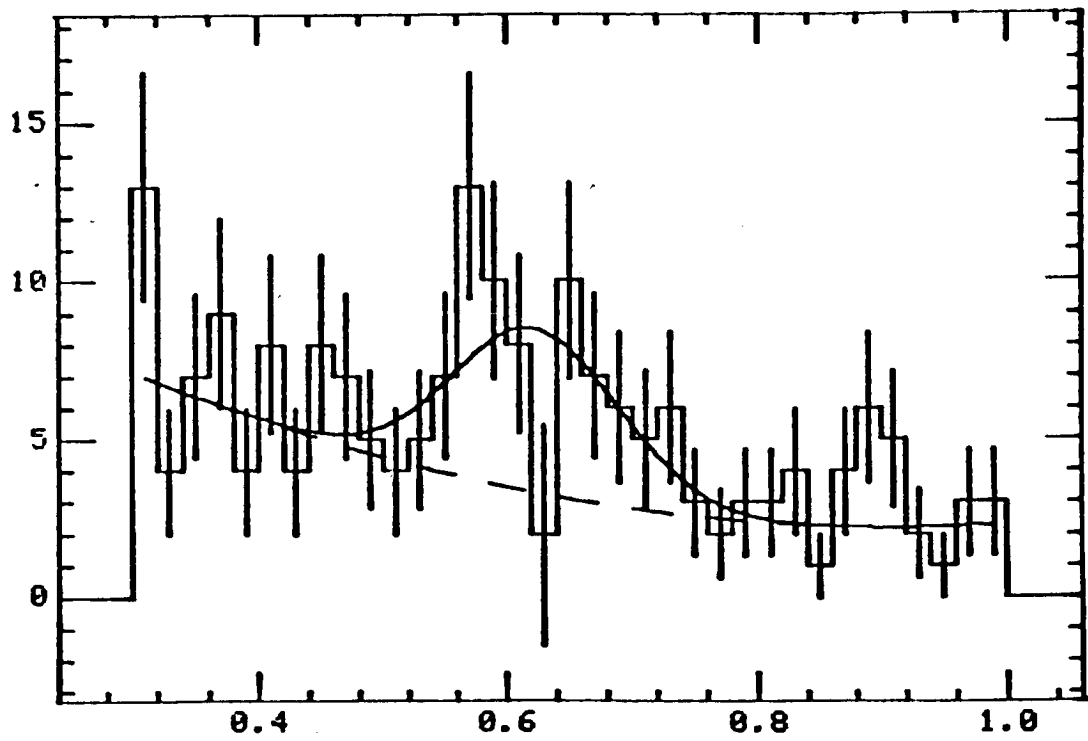
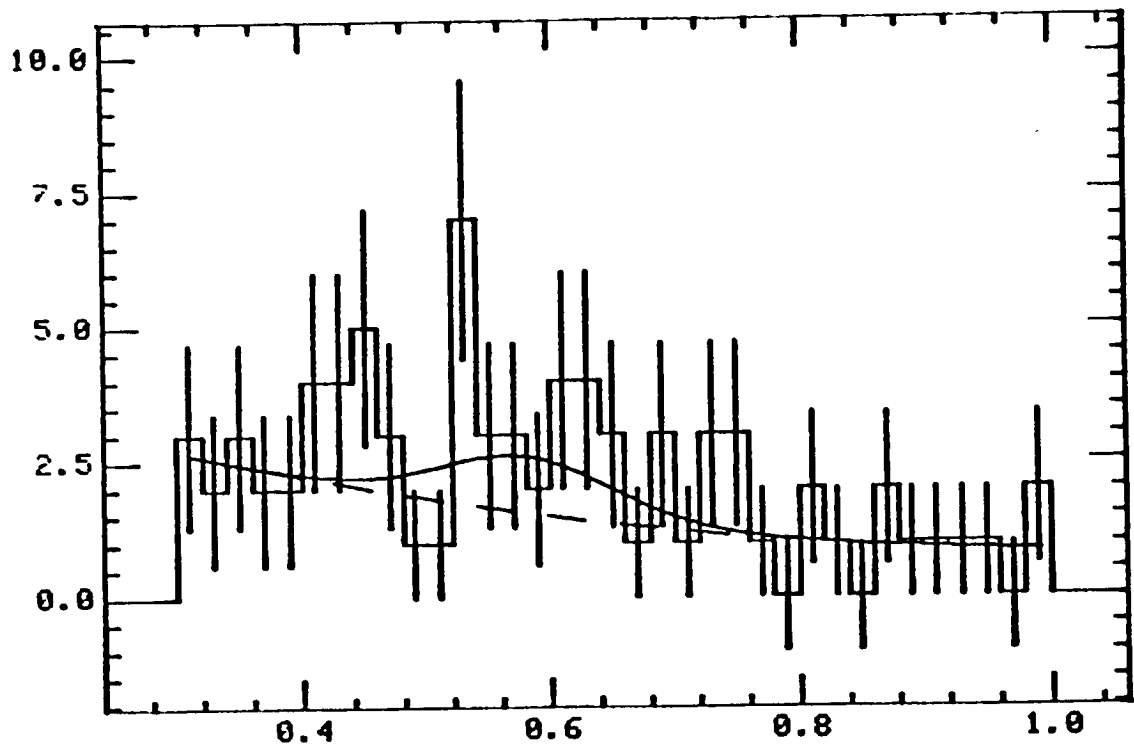


Figure 7.11f.  $m_F^2$  Distribution for Events Surviving all the Cuts  
( $0.50 \leq t \leq 0.85 \text{GeV}^2$ )



<u>t range</u>	<u><math>\Delta N</math></u>	<u><math>\Delta N/\Delta t</math></u>	<u><math>(\Delta N/\Delta t)_{\text{CORR}}</math></u>
0 $\leq t \leq$ 0.07	36 $\pm$ 10 events	$\sim$ 514	$\sim$ 3672
0.07 $\leq t \leq$ 0.14	103 $\pm$ 25 events	$\sim$ 1471	$\sim$ 4664
0-14 $\leq t \leq$ .020	59 $\pm$ 20 events	$\sim$ 983	$\sim$ 3119
0.20 $\leq t \leq$ .030	58 $\pm$ 14 events	$\sim$ 580	$\sim$ 1840
0.30 $\leq t \leq$ 0.50	42 $\pm$ 23 events	$\sim$ 210	$\sim$ 688
0.50 $\leq t \leq$ 0.85	9 $\pm$ 8 events	$\sim$ 26	$\sim$ 82

If we apply to the third column the correction factor  $1.51 \cdot 1.05$  from cut losses and beam attenuation losses and use the detection efficiency correction factors of table 1, we obtain the  $(\Delta N/\Delta t)_{\text{CORR}}$ . The first t bin has too low a value. The estimate of our detection efficiency in that range, most likely, is incorrect. The absence of multiple scattering effects in the Monte Carlo calculation of the detection efficiency is one candidate reason for a serious overestimate of our efficiency at low t. If we drop the first point in a  $d\sigma/dt$  plot, we obtain fig. 7.12. The differential cross section shows an exponential fall-off with a slope

$$b = 8.00 \pm 2.1 \text{ Gev}^2.$$

Our sample of 1173 events was also binned in three energy bins. Gaussian fits above a quadratic background yield (fig. 7.13a,b,c)

52 $\leq E_T \leq$ 70	45 $\pm$ 15 events	$\sim$ 260 $10^{-10}$ events/photon
70 $\leq E_T \leq$ 90	127 $\pm$ 17 events	$\sim$ 699 $10^{-10}$ events/photon
90 $\leq E_T \leq$ 127	157 $\pm$ 36 events	$\sim$ 490 $10^{-10}$ events/photon

Figure 7.12. Differential Cross Section for  $\gamma p \rightarrow \omega p$  -  $d\sigma/dt = Ae^{-bt}$   
with  $b = 8.00 \pm 2.1$ .

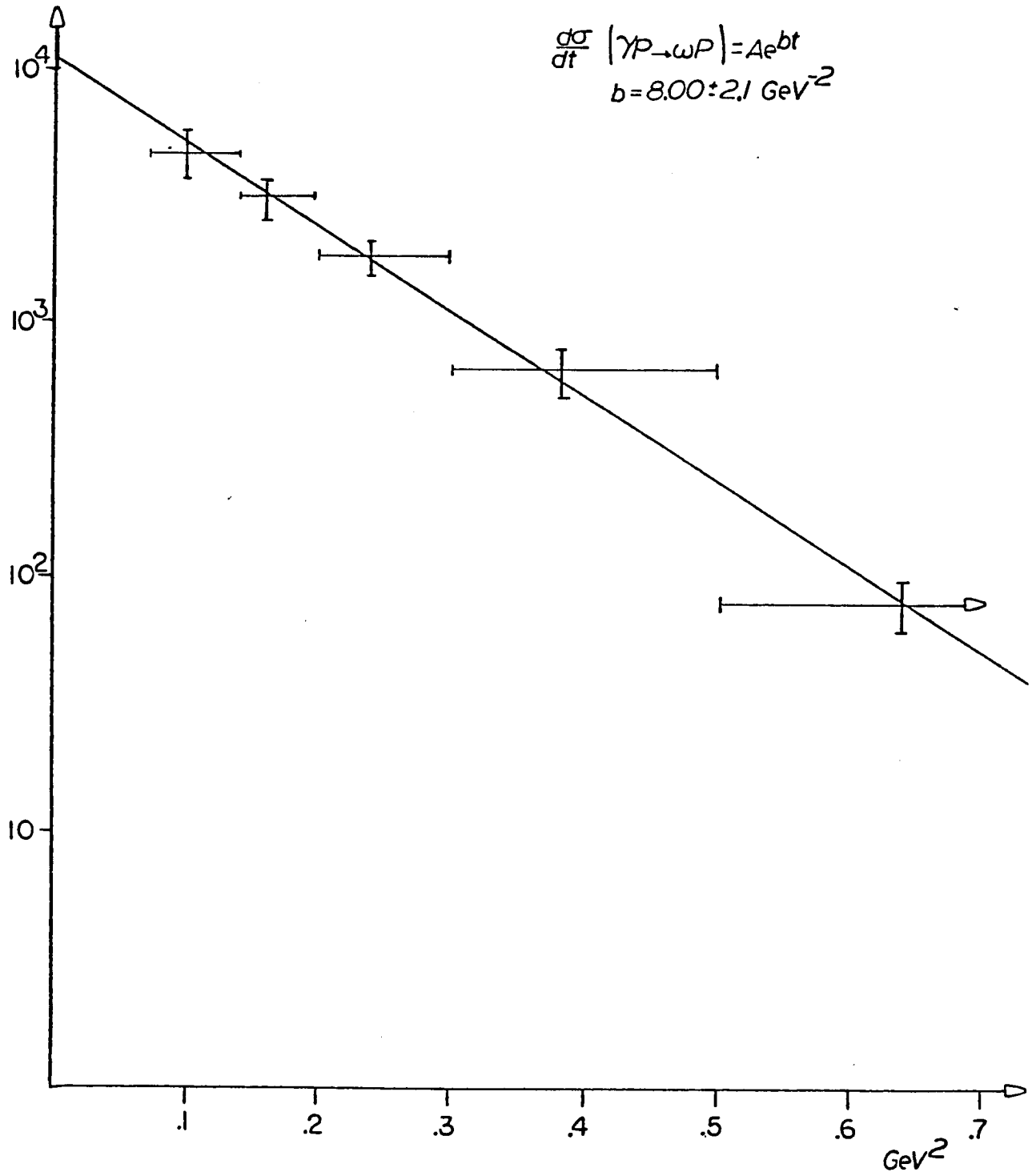




Figure 7.13a.  $m_F^2$  Distribution for Events Surviving all the Cuts  
( $52 \text{ GeV} \leq E_T \leq 70 \text{ GeV}$ )

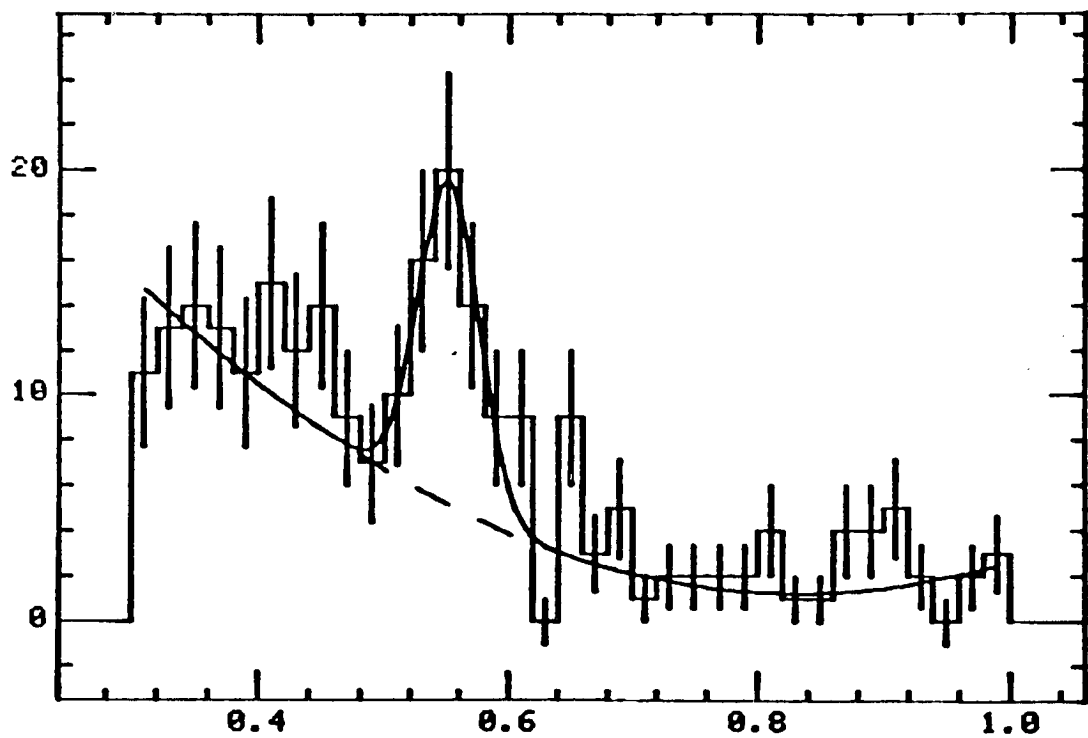


Figure 7.13b.  $m_F^2$  Distribution for Events Surviving all the Cuts  
( $70 \text{ GeV} \leq E_T \leq 90 \text{ GeV}$ )

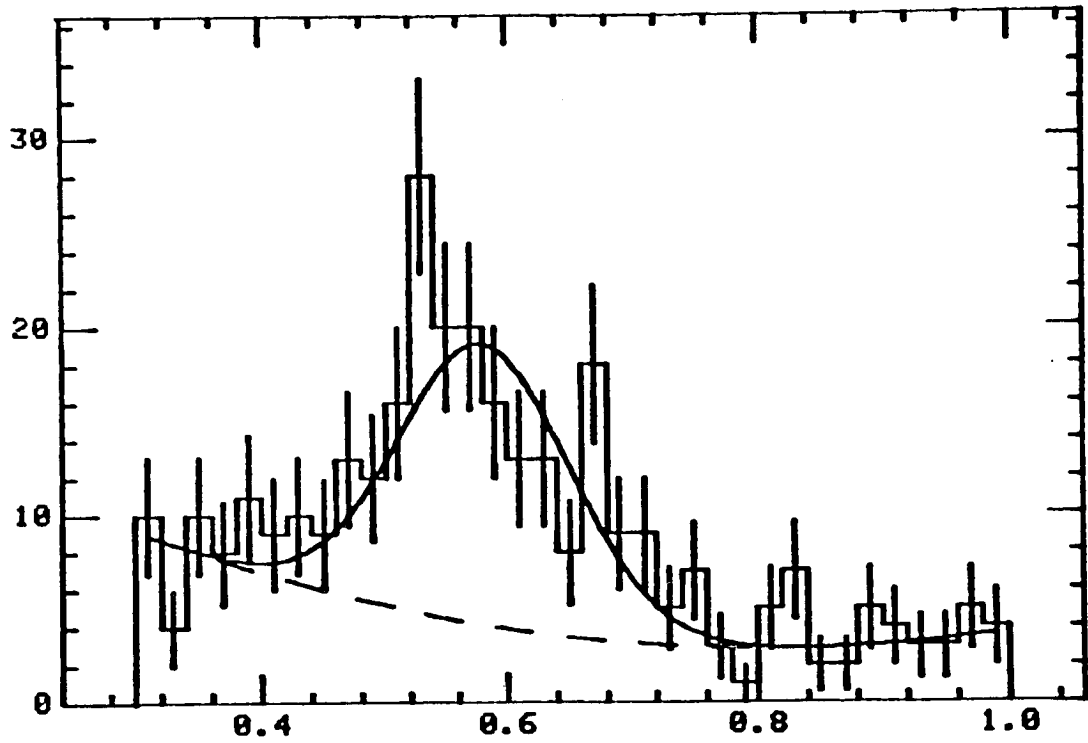
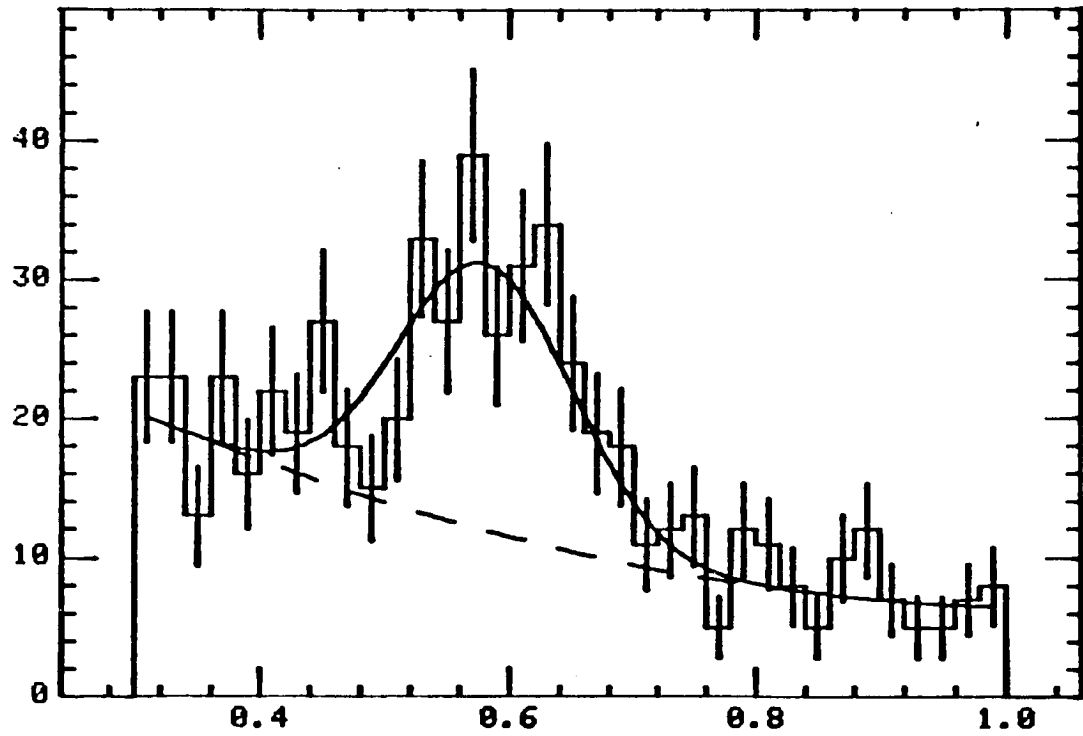


Figure 7.13c.  $m_F^2$  Distribution for Events Surviving all the Cuts  
( $90 \text{ GeV} \leq E_T \leq 127 \text{ GeV}$ )



Using the flux partial totals and the efficiency correction factors of table 2 for the three energy bins, we obtain the values in the third column. The dependence of the rate on the incident photon energy is expected to be flat in this energy region. Once again this result seems to point to the lack of understanding of our detection efficiency corrections, and of its dependence on incoming photon energy.

	Page
APPENDIX A. THE RECOIL DRIFT CHAMBERS	
A1. Mechanical Characteristics of the Chambers	A1
A2. Electrical Characteristics of the Chambers	A5
A3. Choice and Properties of the Gas Mixture	A9
A4. Recoil Cart Geometry	A21
A5. Track Fitting Algorithm	A25
A6. Angle Track Correction	A31
A7. Alignment Procedure	A33
A) Relative Alignment of Modules in a Quadrant	A33
B) Alternative Formalism for Relative Alignment in a Quadrant	A41
C) Relative Alignment of Quadrants	A42
D) Estimate of the Beam Axis Parameters	A47
A8. Pattern Recognition and Left-Right Ambiguity Resolution	A48

## APPENDIX A

## THE RECOIL DRIFT CHAMBERS

## A1. Mechanical Characteristics of the Chambers

Each quadrant of drift chambers consists of two separate modules. Each module contains four drift planes contained in the same case. The two modules in a quadrant differ only in size. We will describe now in some detail the design of the small module.

Each module of chambers can be thought of as a parallelepiped (fig. A.1a) of dimensions 6 cm  $\times$  48 cm  $\times$  80 cm (6 cm  $\times$  96 cm  $\times$  96 cm for the big modules). Its volume is filled with gas. Sense wires are strung across its volume in four planes spaced by about 2 cm. The bottom surface of the parallelepiped is the first plane of sense wires. To each module  $i$  ( $i = 1, 2$ ) in each quadrant  $Q$  ( $Q = 1, 4$ ) we associate an orthogonal reference frame ("module" frame)  $R_i^Q$  with its origin at one of the vertices of the parallelepiped in the bottom plane of wires (fig. 5.2). The  $j$ -th plane of sense wires ( $j = 1, 4$ ) is described, in this frame, by the equation

$$z = (j-1)\Delta$$

where  $\Delta$  is the interplane separation. Wires are strung at different angles with respect to the  $y$  axis of the module frame. These angles are respectively  $90^\circ$ ,  $0^\circ$ ,  $72^\circ$ ,  $108^\circ$ . The equations of the  $k$ -th sense wire in the  $j$ -th plane will be of the form

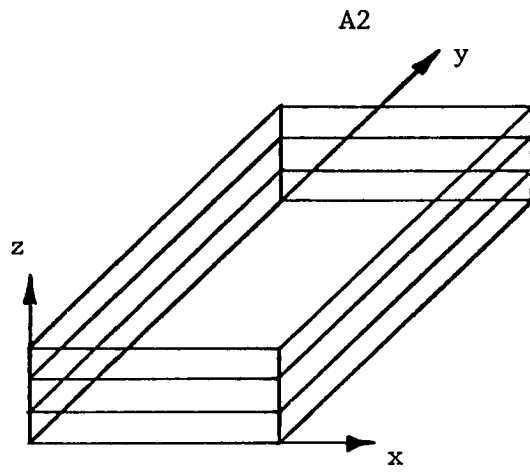


Figure A.1a. Schematic of a (Small) Drift Chamber Module

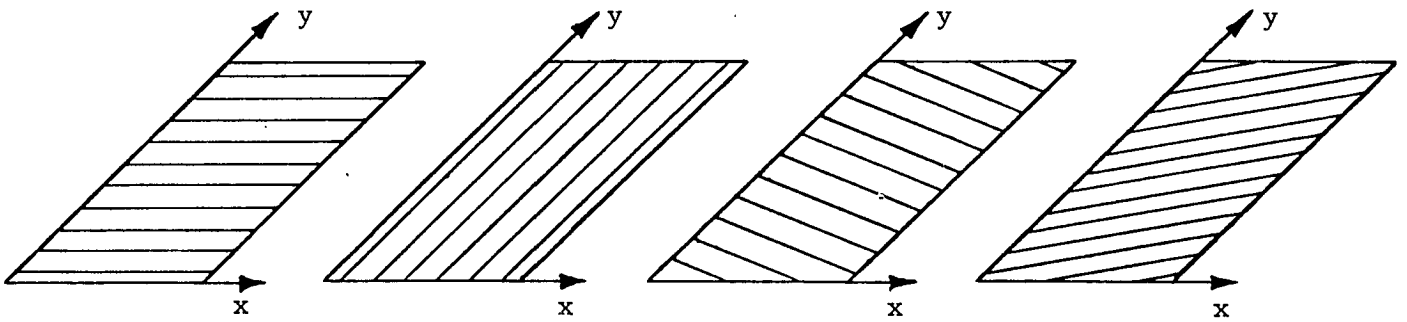


Figure A.1b. The Four Planes of Drift Wires in a Module

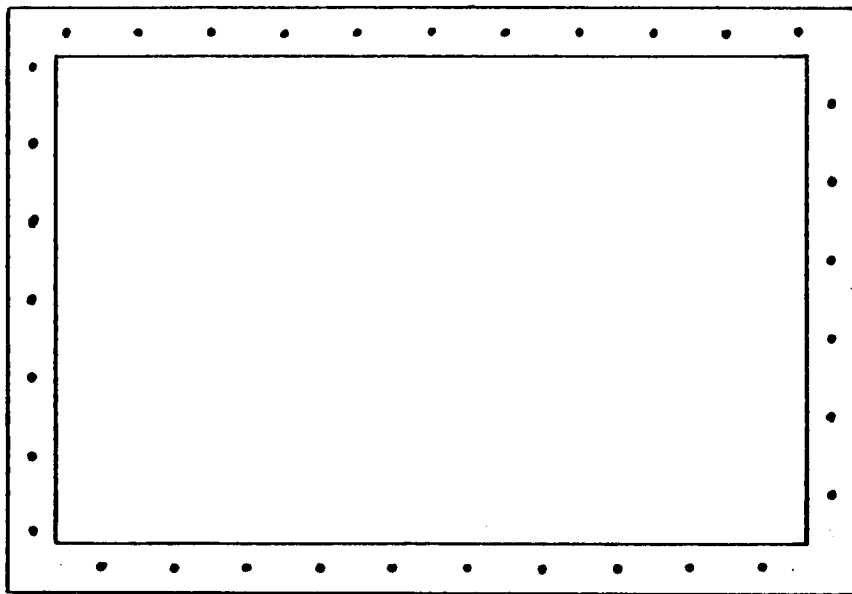


Figure A.1c. Schematic of an Epoxy-Glass (G10) Frame With Precision Machined Fiducial Holes

$$z = (j-1)\Delta \quad (A1.1)$$

$$\alpha_j x + \beta_j y = w_k$$

where (fig. A.1b)

$(\alpha, \beta) = (0, 1)$	for the $90^\circ$ plane ( $j=1$ )	containing 10 sense wires	(12 in big module)
$(1, 0)$	$0^\circ$	( $J=2$ )	6 (12 " )
$(\cos\phi, -\sin\phi)$	$72^\circ$	( $J=3$ )	11 (15 )
$(\cos\phi, \sin\phi)$	$108^\circ$	( $J=4$ )	11 (15 )

and  $\phi = \cos^{-1}(38/40) \approx 72^\circ$ .

A hit recorded on a sense wire will signal the possibility of a charged particle having crossed the sense plane anywhere along one of the two lines (fig. 3.10) parallel to the sense wire at a distance equal to the drift space (the measured drift time times the known drift velocity). The ambiguity in between these two lines is referred to as the right-left ambiguity.

The separation of sense wires is  $w_k - w_{k-1} = 8$  cm for  $90^\circ$  and  $0^\circ$  planes and  $w_k - w_{k-1} = 7.6$  cm for  $72^\circ$  and  $108^\circ$  planes. Drift lengths are therefore respectively 4.0 cm and 3.8 cm.

Each sense frame was built out of two layers of G-10 (epoxy-glass). Both of them had fiducial holes precision machined through them (fig. A.1c). The bottom layer had slots machined with reference to the fiducial holes. Brass tubes were glued inside these slots. The bottom and top layer were glued together and the gold plated tungsten sense wires (20  $\mu$ m radius) were strung through the tubes at a fixed tension (2 oz) and soldered to them. The same procedure was followed for the



thicker (125  $\mu\text{m}$  radius) copper-beryllium field wires that separate the drift cells from each other.

In addition to four sense frames, each module contains eight field shaping frames and three isolation frames. All these frames are also built out of G-10. The wires on these frames are wound (by a winding machine) at a distance of 2 mm from each other.

Each sense frame is sandwiched in between two field shaping frames with wires (copper-beryllium, 125  $\mu\text{m}$  radius) wound parallel to the sense wires. These wires will provide the electric field gradient for the drift of the electrons in the cell. Field shaping wires were glued to their frames after being wound at a fixed tension (8 oz).

In between each pair of drift gaps (i.e., a triplet of field shaping-sense-field shaping frames) an "isolation" frame was inserted, with the usual copper-beryllium wire wound (2 mm apart from each other) and glued on it. These frames electrostatically decouple adjacent drift gaps. The winding angles are, respectively,  $45^\circ$ ,  $135^\circ$ ,  $0^\circ$  for the  $90^\circ - 0^\circ$ ,  $0^\circ - 72^\circ$ ,  $72^\circ - 108^\circ$  separators).

These fifteen G-10 frames in each module are stacked on top of each other; some are glued together, others are stacked (with a gasket in between to provide a gas seal). Gaskets are used instead of gluing, in order to guarantee access to each plane of sense wires for wire replacement. The stacking of the various frames is such that the fiducial holes in each frame fall on top of each other. A lexan plastic tube containing a stainless steel bolt goes through each fiducial hole. Fiducial pins are attached to these bolts. A team of surveyors at Fermilab measured for us the position of these pins in the laboratory

frame. The equations of all the sense wires are known with reference to these pins.

At the end of datataking, the chambers were disassembled and the positions and orientations of all the wires with respect to the fiducial pins were measured in the Fermilab alignment workshop.

## A2. Electrical Characteristics of the Chambers

A typical drift cell was described in the main text (fig. 3.12). Positive high voltages (+HV = 2.4kV) are fed separately to each plane of sense wires. A high voltage bus runs (fig. A.2a) one side of the G-10 frame and all the sense wires are connected to it by a  $5 \text{ k}\Omega$  resistor. These resistors decouple the various sense wires from each other. The pulse induced on a sense wire by the passage of a charged particle travels in both directions along the wire. The resistance of the wire is small with respect to the decoupling resistor; most of the pulse travels away from the bus line. A high voltage capacitor (1 nf) at the other end of the wire filters out the +HV level, the small pulses (a few mV's) induced by the ionization travel on a coaxial cable to a connector on the outside case of the module of chambers. Longer coaxial cables (about 10 meters) transport these pulses to a rack of electronics outside the environmental house containing the entire recoil detector.

Each sense wire is equipped with three sequential circuits (fig. A.3). The first (receiver) is basically an impedance matcher; it has an output impedance of about  $1 \text{ k}\Omega$ , matching the input impedance of the following circuit, which is an amplifier-shaper circuit. This circuit was designed and built at MIT, originally for multiwire proportional chambers, and has

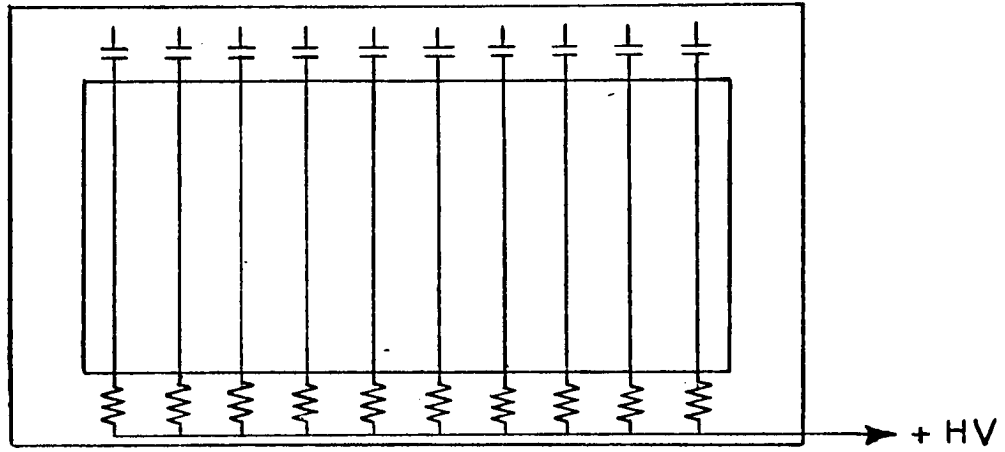


Figure A.2a. Positive High Voltage Distribution (on a  $90^\circ$  Sense Frame)

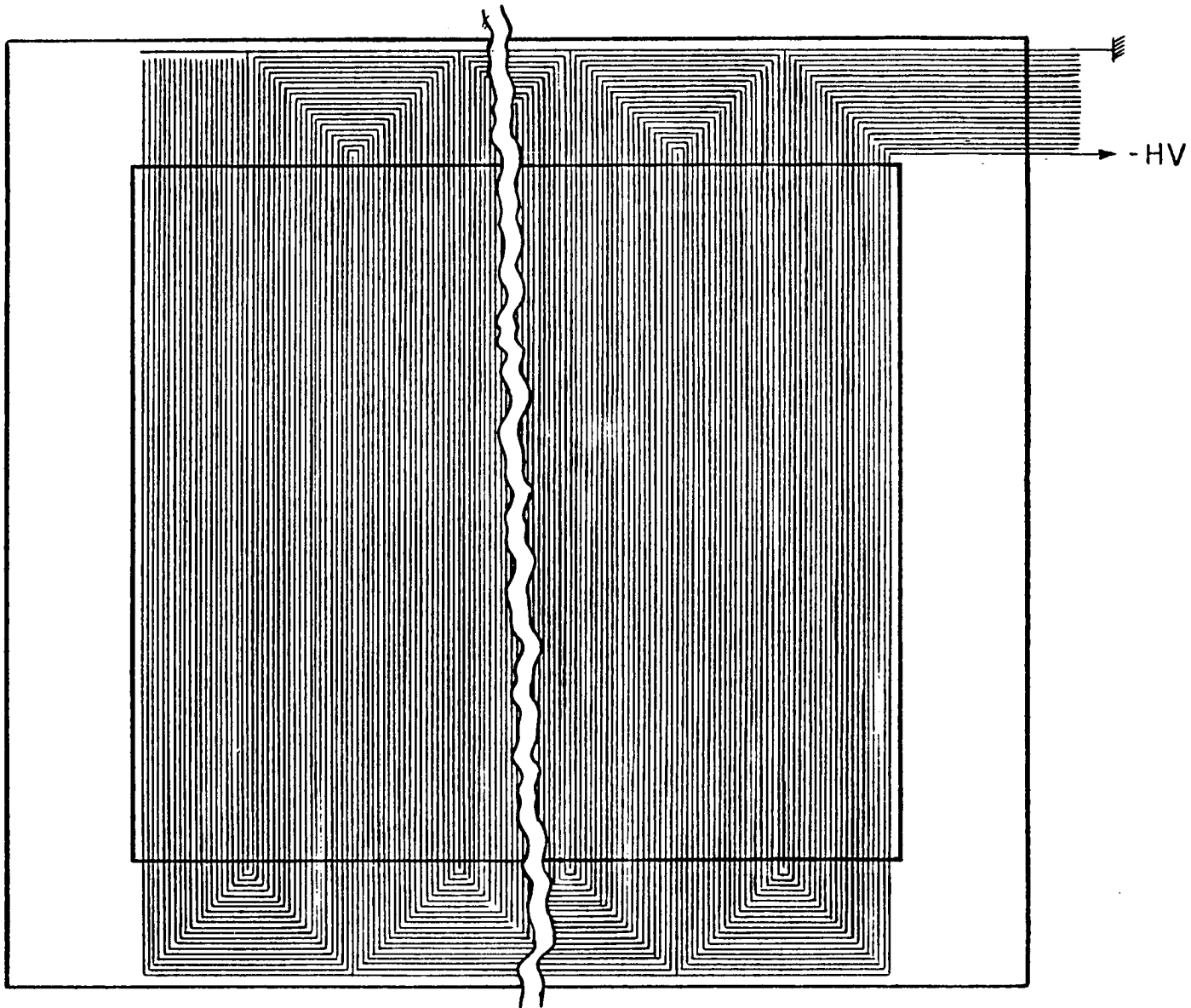
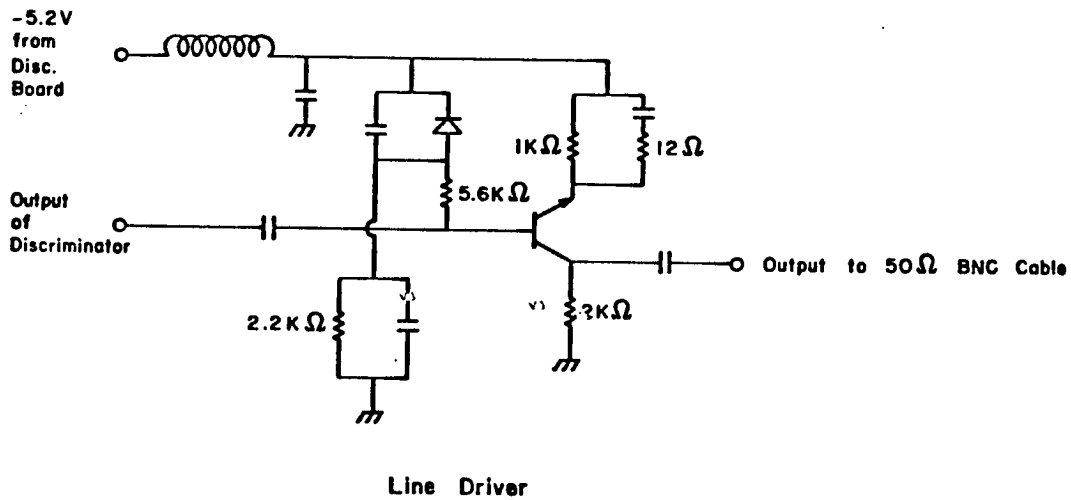
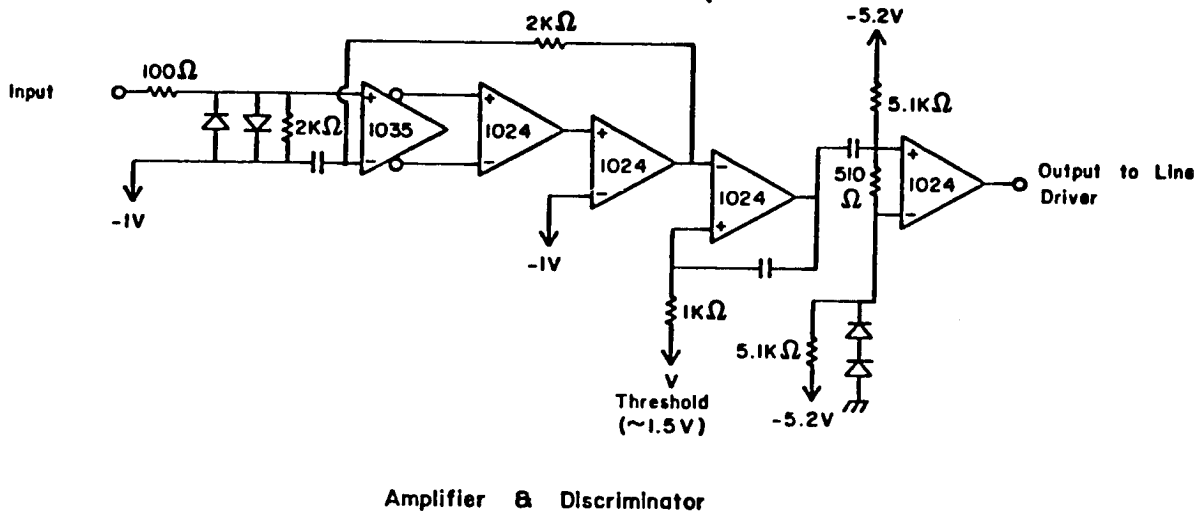
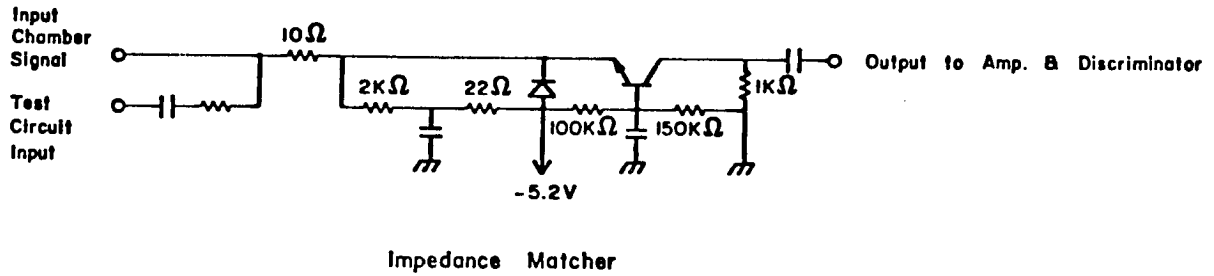


Figure A.2b. Negative High Voltage Distribution (on a  $90^\circ$  Field-Shaping Frame)

Figure A.3.

Drift Chamber Amplifier and Discriminator Circuitry



been used by several Fermilab experiments in the last few years. About 500 channels were made available to us. The pulses provided by these amplifiers (600 mV logic levels) are fed to a line driver circuit that raises their level to about 2 volts. This is necessary in order to overcome the inevitable deterioration of pulse height and risetime in the 60 meters of cable that connect the electronics on the experimental floor to the CAMAC time digitizers in the counting room.

The TDC circuit was designed by Dr. T. Droege at Fermilab and made available to users through the FNAL electronics pool (PREP). Each unit has eight channels, to service eight sense wires. Each channel provides a CAMAC word. The right-most 8 bits contain the (digitized) measurement of the time interval between a start pulse (from the wire) and a stop pulse (the event trigger, delayed by about 1  $\mu$ s). The left-most 8 bits contain the CAMAC station (1 through 23) and substation (0 through 7) information, necessary to identify the wire. An array of CAMAC words, to be decoded,

CAMAC word  $\rightarrow$  (wire number, drift time)

is the input to the track reconstruction program. Only wires which are hit are read in by the computer.

Field shaping wires have to be fed uniformly decreasing negative high voltage levels from the edge to the center of each drift cell. Negative high voltage ( $-HV \approx 5$  KV) is fed separately to each pair of field shaping planes sandwiching a sense frame. A resistor chain of 20  $10$  M $\Omega$  resistors creates 20 uniformly spaced voltage levels. These levels are distributed to all the copper-beryllium wires in the field shaping frame through a printed circuit board glued to the frame.

Fig. A.2b illustrates the role of this PC board. Surface stray currents develop on these PC boards if they are not perfectly clean and perfectly dry. The surface resistivity can be very low in a humid environment. These stray currents destroy the uniformity of the voltage level spacings. The chambers were built in special clean rooms and the PC boards coated after final clean-up. The environmental house containing the recoil detector maintained a very low humidity level for the good operation of the chambers throughout the duration of the experiment. All the wires of an isolation frame are held at the same negative voltage level, chosen to be about -2.5 kV.

### A3. Choice and Properties of the Gas Mixture

Among the desirable properties for the gas to be used for drift chambers are saturation of the drift velocity and minimal diffusion of the electrons in the gas. Experimental work<sup>24)</sup> on the optimization of the gas mixtures and attempts<sup>25)</sup> at qualitative and quantitative understanding of these mixtures in the framework of the classical theory of electrons in gases, both suggest the use of mixtures of some noble gas and a moderate (20-40%) percentage of some polyatomic organic gas-like methane, isobutane, etc. Polyatomic gases have been intensively used in MWPC mixtures<sup>26)</sup> as quenching agents. In the case of drift chambers, they also play the role of cooling down the electrons' temperature, lowering their diffusion and providing high spatial resolution. Besides, some of these mixtures exhibit a flat or a very slowly changing dependence of drift velocity on the applied electric field, which commonly is referred to as drift velocity saturation.

Fig. A.4 shows the data<sup>24,27)</sup> for drift velocities in some pure gases and in several mixtures of argon-isobutane. Argon-isobutane mixtures have been used by many groups, following the pioneering work of Charpak et al. at CERN. The general features of these data can be described<sup>25,28)</sup> by solving numerically the Boltzmann transport equation for electrons in a gas. Qualitative arguments can be made also. If we assume that the mean free path,  $\ell_e$ , for electron-gas molecule collisions and the mean fractional energy loss per collision,  $\Lambda$ , depend on the electron energy  $\epsilon$  via power laws

$$\Lambda(\epsilon) = \Lambda_0 \epsilon^m,$$

$$\ell_e(\epsilon) = \ell_0 \epsilon^{-n}, \quad (\text{implying } \sigma_e \sim 1/\ell_e \sim \epsilon^n),$$

it can be shown that the dependence of the drift velocity  $w$  on the electric field  $E$  is

$$w \sim E^{m+1/m+2n+2}.$$

Therefore,  $w$  will rise slowly if  $\sigma_e$  rises rapidly or if  $\Lambda$  decreases with  $\epsilon$  ( $-1 < m < 0$ ). If  $m \leq -1$ ,  $w$  will even decrease. Drift velocities in noble gases (Ar, Kr, Xe) can be described in this simple way over several orders of magnitude<sup>25,28)</sup>. In particular, the slow rise of  $w$  in fig. A.4 is due to the fast rise of  $\sigma_e$  after the "Raumsauer dip"<sup>28)</sup> at  $\epsilon = 0.3$  eV (fig. A.5). For polyatomic gases, saturation of  $w$  (at some higher field than Ar) occurs because of an effective  $\Lambda \sim \epsilon_{\max}/\epsilon$  ( $m \approx -1$ ) at energies above the last significant vibrational energy level. As far as mixtures are concerned, the mechanism proposed in ref. 25) to understand the data is the following: Let us add to argon a hypothetical polyatomic gas, X, of

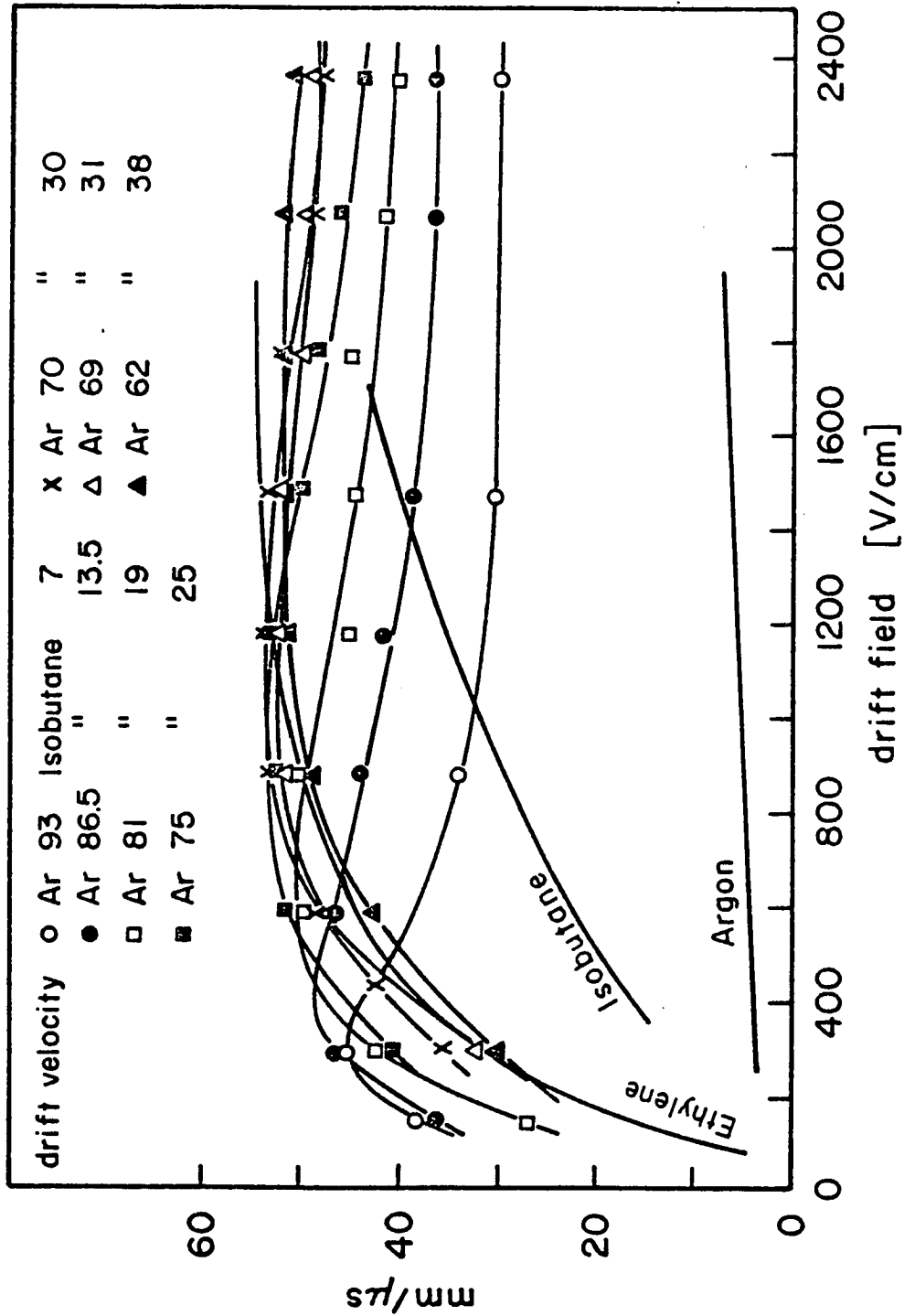
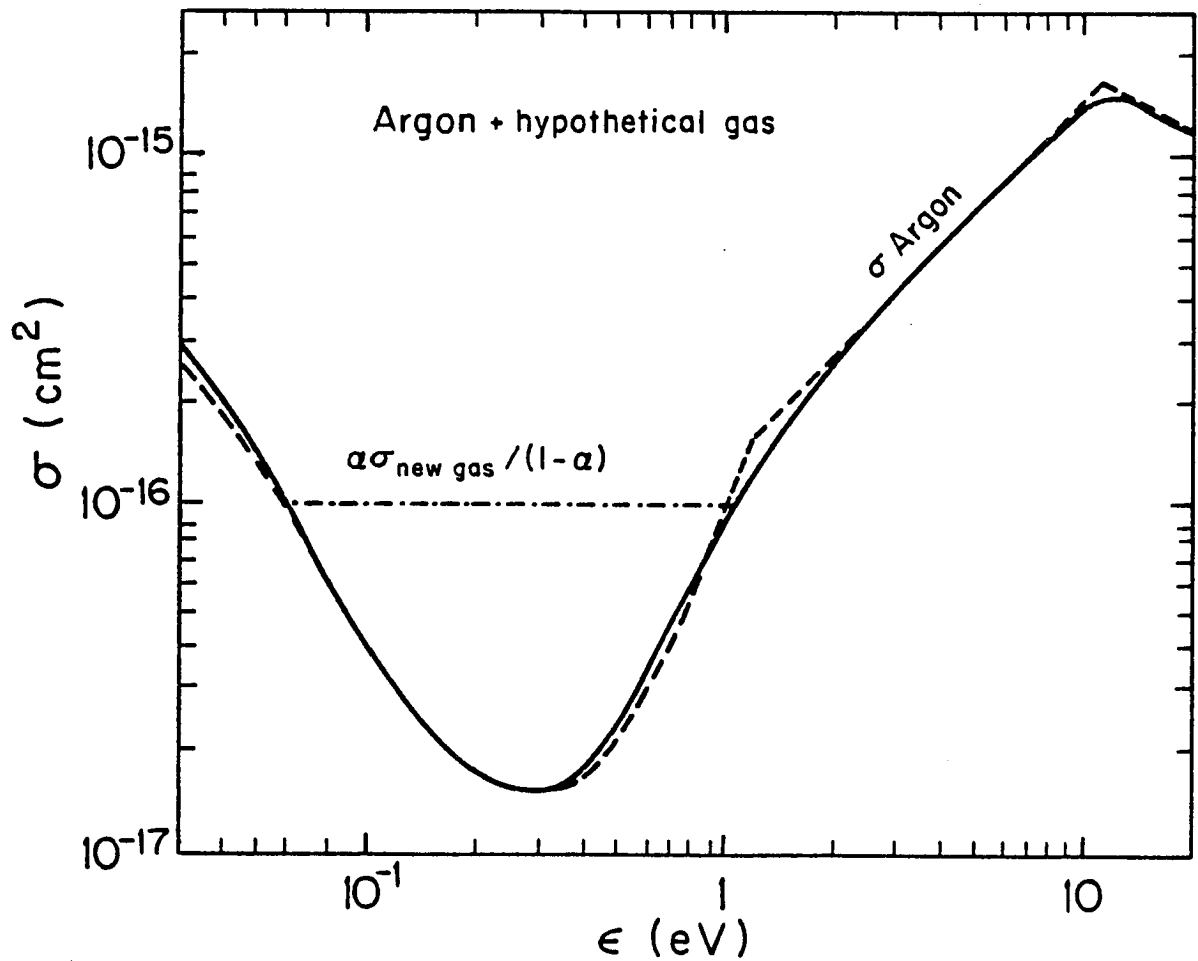


Figure A.4. Drift Velocity vs. Electric Field for Argon, Ethylene, Isobutane and Several Argon-Isobutane Mixtures.



Figure A.5. Momentum Transfer Cross Sections for Electrons in Argon. Notice the Ramsauer dip at 0.3 eV for the electron energy. The dotted line is a fit made for numerical applications. The dashed-dotted line shows the contribution of the new gas [its ratio to Argon is  $\alpha/(1-\alpha)$ ] to the cross section in the energy region where it dominates.



roughly constant  $\sigma_e$  and  $\Lambda$  (at least before the onset of the  $\Lambda \sim \epsilon^{-1}$  behavior). The cross section will be  $\sigma = (1-\alpha)\sigma_{Ar} + \alpha\sigma_x$  (where  $\alpha$  is the concentration of gas X). Because of the Ramsauer dip, the gas X will dominate for small  $\epsilon$ ,  $m \approx n \approx 0$ , and  $w$  will rise with  $E$ ; this will last until  $(1-\alpha)\sigma_{Ar}$  becomes comparable with  $\alpha\sigma_x$ . From this energy on,  $\lambda_e$  and  $\Lambda$  will decrease (the collisions being increasingly dominated by elastic scattering off argon atoms, with very little energy loss), and the drift velocity will level off. However, if  $\alpha$  is too big, this will never happen, and the advantages of the mixture will be lost. The drift velocity will saturate only at higher fields, due to the mentioned  $\Lambda \sim \epsilon^{-1}$  behavior of the polyatomic gas itself.

We started a program investigating the properties of argon-ethylene ( $C_2H_4$ ) mixtures;  $C_2H_4$  saturates its own drift velocity earlier than the more commonly used isobutane (fig. A.4), so that a longer drift length (4 cm) can be used with a reasonably low negative voltage applied to the drift cells of the chambers. For this investigation, we used a small drift chamber with electrical design identical to the one to be used later for the larger chambers used in the experiment. We used particles originating from a collimated  $^{90}Ru$  source. A scintillation counter gave the start signal, the drift chamber pulse gave the stop signal after being shaped by an amplifier and discriminator. This time interval was digitized by a LRS TDC unit.

Fig. A.6 shows the results of our investigation. For low  $C_2H_4$ -Ar ratios  $[R = \alpha/(1-\alpha)]$ , the velocity appears to saturate for field values as low as 700 V/cm, as compared to 1400 V/cm in a 69% AR, 31% isobutane mixture used at CERN.<sup>24)</sup> The saturation of the drift velocity moves to

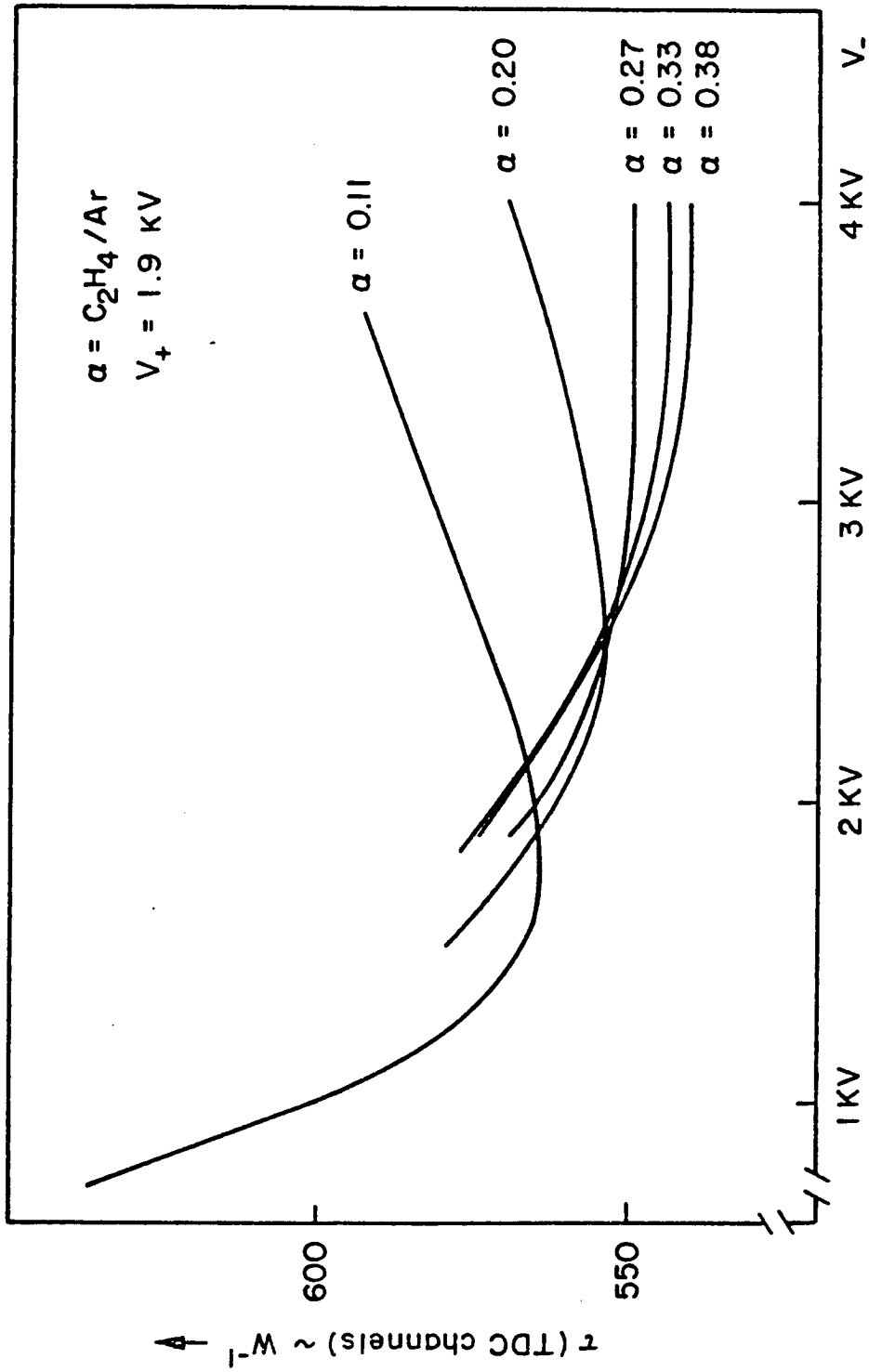


Figure A.6. Arrival Time of Electrons (in Arbitrary Units) on the Sense Wires of a 4 cm. Long Drift Cell, as a Function of Total Negative Voltage Applied to the Cell. Curves are for different concentrations of  $\text{C}_2\text{H}_4$  in Argon. Positive voltage is +1.9kV.

higher fields with increasing  $\alpha$  (at  $\alpha = 1$ , the saturation occurs due to  $C_2H_4$  itself, around 1000 V/cm). This is in agreement with the mechanism outlined above. The fact that, in the range of  $\alpha$  from 0.6 to 1.0 (fig. A.7),  $w$  does not exhibit any significant dependence on  $\alpha$ , also suggests that the presence of argon becomes unimportant for the drift velocity as soon as the Ramsauer dip is completely filled.

The convenient feature of drift velocity saturation at low electric field values in  $C_2H_4$ -Ar mixtures with low  $\alpha$  is counterbalanced by the fact that, at low ratios, the singles noise in the chamber (pulses not correlated with particles) gets unpleasantly high ( $\leq 10$  kHz). The reason for this is probably that  $C_2H_4$  is not as effective a quencher as isobutane. The precocious saturation therefore cannot be exploited with our positive voltage ( $>2$  kV) and threshold ( $\approx 400$   $\mu$ V) in our electronics. Nevertheless, the  $C_2H_4$ -Ar mixtures with high  $\alpha$  appears to be quite reliable in keeping the singles count down; they saturate certainly earlier than Ar-isobutane mixtures, and present rather loose requirements on the exact composition of the mixture (due to the near independence of  $w$  on  $\alpha$  for  $\alpha > 0.6$ ). Our final choice was to use pure ethylene in our chambers. In this way we avoided entirely the problem of premixing the gasses.

We proceeded to investigate the space-time relationship in the drift cell filled with  $C_2H_4$ . This was done with the Ruthinium  $\beta$  source and a collimated scintillator on the back of the chamber. The chamber was moved with a micrometric device so that the cone defined by the source and the collimator would hit different positions in the chamber for each high statistics run. Due to multiple scattering of the 2 MeV electrons in air and chamber windows, our resolution was not improved by collimating to

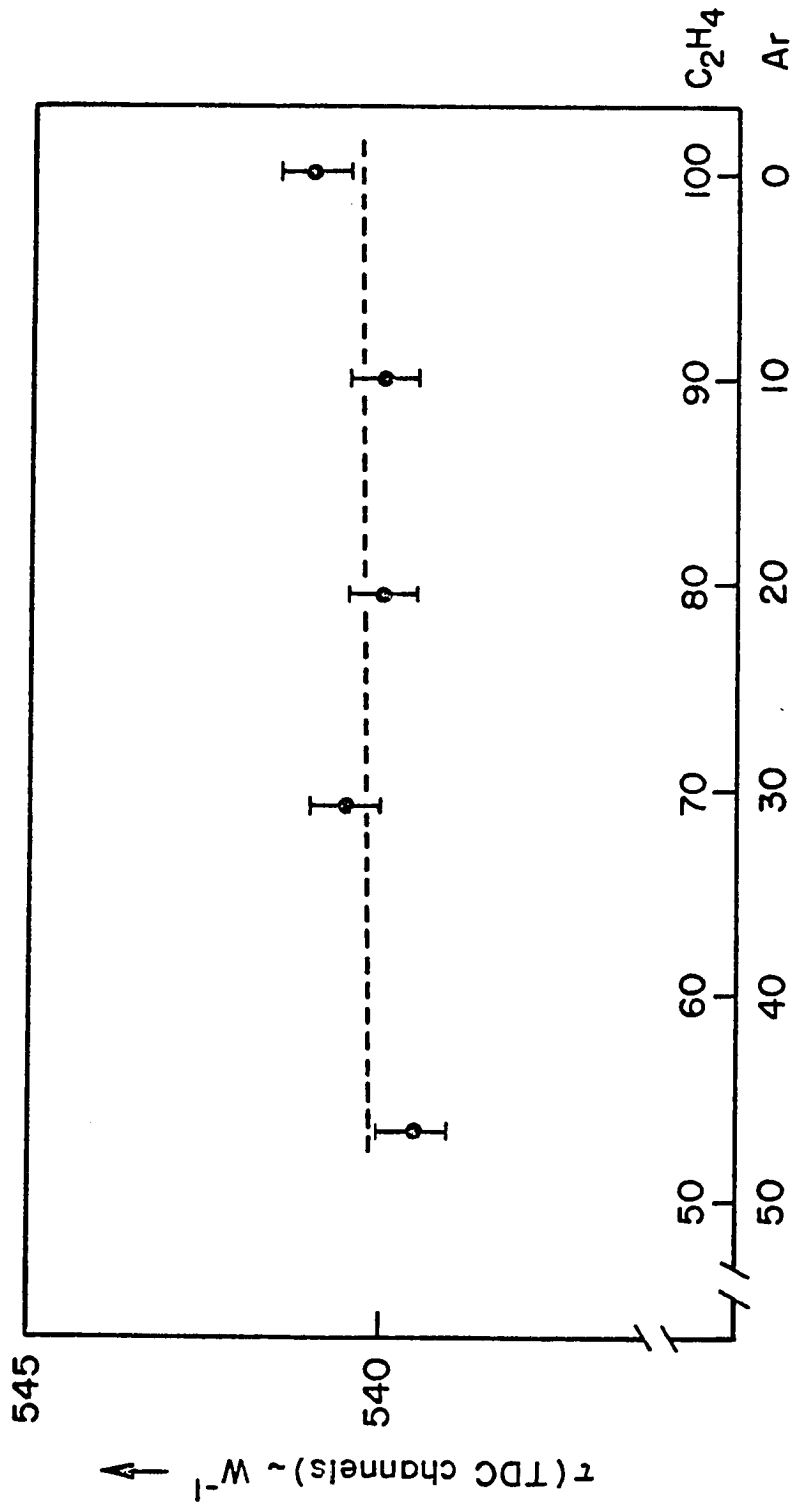


Figure A.7. Arrival Time of Electrons at -4.5 kV, -2.5 kV of Applied High Voltages as a Function of the Concentration of  $C_2H_4$  in Argon. Notice the expanded scale on the ordinate (same units as Fig. A.6).

better than 5 mm. Distributions are very wide but center finding was reproducible within 1 or 2 TDC channels ( $\frac{1}{2}$  ns/ch = 25  $\mu$ m/ch). Fig. A.8 shows the time-space relationship we obtained ( $w$  = drift velocity  $\approx$  50 mm/ $\mu$ s) and together with it the curve of relative inefficiency. This is constant over the 8 cm length from one field wire to the next field wire, and drops very fast at the edge of the chamber. We plot relative inefficiency ( $\sim$  10% in the flat region) since we were using only one scintillator and would get start signals from photomultiplier accidentals and photons from the source.

With the same set-up, we have investigated the dependence of the drift chamber performance on various parameters. For the usual gas mixture, fig. A.9 shows the efficiency plateau vs. +HV (which starts at 2.1 kV, and is at least as wide as 500 volts) and the dependence of the arrival time of the avalanches vs. the same +HV. These curves refer to a fixed position half way down the drift cell at about 2 cm from the sense wire. There is a dependence of arrival time on the amplifying high voltage (which is expected from a fixed threshold and increasing pulse height). Taking an inverse drift velocity  $\approx$  20 ns/mm, we find the slope of this effect to be safely small,  $\Delta x/\Delta V^+ = 164 \mu\text{m}/100 \text{ Volts}$ .

The dependence of the efficiency on the negative voltage (-HV) is flat except for values below -2 kV. The dependence of arrival time (fig. A.10) shows the saturation of the drift velocity starting just above a negative voltage of -4.0 kV ( $\sim$  1 kV/cm). From 4 to 4.5 kV our data give  $\Delta x/\Delta V^- \lesssim 160 \mu/100 \text{ V}$  or  $\frac{\Delta x/x}{\Delta V^-} = \frac{0.4\%}{100 \text{ Volts}}$ . We operated the chambers at a value of -4.9 kV.

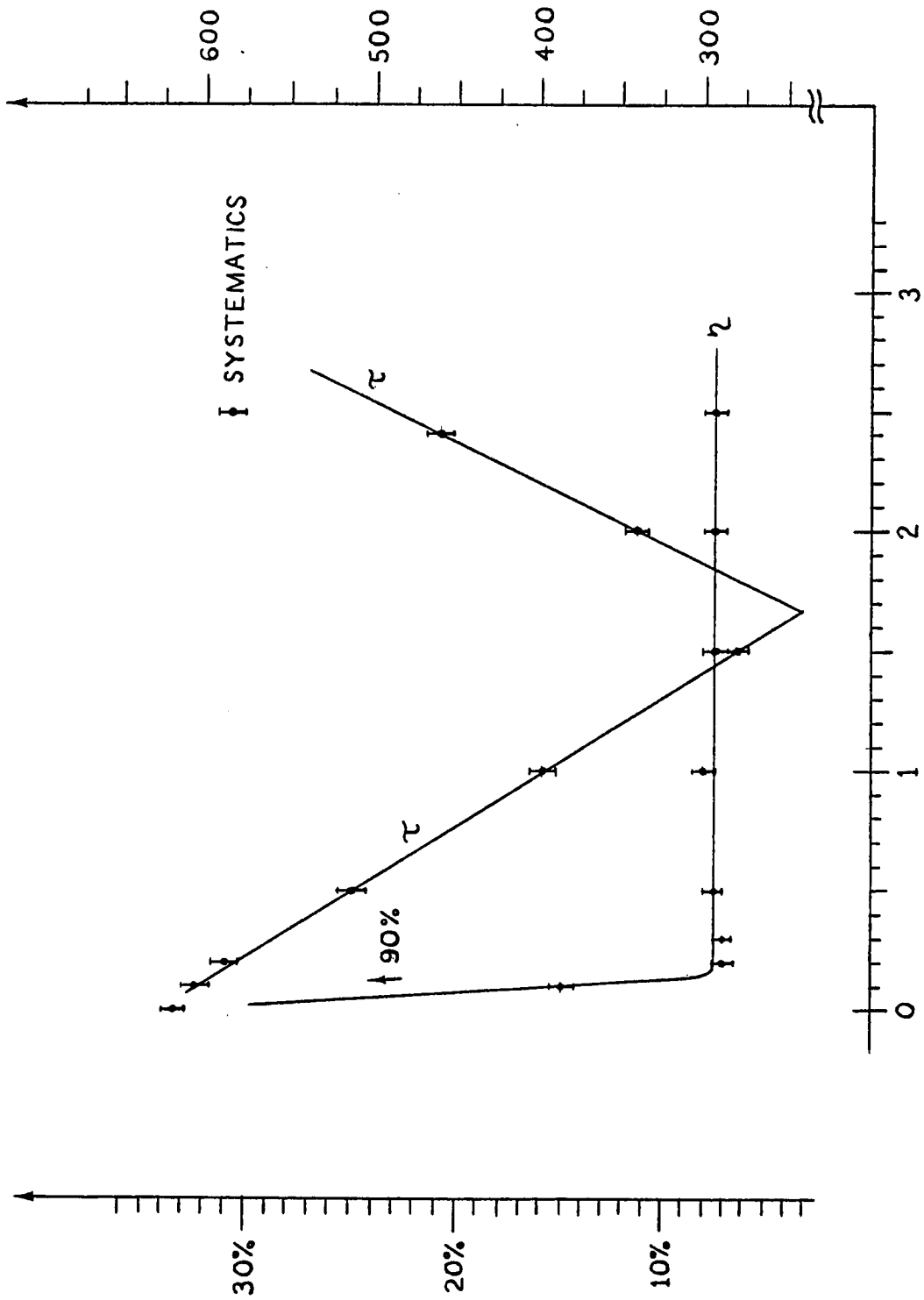


Figure A.8. Drift Electrons Arrival Time  $\tau$  (in Arbitrary Units) and Relative Inefficiency  $\eta$  vs. Positron in a Drift Cell (Inches). Gas is pure ethylene, negative voltage -4.5 kV, positive voltage +2.4.

Figure A.9. Drift Electrons Arrival Time  $\tau$  and Relative Efficiency vs. Positive High Voltage on the Sense Wire. Negative high voltage is -4.5 kV.

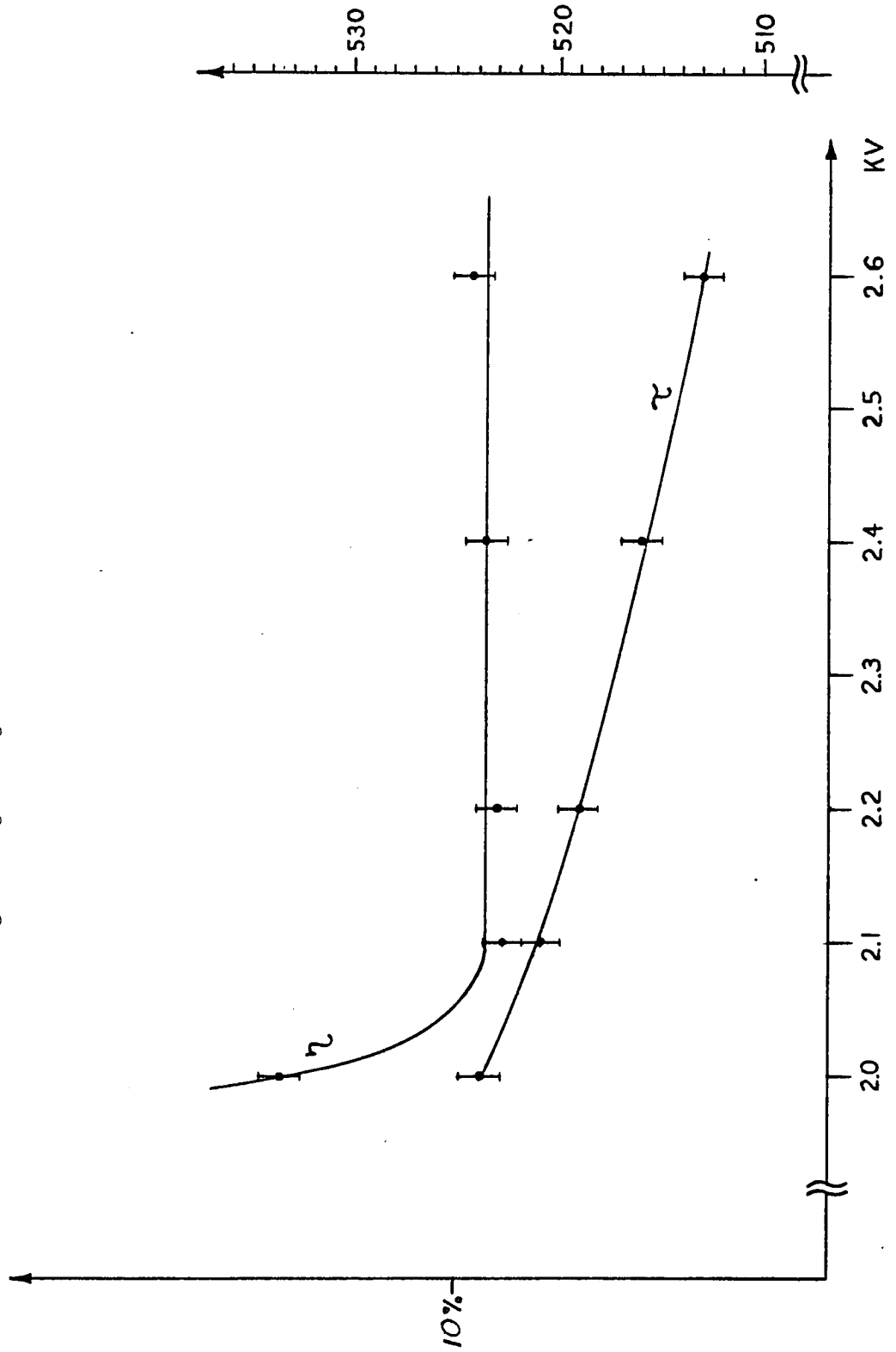
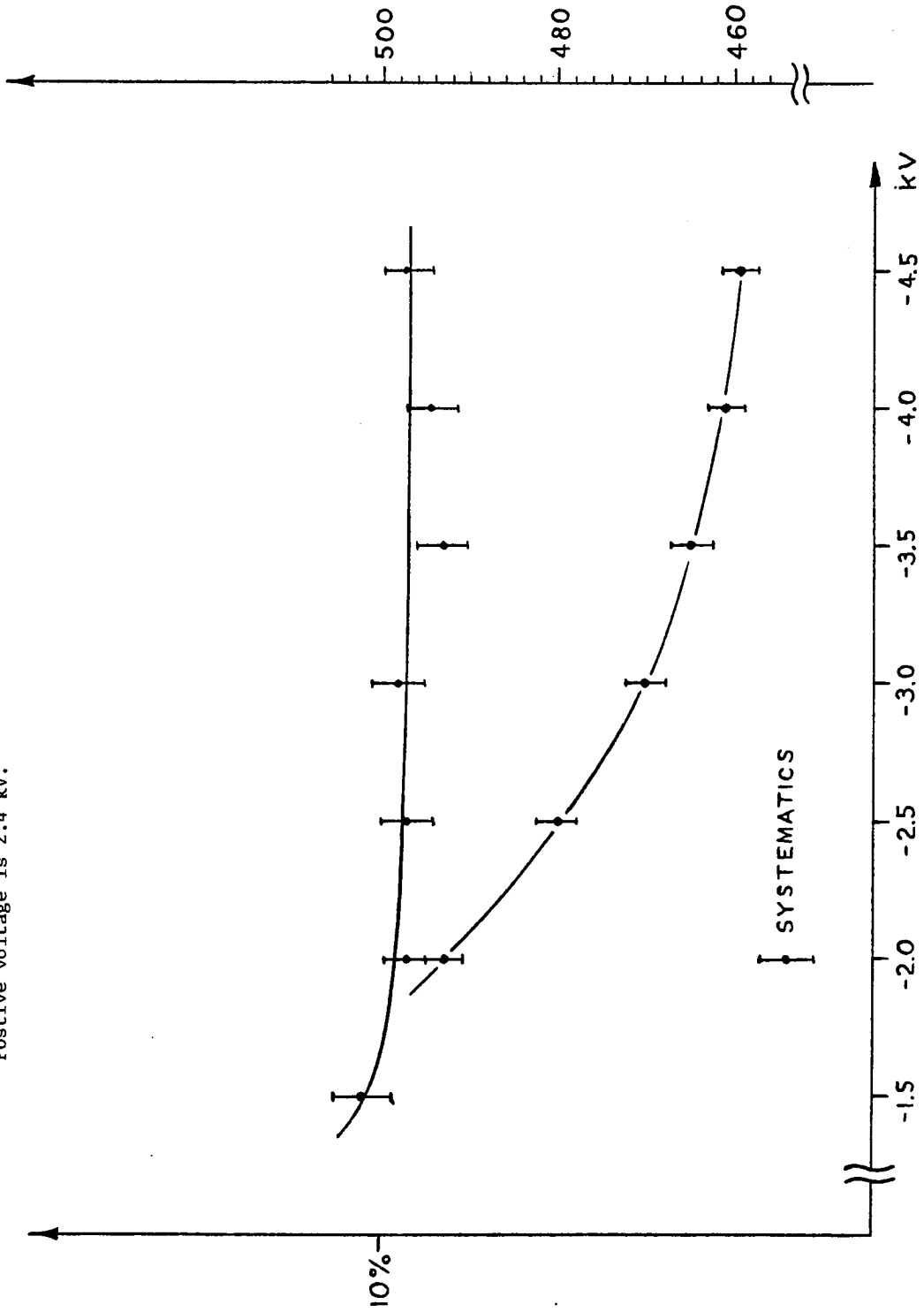




Figure A.10. Drift Electron Arrival Time  $\tau$  and Relative Inefficiency  $\eta$  vs. Negative High Voltage.  
Positive voltage is 2.4 kV.



The same prototype chamber was taken to SLAC for some tests in an accelerator environment. Full efficiency ( $>.999$ ) of the chamber was detected when triggering on the beam defining counters. For minimum ionizing electrons, the start of the +HV plateau shifted some 200 volts higher than for the  $\beta$  particles. Using a small drift chamber with 1 cm drift space, the spread of arrival time on the sense wires on the 4 cm prototype cell (for a fixed arrival time on the sense wire of the smaller chamber) allowed us to determine a crude upper limit of 250  $\mu\text{m}$  for the spatial resolution of our prototype.

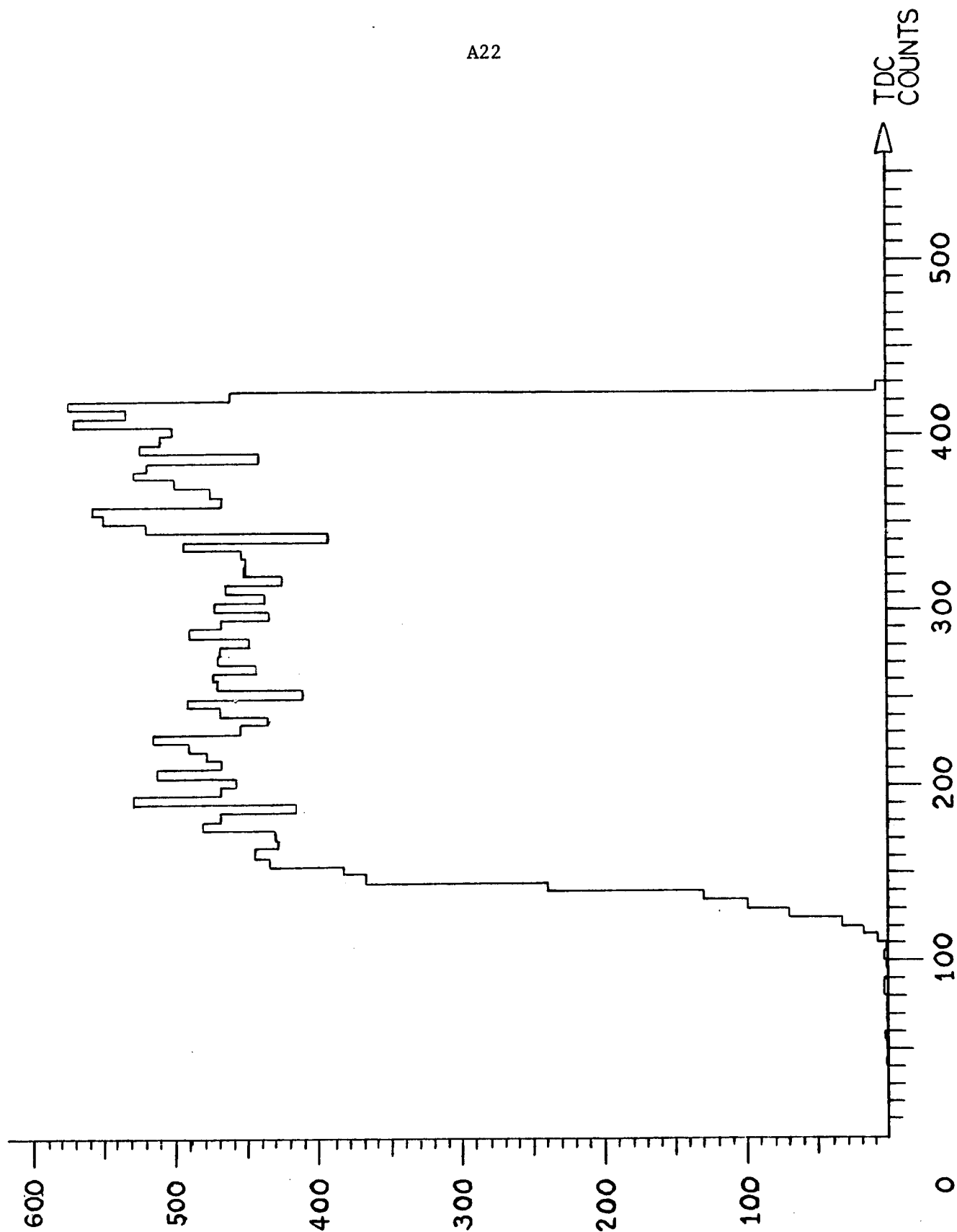
The same results for resolution were obtained when the chambers were exposed to the electron beam in the Fermilab tagged photon laboratory. We routinely performed a list of overall reliability; that is, we took, continuously, drift time spectra from various cells in our setup. If the cell is uniformly illuminated, the electric field approximately constant and the drift velocity close to saturation, these spectra have to be flat over the entire length of the cell. A typical spectrum taken during cosmic ray runs is shown in fig. A.11.

#### A4. Recoil Cart Geometry

The eight modules of drift chambers are assembled around the target in the recoil cart in the geometry of fig. 3.9. . In chapter 5, section D, we introduced the eight reference frames  $R_i^Q$  ( $i = 1,2, Q = 1,4$ ) associated to the eight modules and the laboratory reference frame R (fig. 5.2).

The assembly of the chambers on the cart is such that, for any  $Q = 1,4$ , the axis of  $R_1^Q$  and  $R_2^Q$  are (ideally) parallel and the x and z axes of  $R_1^Q$  are rotated with respect to the same axes of R by an angle

Figure A.11. Spectrum of Drift Electrons Arrival Time  $\tau$  for a Cosmic Ray Run.



that is (ideally) a multiple of ninety degrees ( $90^0$  for quadrant 1,  $0^0$  for quadrant 2,  $270^0$  for quadrant 3,  $180^0$  for quadrant 4). If this ideal assembly is assumed, the coordinate transformation that translates coordinates  $\underline{x}^1 = (x^1, y^1, z^1)$  in  $R_1^Q$  into coordinates  $\underline{x}^2 = (x^2, y^2, z^2)$  in  $R_2^Q$  is of the form

$$\underline{x}^2 = A\underline{x}^1 + \underline{d} \quad (\text{A4.1})$$

where  $\underline{d} = (d_x, d_y, d_z)$  is a vector whose components are the coordinates of the origin of  $R_1^Q$  in  $R_2^Q$  and A is just the unit matrix I

$$A = I = \begin{pmatrix} 1 & 0 & 0 \\ 0 & 1 & 0 \\ 0 & 0 & 1 \end{pmatrix}$$

and the coordinate transformation that translates coordinates  $\underline{x}^1$  in  $R_1^Q$  into coordinates  $\underline{x} = (x, y, z)$  in R is of the form

$$\underline{x} = A\underline{x}^1 + \underline{d} \quad (\text{A4.2})$$

where  $\underline{d} = (d_x, d_y, d_z)$  is now a vector whose components are the coordinates of the origin of  $R_1^Q$  in R and the matrix A is

$$A = A_1 = \begin{pmatrix} 0 & 0 & -1 \\ 0 & 1 & 0 \\ 1 & 0 & 0 \end{pmatrix} \quad \text{for quadrant 1}$$

$$A = A_2 = \begin{pmatrix} 1 & 0 & 0 \\ 0 & 1 & 0 \\ 0 & 0 & 1 \end{pmatrix} \quad \text{for quadrant 2}$$

$$A = A_3 = \begin{pmatrix} 0 & 0 & 1 \\ 0 & 1 & 0 \\ -1 & 0 & 0 \end{pmatrix} \quad \text{for quadrant 3}$$

$$A = A_4 = \begin{pmatrix} -1 & 0 & 0 \\ 0 & 1 & 0 \\ 0 & 0 & -1 \end{pmatrix} \quad \text{for quadrant 4 .}$$

We assume that the deviations from this ideal assembly are small; in particular we assume that the matrix A in (A4.1) is almost diagonal, i.e., of the form

$$A = \begin{pmatrix} 1 & \theta & \phi \\ -\theta & 1 & \psi \\ -\phi & -\psi & 1 \end{pmatrix}$$

where  $\theta, \phi, \psi$  are small rotation angles and that, for each quadrant  $Q = 1, 4$ , the matrix A in (A4.2) can be written as

$$A = A_Q \cdot \begin{pmatrix} 1 & \theta & \phi \\ -\theta & 1 & \psi \\ -\phi & -\psi & 1 \end{pmatrix} \quad Q = 1, 4$$

i.e., 3 small angle rotations have to be performed before a rotation by an angle multiple of  $90^\circ$  around the y axis.

We introduce, for each coordinate transformation of the type (A4.1) or (A4.2) a 6-dimensional vector  $\underline{v} = (d_x, d_y, d_z, \theta, \phi, \psi)$  that identifies uniquely the transformation. As mentioned earlier, fiducial pins on the outside case of each module of drift chambers were surveyed with respect to a reference frame with its origin on the nominal beam line in the tagged photon laboratory, its axis coincident with that nominal beam line, its z axis vertical and its x axis defined by the left-hand rule. These measurements provided us with an estimate of the 6 components of all the vectors  $\underline{v}$  identifying the coordinate transformations from any of the nine above mentioned frames to any of the others.

## A5. Track Fitting Algorithm

The passage of a charged particle through the eight drift gaps in a quadrant is recorded by our data acquisition system in the form of 8 CAMAC words read-out of the TDC's corresponding to the hit wires. Each of these words contains the information to identify the sense wire of interest and the drift time of the ionization electrons from the hit point to the sense wire. If the hit wire is the  $k$ -th wire on the  $j$ -th drift plane ( $j = 1,8$ ), the hit point of the track in that plane will be anywhere on a straight line of equations (in the "module" frame)

$$z = z_{j'} = (j'-1)\Delta \quad \text{with } j' = j - 4((j-1/4)); j' = 1,4 \quad (\text{A5.1})$$

$$\alpha_j x + \beta_j y = \xi_j \quad \text{with } \xi_j = w_j + \epsilon_j s_j \quad ; j = 1,8$$

where  $s_j$  is the drift length to the sense wire on plane  $j$ ,  $\epsilon_j$  can be  $\pm 1$  because of the right-left ambiguity and  $w_j = w_k$  is defined by (A1.1). We will discuss later the solution of the right-left ambiguity and will proceed now to discuss the extraction of the track parameters obtained from the knowledge of an octuple of  $\xi_j$ 's.

A straight line in space is described with respect to a frame of reference  $Oxyz$  by the parametric equations

$$x = x_0 + p_x \rho$$

$$y = y_0 + p_y \rho \quad (\text{A5.2})$$

$$z = z_0 + p_z \rho$$

where  $(x_0, y_0, z_0)$  are the coordinates of one point on the line and  $p_x, p_y, p_z$  its direction cosines. This parametrization is redundant. The

identification of a straight line in space only requires 4 parameters. For instance, solving the third equation (A5.2) for the parameter  $\rho$  and substituting in the other two we obtain the alternate (non-redundant) parametrization

$$\begin{aligned}x &= p + \ell z \\y &= q + mz .\end{aligned}\tag{A5.3}$$

This amounts to choosing the  $z$  coordinate as the running parameter. A third (banal) equation  $z = 0 + lz$  completes the parametrization. We will refer to the track parameters as a 4-dimensional vector  $t$ . Given a parametrization of the type (A5.2) the components of the vector  $t$  are given by

$$t = \begin{bmatrix} p \\ \ell \\ q \\ m \end{bmatrix} = \begin{bmatrix} x_0 - \ell z_0 \\ p_x/p_z \\ y_0 - mz_0 \\ p_y/p_z \end{bmatrix} .\tag{A5.4}$$

In each of two module frames in a quadrant the track will be described by a set of equations of the form (A5.3) (or (A5.2)). If  $R_1^0$  is the reference frame attached to the small module (coordinates  $\underline{x}^1 = (x^1, y^1, z^1)$ ) and  $R_2^0$  the one attached to the big module (coordinates  $\underline{x}^2 = (x^2, y^2, z^2)$ ) we have two representations of the track

$$\begin{aligned}x^1 &= p^1 + \ell^1 z^1 & x^2 &= p^2 + \ell^2 z^2 \\y^1 &= q^1 + m^1 z^1 & y^2 &= q^2 + m^2 z^2\end{aligned}\tag{A5.5'} \tag{A5.5''}$$

with the coordinates  $\underline{x}^1$  and  $\underline{x}^2$  related by the coordinate transformation (A4.1). The track parameters in  $R_1^0$  can be extracted from the knowledge of an 8-ple of  $\xi_j$ 's from (A5.1) in the following way. We have

$$\xi_j = \alpha_j x^1 + \beta_j y^1 \quad \text{for } j = 1, 4 \quad (\text{A5.6}')$$

$$\xi_j = \alpha_j x^2 + \beta_j y^2 \quad \text{for } j = 5, 8 \quad (\text{A5.6}''')$$

where  $j' = 1, 4$ . The second of (A5.6) can be rewritten as

$$\xi_j = \alpha_j \left[ \sum_{\ell=1}^3 A_{1\ell} x_{\ell}^1 + d_x \right] + \beta_j \left[ \sum_{\ell=1}^3 A_{2\ell} x_{\ell}^1 + d_y \right]. \quad (\text{A5.6}''')$$

Substituting (A5.5') into (A5.6') and (A5.6''') we obtain a matrix equation

$$\underline{\xi} = Ft + \underline{\xi}_0 \quad (\text{A5.7})$$

where  $t$  is the 4-dimensional vector providing the track parameters in  $R_1^Q$ ,  $\underline{\xi}$  and  $\underline{\xi}_0$  are 8-dimensional vectors and  $F$  is an  $8 \times 4$  matrix.

Explicitly

$$\underline{\xi} = \begin{bmatrix} \xi_1 \\ \xi_2 \\ \xi_3 \\ \xi_4 \\ \xi_5 \\ \xi_6 \\ \xi_7 \\ \xi_8 \end{bmatrix} \quad \underline{\xi}_0 = \begin{bmatrix} 0 \\ 0 \\ 0 \\ 0 \\ \alpha_1 d_x + \beta_1 d_y + (\alpha_1 A_{13} + \beta_1 A_{23}) z_5^1 \\ \alpha_2 d_x + \beta_2 d_y + (\alpha_2 A_{13} + \beta_2 A_{23}) z_6^1 \\ \alpha_3 d_x + \beta_3 d_y + (\alpha_3 A_{13} + \beta_3 A_{23}) z_7^1 \\ \alpha_4 d_x + \beta_4 d_y + (\alpha_4 A_{13} + \beta_4 A_{23}) z_8^1 \end{bmatrix} \quad (\text{A5.7}')$$



$$\begin{aligned}
 & \left[ \begin{array}{cccc}
 \alpha_1 & \alpha_1 z_1^1 & \beta_1 & \beta_1 z_1^1 \\
 \alpha_2 & \alpha_2 z_2^1 & \beta_2 & \beta_2 z_2^1 \\
 \alpha_3 & \alpha_3 z_3^1 & \beta_3 & \beta_3 z_3^1 \\
 \alpha_4 & \alpha_4 z_4^1 & \beta_4 & \beta_4 z_4^1
 \end{array} \right] \\
 & \left[ \begin{array}{cccc}
 (\alpha_1 A_{11} + \beta_1 A_{21}) & (\alpha_1 A_{11} + \beta_1 A_{23}) z_5^1 & (\alpha_1 A_{12} + \beta_1 A_{22}) & (\alpha_1 A_{12} + \beta_1 A_{22}) z_5^1 \\
 (\alpha_2 A_{11} + \beta_2 A_{21}) & (\alpha_2 A_{11} + \beta_2 A_{23}) z_6^1 & (\alpha_2 A_{12} + \beta_2 A_{22}) & (\alpha_2 A_{12} + \beta_2 A_{22}) z_6^1 \\
 (\alpha_3 A_{11} + \beta_3 A_{21}) & (\alpha_3 A_{11} + \beta_3 A_{23}) z_7^1 & (\alpha_3 A_{12} + \beta_3 A_{22}) & (\alpha_3 A_{12} + \beta_3 A_{22}) z_7^1 \\
 (\alpha_4 A_{11} + \beta_4 A_{21}) & (\alpha_4 A_{11} + \beta_4 A_{23}) z_8^1 & (\alpha_4 A_{12} + \beta_4 A_{22}) & (\alpha_4 A_{12} + \beta_4 A_{22}) z_8^1
 \end{array} \right] \\
 & \text{F =} \\
 & \text{(A5.7'')}
 \end{aligned}$$

$$t = \begin{bmatrix} p^1 \\ \ell^1 \\ q^1 \\ m^1 \end{bmatrix} = \begin{bmatrix} p \\ \ell \\ q \\ m \end{bmatrix} \quad \text{for sake of simplicity} \quad (\text{A5.7''''})$$

and

$$\begin{aligned} z_j^1 &= z_{j'}^1, \quad \text{for } j = j' = 1, 4 \\ z_j^1 &= (z_{j'}^1 - A_{31}p - A_{32}q - d_z) / (A_{31}\ell + A_{32}m + A_{33}) \quad \text{for } j = 5, 8. \end{aligned} \quad (\text{A5.8})$$

The second of (A5.8) is obtained from

$$z^2 = \sum_{\ell=1}^3 A_{3\ell} x_{\ell}^1 + d_z.$$

Equation (A5.7), therefore, is not strictly a linear dependence of  $\underline{\xi}$  on  $t$ .  $F$  and  $\underline{\xi}_0$  depend on the  $z_j^1$  ( $j = 1, 8$ ) which, for  $j = 5, 8$ , are not constant but are a function of the vector  $t$  itself.

The solution of a linear fit of the type (A5.7) for the 8  $\xi_j$ 's measurements in terms of the four parameters in  $t$  would be given<sup>29)</sup> by

$$t = H^{-1} F^+ G^{-1} (\underline{\xi} - \underline{\xi}_0) \quad (\text{A5.9})$$

where  $F^+$  is the transpose of  $F$

$$H = F^+ G^{-1} F \quad (\text{A5.10})$$

and

$$G = \langle (\delta \underline{\xi})^+ (\delta \underline{\xi}) \rangle \quad (\text{A5.11})$$

is the  $8 \times 8$  error matrix on the measurement vector  $\underline{\xi}$ . This matrix is assumed to be diagonal, of the form  $G_{\xi} = \sigma^2 I$ , where  $\sigma$  is the error on each individual measurement.

The  $4 \times 4$  error matrix for the track parameters  $t$  will be

$$G_t = \langle (\delta t)^+ (\delta t) \rangle = H^{-1} \quad (\text{A5.12})$$

and the  $\chi^2$  of the fit is

$$\chi^2 = (\underline{\xi} - \underline{\xi}_F)^+ G_{\xi}^{-1} (\underline{\xi} - \underline{\xi}_F) \quad (\text{A5.13})$$

where

$$\underline{\xi}_F = Ft + \underline{\xi}_0 \quad (\text{A5.14})$$

where we have substituted in (A5.7) the values (A5.9).

The matrix  $A$ , as mentioned earlier, is nearly a unit matrix.  $R_1^Q$  and  $R_2^Q$  have axes nearly parallel. In that limit

$$z_j^1 = z_j^0 - d_z \quad \text{for } j = 5, 8, \quad (\text{A5.15})$$

i.e., all the  $z_j^1$  are constant and our fit is strictly linear. We can still apply (A5.9), coupled to an iterative procedure. A first linear fit is performed using the value (A5.15), then equation (A5.8) is used to obtain the input to successive linear fits. Arbitrary precision can be achieved by multiple iterations.

The numerical values of the  $d_i$ 's,  $\alpha_i$ 's,  $\beta_i$ 's and of the six parameters  $d_x, d_y, d_z, \theta, \phi, \psi$  that identify the coordinate transformation (A4.1) are such that the diagonal elements of the error matrix  $G_t$  are

$$G_t = \begin{bmatrix} (1.01\sigma)^2 & & & \\ & (.051\sigma)^2 & & \\ & & (.671\sigma)^2 & \\ & & & (.032\sigma)^2 \end{bmatrix}$$

Non-diagonal elements are generally not small. Particularly large are the terms  $\langle \delta p \delta l \rangle = \langle \delta l \delta p \rangle$  and the terms  $\langle \delta q \delta m \rangle = \langle \delta m \delta q \rangle$ .

#### A6. Angle Track Correction

The iteration procedure mentioned above is useful also to introduce a further correction to the algorithm for the extraction of the track parameters. The necessity for such a correction was pointed out by Charpak and coworkers.<sup>24)</sup> It is illustrated in fig. A.12. Due to the rather high gains ( $\sim 10^6$ ) of the anode wires and to the low threshold (less than  $\frac{1}{2}$  mV) of our electronics, we are essentially triggering on the first few primary electrons arriving at the wire. For perpendicular tracks the shortest distance of drift lies in the plane of the sense wires. The space-time relationship is then very simple

$$s = wt \tag{A6.1}$$

where  $w$  is the drift velocity,  $t$  the measured drift time,  $s$  the distance of the wire from the intersection point of the track with the plane of the sense wire.

For inclined tracks, however, the shortest trajectory corresponds to electrons drifting along one cathode plane and then to the anode, following the field lines. These lines are radial around the anode wire and then more or less parallel to the sense wire plane. One needs therefore

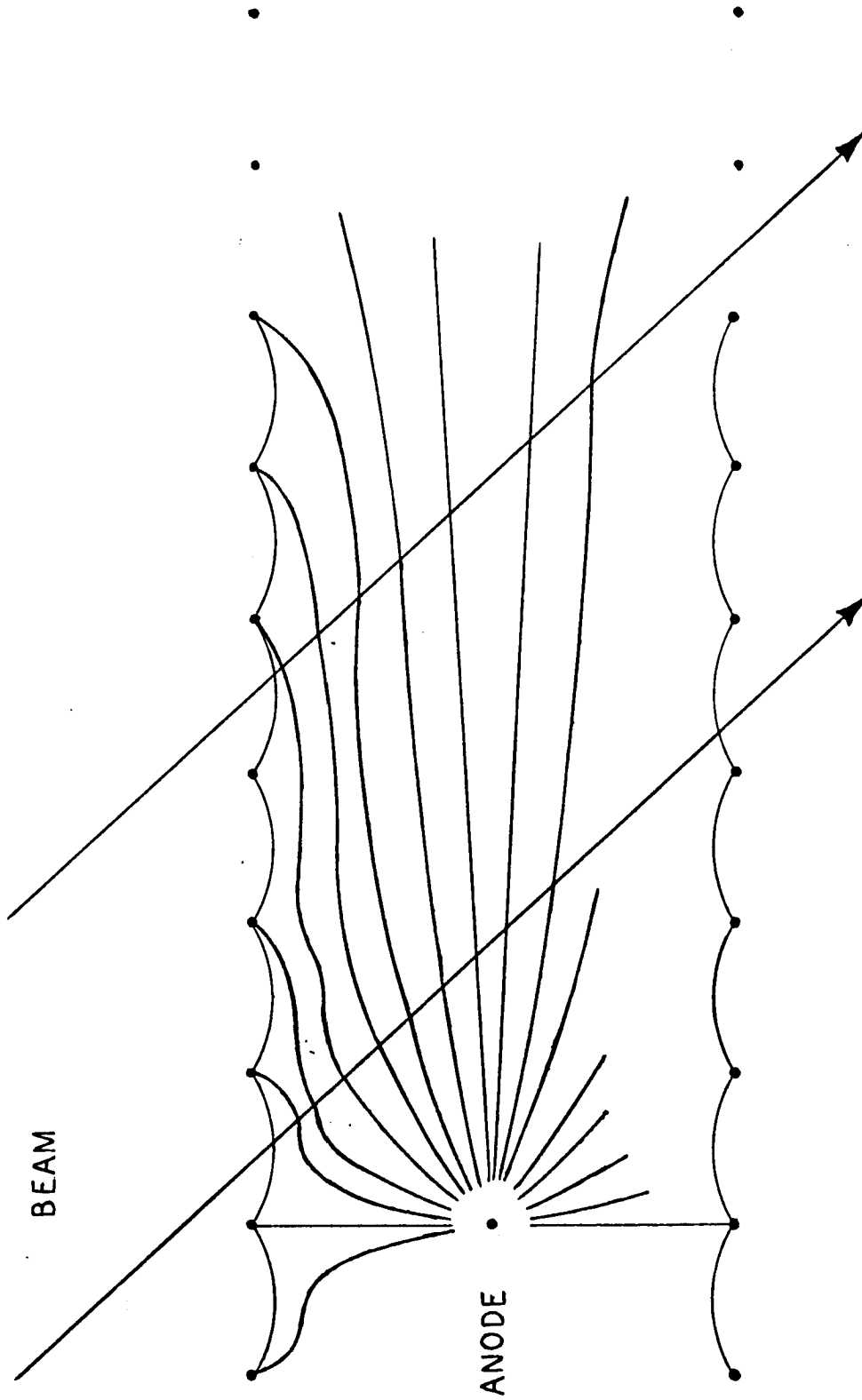


Figure A.12. Drift Trajectories (Along Electric Field Lines) for Inclined Tracks

a correction in the calculation of  $s$  from the measured drift time  $t$  depending on the knowledge of the incidence angle  $\theta$ . The first iteration of the fitting routine uses simply the linear relationship  $s = wt$ . A first estimate of the track parameters  $t$  is obtained. These parameters are used in (A5.8) and also calculated to estimate  $\theta$ . Then the following algorithm is implemented. It assumes that the trajectory of the closest electrons drifting towards the anode is radial on a direction perpendicular to the track from the anode up to the cathode plane and then coincident with the cathode plane itself. The prescription to calculate the distance  $s$  from the measured drift time  $t$  is

$$s = wt/\cos\theta \quad \text{for } 0 \leq t \leq g/w \cdot \sin\theta$$

$$s = wt + (g/\sin\theta) (1/\cos\theta - 1) \quad \text{for } t > g/w \cdot \sin\theta$$

where  $2g$  is the gap in between cathode planes (4 mm). The  $\xi_j = w_j + \epsilon_j s_j$  are calculated for  $j = 1, 8$  according to this algorithm and a new fit performed with these new values.

## A7. Alignment Procedure

### A) Relative Alignment of Modules in a Quadrant

A precise knowledge of the vector  $\underline{v} = (d_x, d_y, d_z, \theta, \phi, \psi)$  that identifies the coordinate transformation (A4.1) is necessary to avoid a systematic error in the determination of the track parameters from a fit to (A5.7). The determination of the vector  $\underline{v}$  obtained from the surveyors' information can be used only as an initial guess. We will now outline a procedure to extract a better approximation from a sample of clean identified tracks. These tracks were provided by the special cosmic rays runs described in chapter 5.

Let's assume to have a large number  $N$  of tracks identified as such using approximate values of the components of the 6-dimensional vector  $\underline{v}$ . We will refer to them as  $\underline{v}' = (d_x', d_y', d_z', \theta', \phi', \psi')$ . For each track we have a set  $\{\xi\}$  of 8 measured  $\xi_j$  values. We can divide them in two sets of 4 each,  $\{\xi_1\}$  and  $\{\xi_2\}$ , respectively in module 1 and 2. Substituting (A5.5') in (A5.6') and (A5.5'') in (A5.6'') we obtain two systems of 4 homogeneous linear equations in 4 unknowns

$$\underline{\xi}_1 = F_1 t_1$$

$$\underline{\xi}_2 = F_2 t_2$$

where

$$\underline{\xi}_1 = \begin{bmatrix} \xi_1 \\ \xi_2 \\ \xi_3 \\ \xi_4 \end{bmatrix} \quad \underline{\xi}_2 = \begin{bmatrix} \xi_5 \\ \xi_6 \\ \xi_7 \\ \xi_8 \end{bmatrix} \quad t_1 = \begin{bmatrix} p_1 \\ l_1 \\ q_1 \\ m_1 \end{bmatrix} \quad t_2 = \begin{bmatrix} p_2 \\ l_2 \\ q_2 \\ m_2 \end{bmatrix}$$

and

$$F_1 = F_2 = \begin{bmatrix} (\alpha_1) & (\alpha_1 z_1) & (\beta_1) & (\beta_1 z_1) \\ (\alpha_2) & (\alpha_2 z_2) & (\beta_2) & (\beta_2 z_2) \\ (\alpha_3) & (\alpha_3 z_3) & (\beta_3) & (\beta_3 z_3) \\ (\alpha_4) & (\alpha_4 z_4) & (\beta_4) & (\beta_4 z_4) \end{bmatrix}$$

The solution of these two systems

$$t_1 = F_1^{-1} \underline{\xi}_1$$

$$t_2 = F_2^{-1} \underline{\xi}_2$$

provide us with two independent determinations of the track parameters, in the two frames  $R_1^Q$  and  $R_2^Q$ . Each solution is accompanied by a  $4 \times 4$  error matrix

$$G_{t_1} = G_{t_2} = \langle (\delta t_1)^+ (\delta t_1) \rangle = \langle (\delta t_2)^+ (\delta t_2) \rangle = (F_1^+ G_1^{-1} F_1)^{-1} = (F_2^+ G_2^{-1} F_2)^{-1}$$

where

$$G_1 = G_2 = \langle (\delta \xi_1)^+ (\delta \xi_1) \rangle = \langle (\delta \xi_2)^+ (\delta \xi_2) \rangle = \sigma^2 I$$

are two  $4 \times 4$  error matrices.  $\alpha_i$ 's,  $\beta_i$ 's and  $z_i$ 's ( $i=1,4$ ) are such that

$$G_{t_1} = G_{t_2} = \begin{bmatrix} (2.42\sigma)^2 & & & \\ & (.90\sigma)^2 & & \\ & & (1.00\sigma)^2 & \\ & & & (0.26\sigma)^2 \end{bmatrix}$$

with non-negligible non-diagonal terms.

We want to extract from these independent determinations of the track parameters a better estimate of the components of the vector  $\underline{v}$ . In other words we want to obtain an estimate of the 6-dimensional vector  $\underline{\Delta}$

$$\underline{\Delta} = (\Delta_x, \Delta_y, \Delta_z, \Delta_\theta, \Delta_\phi, \Delta_\psi)$$

such that the difference of the "true" vector  $\underline{v}$  and the approximate vector  $\underline{v}'$  is given by

$$\underline{v} - \underline{v}' = \underline{\Delta}$$

$\underline{v}$  identifies the coordinate transformation

$$\underline{x}^2 = A \underline{x}^1 + \underline{d} \quad (A4.1)$$



from  $R_1^Q$  to  $R_2^Q$ .  $\underline{v}'$  identifies the coordinate transformation

$$\underline{x}^I = A' \underline{x}^1 + \underline{d}' \quad (\text{A7.1})$$

connecting  $R_1^Q$  to a frame  $R_I^Q$  (with coordinates  $\underline{x}^I$ ) which would coincide with  $R_2^Q$  if our knowledge of  $\underline{y}$  were exact.

Let's define the coordinate transformation connecting  $R_1^Q$  and  $R_2^Q$

$$\underline{x}^I = \mathcal{A} \underline{x}^2 + \underline{\mathcal{D}} \quad (\text{A7.2})$$

identified by the 6-dimensional vector  $\underline{\delta} = (\delta_x, \delta_y, \delta_z, \delta_\theta, \delta_\phi, \delta_\psi)$ . We will have

$$\begin{aligned} \underline{\mathcal{D}} &= (\delta_x, \delta_y, \delta_z) \\ \mathcal{A} &= \begin{pmatrix} 1 & \delta_\theta & \delta_\phi \\ -\delta_\theta & 1 & \delta_\psi \\ -\delta_\phi & -\delta_\psi & 1 \end{pmatrix} \end{aligned} \quad (\text{A7.2}')$$

Inverting (A4.1) and substituting into (A7.1), we obtain

$$\underline{x}^I = (A' A^{-1}) \underline{x}^2 + [\underline{d}' - (A' A^{-1}) \underline{d}] \quad (\text{A7.3})$$

i.e.,

$$A = \mathcal{A}^{-1} A' = \begin{pmatrix} 1 & \theta' - \delta_\theta & \phi' - \delta_\phi \\ -(\theta' - \delta_\theta) & 1 & \psi' - \delta_\psi \\ -(\phi' - \delta_\phi) & -(\psi' - \delta_\psi) & 1 \end{pmatrix} \quad (\text{A7.3}')$$

$$\underline{d} - \underline{d}' = \mathcal{A}^{-1} (\underline{d}' - \underline{\mathcal{D}}) - \underline{d}' \quad .$$

This reads

$$\Delta = \begin{bmatrix} \Delta_x \\ \Delta_y \\ \Delta_z \\ \Delta_\theta \\ \Delta_\phi \\ \Delta_\psi \end{bmatrix} = \begin{bmatrix} -1 & \delta_\theta & \delta_\phi & -d'_x & -d'_z & 0 \\ -\delta_\theta & -1 & \delta_\psi & d'_x & 0 & -d'_z \\ -\delta_\phi & -\delta_\psi & -1 & 0 & d'_x & d'_y \\ 0 & 0 & 0 & -1 & 0 & 0 \\ 0 & 0 & 0 & 0 & -1 & 0 \\ 0 & 0 & 0 & 0 & 0 & -1 \end{bmatrix} \begin{bmatrix} \delta_x \\ \delta_y \\ \delta_z \\ \delta_\theta \\ \delta_\phi \\ \delta_\psi \end{bmatrix} \quad (\text{A7.4})$$

From (A7.1) we can calculate the parameters  $t_I$  of our track in  $R_I^Q$  from the parameters  $t_1$  in  $R_1^Q$  as

$$\begin{aligned} p_I &= (p_1 + d'_x + \theta'q_1) - l_I(d'_z - \phi'p_1 - \psi'q_1) \\ l_I &= (l_1 + \theta'm_1 + \phi') / (1 - \phi'l_1 - \psi'm_1) \\ q_I &= (q_1 + d'_y - \theta'p_1) - m_I(d'_z - \phi'p_1 - \psi'q_1) \\ m_I &= (m_1 - \phi'l_1 + \psi') / (1 - \phi'l_1 - \psi'm_1) \end{aligned} \quad (\text{A7.5})$$

From (A7.2) we obtain, in a similar way

$$\begin{aligned} p_I &= (p_2 + \delta_x + \delta_\theta q_2) - l_I(\delta_z - \delta_\phi p_2 - \delta_\psi q_2) \\ l_I &= (l_2 + \delta_\theta m_2 + \delta_\phi) / (1 - \delta_\phi l_2 - \delta_\psi m_2) \\ q_I &= (q_2 + \delta_y - \delta_\theta p_2) - m_I(\delta_z - \delta_\phi p_2 - \delta_\psi q_2) \\ m_I &= (m_2 - \delta_\theta l_2 + \delta_\psi) / (1 - \delta_\phi l_2 - \delta_\psi m_2) \end{aligned} \quad (\text{A7.8})$$

If we neglect products of components of vector  $\underline{\delta}$  (A7.8) becomes

$$\begin{bmatrix} p_1 - p_2 \\ \ell_1 - \ell_2 \\ q_1 - q_2 \\ m_1 - m_2 \end{bmatrix} = \begin{bmatrix} 1 & 0 & -\ell_2 & q_2 & \ell_2 p_2 & \ell_2 q_2 \\ 0 & 0 & 0 & m_2 & (1 + \ell_2^2) & p_2 m_2 \\ 0 & 1 & -m_2 & -m_2 & m_2 p_2 & m_2 q_2 \\ 0 & 0 & 0 & -\ell_2 & m_2 \ell_2 & (1 + m_2^2) \end{bmatrix} \begin{bmatrix} \delta_x \\ \delta_y \\ \delta_z \\ \delta_\theta \\ \delta_\phi \\ \delta_\psi \end{bmatrix} \quad (\text{A7.8'})$$

that is a matrix equation of the form

$$(t_1 - t_2) = \mathcal{M} \delta \quad (\text{A7.8''})$$

where  $\mathcal{M}$  is the  $4 \times 6$  matrix in (A7.8').

A sample of  $N$  tracks will provide therefore  $N$  sets of 4 constraints of the type (A7.8'') on the 6 components of  $\underline{\delta}$ . If we define the  $4N$  dimensional vector  $\Delta t$  and the  $4N \times 6$  dimensional matrix  $M$  such that

$$\Delta t^i = (t_1^j - t_2^j)^k$$

$$M_{i\ell} = \mathcal{M}_{j\ell}^k$$

where

$$j = \text{track parameter index} \quad ; j = 1, 4$$

$$k = \text{track index} \quad ; k = 1, N$$

$$\ell = \delta \text{ component index} \quad ; \ell = 1, 6$$

$$i = \text{constraint index} = 4(k-1) + j; i = 1, 4N$$

then we will obtain a global matrix equation

$$\Delta t = M\delta \quad (\text{A7.9})$$

Using (A5.9) we conclude that an estimate of  $\delta$  from our sample of  $N$  tracks is given by

$$\delta = (M^+ G_{\Delta t}^{-1} M)^{-1} M^+ G_{\Delta t}^{-1} \Delta t \quad (\text{A7.10})$$

where  $G_{\Delta t}$  is the  $4N \times 4N$  dimensional error matrix built up, track by track, by the  $4 \times 4$  error matrices on the track parameter differences  $t_I - t_2$

$$G_{\Delta t} = G_{t_2} + G_{t_I} = G_2 + G_I.$$

Equation (A7.5), in the approximation  $\theta' = \phi' = \psi' = 0$  is of the form

$$t_I = T t_j + \text{constant terms}$$

where  $T$  is the  $4 \times 4$  matrix

$$T = \begin{bmatrix} 1 & -d'_z & 0 & 0 \\ 0 & 1 & 0 & 0 \\ 0 & 0 & 1 & -d'_z \\ 0 & 0 & 0 & 1 \end{bmatrix}.$$

Then by the law of propagation of error<sup>29)</sup> we obtain

$$G_I = T G_I T^+.$$

This implies, from the order of magnitude of  $d_z$  in our recoil set-up,

$$G_I = \begin{bmatrix} (21\sigma)^2 & & & & & \\ & (1.27\sigma)^2 & & & & \\ & & (6.26\sigma)^2 & & & \\ & & & (.37\sigma)^2 & & \\ & & & & & \\ & & & & & \end{bmatrix} \quad (A7.11)$$

The  $6 \times 6$  error matrix on the estimate (A7.10) of the components of  $\delta$  is

$$G_\delta = (M^+ G_{\Delta t}^{-1} M)^{-1} \quad (A7.12)$$

We can now use (A7.4) to obtain the components of  $\underline{\Delta}$ . Equation (A7.4) can be written as

$$\underline{\Delta} = T \underline{\delta} + \text{second order terms}$$

with

$$T = \begin{bmatrix} -1 & 0 & 0 & -d'_x & -d'_z & 0 \\ 0 & -1 & 0 & d'_x & 0 & -d'_z \\ 0 & 0 & -1 & 0 & d'_x & d'_y \\ 0 & 0 & 0 & -1 & 0 & 0 \\ 0 & 0 & 0 & 0 & -1 & 0 \\ 0 & 0 & 0 & 0 & 0 & -1 \end{bmatrix}$$

The error matrix of the  $\Delta$  parameters will be then

$$G_\Delta = T G_\delta T^+ \quad (A7.13)$$

$G_\Delta$  and  $G_\delta$  will depend on the sample of tracks determining the elements of matrix  $M$  in (A7.9).

## B) Alternative Formalism for Relative Alignment in a Quadrant

An alternative approach to the problem of estimating the 6 components of the vector  $\underline{\Delta}$  was also tried on the data. It tries to use on the same level the 8  $\xi$  measurements on each track, rather than comparing track parameter estimates in the two modules of a quadrant.

Let's define the 8-dimensional vector

$$\underline{r} = \underline{\xi}_F - \underline{\xi} \quad (\text{A7.14})$$

where  $\underline{\xi}_F$  is given by (A5.14). The components of  $\underline{r}$  are the residuals of the fit that provides the track parameters (A5.9)

$$\underline{t} = (F^+ G_\xi^{-1} F)^{-1} F^+ G_\xi^{-1} (\underline{\xi} - \underline{\xi}_0) \quad (\text{A7.15})$$

IF  $G_\xi = \sigma^2 I$ , as we have assumed,

$$\underline{t} = (F^+ F)^{-1} F^+ (\underline{\xi} - \underline{\xi}_0) = M \underline{\xi} + V \quad (\text{A7.16})$$

where

$$M = (F^+ F)^{-1} F^+ \quad \text{is a } 4 \times 8 \text{ matrix}$$

$$V = -M \underline{\xi}_0 \quad \text{is a 4 dimensional vector}$$

Differentiating (A5.14) with respect to the components of the vector

$\underline{v} = (d_x, d_y, d_z, \theta, \phi, \psi)$  we obtain

$$\Delta \xi_i = r_i = \sum_j \frac{\partial (Ft + \xi_0)_i}{\partial v_j} \Delta_j = \sum_j c_{ij} \Delta_j \quad (\text{A7.18})$$

or in matrix formalism

$$\underline{r} = C \underline{\Delta} \quad (\text{A7.19})$$

The coefficients  $c_{ij}$  of the expansion (A7.18) are

$$c_{ij} = \sum_{k=1}^4 \frac{\partial F_{ik}}{\partial v_j} t_k + \sum_{k=1}^4 F_{ik} \frac{\partial t_k}{\partial v_j} + \frac{\partial \xi_{0,i}}{\partial v_j} .$$

Using (A7.16) one gets

$$c_{ij} = \sum_{k=1}^4 \frac{\partial F_{ik}}{\partial v_j} t_k + \sum_{k\ell} F_{\ell k} \left[ \frac{\partial M_k}{\Delta v_j} \xi_{\ell} \right] - \sum_k F_{ik} \frac{\partial v_k}{\partial v_j} + \frac{\partial \xi_{0,i}}{\partial v_j} . \quad (\text{A7.20})$$

The dependence of  $F$  and  $\xi_0$  on the components of  $\underline{v}$  is known from (A5.7') and the same is true for  $M$  and  $V$ . The evaluation of the derivatives in (A7.20) is algebraically prohibitive. One can, however, evaluate them numerically around the value  $\underline{v}'$ . Once the  $c_{ij}$  are so obtained, one can extract  $\underline{\Delta}$  as

$$\underline{\Delta} = (C^+ G_r C)^{-1} C^+ G_r^{-1} \underline{r} \quad (\text{A7.21})$$

where the error matrix of the residuals is given<sup>29)</sup> by

$$G_r = G_{\xi} - F (F^+ G_{\xi} F)^{-1} F^+$$

and the error matrix of the  $\Delta$  components is

$$G_{\Delta} = (C^+ G_r^{-1} C)^{-1} . \quad (\text{A7.22})$$

### C) Relative Alignment of Quadrants

The surveying information provides also a first estimate of the components of the vector  $\underline{v} = (d_x, d_y, d_z, \theta, \phi, \psi)$  that identifies the coordinate transformation

$$\underline{x}^R = A\underline{x}^A + \underline{d} \quad (\text{A7.23})$$

to the frame  $R_1^2 = R_1^R$  in quadrant 2 (chosen as reference quadrant) from any of the frames  $R_1^Q = R_1^A$  ( $Q = A = 1, 4$ ;  $Q \neq R = 2$ ) in the other three quadrants. A precise knowledge of these three coordinate transformations (coupled to a precise knowledge of the coordinate transformation from the laboratory frame  $R$  to  $R_1^R$ ) is necessary to avoid systematic errors in the determination of the proton scattering angles. A better estimate of the three vectors  $\underline{v}$  (for the quadrant pairs 2-1, 2-3, 2-4) can be obtained from a sample of cosmic ray tracks traversing pairs of quadrants.

Let's assume to have a sample of  $N$  tracks having been identified as such in  $R_1^R$  and  $R_1^A$ . Two fits of the type (A5.7) have been performed and have provided the independent estimates  $t_R$  and  $t_A$  of the track parameters in  $R_1^R$  and  $R_1^A$ . The two determinations are accompanied by two error matrices  $G_R$  and  $G_A$

$$G_R = G_A = G_t$$

with  $G_t$  given by (A5.11). We want to obtain an estimate of the 6-dimensional vector  $\underline{\Delta}$

$$\underline{\Delta} = (\Delta_x, \Delta_y, \Delta_z, \Delta_\theta, \Delta_\phi, \Delta_\psi)$$

such that the difference of the "true" vector  $\underline{v}$  and the available approximate determination  $\underline{v}' = (d'_x, d'_y, d'_z, \theta', \phi', \psi')$  is

$$\underline{v} - \underline{v}' = \underline{\Delta} .$$



$\underline{v}'$  identifies the coordinate transformation

$$\underline{x}^R = A' \underline{x}^I + \underline{d}' \quad (\text{A7.24})$$

connecting  $R_1^R$  to a frame  $R^I$  (with coordinates  $\underline{x}^I$ ) that would coincide with  $R_1^A$  if our knowledge of  $\underline{v}$  were exact.

Let's define the coordinate transformation connecting  $R^I$  and  $R_1^A$

$$\underline{x}^I = A \underline{x}^A + \underline{\mathcal{D}} \quad (\text{A7.25})$$

defined by the 6-dimensional vector  $\underline{\delta} = (\delta_x, \delta_y, \delta_z, \delta_\theta, \delta_\phi, \delta_\psi)$  with  $A$  and  $\underline{\mathcal{D}}$  given by (A7.2'). Substituting (A7.25) in (A7.24) we obtain

$$\begin{aligned} A &= A' A \\ \underline{d} - \underline{d}' &= A' \underline{\mathcal{D}} \end{aligned} \quad (\text{A7.26})$$

which reads

$$\Delta = \begin{bmatrix} \Delta_x \\ \Delta_y \\ \Delta_z \\ \Delta_\theta \\ \Delta_\phi \\ \Delta_\psi \end{bmatrix} = \begin{bmatrix} 1 & \theta' & \phi' & 0 & 0 & 0 \\ -\theta' & 1 & \psi' & 0 & 0 & 0 \\ -\phi' & -\psi' & 1 & 0 & 0 & 0 \\ 0 & 0 & 0 & 1 & 0 & 0 \\ 0 & 0 & 0 & 0 & 1 & 0 \\ 0 & 0 & 0 & 0 & 0 & 1 \end{bmatrix} \begin{bmatrix} \delta_x \\ \delta_y \\ \delta_z \\ \delta_\theta \\ \delta_\phi \\ \delta_\psi \end{bmatrix} = T \underline{\delta} \quad (\text{A7.27})$$

The track parameters  $t_I$  in the frame  $R^I$  can be calculated from the parameters  $t_R$ , using the inverse of (A7.24). The form of the functional dependence

$$\begin{aligned}
p_I &= p_I (p_R, \ell_R, q_R, m_R; \underline{v}') \\
\ell_I &= \ell_I (p_R, \ell_R, q_R, m_R; \underline{v}') \\
q_I &= q_I (p_R, \ell_R, q_R, m_R; \underline{v}') \\
m_I &= m_I (p_R, \ell_R, q_R, m_R; \underline{v}')
\end{aligned}
\tag{A7.28}$$

will depend on the particular pair of quadrants the track is traversing.

Using (A7.25) we obtain

$$\begin{aligned}
p_I &= (p_A + \delta_x + \delta_\theta q_A) - \ell_I (\delta_z - \delta_\phi p_A - \delta_\psi q_A) \\
\ell_I &= (\ell_A + \delta_\theta m_A + \delta_\phi) / (1 - \delta_\phi \ell_A - \delta_\psi m_A) \\
q_I &= (q_A + \delta_y - \delta_\theta p_A) - m_I (\delta_z - \delta_\phi p_A - \delta_\psi q_A) \\
m_I &= (m_A - \delta_\theta \ell_A + \delta_\psi) / (1 - \delta_\phi \ell_A - \delta_\psi m_A)
\end{aligned}$$

which (neglecting products of components of  $\underline{\delta}$ ) can be linearized to

$$\begin{bmatrix} p_I - p_A \\ \ell_I - \ell_A \\ q_I - q_A \\ m_I - m_A \end{bmatrix} = \begin{bmatrix} 1 & 0 & -\ell_A & q_A & \ell_A p_A & \ell_A q_A \\ 0 & 0 & 0 & m_A & (1 + \ell_A^2) & \ell_A m_A \\ 0 & 1 & -m_A & -p_A & m_A p_A & m_A q_A \\ 0 & 0 & 0 & -\ell_A & m_A \ell_A & (1 + m_A^2) \end{bmatrix} \begin{bmatrix} \delta_x \\ \delta_y \\ \delta_z \\ \delta_\theta \\ \delta_\phi \\ \delta_\psi \end{bmatrix}
\tag{A7.29}$$

that is, a matrix equation of the form

$$(t_I - t_A) = \mathcal{M} \delta .
\tag{A7.29'}$$

Using a sample of N track traversing quadrant R and quadrant A we can obtain in the same way as (A7.9) a global matrix equation

$$\Delta t = M\delta \quad (\text{A7.30})$$

where  $\Delta t$  is a  $4N$  dimensional vector,  $M$  a  $4N \times 6$  dimensional matrix. An estimate of  $\delta$  will be given by (A7.10). Here  $G_{\Delta t}$  is

$$G_{\Delta t} = G_{t_A} + T_{t_I} = G_t + G_I .$$

We can obtain  $G_I$  by linearizing the functional dependence (A7.28) to a form

$$t_I = T t_R + \text{constant terms}$$

(where  $T_{1_J} = (\partial t_I^i / \partial t_R^j)$ ). This will give us

$$G_I = T G_t T^+ .$$

From the recoil cart geometry we obtain for the diagonal elements of the  $G_I$  matrix

$$G_I = \begin{bmatrix} (3.72\sigma)^2 & & & \\ & (.071\sigma)^2 & & \\ & & (2.42\sigma)^2 & \\ & & & (.046\sigma)^2 \end{bmatrix} \text{ or } \begin{bmatrix} (1.17\sigma)^2 & & & \\ & (.064\sigma)^2 & & \\ & & (.82\sigma)^2 & \\ & & & (.045\sigma)^2 \end{bmatrix}$$

$$\text{or } \begin{bmatrix} (2.51\sigma)^2 & & & \\ & (.71\sigma)^2 & & \\ & & (1.36\sigma)^2 & \\ & & & (.061\sigma)^2 \end{bmatrix}$$

The three matrices above are respectively for tracks through quadrants 2 and 4, 2 and 1, 2 and 3. The error matrix  $G_\delta$  of the fitted parameters  $\delta$  will be of the form (A7.12) and from (A7.27) we can obtain an error matrix  $G_\Delta$  of the form (A7.13).

#### D) Estimate of the Beam Axis Parameters

Inelastic photon-proton interactions producing 2 tracks in 2 different quadrants are used to obtain the parameters of the beam axis. If the equation of the two tracks are (A5.2)

$$\vec{x}_1 = \vec{x}_1^0 + \vec{p}_1 \rho$$

$$\vec{x}_2 = \vec{x}_2^0 + \vec{p}_2 \tau$$

in the nominal laboratory frame, the coordinates  $\vec{x}_v$  of the vertex of the interaction, defined as the point that minimizes

$$\chi^2 = (\vec{x}_1 - \vec{x}_v)^2 + (\vec{x}_2 - \vec{x}_v)^2$$

are given by

$$\vec{x}_v = \frac{\vec{x}_1^0 + \vec{p}_1 \rho_v + \vec{x}_2^0 + \vec{p}_2 \tau_v}{2}$$

with

$$\begin{pmatrix} \rho_v \\ \tau_v \end{pmatrix} = \frac{1}{1 - (\vec{p}_1 \cdot \vec{p}_2)^2} \begin{bmatrix} 1 & \vec{p}_1 \cdot \vec{p}_2 \\ \vec{p}_1 \cdot \vec{p}_2 & 1 \end{bmatrix} \begin{bmatrix} (\vec{x}_2^0 - \vec{x}_1^0) \cdot \vec{p}_1 \\ (\vec{x}_1^0 - \vec{x}_2^0) \cdot \vec{p}_2 \end{bmatrix} .$$

The equations of the beam axis are, in the nominal laboratory frame

$$x = \ell y + p$$

$$z = m y + q$$

Its parameters can be estimated as

$$\begin{pmatrix} p \\ \ell \end{pmatrix} = \begin{bmatrix} N & \sum_k (y_v)_k \\ \sum_k (y_v)_k & \sum_k (y_v)_k^2 \end{bmatrix}^{-1} \begin{bmatrix} \sum_k (x_v)_k \\ \sum_k (x_v)_k (y_v)_k \end{bmatrix}$$

$$\begin{pmatrix} q \\ m \end{pmatrix} = \begin{bmatrix} N & \sum_k (y_v)_k \\ \sum_k (y_v)_k & \sum_k (y_v)_k^2 \end{bmatrix}^{-1} \begin{bmatrix} \sum_k (z_v)_k \\ \sum_k (z_v)_k (y_v)_k \end{bmatrix}$$

where  $k = 1$ , number of reconstructed event vertices. Scattering angles of recoil protons are calculated with respect to this axis.

#### A8. Pattern Recognition and Left-Right Ambiguity Resolution.

In section A5 we discussed the extraction of the parameters of a track from the knowledge of the eight  $\xi_j$  measurements

$$\xi_j = w_j + \varepsilon_j s_j \quad (j = 1,8) \quad \varepsilon_j = \pm 1 .$$

Let  $n_j$  be the number of hits recorded on the  $j$ -th plane of drift wires in a quadrant. There are  $N = \prod_{j=1}^8 n_j$  ways these hits can be combined to form an octuple of hits (i.e., a track candidate). Pattern recognition, i.e., the identification of track candidates that are worth processing further, consists of the following two requirements:

- a) a fit of the type (A5.7) is performed, with  $\xi_j = w_j$  ( $j = 1,8$ ), using the wire positions as a first gross estimate of  $\xi$ . The  $\chi^2$  of the fit ( $\chi_a^2$ ) is given by (A5.13).  $G_\xi$  is set to the unit matrix  $I$ , i.e., equal errors are assigned to all the  $\xi$  measurements. From Monte Carlo simulation of tracks in our recoil

system we obtained a distribution of  $\chi_a^2$  for simulated tracks (and a similar  $\chi_a^2$  distribution for randomly associated octuples of hits). Only less than .1% of the simulated tracks have  $\chi_a^2 > 80$ .  $\chi_a^2 \leq 80$  is therefore required in order to process an octuple further.

- b) another fit of the type (A5.7) is performed to provide  $\chi_b^2$ , still with  $\xi_j = w_j$  ( $j = 1,8$ ); the elements of  $G_\xi$ , however, are  $(G_\xi)_{ij} = \delta_{ij} s_j^2$ . The matrix is still diagonal, but to  $\xi_j$  an error  $s_j$  (i.e., the drift length) is assigned. Monte Carlo simulation suggested a  $\chi_b^2 \leq 15$  requirement.

An octuple surviving a) and b) is processed further. The right-left ambiguity has to be solved. There are  $2^8 = 256$  possible ways of choosing an octuple of  $\epsilon_j$ 's. If we can solve a number  $m < 8$  of ambiguities in a different way, however, only  $2^{8-m}$  combinations will be left. The following procedure was adopted. Step b) above provides:

$$\chi_1^2 = \chi_b^2 = \underline{r}^+ G_\xi^{-1} \underline{r} = \sum_{ij} r_i (G_\xi^{-1})_{ij} r_j$$

where  $\underline{r}$  is given by equation (A7.14). Its components are the residuals of the fit. The ratio

$$R_j = r_j / s_j$$

is calculated for  $j = 1,8$ . We then set

$$\xi_j = w_j + \epsilon_j s_j \quad (A8.1)$$

$$(G_\xi)_{ij} = \delta_{ij} \left[ \sigma^2 + |\epsilon_j| (s_j^2 - \sigma^2) \right] \quad (j = 1,8) \quad (A8.2)$$

where

$$\epsilon_j = R_j / |R_j| \quad \text{if } R_{\min} \leq |R_j| \leq R_{\max} \quad (\text{A8.3'})$$

$$\epsilon_j = 0 \quad \text{if } |R_j| < R_{\min} \quad \text{or} \quad |R_j| > R_{\max} \quad (\text{A8.3''})$$

and  $\sigma = 500$  microns. The right-left ambiguity is considered solved, if condition (A8.3') is true.  $\xi_j$  is reset to the value (A8.1) and a small error  $\sigma$  is assigned to it. A new fit is performed with the values (A8.1) and the error matrix (A8.2) until the condition (A8.3') is verified for at least one plane, i.e., until the procedure is effective in solving ambiguities. If  $m < 8$  is the number of ambiguities solved in this way, the remaining  $8-m$  will be solved by trying all the possible  $(8-m)$ -ples of  $\epsilon_j$ 's in (A8.1) and (A8.2) and selecting the one which yields the lowest  $\chi^2$ . Equation (A5.9) will provide the track parameters of the identified track.

Monte Carlo studies showed this procedure to be quite reliable. If hits on each of the planes are generated with a random error of  $500\mu$ , the number of misassignments is below 2%. Optimal values for  $R_{\min}$  and  $R_{\max}$  were found to be .75 and 1.5.

## REFERENCES

- 1) Wilson, R.R. (1958) Phys. Rev. 110, 1212.
- 2) Braunschweig et al. (1975) Phys. Lett. 57B, 407.
- 3) Bloom, E. 1979 Photon-Lepton Symposium Proceedings.
- 4) Moorhouse, R.G. Electromagnetic interaction of hadrons, vol. I. Plenum Press. New York and London (1978).
- 5) Leith, D.W. G.S. Electromagnetic interaction of hadrons, vol. I. Plenum Press. New York and London (1978).
- 6) Kogan, E. et al. SLAC-PUB-1857.
- 7) Caldwell et al. (1978), Phys. Rev. Lett. 40, 1222.
- 8) Benaksas et al. (1972), Phys. Lett. B39, 289; B42, 507; B48, 155; B40, 685.  
Salvini et al. (1974), Italian Physics Society Summer Meeting, Proc.
- 9) Taylor, R.E. (1975), Lepton-Photon Symposium, Proc.
- 10) Bjorken and Paschos (1969), Phys. Rev. 185, 1975.
- 11) Egloff, R.M. Ph.D. Thesis. Univ. of Toronto (1979).
- 12) Storrow, J.K. Electromagnetic interaction of hadrons, vol. I. Plenum Press. New York and London (1978).
- 13) Primakoff, H. (1951), Phys. Rev. 81, 899.
- 14) Particle Data Group. LBL100 (1978).
- 15) Grillo, A.A. Ph.D. Thesis, Univ. of California, Santa Cruz (1980).
- 16) Alvensleben et al. (1971), Nucl. Phys. B25, 342.
- 17) Ballam et al. (1972), Phys. Rev. D5, 545.
- 18) Joos, H. (1967), Acta Phys. Austriaca, Suppl. IV.
- 19) Lipkin, H.J. (1966), Phys. Rev. Lett. 16, 1015.
- 20) Oakes et al. (1967), Phys. Rev. Lett. 19, 1266  
Das et al. (1967), Phys. Rev. Lett. 19, 470.



- 21) Gell-Mann, M. et al. (1962), Phys. Rev. Lett. 8, 261.
- 22) Bauer et al. (1978), Rev. of Mod. Physics, 50, Vol. 2, 261.
- 23) Breakstone, A.M., Ph.D. Thesis, Univ. of California, Santa Cruz (1980).
- 24) Breskin, A., et al. (1974), N.I.M. 119, 9.
- 25) Palladino, V. and B. Sadoulet (1975), N.I.M. 128, 323.
- 26) Bouclier, R. et al. (1970) N.I.M. 88, 149.
- 27) Cheng, D.C., et al. (1973), Harvard Preprint.
- 28) Holstein, T. (1946), Phys. Rev. 70, 367.
- 29) Solmitz (1961), Ann. Rev. Nucl. Sci.